Condensation and homogenization of cross sections for the deterministic transport codes with Monte Carlo method : Application to the GEN IV fast neutron reactors

Li Cai

UNIVERSITÉ PARIS SUD
Comprendre le monde, construire l'avenir®

DE LA RECHERCHE À L'INDUSTRIE
cea

Université Paris-Sud 11
ED 534 MIPEGE
Modélisation et Instrumentation en Physique, Energies, Geosciences et Environnement

Université Paris-Sud

Ecole Doctorale 534:
MODÉLISATION ET INSTRUMENTATION EN PHYSIQUE, ÉNERGIES, GÉOSCIENCES ET ENVIRONNEMENT

Laboratoire d'Étude de Physique

Discipline : Physique

Thèse de doctorat

Soutenue le 30/10/2014 par

Li CAI

Condensation et homogénéisation des sections efficaces pour les codes de transport déterministes par la méthode de Monte Carlo

: Application aux réacteurs à neutrons rapides de GEN IV

Directeur de thèse :	M. Cheikh M. DIOP	Directeur de Recherche (CEA)
Encadrant de thèse :	M. Yannick PÉNÉLIAU	Ingénieur-Chercheur (CEA)

Composition du jury :

Rapporteurs :	M. Alain HÉBERT	Professeur (École Polytechnique de Montréal)
	M. Alexis NUTTIN	Maître de Conférences HDR (PHELMA/LPSC)
Examinateurs :	M. Enrico GIRARDI	Docteur (EDF)
	M. Laurent TASSAN-GOT	Directeur de Recherche (Univ. PARIS SUD 11)
	M. Christos TRAKAS	Docteur (AREVA)

Résumé

Dans le cadre des études de neutronique menées pour les réacteurs de GEN-IV, les nouveaux outils de calcul des cœurs de réacteur sont implémentés dans l'ensemble du code APOLLO3® pour la partie déterministe. Ces méthodes de calculs s'appuient sur des données nucléaires discrétisées en énergie (appelées multi-groupes et généralement produites par des codes déterministes eux aussi) et doivent être validées et qualifiées par rapport à des calculs basés sur la méthode de référence Monte-Carlo. L'objectif de cette thèse est de mettre au point une technique alternative de production des propriétés nucléaires multi-groupes par un code de Monte-Carlo (TRIPOLI-4®).

Dans un premier temps, après avoir réalisé des tests sur les fonctionnalités existantes de l'homogénéisation et de la condensation avec des précisions accrues, accessibles aujourd'hui sur les machines actuelles, des incohérences sont mises en évidence. De nouveaux estimateurs de paramètres multi-groupes ont été développés et validés pour le code TRIPOLI-4® à l'aide de ce code lui-même, puisqu'il dispose de la possibilité d'utiliser ses propres productions de données multi-groupes dans un calcul de cœur.

Ensuite, le problème de l'aujourd'hui, notamment introduite par la fuite des neutrons a été étudié. Une technique de correction de la diagonale de la matrice de la section efficace de transfert par diffusion à l'ordre P1 (nommée technique IGSC et basée sur une évaluation du courant des neutrons par une technique introduite par Todorova) est développée. Une amélioration de la technique IGSC dans la situation où les propriétés matérielles du réacteur changent drastiquement en espace est apportée. La solution est basée sur l'utilisation d'un nouveau courant qui est projeté sur l'axe X et plus représentatif dans la nouvelle situation que celui utilisant les approximations de Todorova, mais valable seulement en géométrie 1D.

A la fin, un modèle de fuite B1 homogène est implémenté dans le code TRIPOLI-4® afin de produire des sections efficaces multi-groupes avec un spectre critique calculé avec l'approximation du mode fondamental. Ce modèle de fuite est analysé et validé rigoureusement en comparant avec les autres codes : Serpent et ECCO ; ainsi qu'avec un cas analytique.

L'ensemble de ces développements dans TRIPOLI-4® permet de produire des sections efficaces multi-groupes qui peuvent être utilisées dans le code de calcul de cœur SNATCH de la plateforme PARIS ou dans d'autres codes de coeur. Ce dernier utilise la théorie du transport qui est indispensable pour la nouvelle filière à neutrons rapides. Les principales conclusions sont :

- Le code de réseau en Monte-Carlo est une voie intéressante (surtout pour éviter les difficultés de l'autoprotection, de l'anisotropie limitée à un certain ordre du développement en polynômes de Legendre, du traitement des géométries exactes 3D), pour valider les codes déterministes comme ECCO ou APOLLO3® ou pour produire des données pour les codes déterministes ou Monte-Carlo multi-groupes.
- Les résultats obtenus pour le moment avec les données produites par TRIPOLI-4® sont comparables mais n'ont pas encore vraiment montré d'avantage par rapport à ceux obtenus avec des données issues de codes déterministes tels qu'ECCO.

Mots-clés : Monte-Carlo, condensation, homogénéisation, anisotropie, RNR

Abstract

In the framework of the Generation IV reactors neutronic research, new core calculation tools are implemented in the code system APOLLO3® for the deterministic part. These calculation methods are based on the discretization concept of nuclear energy data (named multi-group and are generally produced by deterministic codes) and should be validated and qualified with respect to some Monte-Carlo reference calculations. This thesis aims to develop an alternative technique of producing multi-group nuclear properties by a Monte-Carlo code (TRIPOLI-4®).

At first, after having tested the existing homogenization and condensation functionalities with better precision obtained nowadays, some inconsistencies are revealed. Several new multi-group parameters estimators are developed and validated for TRIPOLI-4® code with the aid of itself, since it has the capability to use its multi-group constants in a core calculation.

Secondly, the anisotropy effect which is necessary for handling neutron leakage case is studied. A correction technique concerning the diagonal line of the first order moment of the scattering matrix is proposed. This is named the IGSC technique and is based on the usage of an approximate current which is introduced by Todorova. An improvement of this IGSC technique is then presented for the geometries which hold an important heterogeneity property. This improvement uses a more accurate current quantity which is the projection on the abscissa X. The later current can represent the real situation better but is limited to 1D geometries.

Finally, a homogeneous B1 leakage model is implemented in the TRIPOLI-4® code for generating multi-group cross sections with a fundamental mode based critical spectrum. This leakage model is analyzed and validated rigorously by the comparison with other codes: Serpent and ECCO; as well as with an analytical case. The whole development work introduced in TRIPLI-4® code allows producing multi-group constants which can then be used in the core calculation solver SNATCH in the PARIS code platform or any other deterministic code in principle. The latter uses the transport theory which is indispensable for the new generation fast reactors analysis. The principal conclusions are as follows:

- The Monte-Carlo assembly calculation code is an interesting way (in the sense of avoiding the difficulties in the self-shielding calculation, the limited development order of anisotropy parameters, the exact 3D geometries) to validate the deterministic codes like ECCO or APOLLO3® and to produce the multi-group constants for deterministic or Monte-Carlo multi-group calculation codes.

- The results obtained for the moment with the multi-group constants calculated by TRIPOLI-4® code are comparable with those produced from ECCO, but did not show remarkable advantages.

Key words: Monte-Carlo, condensation, homogenization, anisotropy, multi-group, cross section, transport calculation, RNR.

Remerciements

J'ai l'impression que c'était hier que j'arrivais au SPRC, pourtant aujourd'hui trois années se sont écoulées. Si le temps est passé si vite, c'est grâce à toutes les personnes qui ont fait mon quotidien et que je souhaite ici remercier. Dans un premier temps, je tiens à exprimer toute ma reconnaissance à mon encadrant de thèse Yannick Pénéliau. Je n'oublierai jamais les nombreuses feuilles qu'il m'a notées, depuis le premier jour où je suis arrivée avec la présentation sur la structure du SPRC, jusqu'aux dernières remarques sur la répétition de ma soutenance. Il m'a fait bénéficier de toute son expérience sur TRIPOLI et aussi de sa grande sagesse sur les méthodes de travail. Ma gratitude va aussi envers mon directeur de thèse Cheikh Diop qui était mon professeur de neutronique et qui m'a encouragée à poursuivre en thèse. Son attitude extrêmement rigoureuse sur la recherche et le travail est pour moi un modèle.

Je remercie ensuite tous les membres de mon jury : Laurent Tassan-got de présider, MM. Alain Hébert et Alexis Nuttin d'avoir lu consciencieusement ma thèse et de l'avoir rapportée et enfin MM. Christos Trakas et Enrico Girardi d'avoir examiné mon travail et d'avoir apporté leur point de vue du côté industriel. Je les remercie aussi pour les discussions intéressantes autour des sections efficaces micro- et macroscopiques.

Je remercie sincèrement mon chef de laboratoire Cyrille De-Saint-Jean et mon chef de service Frédéric Varaine pour m'avoir accueillie pendant ces 3 ans et surtout pour leurs conseils sur mes perspectives de carrière.

Mes chaleureux remerciements vont bien sûr à tous les membres de LEPh : mon coach déterministe Jean Tommasi qui était presque mon deuxième encadrant non-officiel; Jean-François Vidal qui m'a fait découvrir le flux asymétrique et aussi le fameux modèle de fuite hétérogène ; Gérald Rimpault pour ses critiques pertinentes qui m'ont permis d'avancer ; Pascal Archier qui s'est penché sur mon problème du cœur/réflecteur ; Bénédicte Roque pour ses conseils lors de la préparation de la soutenance ; notre secrétaire dynamique et efficace Alexandra Herrenschmidt et tous les autres permanents du labo qui ont contribué par leur bonne humeur à rendre mon temps de travail plus joyeux. Un grand merci à tous les autres SPRCiens du Bât 230, notamment Coralie Carmouze qui m'a fait partager les bonnes astuces de la vie Aixoise et aussi le super service à domicile pour fluidifier mon discours de soutenance.

Encore beaucoup de remerciements son réservés pour notre armée de thésards. Par ordre d'ancienneté : mon pionner boltzmannien Ansar ; mon expert parisien Simon ; mon cher ex-co-bureau et coach sportif Nicolas (merci à toi d'avoir donné une très bonne ambiance en 007) ; mon accompagnateur toujours pour le bus de 6h30 David; ma conseillère stratégique Florence et Amalia qui vient de loin pour me soutenir. Ensuite, Guillaume (K.) et Cyrille (B.) qui ont commencé en même temps que moi et avec qui on a souvent discuté des démarches de rédaction, de soutenance et de cherche d'emploi. Arrive la vague suivante de forces vives: Léonie avec qui on partage plein de petits secrets au parc de la Torse ; Pierre toujours souriant et disponible pour m'écouter ; Guillame (T.), le maître du flux adjoint et des cookies bayonnais ; Edwin, mon co-bureau qui me soutient pendant toute ma période de rédaction. Enfin, Nans, Maxence et Nicolas (T.) pour leur gentillesse lors de ma phase de rédaction.

Un merci particulier doit être attribué à Liu Feng qui m'a accompagnée tout au long de la thèse et en particulier dans les moments difficiles. Un grand merci également à Jéronimo pour les jambons ibériques et les omelettes.

Merci à mon Aymeric, le trésor et l'énergie éternelle de ma vie.

Tout à la fin, je ne peux pas juste dire merci à mes parents parce que cela ne suffira jamais assez. Ils m'ont tout donné afin que je réussisse mes études.

Contents

General Introduction

The prediction from the International Energy Agency (IEA) points out that the world-wide energy consumption will increase by 63%[10] between 2002 and 2030 because of the population growth and increase in the living standards. Meanwhile, the gradual dwindling of the fossil resources and the socio-political problems associated with carbon emissions force us to search for other cleaner and efficient energy sources. An important effort is being made to determine and develop the future of energy production. Renewable energies such as solar and wind power have still low efficiencies and require large surface areas for setup. Moreover, their integration into electricity grid is quite challenging due to their intermittent availability requiring high storage and backup capabilities as well as "smart" grid operations. Otherwise, fusion power is theoretically a good choice but is still far from being operational.

In this important energy transition period, nuclear fission energy holds an important place with two main advantages as follows: negligible greenhouse gas emissions, large and regular production of electricity. The international community is aware of the important role played by the nuclear fission energy. Well a dozen countries decided to work together for developing the new generation nuclear fission reactors aimed at providing sustainable, safer and efficient energy. Under this background, the fourth generation forum, created in 2000, is the first significant step towards Generation IV (GEN-IV)[46].

GEN-IV reactors aim to exhibit at least the same safety standards as the previous generation and also provide significant advances in future designs. Firstly, the uranium resource, just as the classical energy resources oil or gas, has a limited stock. According to some experts, it is limited to approximate hundreds years[8] consumption with current nuclear reactor systems. So the fast neutron reactor technology, which falls under the aegis of GEN-IV reactors, could extend the utilization of the uranium reserves till several thousand years. Secondly, the nuclear waste management is an embarrassing issue and provokes certain conflicts concerning the potential safety risk. Gen-IV reactors aim to solve this issue by burning a large part of the long-live nuclear wastes, thereby reducing their volume as well as their toxicity. The GEN-IV reactors continue to make efforts to improve the safety of the installation facilities to reduce the risks and potential consequences of an accident while remaining economically viable. Lastly, they provide an unattractive and least desirable route for diversion and theft of weapon-usable materials and hence are resistant to nuclear proliferation. Six types of reactors are proposed and being studied by the researchers from different partner countries participating in the Gen-IV forum. France has chosen to go on with sodium cooled fast reactors mainly because of the maturity of the SFR concept, available know-how, prior experience in the country with reactors such as HARMONIE, RAPSODIE, PHÉNIX[88], SUPERPHÉNIX, consistency with the strategic national objectives of closed fuel cycles and long lived waste management. France, being

one of the leaders in the nuclear energy market, obtains more than 75% of the electricity share from its nuclear power plants consisting of 58 Pressurized light Water Reactors (PWR).

In order to closely supervise and monitor these industrial reactors, the nuclear core modeling and calculations must be performed with high precision and efficiency. Within the framework of industrial calculation, time cost is one of the most important criteria to evaluate a calculation tool. For example, to figure out the optimal loading map, or during the analysis of accidental situations where multi-physics disciplines are concerned, thousands of calculations should be carried out in a limited interval of time ($\sim$ 10 seconds). At the same time, reducing the calculation bias is another long lasting mission for the industrial calculation. The latter encourages the neutronic physicists to develop more accurate and more sophisticated calculation codes which are indispensable for the reactor safety analysis. On the other hand, the complexity of the input data library (continuously dependent on the energy variable and even on the angular variable for some specific data types) and the complication of the reactor geometry make it difficult to fulfil the industrial calculation mission.

In order to reduce the number of unknowns (more than 10^{11}) to be solved, two modeling steps are necessary to accomplish the whole core calculation, namely the sub-assembly calculation step and the core calculation step. This two steps calculation strategy is based on the fundamental mode[1] calculation and implies the concept of "*equivalence*" specifying the necessity to preserve the reactions rates from a realistic configuration to a simplified configuration which is adapted in an industrial core calculation. It could be expressed by Eq (1) where τ represents the reaction rate. The indices (m, g) correspond to the referential configuration which is heterogeneous spatially as well as in energy. And (M, G) correspond to the simplified homogeneous configuration. Therefore, V_m, $\overline{\Sigma}_{m,g}$ and $\overline{\phi}_{m,g}$ are namely the micro-region volume, micro-region homogenized fine-group cross section and flux. On the other hand, V_M, $\overline{\Sigma}_{M,G}$ and $\overline{\phi}_{M,G}$ represent the macro-region and macro-group parameters. The fact of collapsing fine-group g into macro-group G is termed "energy condensation" while merging micro-region m into macro-region M is termed "spatial homogenization" [84]. Graceful to these macroscopic macro-group cross sections, it becomes feasible and efficient to perform a 3D transport calculation on the homogenized whole core geometry.

$$\tau_{M,G} = \sum_{g \in G} \sum_{m \in M} V_m \overline{\Sigma}_{m,g} \overline{\phi}_{m,g} = V_M \overline{\Sigma}_{M,G} \overline{\phi}_{M,G} \tag{1}$$

However, several difficulties are revealed in the above multi-scale calculation methodology. In order to understand where these difficulties come from, a deterministic calculation scheme is at first shown in Figure 1. It contains two parts: one is the illustrative picture stating the relationship between sub-assembly calculation and core calculation; the other one describes precisely each processing step from the nuclear evaluated data towards macro-group cross sections which could finally be used in a core simulation.

The first difficulty exists in the procedure of converting point-wise evaluated data into fine-group cross sections. To obtain the appropriate fine-group cross sections which ensure the preservation of reaction rates with respect to point-wise case, it is indispensable to

[1]The fundamental mode is used to represent a homogeneous infinite medium situation in the first step sub-assembly calculation.

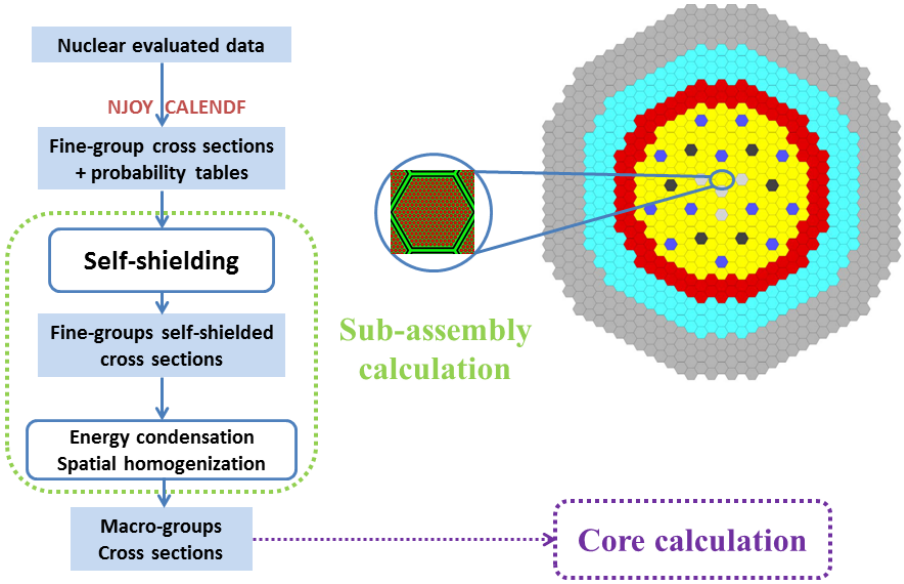

Figure 1: Deterministic calculation scheme. NJOY[37] and CALENDF[91] are both data processing tools

use an appropriate weighting function. Unfortunately, the latter is in fact the solution demanded in the realistic heterogeneous problem and hardly available. Therefore, an approximate weighting function is used which will definitely induce some calculation bias. Meanwhile, the energy collapsing procedure surely results into loss of information, especially in the resonant energy domain. This forms the second difficulty under the name of self-shielding. The latter could be achieved by several methods, such as the method of Livolant-Jeanpierre[36] or the method of sub-group[25, 67]. Although, these methods have more or less some limitations which cause some bias for final results. The third difficulty concerns the ability of handling the heterogeneous geometry. The solvers used to perform the energy condensation and spatial homogenization procedures are usually limited to treat 2D heterogeneous geometries. Recently, the solver method of characteristics (MOC) is able to treat extruded 3D heterogeneous geometries. However, the latter method needs to stock a large amount of neutron trajectories which demands a high memory usage and a long calculation time.

Besides the above mentioned limitations of deterministic calculation scheme, a completely different method is becoming more and more popular in the nuclear reactor analysis field which is under the name of Monte-Carlo[72, 34]. The main characteristic of the Monte-Carlo method is the ability to follow each neutron trajectory history and give out a microscopic score. The ensemble of these microscopic scores could help to estimate the macroscopic physical variables. Thanks to this feature, Monte-Carlo method is able to avoid those approximations which are exploited in deterministic approach. Furthermore, it could be used to validate as well as analyze the deterministic calculation method. Subsequently, it also inspires us to explore the field of sub-assembly calculation (energy condensation and spatial homogenization) with Monte-Carlo method. The main advantages of using Monte-Carlo method produced multi-group homogenized cross sections are as follows:

- exact simulation of interaction between neutron and material,

- directly using point-wise library data and no necessity of self-shielding approximation, except in the unresolved energy domain,
- usage of exact anisotropy data rather than their approximate Polynomial development form,
- calculations of exact three-dimensional geometries

Before deciding which type of the second step core calculations will make use of our Monte-Carlo produced multi-group cross sections, it should recall that this work is initially motivated for the conception and analysis of the ASTRID (Advanced Sodium Technological Reactor for Industrial Demonstration). The latter is a sodium-cooled fast reactor prototype which will be constructed in France around 2020. The main characteristics of this reactor is the use of a new core concept CFV (low void effect core) to improve the safety aspect. This concept implies a high geometrical heterogeneity due to the presence of the sodium plenum in the upper side and a fertile plate in the middle of the fissile sub-assembly. Moreover, different calculation concepts exist in the core calculation step which necessitates different formats of the multi-group cross sections. Mostly, a diffusion theory based core calculation code is sufficient for a PWR core simulation. However, it is not the case for a fast neutron reactor calculation since the latter has usually more heterogeneous geometrical and spectral distributions. This is the reason for that our work aims to supply the produced multi-group cross sections in a transport core calculation code. Additionally, the transport core calculation codes solve more or less the same type of transport equation as in the previous sub-assembly calculation step. This forces us to produce the conventional format multi-group cross sections which are adapted for the existing transport core calculation codes.

The main objective of this work is to produce multi-group cross sections with the Monte-Carlo code TRIPOLI-4® developed at CEA[2] and use these generated multi-group constants in transport theory based core simulation codes. Its principal application is for the fast neutron reactor type sub-assemblies.

Within this context, this document is divided into three parts. The first part summarizes the necessary neutronics background. It starts with some conventional definitions of neutronics parameters followed by an introduction of continuous-energy neutron transport equation and the general problems related to sub-assembly homogenization. Previous works using deterministic method for energy condensation and spatial homogenization are separately presented. The theoretical background ends with a brief presentation about the stochastic method and a listing of worldwide Monte-Carlo codes which are able to produce multi-group cross sections.

The second part presents the improvements carried out on the existing routines of homogenization and condensation procedures in TRIPOLI-4®. First of all, we make sure that the sub-assembly calculation routine in TRIPOLI-4® is able to preserve the infinite multiplicative factor K_∞ as well as the neutronic balance for homogeneous infinite geometries. This work is achieved by implementing three new Monte-Carlo multi-group constants estimators, namely the group-wise energy transfer probabilities; the excess weight and the fission spectrum. Secondly, we continue to enforce the capability of the sub-assembly calculation routines in TRIPOLI-4® code for leakage involved finite geometry cases. For

[2]Commissariat à l'énergie atomique et aux énergies alternatives, France

this, a new technique in charge of multi-group anisotropy construction work is developed. However, this technique is quite efficient for homogeneous finite geometries but is not validated for heterogeneous sub-assembly case. As for this residual problem, a solution is proposed in the next chapter which could overcome the difficulty encountered in highly different material properties geometry case.

The third part focuses on the development of a leakage model in TRIPOLI-4® code. A brief history about the Monte-Carlo based leakage models is summarized after which we choose B_1 homogeneous equation based leakage model for this work. A detailed description is given for the implementation of this leakage model including the corresponding rigorous validation work. The validation study is hardly found in other similar Monte-Carlo codes.

This document ends with a conclusion reminding the principal results and several perspectives for future research.

Part I

Theoretical Background

Chapter 1

Neutronics Background

This chapter is aimed to describe some related neutronics backgrounds which are divided in three parts: interactions between neutrons and materials; physical definition of cross section ; the definitions of neutron flux and reaction rate. These physical backgrounds are particularly helpful to have a better comprehension of the neutron transport codes based on the Monte Carlo method where each neutron trajectory is followed from its birth till the end.

1.1 Neutrons-Materials Interactions

The interactions between neutrons and matter play an important role in nuclear fission reactors. Their reactions mechanism ensures a self-sustained energy release process. In the field of nuclear reactor physics, these interactions refer to those occurring between neutrons and the nuclei existing in the materials. Other reactions, such as neutron-electron or neutron-neutron, are usually neglected by neutronics physicists.

The reasons why neutron-electron interactions can be ignored are the following: first, their collision probability is rather low; secondly, even after colliding with an electron, the neutron will hardly deviate because its mass ($\sim 10^{-27}$ kg) is much greater in comparison to the electron one ($\sim 10^{-31}$ kg). Neutron-neutron reactions are neglected because of the low neutron density in the nuclear reactor medium compared to nuclei density. This simplification leads to a linear neutron transport theory presented by the Boltzmann equation. The linearity is based on the fact that the neutron density in the Boltzmann equation is at order 1.

Return back to the main interactions occurring in a nuclear fission reactor i.e. the neutron-nuclei reactions. They are classified into various reaction types according to the different neutron incident energies. It should be pointed out that neutron-matter interactions mentioned here are mediated by the strong nuclear force which is limited within the range of 10^{-15} m (the same order of magnitude as the nuclei diameter). Therefore, when the incident neutron energy is too low, its wave length is rather large compared with the target nucleus one. Thus, the neutron represented principally by the wave property is scattered by the target nuclear field . This phenomenon is called potential scattering which is similar to the elastic collision between two hard bodies, with conservation of momentum and kinetic energy. This reaction can be performed by all kinds of nuclei with neutron with any incident energy. Beside of the potential scattering, all the other interaction types follow the same pattern: firstly, formation of an excited compound-nucleus which includes

the binding energy as well as the kinetic energy of the incident neutron; then, living life of the created compound-nucleus on an excited state; finally, disintegration of the isotope to a lower level. There exist several different mechanisms of disintegrations which define thus different reaction types. In the field of neutron transport, they are divided specifically into: capture reaction, fission reaction and scattering reaction.

To be marked that the excitation energy of the created compound isotope is rather high. However, the binding energy alone (about $5 \sim 10$ MeV) is not sufficient to induce all types of reactions. Thus, some kinetic energy has to be supplied by the incident neutron to make the reaction possible. This is so-called threshold reactions which could be found in all the three reaction types. In the following table, principal reaction types are listed with their own characteristics. Detailed descriptions about each reaction type will be subsequently presented in the following paragraphs.

Reaction Type		Reaction Formula	Formation of Compound-nucleus	Threshold Reaction
Scattering	Potential elastic scattering	$n + A \Rightarrow A + n$	no	no
	Elastic resonant scattering	$n + A \Rightarrow A + n$	yes	no
	Inelastic resonant scattering	$n + A \Rightarrow A^* + n;\ A^* \Rightarrow A + \gamma$	yes	yes
	Multiplication scattering	$n + A \Rightarrow (A - X) + Xn$	yes	yes
Fission		$n + A \Rightarrow FP_1 + FP_2 + \nu n$	yes	only odd number of neutrons in thermal spectrum
Capture	Radiative capture	$n + A \Rightarrow (A + 1) + \gamma$	yes	no
	Charged particle ejection reaction	$n + A \Rightarrow B/C + p/\alpha$	yes	yes

Table 1.1: Principal reactions occurring in a nuclear fission reactor

1.1.1 Scattering

As shown in Table 1.1, there are mainly four different scattering modes in the nuclear fission reactor domain. The two first of them: potential elastic scattering and elastic resonant scattering are both elastic reactions. Their common feature is that they preserve the total kinetic energy as well as the total momentum of the concerned particles (neutron and target nuclei). In contrary, the two other reactions belong to inelastic scattering reactions where there is a part of the energy which remains in the residual nucleus and finally taken away by the emission of gamma.

In fact, the original difference of these four scattering reactions comes from the different incident neutron energies. Low-energy neutrons usually induce elastic scattering reactions with any kind of isotope. It is particularly the case for potential elastic scattering. When the neutron incident energy increases, the particle begins to interact with the constituent nucleons in the target nuclei. Thus the scattering reaction starts to become resonant. So if the excited compound-nucleus can disintegrate directly to its ground state, this is named elastic resonant scattering. Moreover, there are resolved resonance, unresolved resonance in the resonant energy range and then followed by a continuum range.

When the compound-nucleus reaches the energy region where the excited levels are still discrete and could be detected by experimental measurement, that is termed ″resolved resonance scattering″. If the excited compound-nucleus is always in a distinguishable state but no more measurable, it is called ″un-resolved resonance range″. Special techniques, for example, the probability tables are used to treat this energy domain. Beyond the resonant range where the resonant peaks overlap, this is called the continuum region.

Inelastic scattering occurs always with high incident energy neutron because of the necessity of a threshold energy to make the compound-nucleus reach at least on its first excited level. Then this compound-nucleus decays into an excited state after ejection of a neutron. Finally, the excited nucleus gets down to its ground state via photon-emission. This means that the total energy of the system is, at the end, shared among the emergent neutrons, the target nucleus and also the emitted photons. The separation for the different resonant regions is also available in the inelastic scattering case. However, with the energy limit in the fission reactor physics (below 20 MeV), we may not be able to observe the different resonant regions, particularly for some heavy even-nucleon nuclei.

If the incident neutron energy becomes still higher ($\sim$ MeV), some multiplication scattering reactions could occur where two or more neutrons are emitted. In the nuclear fission reactor simulation codes, these reactions are usually considered as scattering rather than neutron production reactions.

1.1.2 Fission

Nuclear fission of heavy elements was discovered in 1938 by Otto Hahn, Fritz Strassmann and Lise Meitner. It refers to an exo-energetic process that split a heavy nucleus into two fragments and several free neutrons as well as other particles (γ, β, $\overline{\nu}$). Thanks to its characteristics (self-sustained chain reaction and important energy release), it plays a key role in a nuclear fission reactor. There are two kinds of fission considered here: spontaneous fission and fission induced by neutron. The difference between the two reactions is that for some nuclei, an amount of energy needs to be added to initiate the nucleus deformation process. This is illustrated in Figure 1.1. In the liquid drop model, the addition between the surface energy term and the coulomb energy term gives out a mass change curve versus the deformation of the compound-nucleus. It shows a hump at the beginning of deformation which represents a fission barrier.

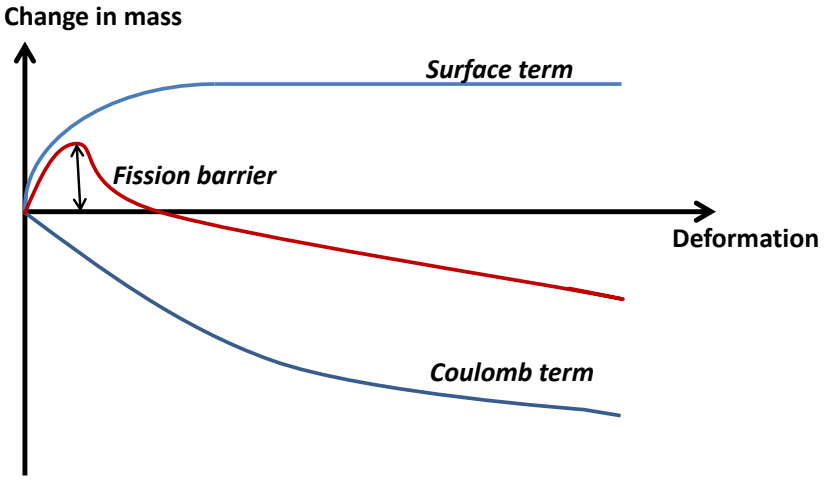

Figure 1.1: Illustration of fission barrier

The height of the fission barrier varies slightly among the different nucleus. Seaborg's formula [80] shows that the barrier for even(proton number Z)-even(neutron number N) nuclei is the lowest. The energy demanded to overcome the fission barrier comes from the binding energy of the absorbed neutron as well as from its kinetic energy. Sometimes, the binding energy is high enough to cover the fission barrier, for example, in the case of ^{235}U. Otherwise, some kinetic energy is necessary for the incident neutron to induce the fission reaction, for example, in the case of ^{238}U. The property highlighted by the two different cases is termed "parity" effect. That is to say if an even(Z)-even(N) compound-nucleus is formed, its binding energy is much greater than an even(Z)-odd(N) one. The kind of nuclei that can carry out a fission reaction with very low incident energy neutrons are called fissile isotopes. The second type of nuclei which are only fissionable with high energy ($\sim$ 1 MeV) neutrons are named fertile isotopes.

According to their birth process, neutrons emitted after a fission are classified into two families: prompt neutrons ($\sim 10^{-17}$ s) and delayed neutrons (about 1 s − 1 min). The number of emitted prompt neutrons varies from 2 to 7. Their energy distribution also called prompt fission spectrum is usually modeled as a Watt spectrum. An example of ^{235}U thermal prompt fission spectrum is showed in Figure 1.2. In contrary, the fission spectrum for delayed neutrons is almost constant except in the high energy domain ($\sim$ 4 MeV). The average prompt neutron energy per fission is about 2 MeV, while for the delayed neutrons, the average energy per fission is about 400 keV. Even though there is a small proportion of delayed neutrons, they help to increase effectively the average life of the emitted neutrons. The latter makes a fission reactor controllable.

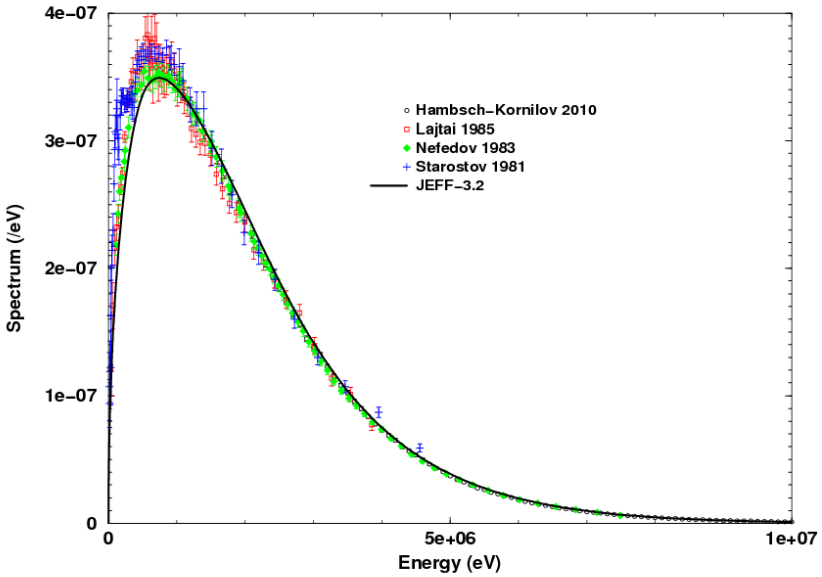

Figure 1.2: ^{235}U thermal fission prompt neutron spectrum

The total energy released during a fission reaction is about 200 MeV. An important

portion of the entire energy is taken away by the two fragments and finally deposited in the fuel composition. Around 3% of the energy is transferred to the kinetic energy of prompt neutrons, and 0.004% for the delayed neutrons. The remaining energy is dispatched among the γ-emissions, β-emissions and neutrino-emissions. There are about 7 MeV gone away with delayed γ and about 7 MeV with delayed β. The two latter constitute the residual power after the shut down of a reactor.

1.1.3 Capture

As shown by the capture formula in Table 1.1, we notify that there is no neutron emitted from capture interactions. This makes it different from other interactions types. In the nuclear reactor field, we name fission and capture together as absorption.

The most common capture mode is the radiative capture because it is a no-threshold reaction, and noted as $(n,\ \gamma)$. The incident neutron is combined with the target nucleus, the excited compound-nucleus decays to its ground state with emission of photons. Equation 1.1 gives an example for ^{238}U. These gamma particles deposit their energy on the nuclear reactor structure which is currently a problematic issue.

$$^{238}U + n \rightarrow^{239} U^* \rightarrow^{239} U + \gamma \tag{1.1}$$

Other capture interaction modes refer to the ejection of a charge particle like $(n,\ p)$, $(n,\ \alpha)$ or $(n,\ ^3He)$. They are usually threshold reactions except for some light isotopes as shown in Equation 1.2.

$$^{10}B + n \rightarrow^{11} B^* \rightarrow^{7} Li +^{4} He \tag{1.2}$$

The resonance exists also in capture interaction as for scattering reaction. At low energy, the resonance peaks are distinguishable. The unresolved resonance range begins generally from several keV for heavy nuclei. It turns always into a continuum region at the end. Detailed curves will be presented in the Section 1.2.

1.2 Definition of the Cross Section

In the previous section, we talked about the different interactions between neutron and matter. To be able to quantify the interactions rates, another demanded essential information concerns their different interactions probabilities. In the field of nuclear physics, the reaction probability between neutron and a target nuclide is defined as a parameter named cross section with the dimension of a surface ($[cm^2]$). The simplest way to explain a reaction probability by a cross section is illustrated in Figure 1.3. In order to have a collision with the target nucleus, the mass center of the neutron has to enter the dashed circle whose radius equals to the sum of those of the neutron and the target nucleus. Thus the surface of this dashed circle represents the cross section noted as σ. Since the radius of a nucleus is on the order of 10^{-14} m, it results that the order of magnitude of the cross section is $\sim\ 10^{-28}$ m^2. In addition, this classical concept agrees well with the experimental measurement values for σ. By the way, cross section is conventionally expressed in unit barns: 1 barn $=\ 10^{-24}$ cm^{-2}.

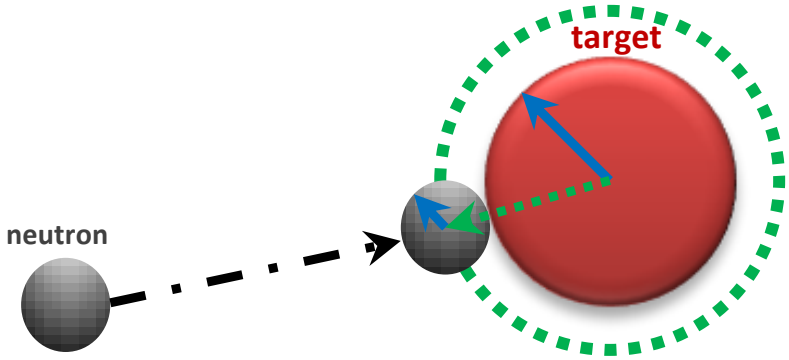

Figure 1.3: Intuitive explanation of cross section

However, the surface area explanation for cross section may not always be available. From the experimental measurements, we observe important discrepancies of σ between different target nuclei as well as for different incident neutron energies. The variation tendencies of cross sections depend on the reaction types. Firstly, if we focus on absorbing kind interactions (fission and capture), a $\frac{1}{v}$ decreasing law dominates generally the whole energy domain, v represents the velocity of the incident neutron. This is confirmed by both Figures 1.4 and 1.5 which are respectively the fission cross section for ^{235}U and the radiative capture cross section for ^{238}U. The $\frac{1}{v}$ tendency could be reasoned with a rather intuitive physical way: to have been absorbed by any nucleus for a neutron, the probability decreases if its velocity increases because it spends less time to pass through the nucleus' nuclear field. Moreover, irregularities begin to appear when resonances are involved. As presented in the previous section, each visible peak in the cross section curve corresponds to a resolved resonance. Then, the resonant peaks are so crowded, which turns to the unresolved resonance region. Finally, resonant peaks overlap completely where the cross section enters the continuum domain.

Figure 1.6 and Figure 1.7 show the elastic scattering cross sections for ^{1}H, ^{12}C which are usually used as moderator elements in thermal nuclear reactors. Their cross section curves are almost constant, unlike the absorbing case. This constant domain results from elastic potential scattering which is predominant at low energy scale. Resonance always exists for elastic scattering (except for ^{1}H) which can be observed from $\sim$ 2 MeV. The very beginning part of the curve shows a decreasing tendency. This is an interesting research topic in the nuclear data field. This non-constant shape comes from the thermal agitation effect[6].

All the cross sections mentioned above are microscopic cross sections which represent the interactions between a single neutron and a single nucleus. Though, in a real nuclear reactor, there are numerous neutrons and nuclei which can interact. To study the propagation of neutrons in matter, it is useful to introduce the variable Σ which describes the material interaction characteristic and is defined as macroscopic cross section calculated by Equation 1.3:

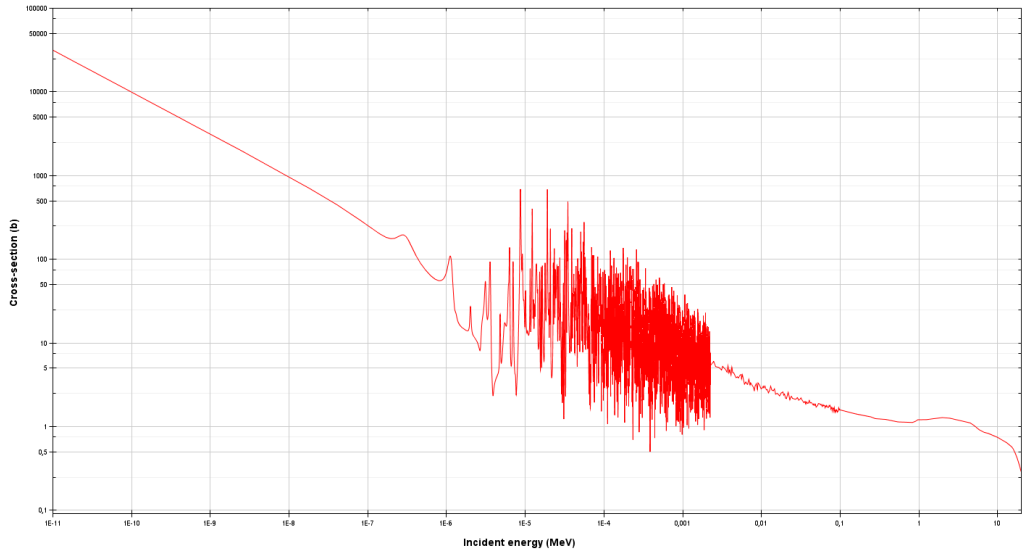

Figure 1.4: ^{235}U fission cross section from JEFF3.1.1

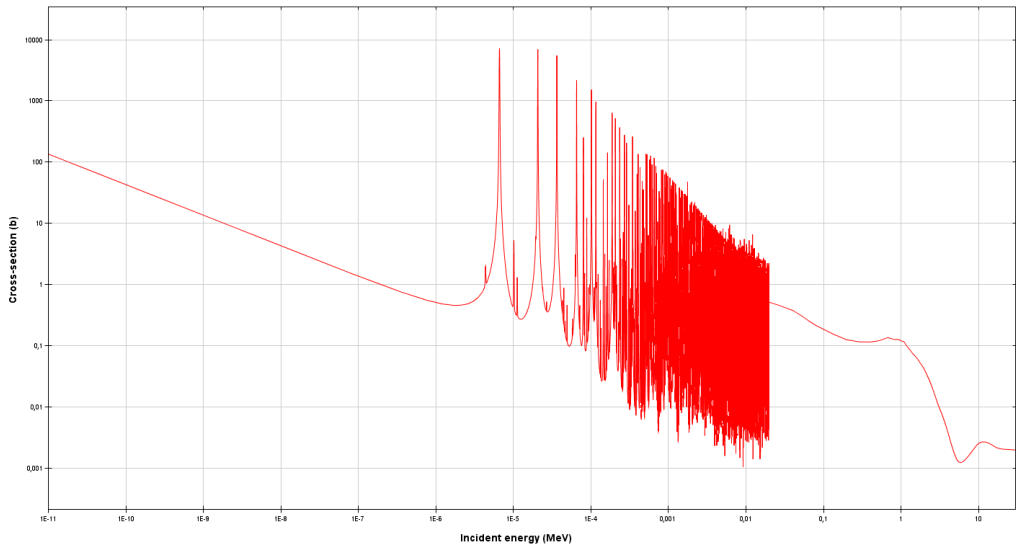

Figure 1.5: ^{238}U radiative capture cross section from JEFF3.1.1

$$\Sigma(\mathbf{r}, E, t)[cm^{-1}] = N(\mathbf{r}, t)\sigma(E) \tag{1.3}$$

with $N(\mathbf{r},\ t)$: the atomic density of the target nucleus at a given moment t. The macroscopic cross section helps to deduce the neutron-matter interaction probability per length unit.

The microscopic and macroscopic cross sections (σ; Σ) defined previously are related to a specific interaction type. Thus, we use index i for marking every different cross section (σ_i; Σ_i) where i could stand for fission, capture or scattering. The sum of the fission cross section and the capture cross section is named the *absorption cross section* (Eq 1.4). By addition to the scattering cross section, one obtains the total cross section (Eq 1.5).

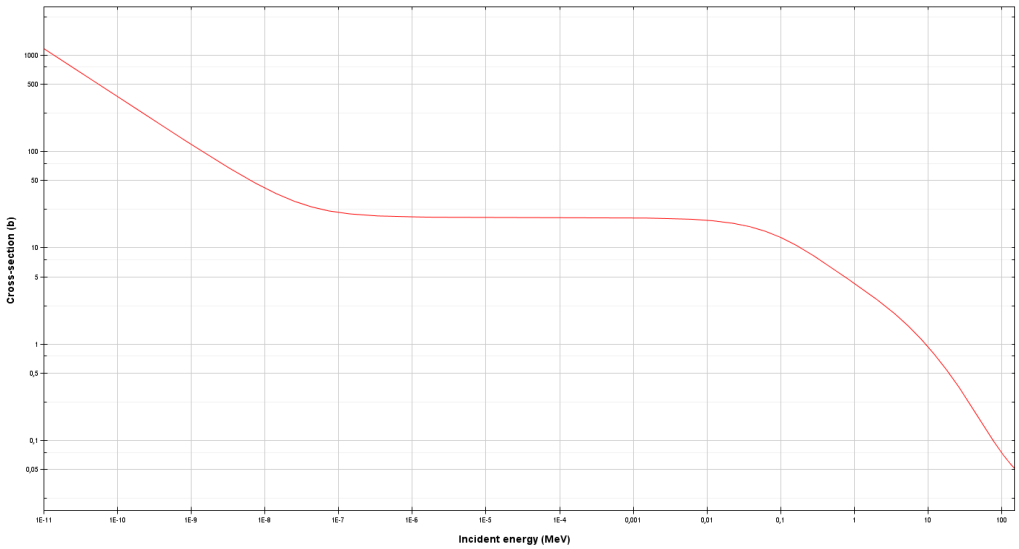

Figure 1.6: ^{1}H elastic scattering cross section from JEFF3.1.1

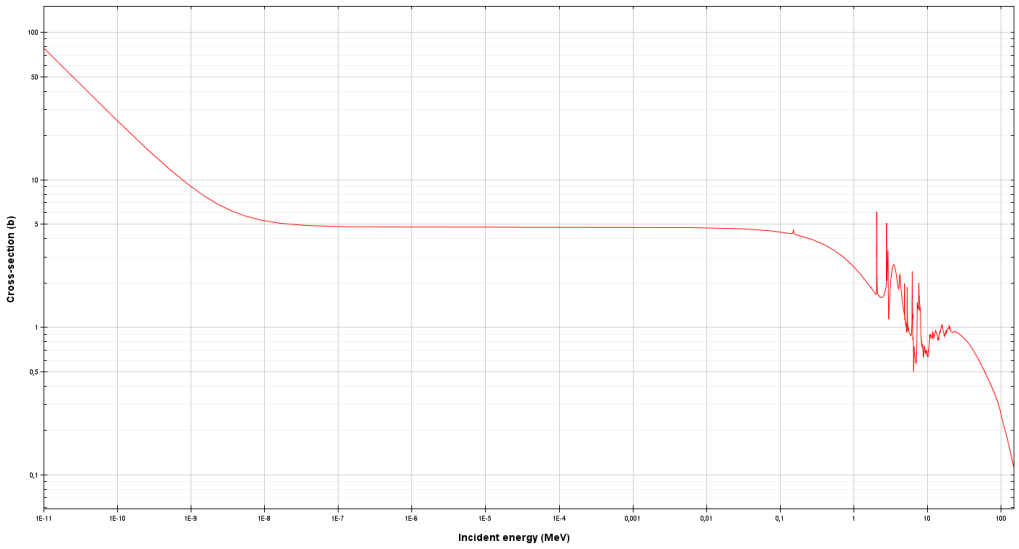

Figure 1.7: ^{12}C elastic scattering cross section from JEFF3.1.1

$$\sigma_a = \sigma_f + \sigma_c; \Sigma_a = \Sigma_f + \Sigma_c \tag{1.4}$$

$$\sigma_t = \sigma_a + \sigma_s; \Sigma_t = \Sigma_a + \Sigma_s \tag{1.5}$$

1.3 Definitions of the Neutron Flux and the reaction rate

From the above sections, we characterized the neutron-matter interaction modes as well as their corresponding interactions cross sections $\sigma_i(E)$ or $\Sigma_i(\mathbf{r}, E, t)$. As shown by its

own definition in Eq 1.3, the macroscopic cross section $\Sigma_i(\mathbf{r}, E, t)$ contains not only the information about the neutron-nucleus interaction probability but also the related material characteristics. Beside of these, we need the information about the neutron population existing in the medium. The neutron population is sufficiently large ($\sim\ 10^8\ cm^{-3}$) to use the common statistical concept "density"to manipulate its variation. The neutron density noted as $n(\mathbf{r}, E, \hat{\Omega}, t)$ represents the number of neutrons per volume of phase space ($\mathbf{r}$, E, $\hat{\Omega}$) $[m^{-3} \cdot eV^{-1} \cdot Sr^{-1}]$ at a certain moment t. For one neutron, the possibility to have a collision with the matter within a distance dx is $\Sigma_t(\mathbf{r}, E, t)dx$. Thus, the total collision number occurred in this elemental volume of phase space is $n(\mathbf{r}, E, \hat{\Omega}, t)\Sigma_t(\mathbf{r}, E, t)dx$. The distance dx could be considered as a path traveled by a neutron with the velocity v during a time dt: $dx = v(\mathbf{r}dt)$. Finally, we obtain a useful quantity describing the number of interactions occurred per unit volume and per unit time in Eq (1.6). This is named reaction rate which is the only neutronic variable in a reactor experiment. Obviously, the total macroscopic cross section Σ_t in the below equation could be replaced by other reaction types, for example, fission or absorption.

$$R[cm^{-3}.s^{-1}] = \Sigma_t(\mathbf{r}, E, t)n(\mathbf{r}, E, \hat{\Omega}, t)v \tag{1.6}$$

If we pay more attention to Eq (1.6), we notice that the reaction rate R is in fact a product between the macroscopic cross section Σ_t and another production term $n(\mathbf{r}, E, \hat{\Omega}, t)v$. The later is defined as the neutron angular flux which depends on the neutron position $\mathbf{r}$, its velocity v or energy E ($E = \frac{1}{2}mv^2$), its direction $\hat{\Omega}$ as well as the time t :

$$\varphi(\mathbf{r}, E, \hat{\Omega}, t) = n(\mathbf{r}, E, \hat{\Omega}, t)v \tag{1.7}$$

If we perform an integration of the angular flux over the whole solid angle, we obtain the expression of scalar flux as below:

$$\phi(\mathbf{r}, E, t) = \int_{4\pi} \varphi(\mathbf{r}, E, \hat{\Omega}, t)d^2\Omega \tag{1.8}$$

For interactions like fission in which the secondary neutrons are emitted isotropically, the scalar flux is more often used to calculate the reaction rates. In contrary, for reactions in which the cross section depends on the angular deviation, the angular flux is used to calculate the reaction rate. These will be shown in the next chapter while talking about the neutron transport equation.

It should be pointed out that both of the fluxes used in neutronic field are different from their conventional definition which describes a quantity passing through a unit surface per unit time. The conventional definition of flux is named as *current* by neutronic physicists and is written as $\mathbf{J}$. It is obtained from the angular flux weighted by the direction $\hat{\Omega}$. Therefore, there always exist an angular current and a scalar current which are defined as below. The scalar current is in fact a net current passing through an unit surface (specified with its normal direction $\mathbf{N}$) with a certain direction. This quantity vanishes when the angular flux is isotropic.

$$\mathbf{J}(\mathbf{r}, E, \hat{\Omega}, t) = \hat{\Omega}\varphi(\mathbf{r}, E, \hat{\Omega}, t) \tag{1.9}$$

$$\mathbf{J}(\mathbf{r}, E) = \int_{4\pi} \mathbf{J}(\mathbf{r}, \hat{\Omega}, E) \cdot \mathbf{N}d^2\Omega \tag{1.10}$$

Chapter 2

Neutron Transport Theory and General Problem of Homogenization in Nuclear Reactor Physics

This chapter will introduce at first the Boltzmann equation or more precisely the neutron transport theory which governs the neutron propagation in the matter. Two different forms of the transport equation will be presented as well as their own numerical approaches, namely the deterministic method and the Monte-Carlo method[66, 89, 90]. A brief comparison between these two methods will be followed. Then, we shall introduce the main issues on which this work is carried out: the energy condensation and spatial homogenization. These two items together could be termed "sub-assembly homogenization". Finally, some general problems related to the sub-assembly homogenization will be pointed out.

2.1 Neutron Transport Theory

Integral-differential transport equation

For nuclear reactor analysis, it is indispensable to be able to control the global neutron population variation for both operation and safety issues. Neutron physicists have to predict neutron behavior which forms principally the neutron transport theory. Since the neutrons in a reactor core have a rather large population, they are treated by the statistical concept with a conventional density variable. As mentioned in the previous chapter, this density function is the neutron angular flux $\varphi(\mathbf{r}, E, \hat{\Omega}, t)$.

In a nuclear reactor core, the neutron density is very low compared with atoms densities. This leads to consider the neutrons behaviors in a reactor core as a perfect low-density mono-atomic gas. The later has originally been treated by Ludwig Boltzmann [14] with a particle transport equation in 1872. Several approximations [12] are imposed to obtain this Boltzmann transport equation:

- Neutron-neutron and neutron-electron interactions are neglected.

- The neutron trajectory between two collisions is a straight line.

- All the relativistic effects are not considered because the neutron kinetic energy is not high enough to use Lorentz correction law. In reactor physics, the maximal energy for neutron is limited to 20 MeV.

- The neutron average life time is very short in the reactor core compared to its decay constants, thus the neutron radioactivity is ignored.

The basic idea of the Boltzmann equation is in fact to follow up the neutron population variation via accounting the arrival and the departure neutrons within an elemental unit of phase space $(d^3\mathbf{r}, d^2\Omega, dE)$. The whole perturbation is divided into five terms:

- The streaming term or leakage term: the part of neutrons that escape out of the elemental volume of the phase space;

- The collision disappearance term: neutrons absorbed or scattered to another elemental unit of phase space;

- The collision arrival term: neutrons scattered into the considered elemental volume of the phase space;

- The fission production term: secondary neutrons created from fission reactions;

- The external source term: neutrons emitted from a fixed source.

Taking into consideration all the above terms, we obtain finally the time-dependent integral-differential neutron transport equation (2.1):

$$\begin{aligned}\frac{1}{v}\frac{\partial\varphi(\mathbf{r},E,\hat{\Omega},t)}{\partial t} &= -div[\hat{\Omega}\varphi(\mathbf{r},E,\hat{\Omega},t)] - \Sigma_t(\mathbf{r},E,t)\varphi(\mathbf{r},E,\hat{\Omega},t) \\ &+ \int_0^\infty dE' \int_{4\pi} d^2\Omega'\Sigma_s(\mathbf{r},E'\to E,\hat{\Omega}'\to\hat{\Omega},t)\varphi(\mathbf{r},E',\hat{\Omega}',t) \\ &+ \frac{1}{4\pi}\int_0^\infty dE'\chi(E'\to E)\nu\Sigma_f(\mathbf{r},E',t)\phi(\mathbf{r},E',t) + S_{\text{ext}}(\mathbf{r},E,\hat{\Omega},t) \quad (2.1)\end{aligned}$$

As shown in the fission creation term, we consider that the neutrons out-coming from fission are isotropic in the laboratory reference. Moreover, the created fission neutrons respect certain energy distribution spectra $\chi(E'\to E)$ which is associated to each fissile isotope. For example, ^{235}U thermal neutron induced prompt fission spectrum is illustrated in Fig 1.2. When the arrival terms and the departure terms hold the balance, all the time-dependence disappears in Eq (2.1) and it yields a critical stationary state. If this natural critical state is not attained, we need to introduce a parameter K_{eff} helping to balance the appearance and disappearance terms as shown in the following equation:

$$
\begin{aligned}
&div[\hat{\Omega}\varphi(\mathbf{r},E,\hat{\Omega})] + \Sigma_t(\mathbf{r},E)\varphi(\mathbf{r},E,\hat{\Omega}) \\
&\qquad = \int_0^\infty dE' \int_{4\pi} d^2\Omega' \Sigma_s(\mathbf{r},E'\to E,\hat{\Omega}'\to\hat{\Omega})\varphi(\mathbf{r},E',\hat{\Omega}') \\
&\qquad\quad + \frac{1}{4\pi K_{\text{eff}}} \int_0^\infty dE' \chi(E'\to E)\nu\Sigma_f(\mathbf{r},E')\phi(\mathbf{r},E') + S_{ext}(\mathbf{r},E,\hat{\Omega}) \quad (2.2)
\end{aligned}
$$

The K_{eff}, defined as the effective multiplication factor, is the eigenvalue of the above equation. At the same time, it can characterize the reactor state, such as: if $K_{\text{eff}} = 1$, the reactor is in the critical state; if $K_{\text{eff}} > 1$, the reactor is in a super-critical state; and if $K_{\text{eff}} < 1$, the reactor is in a sub-critical state.

Integral transport equations

Before going to the details which concern how to obtain an integral form transport equation, it is helpful to present two other density functions regularly used by neutronic physicists. They are namely emission density χ and collision density Ψ. The emission density is also called outgoing density representing the neutrons emitted by fission or other source as well as those from scattering reaction. The collision density is, in contrary, called incoming density which is the product of total macroscopic cross section and neutron flux:

$$\Psi(\mathbf{r},E,\hat{\Omega}) = \Sigma_t(\mathbf{r},E)\varphi(\mathbf{r},E,\hat{\Omega}) \quad (2.3)$$

The relationship among these density functions are illustrated in Fig 2.1. The two connection points are respectively the emission density χ (outgoing density) and the collision density Ψ (incoming density). $\mathbf{S}$ represents the external source. They are related to each other through transport operator $\mathbf{T}$ or collision operator $\mathbf{C}$ whose explicit expressions will be presented later. Thus, two equations can be written to establish their relationship as following:

$$\chi = \mathbf{C}\Psi + \mathbf{S} \quad (2.4)$$

$$\Psi = \mathbf{T}\chi \quad (2.5)$$

After substituting one equation in the other one, we obtain two different forms of the transport equation which are shown in Eq (2.6) and Eq (2.7). Each of them contains only one density function. Furthermore, in the steady-state situation, the transport problem could be divided into two different subjects depending on whether the external source $\mathbf{S}$ exists or not. The first is the fixed source problem which is usually encountered in a non fissionable medium and possess an unique solution. The second and also the much more applicable case is named criticality problem where the external source is neglected. Thus, both of Eq (2.6) and Eq (2.7) turn to homogeneous equations which implies that their solutions exist only under critical condition.

$$\Psi = \mathbf{T}(\mathbf{C}\Psi + \mathbf{S}) \quad (2.6)$$

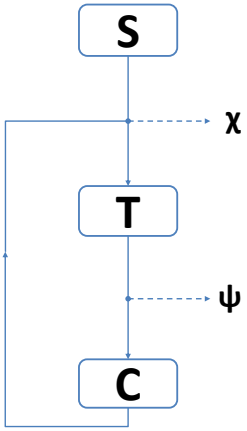

Figure 2.1: Neutron transport illustration scheme

$$\chi = \mathbf{C}\mathbf{T}\chi + \mathbf{S} \tag{2.7}$$

From another point of view, the two different neutron transport balance equations offer two different ways to solve the transport problem. In this part, we focus on the collision density involved equation (2.6). Without consideration of the external source, Eq (2.6) becomes:

$$\Psi(\mathbf{r}, E, \hat{\Omega}) = \int_V d^3r' \mathbf{T}(\mathbf{r}' \to \mathbf{r}, E, \hat{\Omega}) \int_0^\infty dE' \int_{4\pi} d^2\Omega' \mathbf{C}(\mathbf{r}', E' \to E, \hat{\Omega}' \to \hat{\Omega}) \Psi(\mathbf{r}', E', \hat{\Omega}') \tag{2.8}$$

It should be kept in mind that the two operators $\mathbf{T}(\mathbf{r}' \to \mathbf{r}, E, \hat{\Omega})$ and $\mathbf{C}(\mathbf{r}', E' \to E, \hat{\Omega}' \to \hat{\Omega})$ in Eq (2.8) are different from $\mathbf{T}$ and $\mathbf{C}$ in Eq (2.6). However, they could be related by an integral relationship as in Eq (2.9). The first one is indeed the kernel part of the second one.

$$\mathbf{T} = \int_V \mathbf{T}(\mathbf{r}' \to \mathbf{r}, E, \hat{\Omega}) d^3r' \tag{2.9}$$

Eq (2.8) is indeed the origin of the integral transport equation. In order to derive the conventional integral form, it is necessary to present the explicit forms of the two operator kernels. They are respectively expressed in Eq (2.10) and Eq (2.11).

$$T(\mathbf{r}' \to \mathbf{r}, E, \hat{\Omega}) = \Sigma_t(\mathbf{r}, E) \exp\left(-\int_0^s \Sigma_t(\mathbf{r} - s'\hat{\Omega}, E) ds'\right) \tag{2.10}$$

$$C(\mathbf{r}', E' \to E, \hat{\Omega}' \to \hat{\Omega}) = \frac{\Sigma_s(\mathbf{r}', E' \to E, \hat{\Omega}' \to \hat{\Omega}) + \frac{\chi(E' \to E)}{4\pi K_{\text{eff}}} \nu\Sigma_f(\mathbf{r}', E')}{\Sigma_t(\mathbf{r}', E')} \tag{2.11}$$

Within the transport operator, a physical variable termed "optical path" noted as τ is implicitly used and its definition is given as follows:

$$\tau = \int_0^s \Sigma_t(\mathbf{r} - s'\hat{\Omega}, E) ds' \tag{2.12}$$

The above optical path helps to determine the probability to travel the distance s without any collision as $\exp(-\tau)$.

From Eq (2.11), we note that the collision operator is in fact composed of two parts: one is related to the scattering reaction; the other one is related to the fission reaction. However, different properties of the two cross sections result in different expressions in the collision kernel. In fission neutron emission mechanism, the angular deviation is uniformly distributed in the whole solid angle which makes the angular concerned term get out of the production cross section and become a constant $\frac{1}{4\pi}$. And the K_{eff} value in Eq (2.11) helps to balance neutron disappearance and production rates.

Due to the above reasons, it is normal to distinguish the pure diffusion collision kernel and the fission collision kernel as follows:

$$C(\mathbf{r}', E' \to E, \hat{\Omega}' \to \hat{\Omega}) = C_s(\mathbf{r}', E' \to E, \hat{\Omega}' \to \hat{\Omega}) + C_f(\mathbf{r}', E' \to E) \tag{2.13}$$

$$C_s(\mathbf{r}', E' \to E, \hat{\Omega}' \to \hat{\Omega}) = \frac{\Sigma_s(\mathbf{r}', E' \to E, \hat{\Omega}' \to \hat{\Omega})}{\Sigma_t(\mathbf{r}', E')} \tag{2.14}$$

$$C_f(\mathbf{r}', E' \to E) = \frac{1}{4\pi K_{\text{eff}}} \frac{\chi(E' \to E)\nu\Sigma_f(\mathbf{r}', E')}{\Sigma_t(\mathbf{r}', E')} \tag{2.15}$$

Substituting the detailed expressions of the two operators in Eq (2.8), the conventional integral transport equation could be deduced as in Eq (2.16).

$$\begin{aligned}\varphi(\mathbf{r}, E, \hat{\Omega}) = &\int_0^\infty ds \exp\left(-\int_0^s \Sigma_t(\mathbf{r} - s'\hat{\Omega}, E)ds'\right) \\ &\cdot \left[\int_0^\infty dE' \int_{4\pi} d^2\Omega' \Sigma_s(\mathbf{r} - s\hat{\Omega}, E' \to E, \hat{\Omega}' \to \hat{\Omega})\varphi(\mathbf{r} - s\hat{\Omega}, E', \hat{\Omega}')\right. \\ &\left. + \frac{1}{4\pi K_{\text{eff}}} \int_0^\infty dE' \chi(E' \to E)\nu\Sigma_f(\mathbf{r} - s\hat{\Omega}, E')\phi(\mathbf{r} - s\hat{\Omega}, E')\right]\end{aligned} \tag{2.16}$$

This above integral form describes intuitively the accumulation of neutron flux in the phase space $(\mathbf{r}, E, \hat{\Omega})$ from other different ones $(\mathbf{r}', E', \hat{\Omega}')$. Two consequent steps are identified according to Eq (2.16): a collision operator $C(\mathbf{r}', E' \to E, \hat{\Omega}' \to \hat{\Omega})$ is at first used to change the neutron energy as well as its direction; a transport operator $T(\mathbf{r}' \to \mathbf{r}, E, \hat{\Omega})$ is then applied to shift the neutron from $\mathbf{r}'$ to $\mathbf{r}$ keeping the same energy and the same direction.

2.2 General Principle of Solving Transport Equation

The previous section presented the integral-differential and integral forms of neutron transport equations. However, the real challenge is how to solve them since the neutronic flux is complicatedly coupled among three different aspects, namely the energy variable E, the angular variable $\hat{\Omega}$ and the spatial variable $\mathbf{r}$. Most of time, analytical solutions are hardly available for neither form of the transport equations. That is why a lot of efforts are paid by neutronic physicists in the development of numerical methods. The following Figure

2.2 summarizes the existing numerical methods which are capable of solving the transport equation (integral-differential or differential forms).

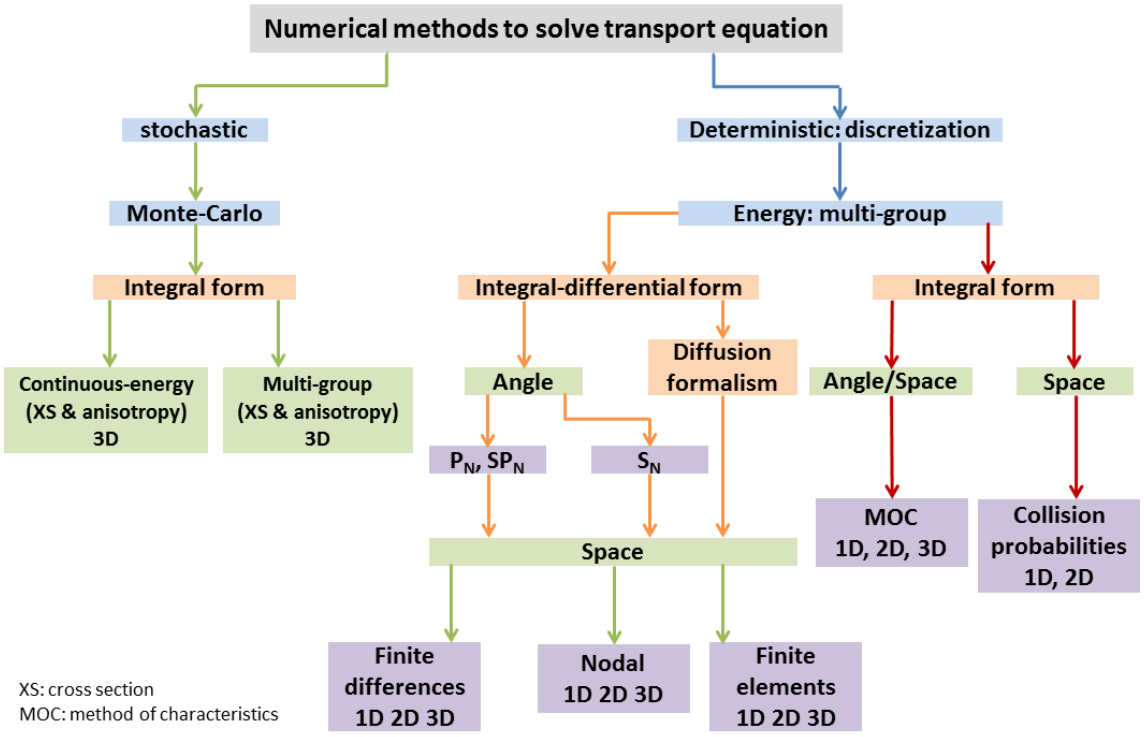

Figure 2.2: Illustration of various numerical methods solving the neutron transport equation

It could be clearly found from Figure 2.2[20] that two different branches: deterministic and stochastic approaches exist for solving the transport equation. Even though they do not result in the same mathematical formula, the same physical justification is shared by both. For the deterministic method, it is mostly used to handle the integral-differential equation. The main idea of deterministic method is based on the discretization which performs in the whole domain of space phase: the energy, the angle and the space. Usually, the three variables are taken into consideration one after one. For example, the finite difference or nodal or finite elements methods treat the spatial discretization. Then, P_N or SP_N or S_N methods treat the angular discretization. Some exceptions could be found in the deterministic family. Certain methods, such as the method of characteristics (MOC) or collision probabilities handle with the integral form transport equation. We will not develop the exact formalism for each method because they are completely out of our subject. Only some brief description will be listed for each of these methods as follows:

- S_N: named also discrete ordinate method, aims to discretize the angular flux into a set of directions within the whole solid angle 4π: $\{\hat{\Omega}_i; i = 1, 2, \cdots, I\}$. It should be noted that the N associated to the method S_N is not the total quantity of angular division I;

- P_N: named also spherical harmonics method, aims to develop the angular flux as well as the scattering cross section with a real spherical harmonics basis till a certain

order N which is an odd number;

- CP: the collision probability method works with the integral transport equation within each multi-group and spatially discretized. The scalar flux to be solved is supposed to be isotropic in each sub-region. A $I \times I$ (number of regions) matrix whose elements are the collision probabilities connects the source terms and the scalar flux per region.

- MOC: the method of characteristics solves the characteristic form of the transport equation in each multi-group and piecewise homogeneous medium by following the straight neutron path as the neutron moves across the complete domain. This method is quite similar with the CP method but shows two main advantages compared to the previous one. First, the MOC avoids to handle the full square matrix of order equal to the number of sub-regions. Secondly, the CP method is limited to solve the isotropic sources (in laboratory reference) problems. These advantages make the MOC method suitable for the problems where the number of sub-regions is more than a few hundred.

The technical details of the above solvers can be found from [6, 20]. It should just be kept in mind that some approximations are surely used in deterministic approach which could result in certain bias.

On the other hand, it is the stochastic method which works equivalently on the integral transport equation. Compared to the above mentioned deterministic approach, the Monte-Carlo method owns the advantage of using continuous-energy cross sections and exact anisotropy data as input library. Secondly, the Monte-Carlo method focuses to simulate each neutron trajectory as closely as possible. This reduces importantly the approximations exploited in deterministic solvers. It should be marked that the Monte-Carlo method could also use multi-group data library to perform a nuclear core calculation as pointed out in Figure 2.2. More details about the Monte-Carlo method used in solving the integral form neutron transport equation will be presented in Chapter 5.

2.3 General Problem in Sub-assembly Homogenization

After having obtained a global vision about the different methods to solve the transport equation, we return back to the requirements demanded by an industrial calculation. Readers could find detailed explanation in the general introduction part. Here, we emphasize on the time cost criterion. Generally, in a full core (fast reactor type) calculation, the order of magnitude of unknowns to be solved is about $10^5 \times 10^8 \times 10^2$ which corresponds respectively to the following aspects: energy, space and angle. Under this complicated situation and to economize the most possibly the calculation time, an industrial calculation diagram is usually divided into two steps: the sub-assembly calculation[84] and the core calculation. The first calculation step produces homogenized multi-group cross sections for each sub-assembly which are then used in the second core calculation step.

The fundamental concept "*equivalence*" is implicitly exploited in the above two-step calculation strategy and is illustrated in Figure 2.3. The point O represents the realistic heterogeneous problem whose exact solution is hardly available in a limited time with current computational technique. In contrary, it is possible to solve the reference solution

for the simplified problem (point R). The latter is based on a 2D or 3D heterogeneous sub-assembly geometry using fine-group microscopic cross sections. The next step is to establish a homogenized simplified problem noted as point M using macroscopic few-group cross sections. The "*equivalence*" concept is indeed affected on points R and M whose aim is to preserve the global reaction rates as following relationship:

$$\overline{\Sigma}_{M,G} V_M \overline{\phi}_{M,G} = \sum_{m \in M} \sum_{g \in G} V_m \overline{\Sigma}_{m,g} \overline{\phi}_{m,g} \tag{2.17}$$

This helps to yield the general formulation of the homogenized multi-group cross sections as expressed in Eq (2.18). Finally, these homogenized multi-group cross sections will be used in a core calculation noted as point C in Figure 2.3.

$$\overline{\Sigma}_{M,G} = \frac{\sum_{m \in M} \sum_{g \in G} V_m \overline{\Sigma}_{m,g} \overline{\phi}_{m,g}}{V_M \overline{\phi}_{M,G}} \tag{2.18}$$

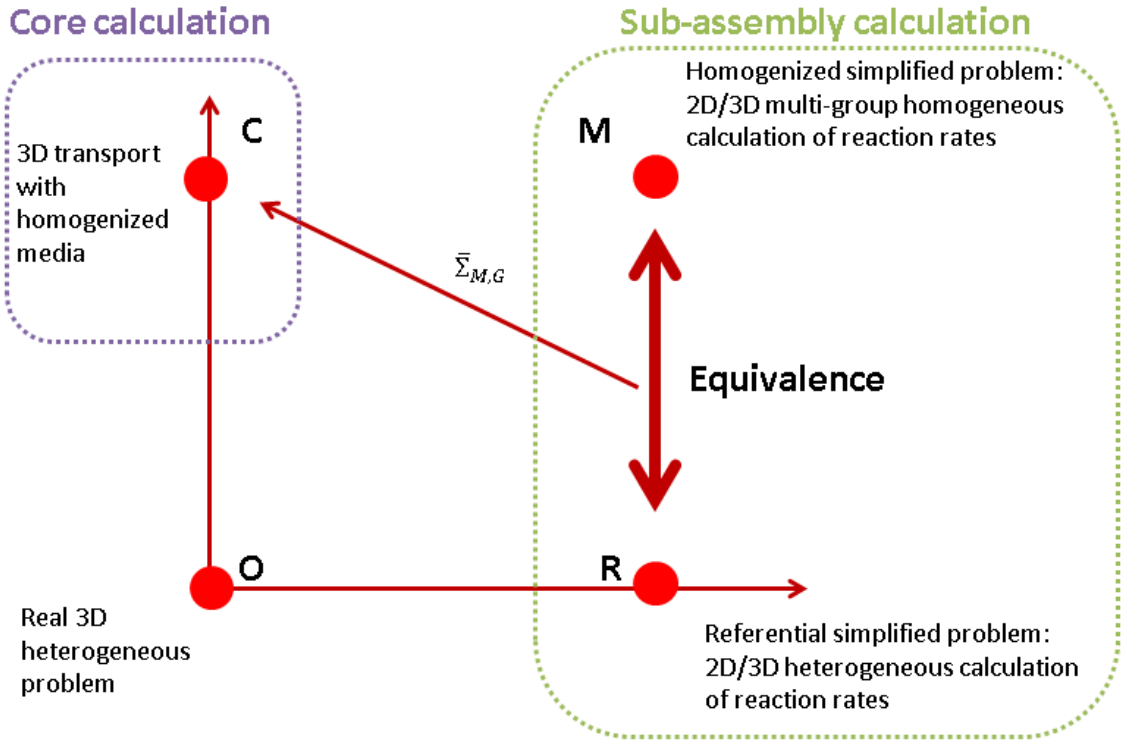

Figure 2.3: Equivalence fundamental conception illustration

However, from the point of view of a deterministic code, the energy condensation and the spatial homogenization are clearly separated and carried out one after another. Each of them will be explicitly presented in Chapter 3 and Chapter 4. Here, the author insists to point out the most embarrassing problem related to the energy condensation aspect.

Retaking a look at the integral-differential transport equation as shown in Section 2.1, the expected solution is the angular flux $\varphi(\mathbf{r}, E, \hat{\Omega})$. With use of this latter angular dependent weighting function, the group-wise total cross section collapsed from point-wise one depends also on the angular variable. This could be proved by Eq (2.19).

$$\Sigma_{t,g}(\mathbf{r},\hat{\Omega}) = \frac{\int\limits_{E\in g} \Sigma_t(\mathbf{r},E)\varphi(\mathbf{r},E,\hat{\Omega})dE}{\int\limits_{E\in g} \varphi(\mathbf{r},E,\hat{\Omega})dE} \tag{2.19}$$

Unfortunately, in the second core calculation step, the transport equation to be solved remains the same as Eq (2.2) which uses non-angular dependent multi-group total cross sections. This enforces us to search a conventional form for total cross sections which should always be able to preserve the neutronic balance. The latter is not a easy task for neutronic physicists. Several solutions proposed from previous research work will be presented in Chapter 3.

Chapter 3

Energy Condensation theory

Introduction

For any reactor physics calculation code (Monte-Carlo or deterministic), the reliability of the input cross sections is an dispensable factor in obtaining adequate results from the complex transport equations as mentioned in the previous chapter. These input cross sections are derived from *evaluated nuclear data libraries* which are based on experimental measurements and theoretical nuclear models. However, they could not be used directly in reactor simulation codes. A series of treatments is necessary to convert them into continuous-energy cross section format which is usable by reactor physics codes. A very widely used data processing system is named **NJOY**[37] and is being used developed at the Los Alamos National Laboratory (USA).

The energy and angle point-wise data produced above could serve in two kinds of calculation methodologies. An illustration scheme is plotted in Figure 3.1. The left branch represents the deterministic method based calculation flow. Its main challenge in finding the solution comes from the complex angular- and energy-dependent nuclear data. The solution adopted by all the deterministic codes is to use the energy and spatial variable discretization technique. The energy discretization is the main topic of this chapter which is also under the name of energy condensation. The spatial variable discretization will be presented in Chapter 4. These two discretization actions together make the whole core one-through calculation divide into two steps, namely the sub-assembly calculation and the core calculation. The first step is performed on each single sub-assembly in order to obtain a set of homogenized multi-group constants which are representative of the whole sub-assembly, especially in the next step core calculation.

To have a further look at the energy variable discretization, it is also done in two steps. As shown in Figure 3.1, the module **GROUPR** from the **NJOY** code is at first in charge of converting the point-wise nuclear data into fine group-wise format. Then, another condensation module usually provided by the sub-assembly calculation codes collapses the fine-group constants into coarse-group constants with consideration of self-shielding effect. This step facilitates the next core calculation step.

The same procedure is applied to generate fine-group constants as well as coarse-group constants for the purpose of preserving the physical consistency (in most cases, it refers to different types of reaction rates). Thus, a fundamental problem is revealed by the two energy condensation steps in deterministic transport calculation. It means that the flux

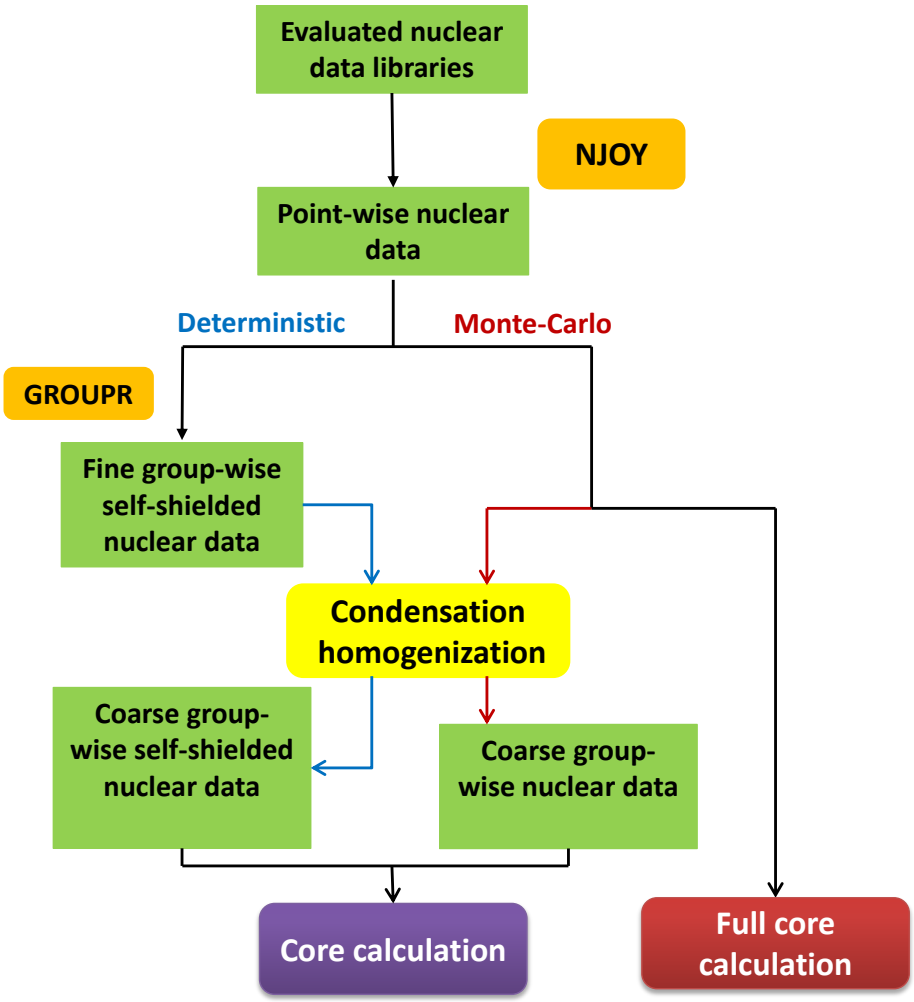

Figure 3.1: Illustration of nuclear data treatment with different approaches

solution which is used to calculate the group-wise constant is indeed the solution expected from the transport equation. To overcome the difficulty, an analytical energy spectrum is used by **GROUPR** to produce the fine-group cross sections. This analytical spectrum could consists of a fission spectrum for the high-energy range; a slowing-down spectrum for the intermediate range and a Maxwellian thermal spectrum for the energy domain where E is lower than 0.625 eV.

In contrast, the Monte-Carlo calculations which occupy the right-hand side of Figure 3.1, could avoid the above approximation in deterministic codes. They use the point-wise nuclear data directly which is more accurate and much closer to the original evaluation. It is thus reasonable to use Monte-Carlo codes as a reference in carrying out full-core calculation. Recently, the Monte-Carlo method was also used to produce multi-group constants which are represented by the red arrow lines in Figure 3.1. This new approach maintains the advantage of the general Monte-Carlo method which is supposed to obtain more adequate multi-group constants. It is also the original motivation of this work. More explicit developments and analysis about the new approach will be discussed in the following parts.

In the present chapter, we focus on the coarse-group cross sections generation problem in the deterministic branch. The energy condensation procedure results generally in a loss of information about energy resolution as well as accuracy. Since this problem has been investigated for a long time, several solutions were proposed. *Rahnema et al.* calculated the orthogonal expansion moments of the coarse-group constants. The flux solution is thus also represented by a series of moments within each coarse group which can then be used to construct the fine-group energy spectrum in the core calculation exactly. This method is named "the generalized energy condensation method" because the standard condensation method is just a special case (expansion order limited to 0) in the general theory. The standard few-group constants are calculated on the basis of preservation of the global reaction rates. Readers are suggested to consult Rahnema's papers [79, 83] which give detailed explanations of the generalized energy condensation method. Additionally, some methods intend to preserve the leakage rates, while some others make use of the perturbation theory in order to conserve a reactivity effect (e.g. the Na voiding coefficient or control rod cross sections). With the same idea as the generalized condensation method, a conservative method tries to weight the fine-group cross sections with the flux moment projected on the spherical harmonic basis. The originality of this way of doing things is to find a conventional form of multi-group cross sections in order to minimize the deviation from the exact one. In the following sections, these methods will be developed in detail along with their computational implementations in different deterministic codes.

3.1 Generalized Energy Condensation method

In order to establish the fine-group energy spectrum from the coarse group information, a generalized energy condensation theory is developed. This generalized method uses the fine-group transport solution within each sub-assembly as a weighting function to produce multi-group cross sections and reaction rates' orthogonal expansion moments for each region. With knowledge of the expansion moments of the cross sections as well as the reaction rates, a coupled set of modified transport equations could be deduced for the whole core. The solutions from these modified transport equations are the flux moments within each coarse group which can be used finally to reconstruct the fine-group energy spectrum in the whole core.

The deduction of the generalized method starts from a standard integral-differential transport equation which deals with the angular-dependent scattering term with an expansion on the spherical harmonics basis. The energy integrals on the right-hand side of Eq (3.1) are broken up into G groups.

$$\hat{\Omega}\cdot\nabla\phi(\mathbf{r},\hat{\Omega},E)+\Sigma_t(\mathbf{r},E)\phi(\mathbf{r},\hat{\Omega},E)=\sum_{g=0}^{G-1}\sum_{l=0}^{\infty}\sum_{m=-l}^{m=l}\frac{Y_{lm}(\hat{\Omega})}{4\pi}\int_{E'\in g}dE'\Sigma_{s,l}(\mathbf{r},E'\rightarrow E)\phi_l^m(\mathbf{r},E') + \sum_{g=0}^{G-1}\frac{\chi_g(E)}{4\pi K_{\text{eff}}}\int_{E'\in g}dE'\nu\Sigma_f(\mathbf{r},E')\phi(\mathbf{r},E') \quad (3.1)$$

Where

- g: index for energy groups;
- $\phi_l^m(\mathbf{r},E')=\int\limits_{4\pi}d\hat{\Omega}'Y_{lm}(\hat{\Omega}')\phi(\mathbf{r},\hat{\Omega}',E)$: the angular moment of the angular flux;

- $\Sigma_{s,l}(\mathbf{r}, E' \to E) = \int_{-1}^{1} d\mu \Sigma_s(\mathbf{r}, E' \to E, \mu) P_l(\mu)$: the angular moment of the scattering kernel;
- $Y_{lm}(\hat{\Omega})$: normalized spherical harmonics;
- $P_l(\mu)$: l^{th} order of Legendre Polynomials; with $\mu = \hat{\Omega} \cdot \hat{\Omega}'$

Since the angular flux will be expanded according to an arbitrary set of orthogonal basis functions, the group-wise energy intervals need to be adapted to the chosen basis function. For the sake of place, the detailed mathematical formulations can be found in [79]. After splitting Eq (3.1) into G coupled equations whose coarse group boundaries are scaled to respect the orthogonal basis, the neutron balance within group $h_\perp$ is written as following. The index $\perp$ is inherited from Rahnema's notation and stands for the orthogonal basis.

$$\begin{aligned}\hat{\Omega} \cdot \nabla \phi(\mathbf{r}, \hat{\Omega}, E_{h_\perp}) + \Sigma_t(\mathbf{r}, E_{h_\perp}) \phi(\mathbf{r}, \hat{\Omega}, E_{h_\perp}) = \\ \sum_{g_\perp=0}^{G-1} \sum_{l=0}^{\infty} \sum_{m=-l}^{m=l} \frac{Y_{lm}(\hat{\Omega})}{4\pi} \int_{E'_{g_\perp} \in g_\perp} dE'_{g_\perp} \Sigma_{s,l}(\mathbf{r}, E'_{g_\perp} \to E_{h_\perp}) \phi_l^m(\mathbf{r}, E'_{g_\perp}) \\ + \sum_{g_\perp=0}^{G-1} \frac{\chi(E_{h_\perp})}{4\pi K_{\text{eff}}} \int_{E'_{g_\perp} \in g_\perp} dE'_{g_\perp} \nu\Sigma_f(\mathbf{r}, E'_{g_\perp}) \phi(\mathbf{r}, E'_{g_\perp}) \quad (3.2)\end{aligned}$$

An arbitrary set of energy orthogonal functions within coarse group $h_\perp$ is defined as $\xi_i(E_{h_\perp})$. The latter respects the orthogonality relationship for any $E_{h_\perp} \in h_\perp$:

$$\int_{E_{h_\perp} \in h_\perp} dE_{h_\perp} w(E_{h_\perp}) \xi_i(E_{h_\perp}) \xi_j(E_{h_\perp}) = \frac{\delta_{ij}}{\alpha_j} \quad (3.3)$$

Where

- $w(E_{h_\perp})$: weighting function;
- δ_{ij}: Kronecker Delta function;
- α_j: normalization constant determined by the choice of $\xi_i(E_{h_\perp})$ and $w(E_{h_\perp})$.

Before projecting Eq (3.2) on the above orthogonal function basis, it is necessary to introduce another important step: rewrite the total cross section within group $h_\perp$ by two terms.

$$\Sigma_t(\mathbf{r}, E_{h_\perp}) = \Sigma_{t,0}^{h_\perp}(\mathbf{r}) + \delta(\mathbf{r}, E_{h_\perp}) \quad (3.4)$$

Where

- the standard scalar flux weighted total cross section in group $h_\perp$:

$$\Sigma_{t,0}^{h_\perp}(\mathbf{r}) = \frac{\int_{E_{h_\perp} \in h_\perp} dE_{h_\perp} \Sigma_t(\mathbf{r}, E_{h_\perp}) \phi(\mathbf{r}, E_{h_\perp})}{\int_{E_{h_\perp} \in h_\perp} dE_{h_\perp} \phi(\mathbf{r}, E_{h_\perp})} \quad (3.5)$$

- the deviation of the cross section from the standard group-wise value which takes account the variation with respect to the energy variable: $\delta(\mathbf{r}, E_{h_\perp})$.

After preparing all the basic elements, the general condensed form of the transport equation (3.6) is obtained by projecting Eq (3.2) on the orthogonal function $\xi_i(E_{h_\perp})$ and then integrating the product over the energy interval $h_\perp$. However, there is a mathematical processing difference between the left-hand side and the right-hand side terms of Eq (3.2). Rather than condensing the cross sections directly as done for the left-hand side, the expansion into orthogonal functions is performed to the reaction rates for the right-hand side terms.

$$\begin{aligned}\hat{\Omega}\cdot\nabla\phi_{i,h_\perp}(\mathbf{r},\hat{\Omega}) + \Sigma^{h_\perp}_{t,0}(\mathbf{r})\phi_{i,h_\perp}(\mathbf{r},\hat{\Omega}) + \delta_{i,h_\perp}(\mathbf{r},\hat{\Omega})\phi_{0,h_\perp}(\mathbf{r},\hat{\Omega}) \\ = \sum_{g_\perp=0}^{G-1}\sum_{l=0}^{\infty}\sum_{m=-l}^{m=l}\sum_{j=0}^{\infty}\frac{\alpha_j}{4\pi}Y_{lm}(\hat{\Omega})\phi^m_{l,j,g_\perp}(\mathbf{r})\Sigma_{s,l,i,j,g_\perp\to h_\perp}(\mathbf{r}) \\ + \sum_{g_\perp=0}^{G-1}\sum_{j=0}^{\infty}\alpha_j\frac{\chi_{i,h_\perp}(\mathbf{r})}{4\pi k_{\text{eff}}}\nu\Sigma_{f,j,g_\perp}(\mathbf{r})\phi_{j,g_\perp}(\mathbf{r}) \quad (3.6)\end{aligned}$$

Where

- G: number of coarse groups into which the spectrum has been divided;
- $i = 0, 1, 2, \cdots, \infty$: energy expansion order.

The definition of the standard total cross section $\Sigma^{h_\perp}_{t,0}(\mathbf{r})$ is already given. The other coarse group moment constants are defined as follows:

- the moment of flux in group $g_\perp$:

$$\phi_{i,h_\perp}(\mathbf{r},\hat{\Omega}) = \int\limits_{E_{h_\perp}\in h_\perp} dE_{h_\perp}\phi(\mathbf{r}, E_{h_\perp}, \hat{\Omega})w(E_{h_\perp})\xi_i(E_{h_\perp}) \quad (3.7)$$

- the moment of the total cross section perturbation term of which denominator part is dependent only on the 0^{th} order of flux moment:

$$\delta_{i,h_\perp}(\mathbf{r},\hat{\Omega}) = \frac{\int\limits_{E_{h_\perp}\in h_\perp} dE_{h_\perp}\delta(\mathbf{r}, E_{h_\perp})\phi(\mathbf{r},\hat{\Omega}, E_{h_\perp})w(E_{h_\perp})\xi_i(E_{h_\perp})}{\int\limits_{E_{h_\perp}\in h_\perp} dE_{h_\perp}\phi(\mathbf{r},\hat{\Omega}, E_{h_\perp})w(E_{h_\perp})\xi_0(E_{h_\perp})} \quad (3.8)$$

- the moment of the fission spectrum:

$$\chi_{i,h_\perp}(\mathbf{r}) = \int\limits_{E_{h_\perp}\in h_\perp} dE_{h_\perp}\chi(\mathbf{r},\hat{\Omega}, E_{h_\perp})w(E_{h_\perp})\xi_i(E_{h_\perp}) \quad (3.9)$$

- the moment of fission production rate from group $g_\perp$:

$$\nu\Sigma_{f,j,g_\perp}(\mathbf{r})\phi_{j,g_\perp}(\mathbf{r}) = \int\limits_{E'_{g_\perp}\in g_\perp} dE'_{g_\perp}\nu\Sigma_f(\mathbf{r}, E'_{g_\perp})\phi(\mathbf{r}, E'_{g_\perp})w(E'_{g_\perp})\xi_j(E'_{g_\perp})\times \int\limits_{E'_{g_\perp}\in g_\perp} dE'_{g_\perp}\xi_j(E'_{g_\perp}) \quad (3.10)$$

- the moment of scattering rate from group $g_\perp$ to $h_\perp$:

$$\phi^m_{l,j,g_\perp}(\mathbf{r})\Sigma_{s,l,i,j,g_\perp\to h_\perp}(\mathbf{r}) = \int\limits_{E_{h_\perp}\in h_\perp}\left[\int\limits_{E'_{g_\perp}\in g_\perp} dE'_{g_\perp}\phi^m_l(\mathbf{r},E'_{g_\perp})\Sigma_{s,l}(\mathbf{r},E'_{g_\perp}\to E_{h_\perp})w(E'_{g_\perp})\xi_j(E'_{g_\perp})\times\int\limits_{E'_{g_\perp}\in g_\perp} dE'_{g_\perp}\xi_j(E'_{g_\perp})\right]\times w(E_{h_\perp})\xi_i(E_{h_\perp})dE_{h_\perp} \quad (3.11)$$

The solutions of Eq (3.6) are a set of flux moments which could be used to construct an approximation of the angular flux by Eq (3.12):

$$\phi(E_{h_\perp}) = \sum_{i=0}^{I}\alpha_i\phi_i\xi_i(E_{h_\perp}) \quad (3.12)$$

Theoretically, the above multi-group constant definitions are suitable for an arbitrary orthogonal basis. However, for the practical issues, Legendre Polynomials are chosen as the expansion basis because it helps to simplify the cross-section moment definitions and also the condensed form of the transport equation.

The generalized condensation theory is verified by one-dimensional geometry with a discrete ordinates solver. A better estimation of the fine-group flux spectrum within each coarse group confirms its advantage in comparison with the standard condensation method. However, because of the complex mathematical formulation and the non-applicability of the obtained cross section moments in any core calculation code, this generalized condensation method is not applied widely although we could always find its simplified form or special case in other codes.

3.2 Energy Condensation Method in APOLLO2

APOLLO2[85], a French sub-assembly calculation code, developed at the CEA can solve the multi-group transport equation. Its modularity property allows users to chain up the calculations and also control the input parameters from one module to another. It can deal with one-dimensional or two-dimensional geometries, such as cylindrical configurations or lattice geometries based on square or hexagonal patterns.

Before doing any real geometry calculation, APOLLO2 has to convert the continuous-energy cross sections based on the European evaluated data library, JEFF3.1.1[22] for example to fine-group cross sections considering the self-shielding phenomena for resonant nuclei. Then microscopic fine-group cross sections are used as input data to continue the cell calculation.

Different choices for solving the multi-group flux in APOLLO2 exist: the collision probabilities P_{ij}, the discrete ordinates method S_n, and the method of characteristics *MOC*. However, only one methodology is adopted for producing all the types of coarse-group cross sections. It refers to the standard energy condensation method which means the coarse-group constants are weighted by scalar flux. With this basis, the different coarse-group constants are defined as follows:

- the total cross section in macro-group G which is weighted by the scalar flux:

$$\Sigma_{t,G}(\mathbf{r}) = \frac{\sum\limits_{g\in G} \Sigma_{t,g}(\mathbf{r})\phi_g(\mathbf{r})}{\sum\limits_{g\in G} \phi_g(\mathbf{r})} \tag{3.13}$$

- the scattering cross section ($l = 0$) and its moments from group G' to G which are all weighted by scalar flux:

$$\Sigma_{s,l,G'\to G}(\mathbf{r}) = \frac{\sum\limits_{g'\in G'}\sum\limits_{g\in G} \Sigma_{s,l,g'\to g}(\mathbf{r})\phi_{g'}(\mathbf{r})}{\sum\limits_{g'\in G'} \phi_{g'}(\mathbf{r})} \tag{3.14}$$

- the fission spectrum in macro-group G:

$$\chi_G(\mathbf{r}) = \sum_{g\in G} \chi_g(\mathbf{r}) \tag{3.15}$$

- the production fission cross section in macro-group G weighted by the scalar flux:

$$\nu\Sigma_{f,G}(\mathbf{r}) = \frac{\sum\limits_{g\in G} \nu\Sigma_{f,g}(\mathbf{r})\phi_g(\mathbf{r})}{\sum\limits_{g\in G} \phi_g(\mathbf{r})} \tag{3.16}$$

This standard scalar flux weighting technique is in fact a special case of the above generalized condensation method. If we limit the expansion order to 0 ($i = 0$) for the generalized condensation method, their complex coarse-group constants are just simplified as the above definitions. However, this mathematical simplification for the macro-group constants results into macro-group fluxes $\widetilde{\phi}_G(\mathbf{r})$ which are not really the sum of the related micro-group ones.

$$\widetilde{\phi}_G(\mathbf{r}) \neq \sum_{g\in G} \phi_g(\mathbf{r}) \tag{3.17}$$

Thus, the macro-group reaction rates are not properly conserved as shown in Eq (3.18) where i represents any type of reaction.

$$\Sigma_{i,G}(\mathbf{r})\widetilde{\phi}_G(\mathbf{r}) \neq \sum_{g\in G} \Sigma_{i,g}(\mathbf{r})\phi_g(\mathbf{r}) \tag{3.18}$$

Therefore, to cover the inconsistency, APOLLO2 uses an equivalence procedure (*SPH*) to correct the macro-group constants. This *SPH* method will be presented in Chapter 4.

3.3 Energy Condensation Method in JOINT

The Japanese prototype fast breeder reactor *MONJU*[1, 3, 4] is a sodium-cooled loop-type *MOX* fuel reactor. Its analysis work[32, 59] was carried out by the core simulation code *NSHEX*[51] which is a nodal hexagonal geometry 3D transport code. It can solve the neutron transport problem by a discrete ordinate method. The coarse-group constants (18-group or 7-group) used by *NSHEX* are produced by the code *JOINT*[74] which performs an energy collapsing work from fine-group cross sections (70-group). Moreover, the

70-group cross sections are prepared by another cell code, *SLAROM*[75] from the nuclear data library JFS-3-J3.2R[21] based on the Japanese evaluation file JENDL3.2[92]. And the 70-group weighting flux is calculated by the 2D RZ option of the diffusion code, *CITATION*[40].

The *MONJU* core analysis work showed that non-consistent K_{eff} values were obtained by using different sets of multi-group cross sections. Furthermore, the discrepancies of K_{eff} compared to the Monte-Carlo reference value are more important from the transport theory based calculations than from the diffusion theory based calculations. All the observed results pointed out that the previous condensation method in *JOINT* is not able to produce appropriate coarse-group cross sections for a core simulation code. A solution is proposed by the Japanese researchers: rather than weighting the transport cross section by the scalar flux, an approximate current-weighting function is used to do the condensation work. Detailed explanations will be given.

The multi-group transport equation solved by the *NSHEX* code is under the extended P1 approximation[1] related to the anisotropy scattering term. It results in a modified transport equation (3.19) in macro group G:

$$\hat{\Omega}\cdot\vec{\nabla}\phi_G(\mathbf{r},\hat{\Omega})+\Sigma_{tr,G}(\mathbf{r})\phi_G(\mathbf{r},\hat{\Omega})=\sum_{G'=0}^{N-1}\Sigma^*_{s,G'\to G}(\mathbf{r})\phi_{G'}(\mathbf{r})+\frac{\chi_G(\mathbf{r})}{4\pi k_{\text{eff}}}Q_f(\mathbf{r}) \tag{3.19}$$

where

- N: the total number of macro-group energy structure;
- the transport corrected cross section:

$$\Sigma_{tr,G}(\mathbf{r})=\Sigma_{t,G}(\mathbf{r})-\sum_{G'=0}^{N-1}\Sigma_{s1,G\to G'}(\mathbf{r}) \tag{3.20}$$

- the transport corrected scattering cross sections which is implied only for the in-group scattering:

$$\Sigma^*_{s,G'\to G}(\mathbf{r})=\Sigma_{s,G'\to G}(\mathbf{r})-\delta_{G,G'}\Sigma_{s1,G'\to G}(\mathbf{r}) \tag{3.21}$$

- the fission source in all the energy domain:

$$Q_f(\mathbf{r})=\sum_{G'=0}^{N-1}\nu\Sigma_{f,G'}(\mathbf{r})\phi_{G'}(\mathbf{r}) \tag{3.22}$$

Initially, all the group constants in Eq (3.19) are calculated with the standard energy condensation method. As it was presented in the previous section 3.2, this condensation concept does result in a non-conservative neutronic balance. More precisely, for the present case, the problem arises from the fact that we are trying to preserve the "*transport reaction rate*" just as it has been done for the other conventional reaction rates, e.g. the total collision rate. The misunderstanding of collapsing the transport cross section by

[1] P1 approximation is the simplest case of P_N method. The development of angular flux is limited to order 1.

the scalar flux over-estimated its value in certain groups and thereby under-estimated the neutron leakage rate in these groups. This finally caused an over-estimated K_{eff} value as observed in the *MONJU* reactor.

The proposed solution is to weight the transport cross section by the absolute value of current J_g as described in Eq (3.23) in order to preserve the mean neutron free path. The explanation will be followed.

$$\Sigma_{tr,G} = \frac{\sum\limits_{g\in G} \Sigma_{tr,g} J_g}{\sum\limits_{g\in G} J_g} \tag{3.23}$$

In addition, the current could be calculated with the Fick's diffusion law.

$$J = D\vec{\nabla}\phi(\mathbf{r}) \tag{3.24}$$

Where D is the diffusion coefficient and can be expressed as $\frac{1}{3\Sigma_{tr}}$ under the P1 approximation.

In the case of energy condensation, we could use an hypothesis: the spectrum of the gradient of flux is proportional to the spectrum of the flux $\vec{\nabla}\phi(\mathbf{r}) \sim \phi(\mathbf{r})$. With the combination of the diffusion coefficient definition taken from the Fick's law, we could finally write the norm of the current as follows:

$$||J|| = D||\vec{\nabla}\phi(\mathbf{r})|| \sim D\phi(\mathbf{r}) \sim \frac{\phi(\vec{r})}{3\Sigma_{tr}} \tag{3.25}$$

With knowledge of the approximate current spectrum, the new method enabling us to collapse the transport cross section is:

$$\Sigma_{tr,G} = \frac{\sum\limits_{g\in G} \phi_g(\mathbf{r})}{\sum\limits_{g\in G} \frac{\phi_g(\vec{r})}{\Sigma_{tr,g}}} \tag{3.26}$$

If we replace the transport cross section by the neutron mean free path $\Sigma_{tr,g} = \frac{1}{\lambda_g}$, Eq (3.26) could be rewritten as:

$$\lambda_G = \frac{\sum\limits_{g\subset G} \lambda_g \times \phi_g}{\sum\limits_{g\subset G} \phi_g} \tag{3.27}$$

Eq (3.27) implies that we could weight the fine-group neutron mean free path by the scalar flux. After introducing the new condensation method for the transport cross section in *JOINT*, a better estimation of K_{eff} is obtained. However, compared with the Monte-Carlo reference value, the new K_{eff} value showed an under-estimation tendency rather than an over-estimation tendency with the standard condensation method. In order to continue improving the multiplicative factor as well as the conservation of the neutronic balance, Todorova suggested using a weighting function which is dependent on the exponent γ[94]

$$F_g(\mathbf{r}) = (\Sigma_{tr,g})^{\gamma} \phi_g(\mathbf{r}) \tag{3.28}$$

- $\gamma = 0$: the standard energy condensation method, the weighting function is just the scalar flux;

- $\gamma = -1$: is called the conservative method which is supposed to conserve the neutron leakage rate better. It results in the approximative current weighting function given in Eq (3.25).

- $\gamma = -\frac{1}{2}$: is the combined collapsing method. It is a purely mathematical choice between the above two cases. It helped yield a better result for the *MONJU* reactor case. However, it could not promise its efficiency for any case.

3.4 Energy Condensation Method in ECCO

ECCO[44, 69] is a European sub-assembly calculation code from the codes system, ERANOS [24, 30] which is specifically used for fast neutron reactor analysis. ECCO is in charge of producing macro-group constants for the following calculation step: the core simulation. The input data of ECCO is the 1968-group cross sections from the library, JEFF-3.1. The energy condensation steps performed in ECCO are illustrated in Figure 3.2. At first, the 1968-group transport equation is solved under the fundamental mode approximation for a homogeneous or heterogeneous cell geometry. Then, the obtained 1968-group flux is used as a weighting function to collapse the fine-group cross section into certain coarse-group cross sections.

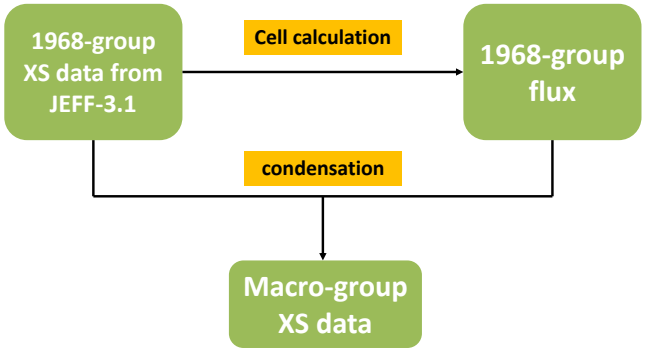

Figure 3.2: Illustration of the energy condensation procedure in ECCO

Within the ECCO code, the angular flux and the scattering cross section are developed with the Legendre Polynomial orthogonal functions until a certain order L. This action could help to decouple the angular dependence from direction and energy ones. In most cases, the development order is limited to $L = 1$. Therefore, the flux and the scattering cross section are expressed as follows:

$$\phi_g(\mathbf{r}, \hat{\Omega}) = \frac{1}{2}\left[\phi_{0,g}(\mathbf{r}) + 3\hat{\Omega}\boldsymbol{\phi}_{1,g}(\mathbf{r})\right] \tag{3.29}$$

$$\Sigma_{s,g\to g'}(\mathbf{r}, \hat{\Omega}' \cdot \hat{\Omega}) = \frac{1}{2}\left[\Sigma_{s0,g\to g'}(\mathbf{r}) + 3(\hat{\Omega}' \cdot \hat{\Omega})\Sigma_{s1,g\to g'}(\mathbf{r})\right] \tag{3.30}$$

After substituting the simplified flux and scattering cross section into a multi-group transport equation, we obtain the *P1 approximate* transport equation:

$$\hat{\Omega}\cdot\vec{\nabla}\left[\frac{1}{2}\phi_{0,g}(\mathbf{r})+\frac{3}{2}\hat{\Omega}\boldsymbol{\phi}_{1,g}(\mathbf{r})\right]+\Sigma_{t,g}(\mathbf{r})\left[\frac{1}{2}\phi_{0,g}(\mathbf{r})+\frac{3}{2}\hat{\Omega}\boldsymbol{\phi}_{1,g}(\mathbf{r})\right]= \sum_{g'=0}^{N_g-1}\left[\frac{1}{2}\phi_{0,g'}(\mathbf{r})\Sigma_{s0,g'\to g}(\mathbf{r})+\frac{3}{2}\hat{\Omega}\boldsymbol{\phi}_{1,g}(\mathbf{r})\Sigma_{s1,g'\to g}(\mathbf{r})\right]+\frac{\chi_g}{4\pi K_{\text{eff}}}Q_f(\mathbf{r}) \quad (3.31)$$

with N_g: the total number of fine energy group structure; $Q_f(\mathbf{r})=\sum_{g=0}^{N_g-1}\nu\Sigma_{f,g}(\mathbf{r})\phi_{0,g}(\mathbf{r})$: the total fission production rate.

Integrating over the whole solid angle of Eq (3.31) and Eq (3.31)$\times\hat{\Omega}$, the flux-current coupled equations system is obtained.

$$\vec{\nabla}\boldsymbol{\phi}_{1,g}(\mathbf{r})+\Sigma_{t,g}(\mathbf{r})\phi_{0,g}(\mathbf{r})=\sum_{g'=0}^{N_g-1}\phi_{0,g'}(\mathbf{r})\Sigma_{s0,g'\to g}(\mathbf{r})+\frac{\chi_g}{K_{\text{eff}}}Q_f(\mathbf{r}) \quad (3.32)$$

$$\frac{1}{3}\vec{\nabla}\phi_{0,g}(\mathbf{r})+\Sigma_{t,g}(\mathbf{r})\boldsymbol{\phi}_{1,g}(\mathbf{r})=\sum_{g'=0}^{N_g-1}\boldsymbol{\phi}_{1,g'}(\mathbf{r})\Sigma_{s1,g'\to g}(\mathbf{r}) \quad (3.33)$$

The condensation work from the fine-group energy structure to coarse-group energy structure is performed on the above Eq (3.32) and Eq (3.33). In fact, the energy collapsing procedure consists in adding all the fine-group equations g which belong to the macro-group G. Thus we obtain:

$$\vec{\nabla}\boldsymbol{\phi}_{1,G}(\mathbf{r})+\Sigma_{t0,G}(\mathbf{r})\phi_{0,G}(\mathbf{r})=\sum_{G'=0}^{N_G-1}\phi_{0,G'}(\mathbf{r})\Sigma_{s0,G'\to G}(\mathbf{r})+\frac{\chi_G}{K_{\text{eff}}}Q_f(\mathbf{r}) \quad (3.34)$$

$$\frac{1}{3}\vec{\nabla}\phi_{0,G}(\mathbf{r})+\Sigma_{t1,G}(\mathbf{r})\boldsymbol{\phi}_{1,G}(\mathbf{r})=\sum_{G'=0}^{N_G-1}\boldsymbol{\phi}_{1,G'}(\mathbf{r})\Sigma_{s1,G'\to G}(\mathbf{r}) \quad (3.35)$$

Where

- the macro-group flux calculated from fine-group flux:

$$\phi_{0,G}(\mathbf{r})=\sum_{g\in G}\phi_{0,g}(\mathbf{r}) \quad (3.36)$$

- the macro-group current which is also the first moment of flux:

$$\boldsymbol{\phi}_{1,G}(\mathbf{r})=\sum_{g\in G}\boldsymbol{\phi}_{1,g}(\mathbf{r}) \quad (3.37)$$

- the macro-group fission spectrum:

$$\chi_G=\sum_{g\in G}\chi_g \quad (3.38)$$

- the 0^{th} order of scattering cross section from macro-group G' to G, weighted by the flux:

$$\Sigma_{s0,G'\to G}(\mathbf{r}) = \frac{\sum\limits_{g'\in G'}\sum\limits_{g\in G}\Sigma_{s0,g'\to g}(\mathbf{r})\phi_{g'}(\mathbf{r})}{\sum\limits_{g'\in G'}\phi_{g'}(\mathbf{r})} \tag{3.39}$$

- the 1^{th} order of scattering cross section from macro-group G' to G, weighted by the current:

$$\Sigma_{s1,G'\to G}(\mathbf{r}) = \frac{\sum\limits_{g'\in G'}\sum\limits_{g\in G}||\Sigma_{s1,g'\to g}(\mathbf{r})\boldsymbol{\phi}_{1,g'}(\mathbf{r})||}{\sum\limits_{g'\in G'}||\boldsymbol{\phi}_{1,g'}(\mathbf{r})||} \tag{3.40}$$

- the flux weighted total cross section in macro-group G:

$$\Sigma_{t0,G}(\mathbf{r}) = \frac{\sum\limits_{g\in G}\Sigma_{t,g}(\mathbf{r})\phi_{0,g}(\mathbf{r})}{\sum\limits_{g\in G}\phi_{0,g}(\mathbf{r})} \tag{3.41}$$

- the current weighted total cross section in macro-group G:

$$\Sigma_{t1,G}(\mathbf{r}) = \frac{\sum\limits_{g\in G}||\Sigma_{t,g}(\mathbf{r})\boldsymbol{\phi}_{1,g}(\mathbf{r})||}{\sum\limits_{g\in G}||\boldsymbol{\phi}_{1,g}(\mathbf{r})||} \tag{3.42}$$

One precision should be made here, the current ($\boldsymbol{\phi}_{1,g}$) used in ECCO is in fact an approximate one which comes from the fundamental mode leakage model. Therefore, the current used in the above Eq (3.40) and (3.42) is a scalar quantity which simplifies greatly the energy condensation procedure.

The obtained macro-group constants will be used in a core simulation. However, the total macro-group cross sections should keep in a consistent form in the transport equation which will be resolved in a core calculation. Therefore, if we choose to use the flux weighted total cross section as in Eq (3.34), the other one Eq (3.35) must be reformulated as:

$$\frac{1}{3}\vec{\nabla}\phi_{0,G}(\mathbf{r}) + \Sigma_{t0,G}(\mathbf{r})\boldsymbol{\phi}_{1,G}(\mathbf{r}) = \sum_{G'=0;G'\neq G}^{N_G-1}\boldsymbol{\phi}_{1,G'}(\mathbf{r})\Sigma_{s1,G'\to G}(\mathbf{r}) + \widetilde{\Sigma}_{s1,G\to G}(\mathbf{r})\boldsymbol{\phi}_{1,G} \tag{3.43}$$

Eq (3.43) implies that the in-group anisotropy law is modified in order to keep a consistent relationship between the flux-current coupled equations. And the in-group anisotropy law is redefined as:

$$\widetilde{\Sigma}_{s1,G\to G}(\mathbf{r}) = \Sigma_{s1,G\to G}(\mathbf{r}) + \Sigma_{t0,G}(\mathbf{r}) - \Sigma_{t1,G}(\mathbf{r}) \tag{3.44}$$

Theoretically, the ECCO condensation method with use of the in-group scattering correction could preserve all the physical quantities from fine-group to macro-group, such as the flux; the current as well as the reaction rates. However, a previous work [77] showed that this method could not be appropriately applied for the case where a reflector interface is involved. This phenomenon confirms the limitation of the ECCO code which means the equation solved by ECCO is under the approximation of fundamental mode. This approximation is well adapted for the center core region but not for the peripheral

area, especially for the steel reflector, where the current behavior (its spectrum and its direction) is completely different from the flux. In order to handle the reflector problem, a new energy condensation method is proposed by Jacquet[77]. This will be detailed in the next section.

Once again, we find that the condensation method used in ECCO is a special case from the generalized condensation theory because it uses the Legendre Polynomial orthogonal basis functions ($L = 1$) to develop the angular flux. This means that the method itself is rather correct except the approximations used to get a mathematical solution. However, this is an inevitable weakness for most deterministic codes.

3.5 Conservative Energy Condensation method

The energy condensation method which will be presented in this section was proposed to deal with the reflector problem encountered in the previous section. The difficulties of the reflector issue exist in the fact that the interface between the fuel and the reflector separates two media with completely different properties. In the fuel, neutrons are mostly absorbed; while in the reflector, the scattering reaction dominates. This provoked an important anisotropy of the angular flux spectrum. To be able to preserve the neutronic balance during the condensation procedure, it is recommended to use the angular flux spectrum as a weighting function for generating the multi-group total cross section as in Eq (3.45). This kind of obtained total cross section is therefore dependent on the angular direction. Here, the idea expressed in the generalized condensation method once again confirms that the macro-group total cross section is coupled between the angular variable and the energy one.

$$\Sigma_{t,G}(\mathbf{r},\hat{\Omega}) = \frac{\sum\limits_{g\in G}\Sigma_{t,g}(\mathbf{r})\phi_g(\mathbf{r},\hat{\Omega})}{\sum\limits_{g\in G}\phi_g(\mathbf{r},\hat{\Omega})} \tag{3.45}$$

However, the non-conventional definition of the total cross section as in Eq (3.45) is not practical for use in a core simulation code. The solution proposed in the generalized condensation method is to decouple the energy- and the angular-dependence by introducing a perturbation term in addition to the standard scalar flux weighted multi-group total cross section. The conservative method suggests a different way of separating the energy and angular dependence. That means developing the total collision term with the spherical harmonic orthogonal functions. The same processing is done for the scattering term. Thus, we obtain the transport equation in macro-group G:

$$\hat{\Omega}\cdot\vec{\nabla}\phi_G(\mathbf{r},\hat{\Omega}) + \sum_{l=0}^{\infty}\frac{2l+1}{4\pi}\sum_{m=-l}^{l}\Sigma_{t,G}^{l,m}(\mathbf{r})\phi_G^{l,m}(\mathbf{r})R_l^m(\hat{\Omega}) = \sum_{G'=0}^{N_G-1}\sum_{l=0}^{\infty}\frac{2l+1}{4\pi}\sum_{m=-l}^{l}\Sigma_{s,G'\to G}^{l,m}(\mathbf{r})\phi_{G'}^{l,m}(\mathbf{r})R_l^m(\hat{\Omega}) + \frac{\chi_G(\mathbf{r})}{4\pi K_{\text{eff}}}Q_f(\mathbf{r}) \tag{3.46}$$

Where R_l^m is the real form of the sperical harmonics. The conventional macro-group variables as $\phi_G(\mathbf{r},\hat{\Omega})$, $\chi_G(\mathbf{r})$ and $Q_f(\mathbf{r})$ always keep the same definitions as in the previous sections.On the other hand, the total cross section and the scattering cross section are expressed by their own moments which are respectively defined as:

$$\Sigma_{t,G}^{l,m}(\mathbf{r}) = \frac{\sum\limits_{g\in G} \Sigma_{t,g}(\mathbf{r})\phi_g^{l,m}(\mathbf{r})}{\sum\limits_{g\in G} \phi_g^{l,m}(\mathbf{r})} \tag{3.47}$$

$$\Sigma_{s,G'\to G}^{l,m}(\mathbf{r}) = \frac{\sum\limits_{g'\in G'}\sum\limits_{g\in G} \Sigma_{s,g'\to g}^{l}(\mathbf{r})\phi_{g'}^{l,m}(\mathbf{r})}{\sum\limits_{g'\in G'} \phi_{g'}^{l,m}(\mathbf{r})} \tag{3.48}$$

With the above defined macro-group cross section moments, the neutronic balance is actually preserved from the fine-group to macro-group passage. Unfortunately, the moments of the macro-group total cross sections are not practical for the core calculation. To adapt the total cross section for the core simulation code, the 0^{th} order moment of flux $\phi_g^{0,0}(\mathbf{r})$ (in fact the scalar flux) is chosen to weight the micro-group total cross section. This makes the macro-group total cross section return to the standard expression $\Sigma_{t,G}(\mathbf{r}) = \dfrac{\sum\limits_{g\in G} \Sigma_{t,g}(\mathbf{r})\phi_g^{0,0}(\mathbf{r})}{\sum\limits_{g\in G} \phi_g^{0,0}(\mathbf{r})}$.

On the right-hand side of Eq (3.46), a modification is applied to the scattering cross section moments to keep the transport equation in balance. The modification rule is like in the ECCO code which results in the new definition of $\Sigma_{s,G'\to G}^{l,m}(\mathbf{r})$:

$$\widetilde{\Sigma}_{s,G'\to G}^{l,m}(\mathbf{r}) = \frac{\sum\limits_{g'\in G'}\sum\limits_{g\in G} \Sigma_{s,g'\to g}^{l}(\mathbf{r})\phi_{g'}^{l,m}(\mathbf{r})}{\sum\limits_{g'\in G'} \phi_{g'}^{l,m}(\mathbf{r})} + \delta_{G,G'}\left(\Sigma_{t,G}(\mathbf{r}) - \Sigma_{t,G}^{l,m}(\mathbf{r})\right) \tag{3.49}$$

Observing the macro-group scattering cross section in Eq (3.49), it always depends on both the orbital and the azimuthal order (l, m). This is not conventional for the use in the core simulation step. A simplified form of the scattering cross section depending only on the orbital order l will be appreciated. Thus the challenge is to find this kind of scattering cross section noted here as $\widehat{\Sigma}_{s,G'\to G}^{l}(\mathbf{r})$ which is the closest to the exact value of $\widetilde{\Sigma}_{s,G'\to G}^{l,m}(\mathbf{r})$. To attain this objective, a discrepancy function $U_l^{G'\to G}$ is defined as in Eq (3.50):

$$U_l^{G'\to G} = \sum_{m=-l}^{l}\left[\left(\widetilde{\Sigma}_{s,G'\to G}^{l,m}(\mathbf{r}) - \widehat{\Sigma}_{s,G'\to G}^{l}(\mathbf{r})\right)\phi_{G'}^{l,m}(\mathbf{r})\right]^2 \tag{3.50}$$

The mathematical technique of minimizing the function $U_l^{G'\to G}$ for any orbital order l which means doing $\dfrac{\partial U_l^{G'\to G}}{\partial \widetilde{\Sigma}_{s,G'\to G}^{l,m}(\mathbf{r})} = 0$ for $\forall l$ could help to find the expected scattering cross section $\widehat{\Sigma}_{s,G'\to G}^{l}(\mathbf{r})$. Finally, the conventional scattering cross section moments are:

$$\widehat{\Sigma}_{s,G'\to G}^{l}(\mathbf{r}) = \begin{cases} \widetilde{\Sigma}_{s,G'\to G}^{0,0}(\mathbf{r}), & \text{if } l = 0 \\ \dfrac{\sum\limits_{m=-l}^{l} \widetilde{\Sigma}_{s,G'\to G}^{l,m}(\mathbf{r})\phi_{G'}^{l,m}(\mathbf{r})^2}{\sum\limits_{m=-l}^{l} \phi_{G'}^{l,m}(\mathbf{r})^2}, & \text{if } l \neq 0 \end{cases} \tag{3.51}$$

This conservative condensation method requires the fine-group flux moments such as the weighting function to calculate the non-0^{th} order of scattering cross section moments. As for the other macro-group constants, they could be obtained by using the standard method. However the flux moments, especially the high order ones, are not accessible for most cell calculation codes. This method has not yet been implemented in any sub-assembly deterministic codes. *Vidal et al.*[29] applied the conservative condensation method for the fuel/reflector calculation in the S_n solver environment SNATCH. The SNATCH solver system could calculate the fine-group flux moments which were then used to obtain the macro-group constants. These calculated macro-group constants do show their advantages in a core simulation compared with those obtained with the ECCO method.

Intrinsically, the conservative energy condensation method maintains the same origin with respect to the generalized method. Both of them assume that the anisotropy effect of the macro-group total cross section plays an important role in preserving the neutronic balance during the energy condensation procedure. Ensuring this common point, they develop their own solutions which are different in the mathematical form.

Chapter 4

Spatial Homogenization Theory

Introduction

In the previous chapter, we focused on the energy condensation method which is aimed at reducing the continuous-energy dependent complexity of the cross section. However, this is not sufficient to perform a whole core calculation even with a very coarse energy structure. The reason comes from the fact that a very large amount of spatial regions exist in a reactor core. Let us take the example of the sodium-cooled fast reactor *SuperPhénix*[48], which contains about 350 fuel assemblies, with each fuel assembly made up of 271 fuel pins. Hence, it requires hundreds of thousands of distinct regions to describe each axial layer in the reactor core explicitly. It was impossible to manage such an amount of memory storage in the past years and even nowadays, it remains a great challenge. Thus, an intuitive solution to this problem is to consider an entire assembly in a certain radial plane as a homogeneous region, as illustrated in Figure 4.1. This procedure is called *Spatial Homogenization* which forms the main topic of this chapter. By virtue of the spatial homogenization and the energy condensation,a more compact cross section library is available for use in the whole core calculation.

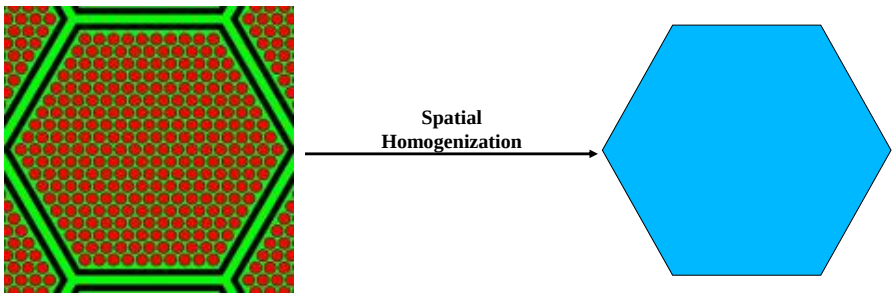

Figure 4.1: Illustration of a fuel assembly spatial homogenization

During a reactor physics calculation, especially in the deterministic field, the spatial homogenization procedure is usually performed after the energy condensation step and makes use of the previous step produced multi-group heterogeneous cross sections. In order to distinguish their different effects on the final homogenized multi-group constants, it is supposed that the used energy condensation method is exact and is capable of producing the appropriate multi-group heterogeneous cross sections which preserve the neutronic

balance from fine-group calculation to macro-group calculation. Therefore, the homogenization procedure starts with searching for the exact heterogeneous flux distribution in a sub-assembly. It could be accomplished by solving the multi-group transport equation containing the conventional multi-group cross sections as follows:

$$\hat{\Omega}\cdot\vec{\nabla}\phi_g(\mathbf{r},\hat{\Omega})+\Sigma_{t,g}(\mathbf{r})\phi_g(\mathbf{r},\hat{\Omega})=\sum_{g'}\sum_{l}\frac{2l+1}{4\pi}\sum_{m=-l}^{m=l}\Sigma_{s,l,g'\to g}(\mathbf{r})\phi_{l,g'}^{m}(\mathbf{r})R_l^m(\hat{\Omega}) + \frac{\sum_{g'}\chi_g\nu\Sigma_{f,g'}(\mathbf{r})\phi_{g'}(\mathbf{r})}{4\pi K_{\text{eff}}} \quad (4.1)$$

The final objective of the spatial homogenization is to preserve the measurable reaction rates as well as the multiplicative factor $K_{\mathbf{eff}}$. Thus, an integral over the whole solid angle is done to Eq (4.1) in order to highlight the different reaction rates. Meanwhile, the non zero-th order scattering reaction rates are all eliminated. Finally, we obtain the reaction rate balance equation (4.2):

$$\vec{\nabla}\cdot\mathbf{J}_g(\mathbf{r})+\Sigma_{t,g}(\mathbf{r})\phi_g(\mathbf{r})=\sum_{g'}\left[\Sigma_{s,0,g'\to g}(\mathbf{r})\phi_{g'}(\mathbf{r})+\frac{\chi_g\nu\Sigma_{f,g'}(\mathbf{r})\phi_{g'}(\mathbf{r})}{K_{\text{eff}}}\right] \quad (4.2)$$

where

- $\mathbf{J}_g(\mathbf{r})=\int_{4\pi}\mathbf{J}_g(\mathbf{r},\hat{\Omega})d^2\Omega$: the angular-independent current vector;
- $\phi_g(\mathbf{r})=\int_{4\pi}\phi_g(\mathbf{r},\hat{\Omega})d^2\Omega$: the scalar flux.

Supposing that the cell calculation code has the technique to solve Eq (4.2) correctly, we obtain the heterogeneous multi-group flux and current as well as the eigenvalue K_{eff} which will be used ultimately as a reference for the results from the homogenization step. We now continue to integrate Eq (4.2) over the entire space which is intended to be homogenized. The integrated form is expressed in Eq (4.3).

$$\int_{\mathbf{r}\in V}d^3\mathbf{r}\left(\vec{\nabla}\cdot\mathbf{J}_g(\mathbf{r})+\Sigma_{t,g}(\mathbf{r})\phi_g(\mathbf{r})\right)=\int_{\mathbf{r}\in V}d^3\mathbf{r}\left(\sum_{g'}\left[\Sigma_{s,0,g'\to g}(\mathbf{r})\phi_{g'}(\mathbf{r})+\frac{\chi_g\nu\Sigma_{f,g'}(\mathbf{r})\phi_{g'}(\mathbf{r})}{K_{\text{eff}}}\right]\right) \quad (4.3)$$

If the scalar flux is always used here as the weighting function as in the standard energy condensation procedure, we should obtain the direct flux-volume averaged homogenized multi-group cross sections as follows:

- the homogenized total cross section in macro-group g and volume V:

$$\overline{\Sigma}_{t,g}^{V}=\frac{\int\limits_{\mathbf{r}\in V}d^3\mathbf{r}\Sigma_{t,g}(\mathbf{r})\phi_g(\mathbf{r})}{\int\limits_{\mathbf{r}\in V}d^3\mathbf{r}\phi_g(\mathbf{r})} \quad (4.4)$$

- the homogenized 0^{th} order scattering cross section averaged in the volume V from group g' to g:

$$\overline{\Sigma}_{s,0,g'\to g}^{V}=\frac{\int\limits_{\mathbf{r}\in V}d^3\mathbf{r}\Sigma_{s,0,g'\to g}(\mathbf{r})\phi_{g'}(\mathbf{r})}{\int\limits_{\mathbf{r}\in V}d^3\mathbf{r}\phi_{g'}(\mathbf{r})} \quad (4.5)$$

- the homogenized fission production cross section where the fission spectrum, the multiplicity factor and the fission cross section are all mixed in both the energy and the spatial phase. This more compact expression of the fission production term is similar to the scattering cross section form. It could simplify the computational treatment for a simulation code:

$$\overline{\chi\nu\Sigma}^V_{f,g'\to g} = \frac{\int\limits_{\mathbf{r}\in V} d^3\mathbf{r}\chi_g\nu\Sigma_{f,g'}(\mathbf{r})\phi_{g'}(\mathbf{r})}{\int\limits_{\mathbf{r}\in V} d^3\mathbf{r}\phi_{g'}(\mathbf{r})} \tag{4.6}$$

So with the above defined homogenized multi-group parameters, Eq (4.3) becomes:

$$\int\limits_{\mathbf{r}\in V} d^3\mathbf{r}\vec{\nabla}\cdot\mathbf{J}_g(\mathbf{r}) + \overline{\Sigma}^V_{t,g}\phi^V_g = \sum_{g'}\left[\overline{\Sigma}^V_{s,0,g'\to g}\phi^V_{g'} + \frac{\overline{\chi\nu\Sigma}^V_{f,g'}\phi^V_{g'}}{K_{\text{eff}}}\right] \tag{4.7}$$

where $\phi^V_g = \int\limits_{\mathbf{r}\in V} d^3\mathbf{r}\phi_g(\mathbf{r})$ represents for the total flux in macro-group g over the entire space. The first term in Eq (4.7) is the overall leakage rate. Under the reflective boundary condition, the leakage rate is canceled: $\int\limits_{\mathbf{r}\in V} d^3\mathbf{r}\vec{\nabla}\cdot\mathbf{J}_g(\mathbf{r}) = 0$. Thus the optimal case is obtained where all of the reaction rates and K_{eff} are preserved simply with the standard scalar flux weighted method.

However, an infinite configuration could not represent any individual sub-assembly under a critical operation condition. Thus, most of the cell calculation codes (especially the deterministic ones) handle the neutron leakage problem with some types of physical leakage models. The neutron leakage effect is also an interesting topic for this work. Detailed descriptions and development will be given in Chapter 9. Presently, the neutron leakage effect is indeed a perturbation term for the spatial homogenization procedure. It breaks the homogeneity property in the transport equation (4.7). Therefore, the solutions of Eq (4.7) $\widetilde{\phi}^V_g$ are no more the sum of the heterogeneous flux, as shown in Eq (4.8). Consequently, the macroscopic reaction rates calculated with the flux-weighted homogenized cross sections are no longer preserved.

$$\widetilde{\phi}^V_g \neq \int_{\mathbf{r}\in V} d^3\mathbf{r}\phi_g(\mathbf{r}) \tag{4.8}$$

The non-preservation phenomenon was observed, for example, in the analysis of a Light Water Reactor [58]. The use of the standard flux-weighted two-group constants showed an over-estimation tendency for the sub-assembly power density. This non-consistent neutronic balance problem revealed in the homogenization procedure, is similar to the one observed in the energy condensation procedure in Chapter 3. The common reason is that the use of homogenized parameters results in an inevitable loss of information compared to the realistic heterogeneous case. Thus, the challenge of a spatial homogenization procedure is to find such homogenized cross sections which could preserve the overall reaction rates as well as the multiplicative factor $K_{\mathbf{eff}}$ in a realistic leakage situation.

Since the homogenization problem has existed for a long time, a lot of research work was carried out not only for the nuclear reactor analysis but also in a larger mathematical range. Compared to the direct flux-weighted method, some more sophisticated methods were proposed. For example, Worley and Henry used the response matrix technique [97]

to calculate the heterogeneous reaction rates and succeeded in avoiding the difficulties involved in determining the overall homogeneous flux. However, its primary drawbacks are the complicated mathematical nature and its low computational efficiency.

Among all of the existing homogenization methods which could more or less preserve the neutronic balance, there is one homogenization concept noted as *Equivalence Theory* [60] which is capable of reproducing the different types of reaction rates and the multiplicative factor. The *equivalence theory* could be specified in different mathematical forms adapting to the different types of core calculation codes. For example, to continue a transport theory based core calculation, only the appropriate homogenized multi-group cross sections are demanded from the equivalence method. However, if a diffusion core simulation code is concerned, the homogenized multi-group diffusion coefficients are eventually required at the same time.

The homogenization problem is investigated more thoroughly in the thermal neutron reactor domain than in the fast neutron reactor. This is because the heterogeneity effect is more important in a thermal core. In the early 80's, two Ph.D work were performed with almost the same objective in view, namely to discover an efficient and precise method for sub-assembly spatial homogenization procedure. Both of the two proposed solutions originated from the equivalence theory. The one performed by *Hébert* at the CEA was inspired by the SuPerHomogenization method noted as SPH [49]. This SPH method , developed by Kavenoky[7], introduces a set of correction factors for the flux-weighted homogenized multi-group cross sections. Using these modified cross sections in the core calculation could preserve the macro region-wise reaction rates and K_{eff}. The other work done by *Smith* led to the birth of the Generalized Equivalence Theory noted as GET [58]. The GET method defines *discontinuity factors* for each lateral interface of the sub-assembly to be homogenized. The use of these discontinuity factors helps to avoid the necessity of iterating loop to evaluate the homogenized parameters. From the point of view of a core calculation, the GET method is more suitable for the nodal diffusion core calculation, while the SPH method does not show its preference between diffusion and transport codes. In the following sections, we shall specify the two methods respectively: the SPH method for a transport core calculation and the GET method for a diffusion core calculation.

4.1 SPH Method

The principal idea of the SPH method is to imply a set of correction factors $\{ \mu_g^V \}$ on the flux-weighted homogenized multi-group cross sections in order to preserve the target reaction rates. It should be pointed out that every correction factor μ_g^V is shared among all types of reaction rates in each macro energy group g as well as the homogenized medium V. According to the functionality of the SPH method, it is located between the energy condensation procedure and edition of the final cross sections. Focusing on the SPH method, it is divided into three steps:

1. Determination of the target macroscopic reaction rates which will be used as reference;
2. Iteration procedure of correction factors $\{ \mu_g^V \}$ until obtaining exactly the reference reaction rates;
3. Output of the corrected homogenized multi-group constants which will be used in the next step core simulations.

Starting with the first step in the SPH method, the reference reaction rates are previously included in Eq (4.3). They are defined respectively as it can be seen below. The symbol, * indicates the reference value.

- $T^{tot*}_{v,g} = \int\limits_{\mathbf{r}\in V} d^3\mathbf{r}\Sigma_{t,g}(\mathbf{r})\phi_g(\mathbf{r})$: the macroscopic total collision rate;

- $T^{s*}_{v,g'\to g} = \int\limits_{\mathbf{r}\in V} d^3\mathbf{r}\Sigma_{s,0,g'\to g}(\mathbf{r})\phi_{g'}(\mathbf{r})$: the macro-group g' to g scattering rate;

- $T^{f*}_{v,g'\to g} = \int\limits_{\mathbf{r}\in V} d^3\mathbf{r}\chi_g\nu\Sigma_{f,g'}(\mathbf{r})\phi_{g'}(\mathbf{r})$: the macro-group g' to g fission production rate.

As a reminder the readers, the multi-group cross sections ($\Sigma_{t,g}(\mathbf{r})$, $\Sigma_{s,0,g'\to g}(\mathbf{r})$, $\chi\nu\Sigma_{f,g'\to g}(\mathbf{r})$) used here for calculating the reference macroscopic reaction rates are obtained from the supposed exact condensation method. And the heterogeneous multi-group flux $\phi_g(\mathbf{r})$ are in fact the solution of Eq (4.3). Thus, we get the full information about the targeted macroscopic reaction rates.

With knowledge of the heterogeneous multi-group flux, we can calculate the direct flux-weighted homogenized cross sections. Their definitions are already given previously. Here, we simply repeat their notations: $\overline{\Sigma}^V_{t,g}$; $\overline{\Sigma}^V_{s,0,g'\to g}$; $\overline{\chi\nu\Sigma}^V_{f,g'\to g}$ where the subscript ^{V} stands for the homogenized medium. With the newly calculated homogenized cross sections, the balance equation is rewritten as:

$$\vec{\nabla}\cdot\widetilde{\mathbf{J}_g}(\mathbf{r}) + \overline{\Sigma}^V_{t,g}\widetilde{\phi_g}(\mathbf{r}) = \sum_{g'}\left[\overline{\Sigma}^V_{s,0,g'\to g}\widetilde{\phi_g}(\mathbf{r}) + \frac{\overline{\chi\nu\Sigma}^V_{f,g'\to g}\widetilde{\phi_g}(\mathbf{r})}{K_{\text{eff}}}\right] \tag{4.9}$$

The solutions of Eq (4.9) $\widetilde{\mathbf{J}_g}(\mathbf{r})$ and $\widetilde{\phi_g}(\mathbf{r})$ deviate from the reference ones ($\mathbf{J}_g(\mathbf{r})$ and $\phi_g(\mathbf{r})$)from Eq(4.3). Thus, the iteration procedure is necessary started. In the next paragraphs, we note n as the iteration index.

For $n = 1$, we could calculate the corrective factors $\mu^V_{g,(n=1)} = \dfrac{\int\limits_{\mathbf{r}\in V} d^3\mathbf{r}\phi_g(\mathbf{r})}{\int\limits_{\mathbf{r}\in V} d^3\mathbf{r}\widetilde{\phi_g}^{(n=1)}(\mathbf{r})}$ for all the macro groups and macro regions. Then, the first set of correction factors $\{\mu^V_{g,(n=1)}\}$ are multiplied to the original homogenized multi-group cross sections.

For $n = 2$, the cross sections used to solve the transport equation are: $\mu^V_{g,(n=1)}\overline{\Sigma}^V_{t,g}$; $\mu^V_{g,(n=1)}\overline{\Sigma}^V_{s,0,g'\to g}$ and $\mu^V_{g,(n=1)}\overline{\chi\nu\Sigma}^V_{f,g'\to g}$. They result in the second loop solutions noted as $\widetilde{\mathbf{J}_g}^{(n=2)}(\mathbf{r})$ and $\widetilde{\phi_g}^{(n=2)}(\mathbf{r})$. Similar to the first iteration step, we can calculate the second set of correction factors.

To be precise here, the normalization rule imposed to every iteration step for searching the flux and current should be the same, for example, respecting the same fission production or the same sources. The iteration procedures continue till the convergence criterion is attained. By the way, this convergence criterion is usually decided by the users. For example, the discrepancy between two consecutive correction factors is smaller to certain tiny value, as following:

$$\frac{|\mu^V_{g,(n+1)} - \mu^V_{g,(n)}|}{\mu^V_{g,(n)}} < 10^{-4} \tag{4.10}$$

Once the convergence criterion has been reached for all the macro energy groups, the SPH procedure is complete and produces the appropriate homogenized multi-group cross section for the core simulation codes. The whole iteration process is summed up in Figure 4.2.

With the SPH method, the target macroscopic reaction rates and the K_{eff} could be perfectly reproduced. This method is applicable to any kind of reactor sub-assembly. For example, the French lattice calculation code, APOLLO2 uses this method to cover up the inconsistent neutronic balance due to the scalar flux weighted homogenized multi-group cross sections. In the present section, the SPH method is shown as a tool used in the transport-transport two-step calculation strategy. Moreover, it could be used for the transport-diffusion calculation scheme. Detailed information could be found in [6]. The only deficiency of this method concerns taking the risk of a long iteration procedure. For this reason, another homogenization method will be presented in the next section which could actually avoid this point.

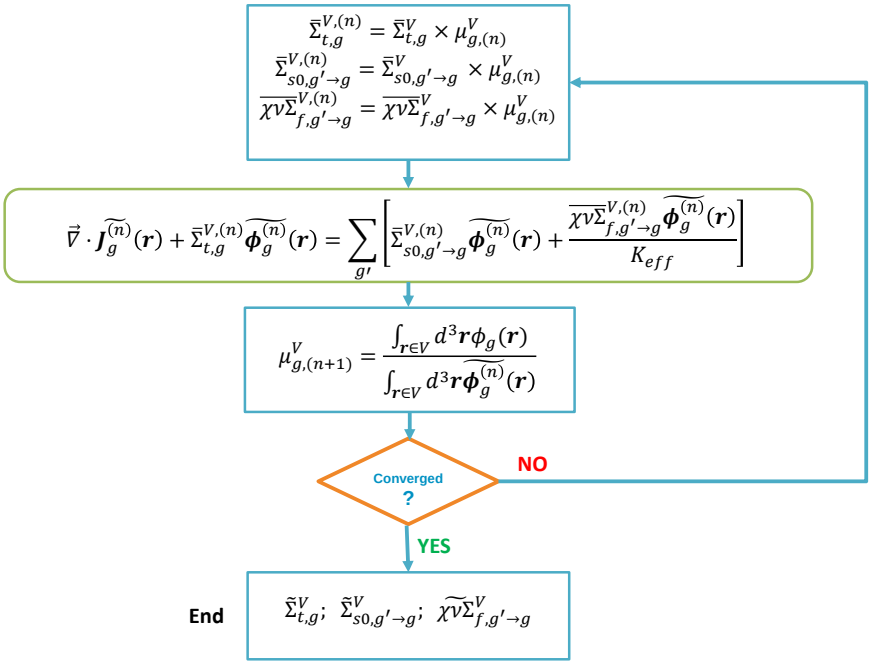

Figure 4.2: Illustration of the SPH iteration method

4.2 GET method

In this section, the Generalized Equivalence Technique (GET) will be presented as an efficient tool in producing homogenized multi-group constants. This computational technique is usually implemented in a Nodal diffusion whole core calculation environment. Thus, in order to have a thorough understanding of this method, a basic knowledge of the Nodal

diffusion theory [6] is necessary. In fact, in a Nodal diffusion calculation, each sub-assembly is considered as a homogeneous node which is presented by a set of homogenized coarse-group constants. These mentioned constants are different types of cross sections (total, absorption, scattering, fission production and fission spectrum); the diffusion coefficients and the discontinuity factors. The last ones exist only in the Nodal method. Explicit demonstrations are followed to reveal how these discontinuity factors are involved.

The initial hypothesis and the final objective are shared between the GET method and the SPH method. This means that the exact energy condensation method is always supposed to be available. Thus we could obtain the "exact" heterogeneous coarse-group constants in the related sub-assembly which will be homogenized in the next step. At the same time, we always insist on preserving the macroscopic reaction rates, the leakage rates and so the K_{eff} value.

It should be pointed out that there is a new challenge in the GET method which consists in conserving every surface current of the homogenized sub-assembly as shown in Eq (4.11).

$$-\int_{S_i^V} D_g(\mathbf{r})\vec{\nabla}\phi_g(\vec{r})\cdot d\mathbf{s} = \int_{S_i^V} \mathbf{J}_g(\mathbf{r})\cdot d\mathbf{s} \tag{4.11}$$

where S_i^V refers to face i of the sub-assembly V. With consideration of the current effect, our attention must be drawn back to Eq (4.7). Before doing the mathematical deductions, it is necessary to fix some conventional notations which will ultimately be used.

- (i, j, k) is used to represent the position of the sub-assembly in the normal Cartesian coordinate. i, j, k are all integers which stand respectively for x, y, z directions.
- h_i^x, h_j^y h_k^z are used to represent the lengths for each direction of the node (i, j, k).
- $V(i, j, k)$ is the volume of the node (i, j, k) which equals to $h_i^x h_j^y h_k^z$.

The above definitions are illustrated in Figure 4.3.

With the new notation rules, the Eq (4.7) could be rewritten as follows:

$$\begin{aligned} &h_j^y h_k^z \left[J_g^x(i+1,j,k) - J_g^x(i,j,k)\right] + h_i^x h_k^z \left[J_g^y(i,j+1,k) - J_g^y(i,j,k)\right] \\ &\qquad + h_i^x h_j^y \left[J_g^z(i,j,k+1) - J_g^z(i,j,k)\right] + \overline{\Sigma}_{t,g}(i,j,k)\overline{\phi_g}(i,j,k)V(i,j,k) \\ &= \sum_{g'}\left[\overline{\Sigma}_{s,0,g'\to g}(i,j,k)\overline{\phi_{g'}}(i,j,k)V(i,j,k) + \frac{\overline{\chi\nu\Sigma}_{f,g'\to g}(i,j,k)\overline{\phi_{g'}}(i,j,k)V(i,j,k)}{K_{\text{eff}}}\right] \end{aligned} \tag{4.12}$$

where all the over-lined macroscopic cross sections are weighted by the "exact" scalar heterogeneous flux. The definitions of these cross sections are already given below in Eq (4.3). As for the flux and the current, they are averaged over the volume and the directional surface respectively, expressed mathematically as follows:

$$\overline{\phi_g}(i,j,k) = \frac{\int_{x_i}^{x_{i+1}} dx \int_{y_j}^{y_{j+1}} dy \int_{z_k}^{z_{k+1}} dz \phi_g(x,y,z)}{V(i,j,k)} \tag{4.13}$$

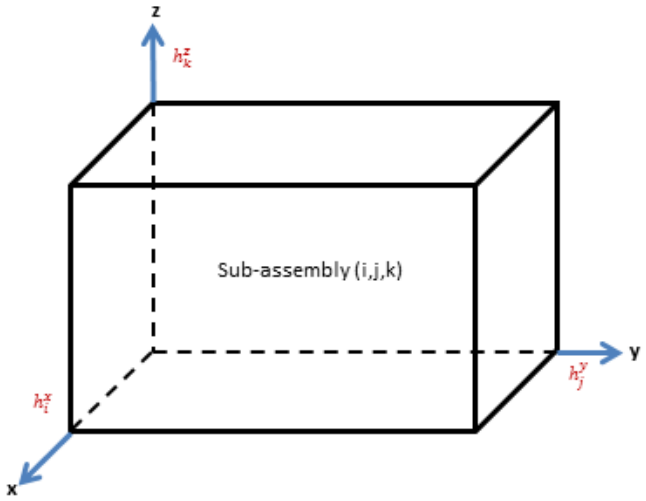

Figure 4.3: Illustration of nodal sub-assembly scheme

$$J_g^x(i,j,k) = \frac{\int_{y_j}^{y_{j+1}} dy \int_{z_k}^{z_{k+1}} dz J_g^x(x_i,y,z)}{h_j^y h_k^z} \tag{4.14}$$

$$J_g^y(i,j,k) = \frac{\int_{x_i}^{x_{i+1}} dx \int_{z_k}^{z_{k+1}} dz J_g^y(x,y_j,z)}{h_i^x h_k^z} \tag{4.15}$$

$$J_g^z(i,j,k) = \frac{\int_{x_i}^{x_{i+1}} dx \int_{y_j}^{y_{j+1}} dy J_g^z(x,y,z_k)}{h_i^x h_j^y} \tag{4.16}$$

If these flux weighted homogenized multi-group cross sections continue to be used in the whole core calculation, it means that Eq (4.12) is also valid in representing the neutronic balance for a homogenized node in the core calculation step. We use another set of notations for the whole core calculation solutions: $\hat{\phi}_g(i,j,k)$; $\hat{\mathbf{J}}_g(\mathbf{r})$; all the overlayed cross sections become hat-wore cross sections without changing the values. By virtue of the same transport equation and the same homogenized multi-group cross sections shared between the core and the sub-assembly calculation, we have to preserve every single term in Eq (4.12).

Thus, we could conclude, at first, that the homogeneous flux solutions ($\hat{\phi}_g(i,j,k)$) from the whole core calculation are identical to the averaged heterogeneous flux as expressed in Eq (4.13) for every sub-assembly node: $\overline{\phi_g}(i,j,k) = \hat{\phi}_g(i,j,k)$. In addition, the macroscopic reaction rates, the leakage rates and the multiplicative factor are preserved.

The second conclusion is made for the surface current terms, the preservation relation is only available for the overall leakage rates. In order to establish a relationship between the homogeneous surface current and the heterogeneous surface-averaged current (Eq 4.14 to Eq 4.16), we need to write the homogeneous current ($\hat{\mathbf{J}}_g(\mathbf{r})$) as the gradient of the homogeneous flux ($\hat{\phi}_g(\mathbf{r})$) according to the principle of the Fick's law. Here, to simplify the mathematical expressions, the following deductions are performed for a one-dimensional problem. Thus the $x-$directional current within node (i,j,k) is expressed as in Eq (4.17).

$$\hat{J}_g^{\,x}(\mathbf{r})|_{(i,j,k)} = -D_g^x|_{(i,j,k)} \frac{\partial \hat{\phi}_g(\mathbf{r})}{\partial x}|_{(i,j,k)} \tag{4.17}$$

where $D_g^x|_{(i,j,k)}$ corresponds to the $x-$directional diffusion coefficient in homogenized node (i,j,k). The idea of using directional dependent diffusion coefficient is proposed by Koebke [60] which is different from the classical Fick diffusion law. With the same idea in mind, we could use a diffusion coefficient tensor $\mathbf{D}_g|_{(i,j,k)}$ to specify the direction dependence. After division by the node volume, the Eq (4.12) could be written as:

$$\begin{aligned} -\nabla \cdot \mathbf{D}_g|_{(i,j,k)} \cdot \nabla \hat{\phi}_g(x,y,z) + \hat{\Sigma}_{t,g}(i,j,k)\hat{\phi}_g(i,j,k) = \\ \sum_{g'} \left[\hat{\Sigma}_{s,0,g'\to g}(i,j,k)\hat{\phi}_{g'}(i,j,k) + \frac{\chi \hat{\nu}\Sigma_{f,g'\to g}(i,j,k)\hat{\phi}_{g'}(i,j,k)}{K_{\text{eff}}} \right] \end{aligned} \tag{4.18}$$

In order to follow the $x-$directional surface averaged current variation tendency, an integration is done to Eq (4.18) over the $y-$ and $z-$ directions of the node (i,j,k). Thus, we obtain the surface averaged equation which is parallel to the plan $y-z$:

$$\begin{aligned} -D_g^x|_{(i,j,k)} \frac{\partial^2 \hat{\phi}_g^{\,x}(x)|_{(i,j,k)}}{\partial x^2} + \hat{\Sigma}_{t,g}(i,j,k)\hat{\phi}_g^{\,x}(x)|_{(i,j,k)} + \hat{L}_g^{\,x}|_{(i,j,k)} = \\ \sum_{g'} \left[\hat{\Sigma}_{s,0,g'\to g}(i,j,k)\hat{\phi}_{g'}^{\,x}(x)|_{(i,j,k)} + \frac{\chi \hat{\nu}\Sigma_{f,g'\to g}(i,j,k)\hat{\phi}_{g'}^{\,x}(x)|_{(i,j,k)}}{K_{\text{eff}}} \right] \end{aligned} \tag{4.19}$$

where the surface averaged flux and leakage terms are defined respectively as below:

- $\hat{\phi}_g^{\,x}(x)|_{(i,j,k)} = \dfrac{\int_{y_j} dy \int_{z_k} dz \hat{\phi}_g(x,y,z)}{h_j^y h_k^z}$: a surface averaged flux which is dependent on the position on the x axis within the node (i,j,k). The surface plan is perpendicular to the x direction.

- $\hat{L}_g^{\,x}|_{(i,j,k)} = \dfrac{-D_g^y(i,j,k)\int_{y_j} dy \int_{z_k} dz \dfrac{\partial^2 \hat{\phi}_g(x,y,z)}{\partial y^2} - D_g^z(i,j,k)\int_{y_j} dy \int_{z_k} dz \dfrac{\partial^2 \hat{\phi}_g(x,y,z)}{\partial z^2}}{h_j^y h_k^z}$: the sum of the two net leakages transverse to the direction x, per unit x, divided by the surface $h_j^y h_k^z$.

In the above Eq (4.19), with the exception of the first boundary condition term, all the rest are supposed to be known. And we have proved previously that the rest of the terms are consistent between the heterogeneous cell calculation step and the homogenized core calculation step. Thus, for the first boundary condition term, we could always preserve the surface currents as shown in Eq (4.11) via choosing the appropriate diffusion coefficients.

As we know that the heterogeneous surface currents are continuous while passing through an interface, thus the continuity property is inherited naturally by the homogenized surface current. This means that in a nodal core calculation, we could write an equilibrium relationship as : $\hat{J}_g^{\,x}(\mathbf{r})|_{(i^+,j,k)} = \hat{J}_g^{\,x}(\mathbf{r})|_{(i+1^-,j,k)}$, with i^+ and $i+1^-$ indicate respectively the positive and negative directions of the interface crossed by two adjacent nodes (i,j,k) and $(i+1,j,k)$.

Since the surface current could be expressed by the surface flux as follows:

$$\hat{J}_g^{\ x}(\mathbf{r})|_{(i^+,j,k)} = -D_g^x|_{(i,j,k)} \frac{\partial \hat{\phi}_g^{\ x}(x)}{\partial x}|_{(i^+,j,k)} \tag{4.20}$$

Thus a relationship could be established between two adjacent surface flux:

$$D_g^x|_{(i,j,k)} \frac{\partial \hat{\phi}_g^{\ x}(x)}{\partial x}|_{(i^+,j,k)} = D_g^x|_{(i+1,j,k)} \frac{\partial \hat{\phi}_g^{\ x}(x)}{\partial x}|_{(i+1^-,j,k)} \tag{4.21}$$

Because the diffusion coefficients are not necessarily identical between the adjacent nodes, we could not tell that the continuity effect is also respected by the surface flux. To overcome this problem, Smith[58] proposed the discontinuity factors for each side of the interface between two adjacent nodes. They are defined as the ratio of the surface averaged flux to the volume-averaged flux:

$$f_g^{x^+}(i,j,k) = \frac{\hat{\phi}_g^{\ x}(i^+)|_{(i,j,k)}}{\hat{\phi}_g(i,j,k)} \tag{4.22}$$

$$f_g^{x^-}(i,j,k) = \frac{\hat{\phi}_g^{\ x}(i^-)|_{(i,j,k)}}{\hat{\phi}_g(i,j,k)} \tag{4.23}$$

With the additional freedom degree, we could eventually preserve the macroscopic reaction rates, the multiplicative factor and the surface current at the same time.

Conclusion

Both of the methods presented in this chapter are involved in the deterministic simulation domain. Eventually, in the Monte-Carlo codes, the energy condensation and the spatial homogenization procedures could not really be clearly distinguished. As the collision density is the a practical variable mastered in a Monte-Carlo simulation, thus the scalar flux could be deduced directly. So the Monte-Carlo codes use this scalar flux as a weighting function to produce homogenized multi-group cross sections. The first innovative scientific contribution of this work is to propose a consistent method for energy condensation and spatial homogenization which is heavily inspired by the above mentioned deterministic methods. Detailed developments will be presented in Part II.

Chapter 5

Homogenized multi-group cross section production with Monte-Carlo codes

Introduction

The two previous chapters described respectively the energy condensation and spatial homogenization issues from a deterministic point of view. However, some inherent approximations and simplifications are involved which result in the limitations of the deterministic energy condensation and spatial homogenization methods. For example, the deterministic methods could not handle all kinds of geometries due to its solver limitation. Even for methods of characteristics (MOC)[35], its capacity to handle 3D geometries is quite restrained. A large amount of trajectories have to be stored which probably induce some hardware problem. That is why the Monte-Carlo method is solicited to produce homogenized multi-group constants. Additionally, the increase in computational capacity enables us to actualize this interesting idea.

This chapter begins with a general introduction of the Monte-Carlo method: its general principles; the related simulation Algorithm used for solving the integral form of neutron transport equation. Then, some descriptions will be given about the Monte-Carlo estimators. The four last sections are dedicated to four worldwide Monte-Carlo codes which are capable of producing the homogenized multi-group constants (the multi-group cross sections as well as the multi-group energy transfer matrix and anisotropy parameters). They are namely: the Finnish code Serpent [63, 64] developed at the VTT technical research center; the Korean code McCARD [27, 28] developed at Seoul National University; the American code MCNP [54, 65] developed at the Los Alamos Laboratory; the French code TRIPOLI-4® [31, 23, 5] developed at the CEA. Of course, these codes can perform a lot of various kinds of analysis work. Here, the author focuses on comparing their use in the multi-group constants production. Concerning the French code TRIPOLI-4®, a summary of the existing functionalities of multi-group constants production will be presented before starting the main part of this thesis work. The newly implemented methods will be explained in the next two parts.

5.1 General Principles of the Monte-Carlo Method

Since the nineteenth century, two different mathematical methods dealing with physical phenomena have been developed. The problems with a few particles are usually treated with conventional mechanics solving some differential equation systems, as described in the previous section. In contrast, for a large amount of particle systems, another completely different methodology was developed from statistical mechanics. With this later method, we are more interested in the whole set of particles properties rather than searching for an exact solution for one particular particle. The set theory [57], the measurement theory [13, 14] and then the probability theory [18] dated from the twentieth century combined allow us to formalize the statistical method that is nowadays termed ¨Monte-Carlo method˝[72].

For a nuclear fission reactor containing about $10^{18} \sim 10^{20}$ neutrons per cube centimeter per second, it is impossible to treat them all with the classical deterministic method avoiding certain approximations, such as discretization. Therefore, the Monte-Carlo method naturally attracts our attention in the field of nuclear reactor physics calculations.

The basic question is how to calculate a physical quantity of interest with the probabilistic method. The principal idea is to find an estimator e for the quantity to be measured. We suppose that there exists a unique solution u which is exactly the expectation of the estimator.

$$E(e) = u \tag{5.1}$$

The next step is how to obtain the expected value. For this, N independent events are realized randomly. Each of them is sampled according to a certain probability distribution $L(u, \sigma)$ and gives out a score noted as e_n, $n = 1, 2, \cdots N$. This used distribution refers to the probability density function (PDF[1]). All these scores $\{e_n\}$ respect the above distribution law which is characterized by its expectation value u and its standard deviation σ. At the same time, an averaged value is obtained from the set of scores $\{e_n\}$ according to Eq (5.2). By using the law of large numbers, we could predict that $\overline{e_N}$ will converge to u while N tends towards infinity as shown in Eq (5.3).

$$\overline{e_N} = \frac{1}{N} \times \sum_{n=1}^{N} e_n \tag{5.2}$$

$$\lim_{N \to \infty} \overline{e_N} = E(e) = u \tag{5.3}$$

The above relationships indicate that $\overline{e_N}$ is indeed an accessible estimator for the expected physical quantity. From now on, we consider the previous N independent events as one sample with an estimated value $\overline{e_N}$. According to the central limit theorem[61, 62, 19], the above estimated variable $\overline{e_N}$ follows a Gaussian distribution law noted as $G(u, \frac{\sigma}{\sqrt{N}})$. Comparing the two distribution laws: $G(u, \frac{\sigma}{\sqrt{N}})$ and $R(u, \sigma)$, it is found that they share the same expected value u but not the same standard deviation. The variance of the Gaussian law is indeed reduced by N with respect to the first unknown distribution law. Eq (5.4) shows the mathematical formula of Gaussian function.

[1]The probability density function describes the relative likelihood for a random variable to take on a given value

$$G(x) = \frac{1}{\sqrt{2\pi}\frac{\sigma}{\sqrt{N}}} e^{-\frac{1}{2}\left(\frac{x-u}{\frac{\sigma}{\sqrt{N}}}\right)^2} \tag{5.4}$$

It is characterized by two parameters:

- u: the expected value of the unique solution ;

- $\frac{\sigma}{\sqrt{N}}$: the standard deviation of the Gaussian distribution.

Then, this work of sampling N independent events is repeated M times. Their results form another set of scores $\{\overline{e_N}^m\}$, $m = 1, 2, \cdots M$. Similarly, the new scores $\{\overline{e_N}^m\}$ construct a Gaussian distribution function noted as $G(u, \frac{\sigma}{\sqrt{N \times M}})$. Till now, the expected value u is always preserved and the standard variance is reduced by the total number of sampled independent events $N \times M$.

It should be noted that both u and $\frac{\sigma}{\sqrt{N \times M}}$ are the exact solutions what we expect from a probabilistic approach. However they could never be obtained exactly because the number of independent random samples is always limited. By the way, u corresponds to the deterministic solution with $\frac{\sigma}{\sqrt{N \times M}} = 0$.

Finally, the estimation of the expected value u noted as $\hat{u}$ is obtained by performing an algebraic average over all the M scores $\{\overline{e_N}^m\}$. As for its standard variance noted as S_M^2, it is estimated from the estimated expectation value $\hat{u}$ as well as each single element in the set $\{\overline{e_N}^m\}$. The detailed formula are as follows:

$$\hat{u} = \frac{1}{M} \times \sum_{m=1}^{M} \overline{e_N}^m \tag{5.5}$$

$$S_M^2 = \frac{1}{M(M-1)} \sum_{m=1}^{M} (\overline{e_N}^m - \hat{u})^2 \tag{5.6}$$

In the Monte-Carlo domain, the standard variance is a very important parameter associated with its own distribution law. With its aid, a confidence interval can be defined which is also named in mathematics the error function $c(e)$. It provides a probability that a random score $\overline{e_N}^m$ enters in the desired interval $\{ u - e \leq \overline{e_N}^m \leq u + e\}$.

$$c(e) = \frac{1}{\sqrt{2\pi} S_M} \int_{u-e}^{u+e} e^{\frac{(\overline{e_N}^m - u)^2}{2S_M^2}} du = \mathrm{erf}(\frac{e}{\sqrt{2} S_M}) \tag{5.7}$$

The most often used confidence intervals are respectively:

$$c(e) = \begin{cases} 0.689 & \text{if} \quad e = S_M \\ 0.954 & \text{if} \quad e = 2S_M \\ 0.997 & \text{if} \quad e = 3S_M \end{cases} \tag{5.8}$$

5.2 Neutron Transport with Monte-Carlo method and its Simulation Algorithm

In this section, we will specify the Monte-Carlo method for the neutron transport problem. The main idea extracted from Monte-Carlo method to treat the neutron transport problem is trying to simulate as closely as possible every neutron traveling story. In order to make the stochastic method applicable in our domain of interest, a principal hypothesis is necessary: each of the neutron movements is considered to be a Markov process. This means that the neutron reactions at any moment depend only on their present state and are completely disconnected from previous situations. This hypothesis makes neutron interactions independent events.

In order to obtain reliable results, numerous neutrons are launched into the nuclear system in a certain kind of arrangement. At first, N neutrons are gathered to form one batch. The batch concept corresponds to the first events set $\{e_n\}$ in the previous section. Then, M batches of neutrons are simulated independently which give out the final estimated results and their standard variations. According to Eq (5.5) and (5.6), we notice that the final estimated values depend on both the number of particles in each batch as well as the number of batches.

Until now, only macroscopic steps have been mentioned concerning how to handle the neutron transport process with the Monte-Carlo method. In the following paragraphs, we shall enter into every single neutron life story.

Each neutron source is born randomly with associated initial characteristics: the energy E_o, the direction $\hat{\Omega}_o$, the position $\mathbf{r}_o$ which are all chosen randomly according to certain distribution rules. An optical path ρ is then selected for the neutron. The sampling of an arbitrary variable relies on the knowledge of its probability density function. In the case of optical path, it is noted as $P(\rho)$ and shown in Eq (5.9). This probability density is related to its existing homogeneous medium macroscopic total cross section.

$$P(\rho) = \Sigma_t(\mathbf{r}, E_o) e^{-\int_0^{\rho} \Sigma_t(\mathbf{r}_o + s\hat{\Omega}, E_o) ds} \tag{5.9}$$

Taking a random number ξ between $[0; 1]$, the latter can help to decide an optical path ρ_o according to an equality relationship:

$$\int_0^{\xi} 1 d\xi' = \xi = \int_0^{\rho_o} \Sigma_t(\mathbf{r}, E_o) e^{-\int_0^{\rho} \Sigma_t(\mathbf{r}_o + s\hat{\Omega}, E_o) ds} d\rho \tag{5.10}$$

Eq (5.10) results into:

$$\rho_o = -\frac{1}{\Sigma_t(\mathbf{r}, E_o)} \ln(1 - \xi) \tag{5.11}$$

The above sampling method is called inverse technique. There are some other techniques, such as rejection technique and composition technique. The details about the Monte-Carlo sampling technique could be found in [81, 70].

We check then if this selected distance ρ_o will cause the neutron to get out of its homogeneous medium. If such is the case, we continue to check if the interface crossed by

the neutron is an internal one or a boundary one. If it is the first case, the neutron will be repositioned at the crossed interface maintaining the same energy and direction. If the interface crossed is a limit boundary which is linked to a vacuum space, the neutron escapes from the reactor medium and will no longer be considered. If the boundary condition is reflective, the neutron will simply change its direction and returns to the first step of selecting an optical path.

We must now look into the case further where the neutron remains in its original homogeneous medium. After having been shifted by this optical path, a nuclide constituting the homogeneous medium will be chosen according to the atomic concentration proportion and the microscopic total cross section to have a collision with the neutron. By knowing the collided nuclide, we need to choose the interaction type. It depends on the nuclide as well as the incident neutron energy. This information is supplied by the cross section data library. So, if the chosen interaction is an absorption, the neutron will be killed. If it is a scattering (elastic or inelastic), the neutron will continue its trajectory with another energy and another direction selected with different rules depending on the scattering types. For example, in the case of an elastic scattering, the deviation angle will be first chosen according to its distribution probability. Then, the outgoing energy can be calculated with the help of the kinetic energy and momentum conservation rules. As for the inelastic interactions, it is much more complicated because of the separation between discrete case and continuum case. In the former case, it is almost the same treatment procedure as for elastic collision with the exception of an initial step involving the choice of an excited level. However, for the latter case, i.e. the continuum inelastic case, we can no longer decide the outgoing energy just with the deviation angle. The two variables are selected independently or with a certain correlation rule between them.

In the absorption family, there is a special reaction type: fission reaction where secondary neutrons are created. These fission secondary neutrons are emitted isotropically in the center of mass of fission fragments system. The kinetic energy of every neutron is sampled according to the related nuclide fission spectrum. Their trajectories will be followed but in the next neutron generation.

At the end of each batch simulation, the scores contributed by every neutron will be averaged and stored. After all the batch calculations have been performed, we obtain the final estimation values with their standard deviations. However, some exceptions exist, for example, the estimation of group-wise energy transfer probability matrix. The latter is obtained at the end of the whole simulation taking account all the simulated neutrons scores. Therefore, it does not possess the statistical deviation. Details about this special variable will be presented in Chapter 7. An illustration scheme is plotted to summarize a neutron life history in Fig (5.1).

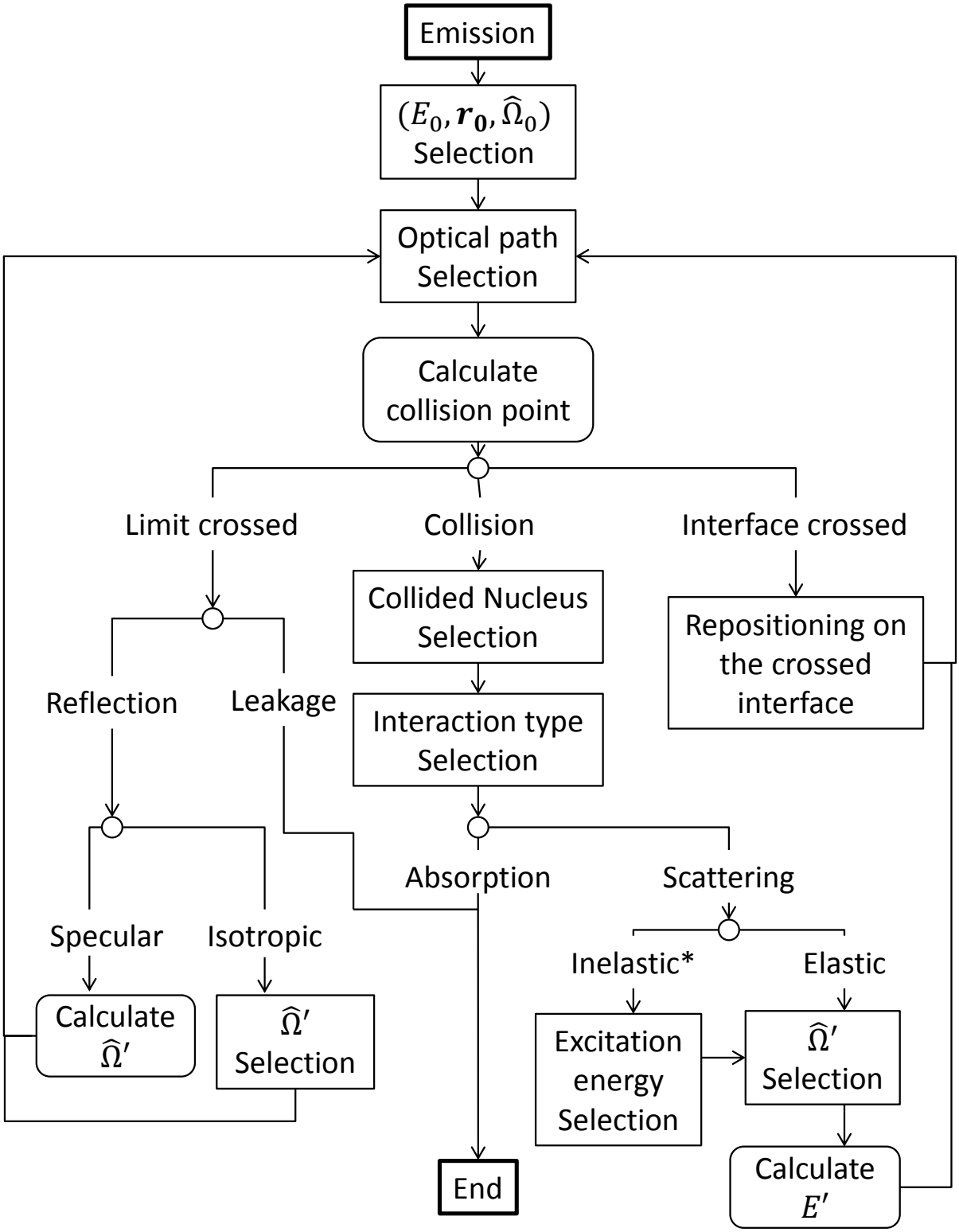

Figure 5.1: Single neutron life history simulated using the Monte-Carlo method

5.3 Monte-Carlo estimation

After assimilating the global idea of the Monte-Carlo method as well as its particular application in the neutron transport problem, it is unavoidable to present the Monte-Carlo simulation estimators which form the topic of the present section. It is divided into two parts: the general Monte-Carlo estimators[11] and the specific ones in charge of estimating the multi-group parameters which will be used in the core calculation step.

5.3.1 General estimators

The most important estimator during a Monte-Carlo simulation is the neutron simulation weight noted as ω. Graceful to this, we are able to estimate directly the collision density and then deduce other neutronic variables.

In a nuclear reactor calculation, the physical quantities such as flux, current and different types of reaction rates are usually required. For that, each of them needs its appropriate estimator. As for the types of estimators, there are three different families corresponding to different spatial domains where the scores are registered. They are respectively: volumetric estimators; surface estimators and point estimators. Table 5.1 summarizes the different estimators and their applications formula associated with different physical quantities. The definitions of the parameters used in the below table are respectively:

- ω: the simulation weight of neutron;
- l: the track length traveled by neutron between two collisions;
- Σ_t: the macroscopic total cross section of the medium where the neutron is propagating;
- Σ_i: the macroscopic cross section of reaction type i for which the reaction rate is desired, in the medium where the neutron is propagating;
- $\hat{\Omega}$: the neutron propagation direction;
- $\mathbf{N}$: the positive normal direction of surface through which neutrons pass;
- $\widetilde{\Sigma}$: optical path between the point of collision and the point where the flux is demanded:

$$\widetilde{\Sigma} = \int_0^s \Sigma_t(\mathbf{r} - s'\hat{\Omega}, E)ds' \tag{5.12}$$

From the above table, it is observed that not all the estimators could be applied to the current nor to the reaction rate. From the neutronic definition of the current, it concerns a quantity passing through a unit surface with a fixed direction per unit time. Thus it is normal that we estimate it only with the surface estimator. As for the reaction rates, it is complete non-sense to calculate them on a surface or at a point. Details about the flux estimators will be followed in the following paragraphs.

The cord estimator also called track length estimator, and the collision estimator, work both within a volumetric domain D. The cord estimator stores every track length l_i of every neutron as well as its simulation weight ω_i where i indicates the trajectories

		Flux	Current	Reaction rate
Volumetric estimators	Cord	$\omega \cdot l$	N.A.	$\omega \cdot l \cdot \Sigma_i$
	Collision	$\frac{\omega}{\Sigma_t}$	N.A.	$\omega \cdot \frac{\Sigma_i}{\Sigma_t}$
Surface estimators		$\frac{\omega}{\hat{\Omega} \cdot \mathbf{N}}$	ω	N.A.
Point estimators		$\omega \cdot \frac{\Sigma_s}{\Sigma_t} \cdot \frac{\exp(-\widetilde{\Sigma})}{s^2}$	N.A.	N.A.

Table 5.1: Different estimators with the applications formula to different physical quantities. N.A. : no application

comprised in the volume V_D. And finally all the stored track length data are averaged over the whole volume as expressed in Eq (5.13). This estimator is particularly suitable and efficient in low density media where collisions occur rather rarely.

$$\hat{\phi} = \frac{1}{V_D} \sum_i \omega_i \cdot l_i \tag{5.13}$$

The other volumetric estimator is called the collision estimator which is privileged for its high density media. It could be obtained via the collision density accumulated in the involved domain D. Its detailed definition is shown in Eq (5.14) where i indicates all the collisions occurred in the concerned domain.

$$\hat{\phi} = \sum_i \frac{\omega_i}{\Sigma_t} \tag{5.14}$$

The surface estimator is mainly dedicated to current estimation, usually for the neutron leakage case. The particle flux point estimator is not exactly performed at one point but rather in a very tiny sphere which is around the calculation point . A divergence problem could be encountered using this estimator if the collisions occurred at the calculation point and/or very close to this point.

5.3.2 Multi-group constant estimators

The Monte-Carlo simulation features decide that producing the flux-weighted homogenized multi-group constants is not a difficult task for any Monte-Carlo code. As the entrance collision density Ψ expressed in Eq (5.15) could be estimated directly during a Monte-Carlo simulation, the scores of Ψ could thus be easily recorded within a certain geometrical volume and also within a specific energy interval.

$$\Psi = \Sigma_t(\mathbf{r}, E)\phi(\mathbf{r}, E) \tag{5.15}$$

One-dimensional macroscopic cross sections

Note here that, the energy condensation and the spatial homogenization procedures are usually mixed together in a Monte-Carlo simulation, especially for a heterogeneous geometry case. Therefore, the homogenized and collapsed cross section which depends only on the incident energy could be defined according to Eq (5.16):

$$\overline{\Sigma}_{i,g}^{V} = \frac{\int\limits_{\mathbf{r}\in V}\int\limits_{E\in g}\Sigma_i(\mathbf{r},E)\phi(\mathbf{r},E)dEd^3\mathbf{r}}{\int\limits_{\mathbf{r}\in V}\int\limits_{E\in g}\phi(\mathbf{r},E)dEd^3\mathbf{r}} = \frac{\int\limits_{\mathbf{r}\in V}\int\limits_{E\in g}\Psi(\mathbf{r},E)\frac{\Sigma_i(\mathbf{r},E)}{\Sigma_t(\mathbf{r},E)}dEd^3\mathbf{r}}{\int\limits_{\mathbf{r}\in V}\int\limits_{E\in g}\frac{\Psi(\mathbf{r},E)}{\Sigma_t(\mathbf{r},E)}dEd^3\mathbf{r}} \tag{5.16}$$

where i stands for the different reaction types, such as: total collision reaction, absorption reaction and fission production reaction. Meanwhile, the index g is the incident energy group of the neutron and V is its macroscopic volume.

Energy transfer probability

To calculate the multi-group energy transfer probabilities that depend on both the incident and the out-going energies, additional attention needs to be paid to classifying the out-going energy into the associated energy group. This could always be obtained naturally with all the existing Monte-Carlo codes. Its general estimation rule is given by Eq (5.17):

$$P(g\to g') = \frac{\int\limits_{\mathbf{r}\in V}\int\limits_{E\in g}\int\limits_{E'\in g'}\Sigma_s(\mathbf{r},E\to E')\phi(\mathbf{r},E)dEdE'd^3\mathbf{r}}{\int\limits_{\mathbf{r}\in V}\int\limits_{E\in g}\Sigma_s(\mathbf{r},E)\phi(\mathbf{r},E)dEd^3\mathbf{r}} \tag{5.17}$$

Anisotropy parameter

However, using the non-angular related homogenized multi-group constants is not sufficient to continue a core calculation. The real challenge is to produce the multi-group anisotropy parameters for the next step core calculation. In fact, the anisotropic effect is shown in two different forms according to the core simulation properties. In the first code family, which is based on the diffusion theory, the anisotropic effect is also related to the neutron leakage effect which is characterized by the specific coefficient D_g under the name of the multi-group diffusion coefficient or leakage coefficient. As for the second code family, it relies on the transport theory and the anisotropic effect is expressed by the high-order ($> 0^{th}$) multi-group scattering matrix.

At present, most of the Monte-Carlo codes that have the capacity to produce the anisotropy parameters aim to supply the diffusion codes with them. However, the diffusion coefficient is not at all involved in a continuous-energy Monte-Carlo simulation. Thus, a lot of studies about how to generate the multi-group diffusion coefficients appropriately were carried out previously. A common feasible solution is deviated from Fick's law which suggests a simple relationship between the multi-group diffusion coefficients and the transport cross sections shown in Eq (5.18).

$$D_g(\mathbf{r}) = \frac{1}{3\Sigma_{tr,g}(\mathbf{r})} \tag{5.18}$$

where $\Sigma_{tr,g}(\mathbf{r})$ is the transport cross section and defined as:

$$\Sigma_{tr,g}(\mathbf{r}) = \Sigma_{t,g}(\mathbf{r}) - \overline{\mu}_g\Sigma_{s,g}(\mathbf{r}) \tag{5.19}$$

The above definition of transport cross section comes from the P_1 approximation and the usage of out-scatter property. The angular-dependent parameter $\overline{\mu}_g$ is hidden in the

expression of the transport cross section in Eq (5.19). It is actually the cosine of the average scattering angle. Its continuous energy form could be obtained as $\overline{\mu}(E) = \int_{-1}^{1} \mu f(\mu, E) d\mu$ where $f(\mu, E)$ is the angular deviation law which comes from the input data library and it is usually coupled with the energy variable once the inelastic scattering reaction enters into the continuum region.

Theoretically, the homogenized multi-group transport cross section should be weighted by the current spectrum according to the linearly anisotropic multi-group diffusion equations [55]. Practically, the concept of using current spectrum as a weighting function is not achievable in a Monte-Carlo simulation. The reason is due to the highly symmetrical distribution of the angular flux in the core geometry which could result in a convergence problem while integrating the current.

In his Ph.D thesis [55], Leppänen showed several existing solutions to avoiding the current weighting problem which are implemented in different codes. There is a common idea shared by Gast [45] and Tohjoh [95]: use of an empirical correction factor to adjust the flux-weighted diffusion coefficient for the whole core calculation. This method works well for certain cases, but is not effective for all reactor cores. Ilas & Rahnema [53] proposed some different processing techniques while analyzing the spent LWR fuel lattice. Their main goal is to preserve the multiplicative factor exactly. The reference value comes from the continuous-energy Monte-Carlo simulation. To reach this objective, the multi-group diffusion coefficients are considered as free variables which are calculated by a genetic algorithm. According to the author's opinion, this idea of intentionally adding degrees of freedom is used similarly in the SPH or GET methods used in deterministic codes. They are all robust mathematical techniques with a precise aim, such as preserving the K_{eff} and/or the macroscopic reaction rates.

Alongside the majority Monte-Carlo codes which serve later for a diffusion calculation, there are always several exceptional ones aiming at producing non-zeroth order scattering matrix which could indeed be used in a transport simulation. One example is the work performed by Redmond II during his Ph.D. studies[50] on the American code MCNP. The angular deviation probability distribution function is established at the same time as calculating the group-transfer cross sections. With the above two multi-group constants, the moments at any order of the scattering matrix could be deduced easily. Another example of the scattering matrix production is the French Monte-Carlo code, TRIPOLI-4®[31, 23, 5]. It is also the main platform where this thesis work is conducted.

Infinite and leakage-corrected spectra

Another concern involved in the homogenized multi-group constants production is the kind of flux or current spectrum to be used. Under a normal operation, the reactor core is in a critical state. Thus the flux spectrum is a "critical" spectrum which corresponds to $K_{\text{eff}} = 1$. However, in a sub-assembly calculation, the limit condition is usually set to be reflective or periodic which presents an "infinite" spectrum. The in-consistency of the spectra used to weight the multi-group constants yields theoretically inconsistent results, especially when an important discrepancy is found between the two spectra. That's the reason why developing a leakage model seems necessary in the deterministic cell calculation.

For a Monte-Carlo cell calculation, the need to have a leakage model in order to produce the multi-group constants weighted by a critical spectrum is also very important. This thesis work is also very much interested in the Monte-Carlo based leakage model. Detailed backgrounds of the neutron leakage effects and a development of a leakage model in the TRIPOLI-4® code make up the main contents of Part III. Most of the existing Monte-Carlo codes calculate the homogenized multi-group constants with an infinite flux spectrum. The few exceptions will be mentioned separately in the following sections.

5.4 Serpent

Serpent is a three-dimensional continuous-energy Monte-Carlo reactor physics burn-up calculation code. It is heavily based on the preliminary code PSG [55] which is the main result of Leppänen's Ph.D. work. The methods used to generate homogenized multi-group constants in Serpent are naturally inherited from the PSG code whose initial motivation is to produce these constants for deterministic whole core calculations. In addition, it was focused to serve in few-group nodal diffusion codes. Thus, the output of the homogenized multi-group constants from Serpent or PSG codes are mainly:

- The conventional homogenized multi-group reaction constants which could be obtained from Eq (5.16) and Eq (5.17).

- The multi-group diffusion coefficients:

  The method used in Serpent code to calculate D_g is totally different in comparison to those presented in the above text. The diffusion coefficient is linked directly to the diffusion area by the following relationship: $D_g = \Sigma_{r,g} L_g^2$, where $\Sigma_{r,g} = \Sigma_{t,g} - \Sigma_{s,g\to g}$ is the removal cross section in group g. The diffusion area L_g^2 could be estimated from the mean square area $\overline{r_g^2}$: $L_g^2 = \dfrac{\overline{r_g^2}}{6}$[55]. Moreover, the mean square area is calculated by accumulating all the distances that neutrons have traveled from the moment of entering in the group g till getting out from g. Finally, an almost exact diffusion coefficient is obtained with the Serpent code. The only approximation involved for obtaining the D_g is the diffusion approximation.

  With knowledge of the multi-group diffusion coefficients, some other parameters could be derived naturally, such as: the multi-group transport cross section, the average scattering cosine, the migration area.

- The scattering cross section matrix :

  This output capacity is up to Legendre order 7 in the Serpent code. However, it is not the problem to get even higher-order of Legendre, because they could be easily obtained by the formula: $\Sigma_{s,l} = \int_{-1}^{1} \Sigma_s(\mu) P_l(\mu) d\mu = \Sigma_{s,0} \int_{-1}^{1} f(\mu) P_l(\mu) d\mu$. $P_l(\mu)$ is the l^{th} order of moment of the Polynomial Legendre where l could be any positive integer. And $f(\mu)$ is the multi-group angular deviation probability distribution function. The embarrassing thing is that the PDF function $f(\mu)$ is weighted by the

scalar flux spectrum which results in that the non zero-th order of the scattering cross sections are indirectly weighted by the flux spectrum rather than the current spectrum. This procedure is assumed to give out inconsistent results compared with the continuous-energy Monte-Carlo simulation.

Even though the Serpent code could generate these non zero-th order scattering matrix, it appears that they are not being used yet in any deterministic code. The validation work is not yet extended to these output parameters since they will focus on producing homogenized multi-group constants for diffusion codes.

Moreover, Serpent is able to calculate the homogenized multi-group constant with a critical flux spectrum. The leakage model used in Serpent is based on the deterministic solution of B_1 equations [41]. A similar technique was developed in an experimental Monte-Carlo code by Martin[71]. It was exploited by Fridman to perform a light water reactor sub-assembly as well as a fast reactor sub-assembly calculation. There is not yet rigorous validation work for the critical spectrum weighted multi-group constants produced by Serpent. The author tried to compare the multi-group leakage model output parameters between this work and the Serpent work. Readers are invited to have a further look in Chapter 10.

5.5 McCARD

McCARD, developed at the Seoul National University, is a Monte-Carlo neutron-photon transport simulation code which is designed for various nuclear reactor and fuel systems. It possesses the capacity to produce the homogenized multi-group constants which are then input into diffusion theory codes for the whole core neutronics analysis. The reason for choosing this code to be presented here is because of the original way it uses the critical spectrum for generating the homogenized multi-group constants.

The principle involved in calculating the conventional multi-group cross sections is mostly the same for all the Monte-Carlo codes. The difficulties arise when non-conventional multi-group constants are demanded, such as the multi-group diffusion coefficient. As the McCARD code uses a critical spectrum from the homogeneous B_1 fundamental equations [6], it naturally gets around the difficulty of the previously mentioned Monte-Carlo studies producing the multi-group diffusion coefficients. The B_1 critical spectrum utilization is in fact a leakage model concept implemented in the McCARD code. This leakage model is based on the deterministic homogeneous fundamental equations which will be deduced explicitly in Chapter 10. Here, in order to explain how the McCARD code calculates the critical spectrum weighted homogenized multi-group constants, the final expression of the B_1 equations are simply given as follows:

$$\Sigma_{t,g}\phi_g \pm iBJ_g = \sum_{g'} \Sigma_{s0}^{g'\to g}\phi_{g'} + \chi_g \tag{5.20}$$

$$\pm iB\phi_g + 3\gamma_g\Sigma_{t,g}J_g = 3\sum_{g'} \Sigma_{s1}^{g'\to g}J_{g'} \tag{5.21}$$

where γ_g is a critical buckling B dependent variable, defined as:

$$\gamma_g = \begin{cases} \dfrac{1}{3}\dfrac{\frac{B}{\Sigma_t}\arctan\frac{B}{\Sigma_t}}{1-\frac{\Sigma_t}{B}\arctan\frac{B}{\Sigma_t}} & \text{if} \quad B^2 > 0 \\ \dfrac{B^2}{3\Sigma_t}\dfrac{\ln\frac{\Sigma_t+Im(B)}{\Sigma_t-Im(B)}}{Im(B)-\Sigma_t\ln\frac{\Sigma_t+Im(B)}{\Sigma_t-Im(B)}} & \text{if} \quad B^2 < 0 \\ 1+\dfrac{4}{15}(\dfrac{B}{\Sigma_t})^2-\dfrac{12}{175}(\dfrac{B}{\Sigma_t})^4+\cdots & \text{if} \quad B^2 \approx 0 \end{cases} \tag{5.22}$$

The procedure used to produce the critical spectrum homogenized multi-group constants in McCARD is divided globally into three steps, without any iteration scheme:

1- Calculation of the fine-group cross sections. It is worthwhile to point out that the first order scattering cross section should be weighted by the continuous current spectrum. McCARD takes the approximation that the continuous current spectrum is proportional to the flux. All the multi-group parameters at this step are obtained for an infinite geometry.

2- Solving the above B1 Equations (5.20) and (5.21) with knowledge of the fine-group cross sections. The detailed method used to solve these coupled equations is not the topic of this section, readers are suggested to find more information in Chapter 10. Thus, the critical fine-group flux and current spectra noted respectively as ϕ_g^B and J_g^B are obtained as solutions, as well as the critical buckling value B.

3- Collapsing the fine-group cross sections into few-group cross sections with the weighting function which is the critical flux spectrum. The formula of the energy collapsing for the conventional reaction cross sections is:

$$\Sigma_{i,G} = \frac{\sum\limits_{g\in G}\Sigma_{i,g}\phi_g^B}{\sum\limits_{g\in G}\phi_g^B} \tag{5.23}$$

where i could stands for the total, absorption, or fission reactions.

As for the few-group diffusion coefficients D_G, it could be calculated in two different ways:

$$D_G = \frac{\pm i\sum\limits_{g\in G}J_g^B}{B\sum\limits_{g\in G}\phi_g^B} \tag{5.24}$$

or

$$D_G = \frac{\sum\limits_{g\in G}D_g\phi_g^B}{\sum\limits_{g\in G}\phi_g^B} \tag{5.25}$$

where the fine-group diffusion coefficient is defined as $D_g = \dfrac{\pm iJ_g^B}{B\phi_g^B}$. We may note that, the few-group diffusion coefficients are indeed weighted by the critical flux spectrum also. This way of doing things may induce some inconsistent results compared to continuous-energy Monte-Carlo simulations.

The critical spectrum weighted homogenized multi-group constants by the McCARD code are validated by two specific cases: a PWR and a VHTR fuel blocks and cores analysis[27]. Moreover, the calculation results clearly indicated that the critical spectrum is necessary to produce the homogenized multi-group constants.

5.6 MCNP

MCNP, developed at the Los Alamos National Laboratory since the 1970s, is a multi-particle (n, γ, e^-) transport Monte-Carlo code. It is worldwide used as a reference code because of its pioneering reputation. The homogenization and energy condensation problem was dealt with by Redmond II[50] as his Ph.D thesis topic in the late 1990s. He completed the capabilities of MCNP by adding the routines for generating the group-to-group scattering cross sections and the associated Legendre expansion of arbitrary order.

Different methods were implemented in MCNP to attain the above objectives. At first, to calculate the group-to-group scattering cross sections, there are two methods which are:

1. The Monte-Carlo Approach: A single scattering event is simulated and based on the incoming and out-going energies. A contribution is made to a single group-to-group scattering bin. This method takes advantage of the standard MCNP scattering routines.

2. The Explicit Approach: A scattering law is sampled and is manipulated to determine the fraction of particles that could scatter into every possible group. A contribution is made to each of these group-to-group scattering bins.

It should be noted that, the first method respects the same principle as expressed in Eq (5.17) to establish an energy transfer matrix. As for calculating the Legendre Components, there were also two methods:

1. $f(\mu)$ Estimation: The angular distribution is accumulated during the calculation by making a contribution to an equiprobable-width cosine bin associated with a group-to-group scattering bin. This distribution is weighted and integrated at the end of the calculation to determine the Legendre components.

2. Direct P_n Estimation: The P_n components of the scattering rate are estimated during the calculation by integrating the angular distribution for each scattering cross section.

To be precise here, the high-order Legendre scattering cross sections were always weighted by the flux spectrum which induced a potential problem. However, the calculation methods were validated by three test problems and the results were found to be consistent when compared to the reference MCNP results[50].

The homogenization work performed by Redmond II was based on the track length estimation which results in low efficiency of calculation. For this reason, Van der Marck et al.[82] from the Netherlands Nuclear Research and Consultancy Group created another feature in MCNP: to use the collision estimator for generating homogenized multi-group cross sections. They made MCNP print a record in a binary file for each interaction simulated. The record contains all the necessary data for later post-processing, such as

position, reaction type, energies and angle. A tool, ELNINJO[82], is used to continue the processing task. This combinational technique is created on purpose for analyzing the High Flux Reactor[82] in Petten, Netherlands. They could only produce the multi-group cross sections under a reflective boundary condition.

Until 2009, Cho et al.[76] from the Korea Advanced Institute of Science and Technology (KAIST) proposed using an albedo-corrected leakage spectrum to weight the multi-group cross sections within the MCNP code. The simulation procedure is iterated between the Monte-Carlo lattice calculation and the deterministic whole core calculation. The MCNP code is in charge of producing the multi-group homogenized nodal parameters which are later used in an arbitrary nodal diffusion code. The output of the nodal diffusion core calculation is the expected albedo conditions on each assembly surface from the point of view of MCNP. Thus, the new multi-group homogenized nodal parameters could be obtained under the albedo condition from the MCNP simulation. The whole iteration procedure ends up reaching the convergence criterion.

This processing method is in fact the concept of a leakage model adapted to a Monte-Carlo lattice calculation. It is usually under the name of Albedo Leakage Model which has the advantage of exactly preserving the surface current compared to other leakage models. The different properties of various leakage models will be explicitly explained in Part III.

Finally, the albedo leakage-corrected critical spectrum weighted multi-group cross sections were tested on a small core mock-up containing a UO_2 and a MOX fuel assembly[76]. And, the results using of the critical spectrum weighted multi-group cross sections match better with the reference values compared to the use of the infinite spectrum weighted parameters.

5.7 TRIPOLI-4®

At the end of this chapter, a brief summary will be given of the French Monte-Carlo code TRIPOLI-4®, focusing on the existing calculation routines contributing to homogenized multi-group cross section generation. This could also help reader(s) to have a clear vision of the basis on which this thesis is carried out.

TRIPOLI-4®[31, 23, 5] is a reference Monte-Carlo code using point-wise cross sections coming from standard evaluations such as ENDFB-VII[16] or JEFF-3.1.1[22]. Compared with other continuous-energy Monte-Carlo codes, it has the capacity to produce and also to use the multi-group cross sections. This means that the obtained homogenized multi-group cross sections could be used by TRIPOLI-4® itself for the purpose of performing a whole core calculation just as it is used in a deterministic core simulation code. In addition, TRIPOLI-4® can take use of multi-group constants generated from APOLLO2[85] which is a deterministic lattice code. Thus, TRIPOLI-4® could serve in both the multi-group cross sections generation and validation works.

The first development work concerning the homogenization and energy condensation in the TRIPOLI-4® code dates from the 1990s[56]. The initial motivation was to validate the homogenized multi-group cross sections calculated by deterministic sub-assembly codes, especially when examining the self-shielding techniques which are indispensable for deterministic approach. Thus, during a continuous-energy Monte-Carlo simulation, TRIPOLI-

4® could provide the necessary multi-group data for subsequently running a multi-group core calculation code. The multi-group data are respectively the one-dimensional cross sections and the multi-dimensional constants which are furthermore divided into: the multi-group diffusion matrix, the multi-group anisotropy law and the fission spectrum.

The one-dimensional multi-group cross sections are calculated in the same way as expressed in Eq (5.16). The directly estimated reaction types in the TRIPOLI-4® are namely: the total collision, the absorption, the fission, and the fission production. As for the scattering cross sections, they could be deduced from the total cross sections and the absorption ones as following:

$$\Sigma_s^g = \Sigma_t^g - \Sigma_a^g \tag{5.26}$$

The multi-dimensional multi-group constants estimation is in fact treated as a distribution function estimation problem in TRIPOLI-4®. The multi-group energy transfer probability matrix is always calculated as in Eq (5.17). With combination of Σ_s^g, the multi-group diffusion matrix could be obtained easily as in Eq (5.27).

$$\Sigma_s^{g\to g'} = \Sigma_s^g \times P(g \to g') \tag{5.27}$$

The anisotropy problem is also treated with the natural approach in TRIPOLI-4® code: establish a distribution function of the angular deviation for each energy transfer $g \to g'$. This distribution function is in fact discretized into 20 equal intervals I_i $(i = 1, 2, \cdots, 20)$ between $[-1; +1]$ which correspond to the entire range of the cosine of the angular deviation μ. In fact, the weight of each scattering event is contributed to the energy transfer score as well as to the angular deviation score. Thus, the probability distribution function of μ in any interval I_i is obtained as follows:

$$P(\mu \in I_i | g \to g') = \frac{\int\limits_{E\in g}\int\limits_{E'\in g'}\int\limits_{\mu\in I_i} \Sigma_s(\mu, E \to E')\phi(E)d\mu dE'dE}{\int\limits_{E\in g}\int\limits_{E'\in g'}\int\limits_{\mu\in[-1,1]} \Sigma_s(\mu, E \to E')\phi(E)d\mu dE'dE} \tag{5.28}$$

The obtained anisotropy distribution function could be directly used in a multi-group TRIPOLI-4® simulation. Meanwhile, the moments of any order l of the scattering anisotropy law could be derived from the above distribution function. With the high order scattering matrix, a deterministic transport core calculation could also be continued.

The multi-group fission spectrum $\chi(g \to g')$ is estimated in the same way as for the energy transfer matrix. Therefore, Eq (5.17) could be used again by replacing the diffusion cross section by the fission section.

Until that time, the homogenization and energy condensation functionalities in TRIPOLI-4® could only be performed under the condition of an infinite geometry. It did not have any leakage model to estimate a critical spectrum weighted multi-group constants. The existing functionalities were tested with a PWR MOX cell and a BWR assembly example. Consistent results were observed in the TRIPOLI-4® simulations and APOLLO2 simulations using the same input data library [56]. This preliminary work was indeed a pioneer in the field of homogenized multi-group cross section production with Monte-Carlo method. It did not include a complete verification and validation work to prove the reliability of the produced multi-group constants. The author could not exactly reproduce the same results as those published in the paper [56]. This comes probably from the different convergence

criteria used in that period. Consequently, a thorough diagnosis work is performed on the whole algorithm about homogenization and energy condensation routines which will be detailed in Part II.

Part II

Improvements of the existing routines for homogenized multi-group constant production in TRIPOLI-4®

Chapter 6

New multi-group constants estimators applied to infinite sub-assembly calculation

Introduction

Section 5.7 summarized the principle of the existing homogenization and energy condensation functionalities in TRIPOLI-4®. The previous pioneer work did not include detailed validation procedure nor further related development. Therefore, our objective is to continue the homogenization and energy condensation work in TRIPOLI-4®, especially for the sake of reinforcing the reliability of the calculation routines and enlarging the application range as well. However, it is impossible during this work to reproduce the same results as shown in [56]. On the other hand, several tested cases point out that the homogenized multi-group cross sections produced by the existing version of TRIPOLI-4® (4.7 with the input library JEFF3.1.1) cannot guarantee the preservation of the infinite multiplicative factor K_∞ between continuous-energy and multi-group TRIPOLI-4® simulations. A few examples which are all homogeneous infinite sub-assembly configurations are listed in Table 6.1. They are calculated under both 6-group and 33-group energy structures.

Sub-assembly	K_∞ reference	ΔK_∞(33gr)	3σ (33gr)	ΔK_∞(6gr)	3σ (6gr)
PWR	1.24425 ± 0.00020	-158	87	86	84
ZPPR-SCF	1.11709 ± 0.00013	15	55	97	55
MAS1B	1.52735 ± 0.00016	37	95	121	95
SPX2	1.34857 ± 0.00012	72	70	166	72
ZPPR-DCF	1.66286 ± 0.00005	324	95	371	98
ZONA2	1.67848 ± 0.00023	204	96	359	98

Table 6.1: First results obtained with the existing version of TRIPOLI-4®

In Table 6.1, the column K_∞ presents the reference infinite multiplicative factors for all the tested sub-assemblies. ΔK_∞ is the discrepancy between continuous-energy TRIPOLI-4® simulation and multi-group simulation using the self-obtained multi-group constants. σ is the combined standard deviation only related to the Monte-Carlo statistics. Both ΔK_∞ and σ values are in the units of pcm. To make clear that this French unit "pcm"

(per hundred thousand translated in English) is usually used as a relative comparison relationship. In this work, pcm will be considered simply as $\times 10^{-5}$. It is observed that ΔK_∞ values generally exceed the associated 3σ. This result does not respect the theoretical deduction given in Chapter 3 which states that for an infinite homogeneous geometry case the flux weighted multi-group constants should preserve exactly the multiplicative factor K_∞ in a later multi-group calculation. This brings some doubt to the adequacy of the reliability of the homogenization and energy condensation routines in the existing TRIPOLI-4®.

In order to verify the calculation details, we need to assimilate how the multi-group constants are estimated in a Monte-Carlo simulation. Therefore, it becomes necessary to get familiar with the collision and transport operator kernels under the multi-group forms. In the following sections, the multi-group Monte-Carlo transport formula will be presented firstly. On the basis of the multi-group Monte-Carlo transport theory, some new multi-group constant estimators will be introduced. The validation work will then be performed on some example cases. A brief conclusion will be made at the end of this chapter.

6.1 Multi-group non-leakage neutron balance

In Chapter 2, the neutron transport equation is presented as a balance relationship of the continuous-energy dependent density quantities, whether in an integral-differential form or in an integral form. The objective of this section is to broaden the neutron transport theory from the continuous-energy domain towards the multi-group domain. Thus, a multi-group neutron density balance equation is assumed to be established. It could be obtained via performing an energy integration within the associated energy interval. We focus at first on the homogeneous non-leakage case which corresponds to a pre-homogenized sub-assembly calculation with reflective or periodic boundary conditions. Since there is no physical difference between the integral-differential and the integral transport equations, here we use the integral-differential one for the following mathematical demonstration.

A simplified continuous-energy neutron balance equation is shown below as:

$$\Sigma_t(E)\phi(E) = \int_0^\infty \Sigma_s^{\text{eff}}(E' \to E)\phi(E')dE' + \frac{1}{K_\infty}\int_0^\infty \chi_f(E' \to E)\nu\Sigma_f(E')\phi(E')dE' \quad (6.1)$$

where Σ_s^{eff} is noted as the effective scattering cross section including the pure scattering cross section and also the multiplication scattering sections: $((n,2n),(n,3n),(n,4n))$. The intention to consider the multiplication scattering as part of the effective scattering reaction is a choice of the TRIPOLI-4® code for processing the corresponding multi-group parameters. Detailed explanation will follow.

$$\Sigma_s^{\text{eff}}(E' \to E) = \Sigma_s(E' \to E) + 2\Sigma_{(n,2n)}(E' \to E) + 3\Sigma_{(n,3n)}(E' \to E) + 4\Sigma_{(n,4n)}(E' \to E) \quad (6.2)$$

We continue to integrate Eq (6.1) over a macro-energy group $g = [E_g; E_{g-1}]$ which leads to :

$$\int_{E_g}^{E_{g-1}} \Sigma_t(E)\phi(E)dE = \int_{E_g}^{E_{g-1}} \int_0^{\infty} \Sigma_s^{\text{eff}}(E' \to E)\phi(E')dE'dE + \frac{1}{K_\infty} \int_{E_g}^{E_{g-1}} \int_0^{\infty} \chi_f(E' \to E)\nu\Sigma_f(E')\phi(E')dE'dE \quad (6.3)$$

By introducing the flux weighted multi-group parameters, the above Eq (6.3) could be arranged into a well synthesized multi-group form:

$$\Sigma_{t,g}\phi_g = \sum_{g'} P(g' \to g)\xi_{g'}^{\text{exces}}\Sigma_{s,g'}^{\text{eff}}\phi_{g'} + \frac{1}{K_\infty}\sum_{g'} \chi_f^{g' \to g}\nu\Sigma_{f,g'}\phi_{g'} \quad (6.4)$$

The multi-group parameters in Eq (6.4) are defined so as to preserve all the reaction rates exactly. The simplest and the most direct treatment is for the total collision rate which gives the multi-group total cross section as:

$$\Sigma_{t,g} = \frac{\int_{E_g}^{E_{g-1}} \Sigma_t(E)\phi(E)dE}{\int_{E_g}^{E_{g-1}} \phi(E)dE} \quad (6.5)$$

During a real TRIPOLI-4® continuous-energy simulation procedure, the upper integration in Eq (6.5) is indeed a summation of all the entrance collision density (noted as $\Psi(E) = \Sigma_t(E)\phi(E)$) which occurs with a point-wise energy E belonging to the group g. It should be mentioned that, the entrance collision density is represented by the neutron simulation weight ω. Thus, the estimator for the multi-group total cross section could be written as:

$$\hat{\Sigma}_{t,g} = \frac{\sum_i \omega(E_i, \mathbf{r}_i)}{\sum_i \frac{\omega(E_i, \mathbf{r}_i)}{\Sigma_t(E_i, \mathbf{r}_i)}} \quad (6.6)$$

where i indicates all the collisions whose incident energy and spatial position $(E_i, \mathbf{r}_i)$ belong to the macro domain (g, V).

The above estimator can be extended for other similar cross sections, such as absorption section, fission section and fission production section. By the way, a collision weight based flux estimator is deduced from the above relation and it agrees well with the formula listed in Table (5.1).

$$\hat{\phi}_g = \sum_i \frac{\omega(E_i, \mathbf{r}_i)}{\Sigma_t(E_i, \mathbf{r}_i)} \quad (6.7)$$

The real challenge is to define the multi-group parameters appropriately at the right-hand side of Eq (6.4). At this stage, inconsistent treatments were found in the existing release of TRIPOLI-4® which resulted in the inconsistent results shown in Table (6.1). The two terms at the right-hand side of Eq (6.4) are respectively the neutron production from scattering and fission reactions. Each of them will be precisely developed in the following sub-sections.

6.1.1 Neutron production from scattering

Returning to the scattering term in the continuous-energy neutron balance equation (6.3), it could be reformed as the product of a sequential terms expressed in Eq (6.8). Please note that, the multiplication scattering reaction is generalized as (n, Xn) where X represents the number of neutrons emitted from the scattering.

$$\begin{aligned}
\int_{E_g}^{E_{g-1}}\int_{0}^{\infty}\Sigma_s^{\text{eff}}(E'\to E)\phi(E')dE'dE &= \sum_{g'}\int_{E_g}^{E_{g-1}}\int_{E_{g'}}^{E_{g'-1}}\Sigma_s^{\text{eff}}(E'\to E)\phi(E')dE'dE \\
&= \sum_{g'}\int_{E_g}^{E_{g-1}}\int_{E_{g'}}^{E_{g'-1}}\left[\Sigma_s(E'\to E)+X\Sigma_{(n,Xn)}(E'\to E)\right]\phi(E')dE'dE \\
&= \sum_{g'}\frac{\int_{E\in g}\int_{E'\in g'}\left[\Sigma_s(E'\to E)+X\Sigma_{(n,Xn)}(E'\to E)\right]\phi(E')dE'dE}{\int_{E'\in g'}\left[\Sigma_s(E')+X\Sigma_{(n,Xn)}(E')\right]\phi(E')dE'} \\
&\times \frac{\int_{E'\in g'}\left[\Sigma_s(E')+X\Sigma_{(n,Xn)}(E')\right]\phi(E')dE'}{\int_{E'\in g'}\left[\Sigma_s(E')+\Sigma_{(n,Xn)}(E')\right]\phi(E')dE'} \\
&\times \frac{\int_{E'\in g'}\left[\Sigma_s(E')+\Sigma_{(n,Xn)}(E')\right]\phi(E')dE'}{\int_{E'\in g'}\phi(E')dE'}\times\int_{E'\in g'}\phi(E')dE' \\
&= \sum_{g'}P(g'\to g)\times\xi_{g'}^{\text{exces}}\times\Sigma_{s,g'}^{\text{eff}}\times\phi_{g'} \qquad (6.8)
\end{aligned}$$

In fact, the sequential terms in Eq (6.8) correspond to those multi-group parameters involved in the scattering production rate. They are listed respectively as follows:

- Multi-group transfer probability, $P(g'\to g)$ from group g' to g:

$$P(g'\to g)=\frac{\int_{E\in g}\int_{E'\in g'}\left[\Sigma_s(E'\to E)+X\Sigma_{(n,Xn)}(E'\to E)\right]\phi(E')dE'dE}{\int_{E'\in g'}\left[\Sigma_s(E')+X\Sigma_{(n,Xn)}(E')\right]\phi(E')dE'} \qquad (6.9)$$

- Excess weight, $\xi_{g'}^{\text{exces}}$ which takes into consideration the multiplication scattering effect:

$$\xi_{g'}^{\text{exces}}=\frac{\int_{E'\in g'}\left[\Sigma_s(E')+X\Sigma_{(n,Xn)}(E')\right]\phi(E')dE'}{\int_{E'\in g'}\left[\Sigma_s(E')+\Sigma_{(n,Xn)}(E')\right]\phi(E')dE'} \qquad (6.10)$$

- Effective multi-group scattering cross section, $\Sigma_{s,g'}^{\text{eff}}$ departing from group g':

$$\Sigma_{s,g'}^{\text{eff}}=\frac{\int_{E'\in g'}\left[\Sigma_s(E')+\Sigma_{(n,Xn)}(E')\right]\phi(E')dE'}{\int_{E'\in g'}\phi(E')dE'} \qquad (6.11)$$

6.1.2 Neutron production from fission

The same method is inherited for processing the fission production rate. Eq (6.12) describes how to change the continuous-energy dependent fission production term into the multi-group form.

$$\int_{E_g}^{E_{g-1}}\int_{0}^{\infty}\chi_f(E'\to E)\nu\Sigma_f(E')\phi(E')dE'dE=\sum_{g'}\int_{E_g}^{E_{g-1}}\int_{E_{g'}}^{E_{g'-1}}\chi_f(E'\to E)\nu\Sigma_f(E')\phi(E')dE'dE$$

$$=\sum_{g'}\frac{\int_{E\in g}\int_{E'\in g'}\chi_f(E'\to E)\nu\Sigma_f(E')\phi(E')dE'dE}{\int_{E'\in g'}\nu\Sigma_f(E')\phi(E')dE'}\times\frac{\int_{E'\in g'}\nu\Sigma_f(E')\phi(E')dE'}{\int_{E'\in g'}\phi(E')dE'}\times\int_{E'\in g'}\phi(E')dE'$$

$$=\sum_{g'}\chi_f^{g'\to g}\times\nu\Sigma_f^{g'}\times\phi_{g'} \quad (6.12)$$

The fission production concerned multi-group parameters are defined respectively:

- Two-dimensional multi-group fission spectrum:

$$\chi_f^{g'\to g}=\frac{\int_{E\in g}\int_{E'\in g'}\chi_f(E'\to E)\nu\Sigma_f(E')\phi(E')dE'dE}{\int_{E'\in g'}\nu\Sigma_f(E')\phi(E')dE'} \quad (6.13)$$

- Fission production multi-group cross section:

$$\nu\Sigma_f^{g'}=\frac{\int_{E'\in g'}\nu\Sigma_f(E')\phi(E')dE'}{\int_{E'\in g'}\phi(E')dE'} \quad (6.14)$$

Comparing Eq (6.13) with Eq (6.9), it is found that the fission spectrum is indeed a matrix form of probabilities distribution. It is different from the deterministic sub-assembly calculation code ECCO where the multi-group fission spectrum is treated as a one-dimensional vector. As for the multi-group fission production cross section, it is defined in the same way as the total cross section. Thus its estimator used in a TRIPOLI-4® simulation will not be repeated here.

6.2 Implementation of new estimators

Previously, we introduced the multi-group parameters definitions to be used in the TRIPOLI-4® code. Several of them were presented accompanied by their Monte-Carlo simulation estimators, such as $\Sigma_{t,g}$. We kept other estimators to be developed in this section. They are namely the multi-group transfer probability $P(g'\to g)$; the excess weight ξ_g^{exces} and the fission spectrum $\chi_f^{g'\to g}$. In addition to this, the differences between the new estimators and the old ones will be pointed out.

6.2.1 Transfer Probability

The theoretical definition of the multi-group energy transfer probability matrix is given in Eq (6.9). Estimating correctly this physical variable requires to calculate the scattering reaction rate appropriately from group g' to g. To accomplish this, it is necessary to understand the principle of simulating a neutron life with associated probabilities. This was qualitatively described in Section 2.3. Here we will do it again but in a quantitative way. The scattering rate from group g' to g is finally analyzed from the microscopic point of view which is shown in Eq (6.15).

$$\begin{aligned}
&\int_{E\in g}\int_{E'\in g'} \Sigma_s^{\text{eff}}(E'\to E)\phi(E')dE'dE = \int_{E\in g}\int_{E'\in g'} \left[\Sigma_s(E'\to E) + X\Sigma_{(n,Xn)}(E'\to E)\right]\phi(E')dE'dE \\
&= \int_{E\in g}\int_{E'\in g'} \left[\phi(E')\Sigma_t(E')\right] \times \sum_j \frac{N_j\sigma_t^j}{\Sigma_t} \times \frac{\sigma_s^j + \sigma_{(n,Xn)}^j}{\sigma_t^j} \times \frac{\sigma_s^j P_s^j(E'\to E) + X\sigma_{(n,Xn)}^j P_{(n,Xn)}^j(E'\to E)}{\sigma_s^j + \sigma_{(n,Xn)}^j} dE'dE
\end{aligned} \tag{6.15}$$

For the sake of space, the microscopic and macroscopic 1D cross sections are all related to the certain energy E'. The definitions of different terms are listed as below:

- $\phi(E')\Sigma_t(E')$: entrance collision density estimated by neutron weight $\omega(E')$;
- $P_j = \dfrac{N_j\sigma_t^j}{\Sigma_t}$: probability of choosing isotope j to be collided with the incident neutron;
- $P_{\text{nabs}}^j = \dfrac{\sigma_s^j + \sigma_{(n,Xn)}^j}{\sigma_t^j}$: non-absorption probability dedicated to the chosen isotope j;
- $\dfrac{\sigma_s^j P_s^j(E'\to E) + X\sigma_{(n,Xn)}^j P_{(n,Xn)}^j(E'\to E)}{\sigma_s^j + \sigma_{(n,Xn)}^j}$: the rule that with which we use to select a specific scattering type for the nuclide j. For example, if the sampled random number is inferior to $\dfrac{\sigma_s^j}{\sigma_s^j + \sigma_{(n,Xn)}^j}$, a pure scattering reaction is chosen. Then, 1 is stored with the related probability $\dfrac{\sigma_s^j}{\sigma_s^j + \sigma_{(n,Xn)}^j}$. If the sampled random number is between $\dfrac{\sigma_s^j}{\sigma_s^j + \sigma_{(n,Xn)}^j}$ and 1, so a multiplication scattering (n, Xn) is selected. Then, X will be stored with its probability $\dfrac{\sigma_{(n,Xn)}}{\sigma_s^j + \sigma_{(n,Xn)}^j}$. Furthermore, in order to distinguish the neutron outgoing energy, additional accumulators are set which are in charge of every different outgoing energy group.

With the help of Eq (6.15), the estimator of the multi-group transfer probability matrix could be defined as:

$$\hat{P}(g' \to g) = \frac{\sum\limits_i w(E'_i, \mathbf{r}_i) \sum\limits_j P_j(E'_i, \mathbf{r}_i) \times P^j_{\text{nabs}}(E'_i, \mathbf{r}_i) \sum\limits_k P^k_j(E'_i, \mathbf{r}_i) \times \{1, X\} \times \Pi(E^k_{i,j} \in g)}{\sum\limits_i w(E'_i, \mathbf{r}_i) \sum\limits_j P_j(E'_i, \mathbf{r}_i) \times P^j_{\text{nabs}}(E'_i, \mathbf{r}_i) \sum\limits_k P^k_j(E'_i, \mathbf{r}_i) \times \{1, X\}} \tag{6.16}$$

Several declarations are necessary for a better understanding of the above equation:

- i: index for the collisions whose incident energy E'_i belongs to group g' and its spatial position $\mathbf{r}_i$ is comprised in the desired domain.
- $\{1, X\}$: an integer to be registered according to the selected scattering reaction type. It could vary between 1 and 4 in the present code.
- $\Pi(E^k_{i,j} \in g)$: the gate function which equals to 1 if the outgoing energy $E^k_{i,j}$ belongs to the group g and equals to 0 for other cases.

Moreover, it should be pointed out that the order for calculating each probability term has to be strictly respected as listed in Eq (6.16). The problem in the old-version of the TRIPOLI-4® code is hidden behind the non-absorption probability which was calculated globally over the macroscopic region but not separately for each specific isotope.

6.2.2 Excess Weight

Returning to Eq (6.10) which mathematically represents for the multi-group excess weight, we can tell that it is in fact a ratio between the realistic scattering produced quantity and the scattered quantity. After reforming the definition formula of the multi-group excess weight, more evident physical terms are found in Eq (6.17).

$$\xi^{\text{excess}}_g = \frac{\int\limits_{E \in g} \phi(E)\Sigma_t(E) \times \dfrac{\Sigma_s(E) + \Sigma_{(n,Xn)}}{\Sigma_t(E)} \times \dfrac{\Sigma_s(E) + X\Sigma_{(n,Xn)}(E)}{\Sigma_s(E) + \Sigma_{(n,Xn)}} dE}{\int\limits_{E \in g} \phi(E)\Sigma_t(E) \times \dfrac{\Sigma_s(E) + \Sigma_{(n,Xn)}}{\Sigma_t(E)} dE} \tag{6.17}$$

where:

- $\phi(E)\Sigma_t(E) \times \dfrac{\Sigma_s(E) + \Sigma_{(n,Xn)}}{\Sigma_t(E)} = w(E) \times P_{\text{nabs}}$: the collision weight modified by the macroscopic non-absorption probability.
- $\dfrac{\Sigma_s(E) + X\Sigma_{(n,Xn)}(E)}{\Sigma_s(E) + \Sigma_{(n,Xn)}(E)} = \xi^{\text{excess}}(E)$: the point-wise excess weight.

Therefore, the estimator of multi-group excess weight is expressed in Eq (6.18).

$$\hat{\xi}^{\text{excess}}_g = \frac{\sum\limits_i w(E_i, \mathbf{r}_i) \times P_{\text{nabs}}(E_i, \mathbf{r}_i) \times \xi^{\text{excess}}(E_i, \mathbf{r}_i)}{\sum\limits_i w(E_i, \mathbf{r}_i) \times P_{\text{nabs}}(E_i, \mathbf{r}_i)} \tag{6.18}$$

with index i always standing for the collision condition $(E_i, \mathbf{r}_i)$ which belongs to the macro domain (g, V_D). Comparing Eq (6.17) with another one-dimensional multi-group cross section calculation method, the difference is that here the weighting function used

is no longer the scalar flux but its corrective form: $\phi(E) \times \big(\Sigma_s(E) + \Sigma_{(n,Xn)}\big)$. It is also with this reason that the old version of the TRIPOLI-4® code made an error here while insisting to weight the excess weight by the scalar flux. The previously corrected definition for ξ_g^{excess} is given below:

$$\xi_g^{\text{excess}} = \frac{\int\limits_{E\in g} \frac{\Sigma_s(E) + X\Sigma_{(n,Xn)(E)}}{\Sigma_s(E) + \Sigma_{(n,Xn)}}\phi(E)dE}{\int\limits_{E\in g}\phi(E)dE} \tag{6.19}$$

6.2.3 Fission Spectrum

The subsection 6.1.2 has given the definition of the multi-group fission spectrum matrix. It must be emphasized that the fission production mentioned in Eq (6.13) should take into account both the prompt and the delayed fission productions. Thus, the formula to calculate fission spectrum is written as:

$$\chi_f^{g'\to g} = \frac{\int\limits_{E\in g}\int\limits_{E'\in g'} \phi(E')\Sigma_t(E') \times \Big[\chi_f^p(E'\to E)\nu^p + \chi_f^d(E'\to E)\nu^d\Big] \times \frac{\Sigma_f(E')}{\Sigma_t(E')}dE'dE}{\int\limits_{E'\in g'}\phi(E')\Sigma_t(E') \times [\nu^p + \nu^d] \times \frac{\Sigma_f(E')}{\Sigma_t(E')}dE'} \tag{6.20}$$

Similarly, its Monte-Carlo estimator is shown as following:

$$\hat{\chi}_f^{g'\to g} = \frac{\sum\limits_i \omega(E'_i, \mathbf{r}_i) \times \sum\limits_j \frac{\nu^j\Sigma_f(E'_i, \mathbf{r}_i)}{\Sigma_t(E'_i, \mathbf{r}_i)} \times \Pi(E_i \in g)}{\sum\limits_i \omega(E'_i, \mathbf{r}_i) \times \sum\limits_j \frac{\nu^j\Sigma_f(E'_i, \mathbf{r}_i)}{\Sigma_t(E'_i, \mathbf{r}_i)}} \tag{6.21}$$

where i indicates the collisions of which incident energy and initial position $(E'_i, \mathbf{r}_i)$ are in the desired macro domain (g', V_D). j is the fission type which could be prompt fission or delayed fission. And $\Pi(E_i \in g)$ is the gate function to select the outgoing energy E_i which should be in the group g.

The problem with the old estimator of the fission spectrum is that the delayed neutron contribution was not taken into consideration. The later part could result in a bias of around 200 pcm in the estimated multiplicative factor.

6.3 Validation of new estimators

In order to evaluate the reliability of the newly implemented estimators, two comparison tools will be used which are namely the validated lattice calculation code ECCO[44] and the Monte-Carlo code TRIPOLI-4®. Several declarations should be made before performing the comparison work:

- All the calculation codes have incorporated more or less approximative methods which probably amount to some biases in their results.
- The same input data library should be used in different codes in order to compare their output parameters.

- Concerning the stochastic property of TRIPOLI-4®, the simulation results are always associated with some statistical deviations. Thus, the comparison work should take this statistical feature into account.

The validation work is processed in two steps. The first one consists of multi-group constants comparison between the continuous-energy TRIPOLI-4® and the deterministic code ECCO[44] simulation results. The second step involves the group constants utilisation in a transport theory core calculation code. Here, we have chosen to feed a multi-group TRIPOLI-4® simulation with the obtained group constants. Detailed comparisons will be presented in the following.

6.3.1 Group constants comparison between TRIPOLI-4® and ECCO

ECCO[44] is a two-dimensional deterministic lattice code developed by several R&D teams working within the framework of the European fast reactor collaboration. The collision probability method is used to solve the neutron transport problem in ECCO. It has the capability of producing multi-group constants in both zero-buckling and fundamental calculation modes. This chapter is focused on the infinite geometry problem, thus we will only use the zero-buckling mode to generate multi-group constants with ECCO.

Since the original aim of this research is to serve in the sodium-cooled fast reactor development, the tested fuel sub-assembly types are mostly in this range including:

- the fuel sub-assemblies from the inner and outer cores of the Superphénix[47] reactor which are noted respectively as SPX1 and SPX2;
- the double-column and a single-column fuel sub-assemblies from the Zero Power Physics Reactor[87, 86, 52], named as ZPPR-DCF and ZPPR-SCF;
- a fuel sub-assembly from the MASURCA-1B experiment noted as MAS1B[96];
- the fuel sub-assembly ZONA2 used in various configurations of the MASURCA reactor[15].

Some illustration figures are given below. They stand for the SPX2, ZPPR-DCF and ZONA2 sub-assemblies.

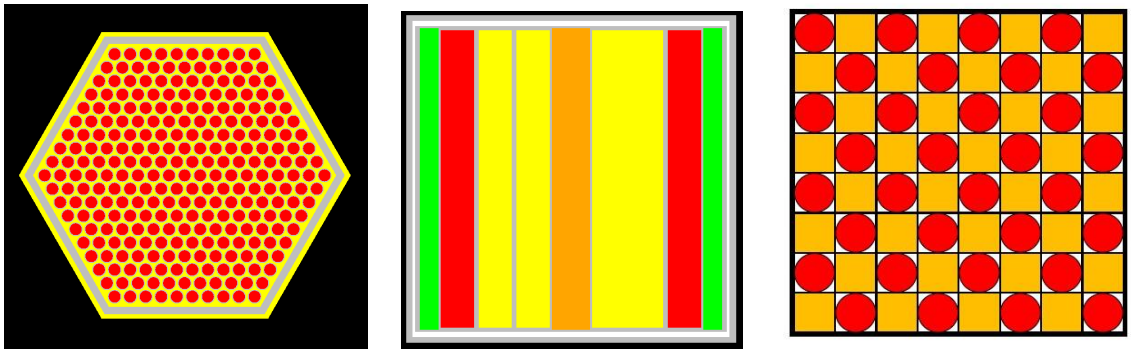

Figure 6.1: Fuel sub-assembly illustration for SPX2, ZPPR-DCF and ZONA2

Please note that all the fuel sub-assemblies are tested in their homogeneous configurations. Their detailed characteristics can be found in Appendix A. Among all the tested cases, two examples will be presented here which are the homogeneous configuration of SPX2 and the homogeneous configuration of ZPPR-DCF.

To make the comparison reliable, the same cross section library, JEFF3.1.1[22] in addition to the probability tables were used by both codes. There are two kinds of energy structures used: 33-group and 6-group. Their detailed group structures are given in Appendix B. Both of them come from the codes system ERANOS[24, 30] and were used for fast neutron reactor analysis in particular.

Table 6.2 shows the infinite multiplicative factors and selected multi-group cross sections using ECCO and TRIPOLI-4® for the SPX2 sub-assembly calculation. At first, let us take a look at the K_∞ values. Even though the estimated results from ECCO and TRIPOLI-4® are not exactly the same, their discrepancy (66 pcm) is small enough for two codes using completely different calculation methods.

Parameter	ECCO	TRIPOLI-4®	Diff
K_∞	1.35298	1.35364 ± 0.00008	-66 pcm
units	cm^{-1}	$cm^{-1}(10^{-3}\%)$	%
Σ_{t1}	1.840E-01	1.841E-01 (1.7)	0.05
Σ_{t2}	2.233E-01	2.234E-01 (1.4)	0.05
Σ_{t3}	2.859E-01	2.858E-01 (1.1)	-0.03
Σ_{t4}	3.977E-01	3.978E-01 (2.0)	0.03
Σ_{t5}	5.797E-01	5.797E-01 (4.2)	0.00
Σ_{t6}	5.350E-01	5.362E-01 (15)	0.22
Σ_{a1}	7.212E-03	7.213E-03 (6.3)	0.01
Σ_{a2}	3.608E-03	3.608E-03 (1.4)	0.00
Σ_{a3}	3.762E-03	3.762E-03 (1.8)	0.00
Σ_{a4}	7.158E-03	7.168E-03 (3.3)	0.14
Σ_{a5}	1.642E-02	1.641E-02 (12)	-0.06
Σ_{a6}	4.217E-02	4.239E-02 (49)	0.52
$\nu\Sigma_{f1}$	1.885E-02	1.884E-02 (5.4)	-0.05
$\nu\Sigma_{f2}$	7.509E-03	7.508E-03 (2.8)	-0.01
$\nu\Sigma_{f3}$	5.710E-03	5.710E-03 (0.2)	0.00
$\nu\Sigma_{f4}$	6.368E-03	6.396E-03 (2.0)	0.44
$\nu\Sigma_{f5}$	1.389E-02	1.386E-02 (14)	-0.22
$\nu\Sigma_{f6}$	4.407E-02	4.430E-02 (59)	0.52

Table 6.2: Comparison of group constants in the 6-group (its energy limits are given in Appendix B) SPX2 homogeneous lattice calculations between ECCO and TRIPOLI-4® codes

Then, comparison is continued on several types of one-dimensional cross sections which are respectively: the total cross section $\Sigma_{t,g}$; the absorption cross section $\Sigma_{a,g}$ and the fission production cross section $\nu\Sigma_{f,g}$. The reason to select them is that they are direct output results from the TRIPOLI-4® simulation. This allows us to obtain their exact statistical errors. As for the ECCO code, $\Sigma_{t,g}$ and $\nu\Sigma_{f,g}$ can be found directly in the out-

put XML file. However, this is not the case for $\Sigma_{a,g}$. In order to deduce the multi-group absorption values from the ECCO output file correctly, it should be kept in mind that the absorption cross section estimated by TRIPOLI-4® does not take into account (n, Xn) reactions and the scattering cross sections calculated by ECCO are in fact the effective scattering cross sections including (n, Xn) reactions: $\Sigma_{s,g}^{ECCO} = \Sigma_{s,g} + X\Sigma_{(n,Xn)}$. Thus, the formula to calculate the appropriate absorption cross sections which are comparable to the ones estimated by TRIPOLI-4® is: $\Sigma_{a,g}^{ECCO} = \Sigma_{t,g}^{ECCO} - \Sigma_{s,g}^{ECCO} + (X-1)\Sigma_{(n,Xn),g}^{ECCO}$. Since the probability of having a high multiplication scattering reaction is remote, we suppose here $X = 2$. So the final formula for calculating the absorption cross sections with ECCO output parameters is: $\Sigma_{a,g}^{ECCO} = \Sigma_{t,g}^{ECCO} - \Sigma_{s,g}^{ECCO} + \Sigma_{(n,Xn),g}^{ECCO}$.

In Table 6.2, it is once again shown that the one-dimensional cross sections are in satisfactory agreement between these two codes results. All the cross sections are in the units of cm^{-1}. The values in brackets within the TRIPOLI-4® column are the corresponding relative statistical errors which are expressed in $\times 10^{-3}\%$. The discrepancies between TRIPOLI-4® and ECCO are limited to 0.52% which is even less important than what is to be expected. According to the comparison shown in Leppänen's thesis, the differences between the PSG[55] and CASMO[68] simulations for a PWR MOX case are in the order of magnitude of 2% even for the simplest 2-group cross sections such as Σ_a and $\nu\Sigma_f$.

If we have a further look into the different energy groups of a certain reaction type, it can be seen that the differences are generally more relevant in the lower energy groups than in the higher ones. For example, the greatest discrepancies are usually found in the 6^{th} group covering the interval [0 keV; 45.4 eV]. This could be explained by the fact that a rather low statistical quantity of events occur in this group which results in a relative high uncertainty.

Σ_{s0} (ECCO)	1	2	3	4	5	6
1	1.385E-01	0	0	0	0	0
2	2.823E-02	1.958E-01	0	0	0	0
3	9.894E-03	2.370E-02	2.765E-01	0	0	0
4	1.320E-04	1.516E-04	5.669E-03	3.811E-01	0	0
5	1.327E-05	2.021E-05	1.760E-05	9.458E-03	5.615E-01	0
6	3.649E-07	1.398E-07	7.682E-08	3.901E-07	1.769E-03	4.929E-01

Figure 6.2: ECCO calculated group transfer cross sections (in units of cm^{-1}) for SPX2 homogeneous sub-assembly

Another important multi-group parameter to be compared between TRIPOLI-4® and the ECCO simulations is the scattering cross section matrix. The later involves the energy transfer probability which is a two-dimensional multi-group parameter. Figure 6.2 and Figure 6.3 illustrate intuitively the scattering matrix calculated by ECCO and TRIPOLI-4®. The index in the green row stands for the departure energy group g; while the vertical pink column indicates the arrival energy group h. Thus, the crossed element corresponds

Σ_{s0} (TRPOLI-4®)	1	2	3	4	5	6
1	1.387E-01	0	0	0	0	0
2	2.805E-02	1.959E-01	0	0	0	0
3	9.976E-03	2.371E-02	2.764E-01	0	0	0
4	1.332E-04	1.523E-04	5.668E-03	3.812E-01	0	0
5	1.781E-05	1.982E-05	1.787E-05	1.363E-02	5.615E-01	0
6	1.838E-06	1.614E-07	1.472E-07	5.109E-07	1.548E-03	4.938E-01

Figure 6.3: TRIPOLI-4® calculated group transfer cross sections (in units of cm^{-1}) for SPX2 homogeneous sub-assembly

$\Delta\Sigma_{s0}$(%)	1	2	3	4	5	6
1	0.04	-	-	-	-	-
2	-0.6	0.05	-	-	-	-
3	0.8	0.05	-0.04	-	-	-
4	0.9	0.5	-0.02	0.01	-	-
5	34.2	-1.9	1.6	44	0.01	-
6	404	16	91.6	31	-13	0.2

Figure 6.4: Relative differences of group transfer cross sections of SPX2 homogeneous sub-assembly between ECCO and TRIPOLI-4® simulations

to $\Sigma_s^{g\to h}$ in units of cm^{-1}. The right upper sides of the two matrix are all zero because in the case of a fast neutron sub-assembly case, the up-scattering hardly ever occurs. It must be mentioned here that we did not provide the statistical errors related to the TRIPOLI-4® results. In fact, the scattering cross section matrix is not a direct product from the TRIPOLI-4® simulation. It is obtained according the formula: $\Sigma_s^{g\to h} = \Sigma_{s,g} \times P(g \to h)$. $\Sigma_{s,g}$ could be calculated easily by doing a subtraction between $\Sigma_{t,g}$ and $\Sigma_{a,g}$. Moreover, $P(g \to h)$ is calculated directly from the TRIPOLI-4® continuous-energy simulation and presented in the form of discrete probability density function. It should be pointed out that this multi-group energy transfer probability is accounted once all the batches are simulated. Therefore, there is not yet precise statistical errors associated to $P(g \to h)$.

Figure 6.4 represents the relative differences in percentage between the above scattering matrix from ECCO and TRIPOLI-4®. Most of the differences are rather slight and are limited to 1%. This is an indication for that the two codes based on completely different calculation methods can produce consistent scattering cross section matrices. However, greater discrepancies (marked in red) are found in the lower rows of Figure 6.4. This

could be explained by the fact that long-range neutron slowing-down rarely happens in a fast neutron case. So the remarkable inconsistency comes from a lack of statistics. For example, in the SPX2 case, there are only 971 scattering events from group $1 \rightarrow 5$ while the total scattering events departing from group 1 is around 9.35×10^7.

The ECCO-TRIPOLI-4® comparisons are performed again on homogeneous ZPPR-DCF lattice calculations. The one-dimensional multi-group cross sections are compared in Table 6.3. The scattering cross sections from ECCO and TRIPOLI-4® simulations are shown in Figures 6.5 and Figure 6.6. Their units are the same as those used for the above SPX2 case. At first, the consistency between ECCO and TRIPOLI-4® calculated multi-group cross sections is confirmed in the ZPPR-DCF case. Moreover, the differences found between the two codes are systematically in the same tendency and of the same order of magnitude.

Parameter	ECCO	TRIPOLI-4®	Diff
K_∞	1.66679	1.66832±0.00009	-153 pcm
units	cm^{-1}	$cm^{-1}(10^{-3}\%)$	%
Σ_{t1}	1.710E-01	1.710E-01 (1.1)	0.00
Σ_{t2}	1.962E-01	1.963E-01 (1.1)	0.05
Σ_{t3}	2.497E-01	2.495E-01 (1.0)	-0.08
Σ_{t4}	3.352E-01	3.354E-01 (1.9)	0.06
Σ_{t5}	5.359E-01	5.358E-01 (4.4)	-0.02
Σ_{t6}	4.907E-01	4.920E-01 (22)	0.26
Σ_{a1}	7.782E-03	7.783E-03 (3.5)	0.01
Σ_{a2}	4.450E-03	4.450E-03 (0.86)	0.00
Σ_{a3}	4.577E-03	4.577E-03 (1.3)	0.00
Σ_{a4}	8.087E-03	8.103E-03 (2.7)	0.20
Σ_{a5}	1.802E-02	1.801E-02 (1.2)	-0.06
Σ_{a6}	4.649E-02	4.678E-02 (78)	0.62
$\nu\Sigma_{f1}$	2.150E-02	2.150E-02 (3.6)	0.00
$\nu\Sigma_{f2}$	1.003E-02	1.003E-02 (1.6)	0.00
$\nu\Sigma_{f3}$	8.110E-03	8.110E-03 (0.16)	0.00
$\nu\Sigma_{f4}$	8.756E-03	8.800E-03 (1.9)	0.50
$\nu\Sigma_{f5}$	1.735E-02	1.733E-02 (15)	-0.12
$\nu\Sigma_{f6}$	5.375E-02	5.407E-02 (90)	0.60

Table 6.3: Comparison of group constants in the 6-groups ZPPR-DCF homogeneous lattice calculations between ECCO and TRIPOLI-4®

The detailed comparison analysis for the other cases will not be presented here for sake of space. However, all the tested cases confirm that TRIPOLI-4® and ECCO could produce consistent multi-group cross sections for infinite lattice calculation. This is the first step towards validating our newly implemented Monte-Carlo estimators. In the following section, we shall check the performance of these produced multi-group constants in a transport core calculation.

6.3.2 Group constants use in TRIPOLI-4®

In this section, we shall use the produced multi-group constants in a transport core calculation code to verify that these constants can preserve the main characteristics of a

Σ_{s0} (ECCO)	1	2	3	4	5	6
1	1.271E-01	0	0	0	0	0
2	2.621E-02	1.711E-01	0	0	0	0
3	9.764E-03	2.047E-02	2.412E-01	0	0	0
4	1.268E-04	1.609E-04	3.857E-03	3.208E-01	0	0
5	1.238E-05	2.191E-05	2.299E-05	6.309E-03	5.171E-01	0
6	2.209E-07	1.022E-07	5.170E-08	4.450E-06	7.699E-04	4.442E-01

Figure 6.5: ECCO calculated group transfer cross sections (in units of cm^{-1}) for a ZPPR-DCF homogeneous sub-assembly

Σ_{s0} (TRPOLI-4®)	1	2	3	4	5	6
1	1.272E-01					
2	2.601E-02	1.712E-01				
3	9.846E-03	2.045E-02	2.411E-01			
4	1.269E-04	1.613E-04	3.853E-03	3.210E-01		
5	1.790E-05	2.226E-05	2.319E-05	6.307E-03	5.171E-01	
6	1.140E-06	1.004E-07	5.634E-07	4.519E-06	7.729E-04	4.452E-01

Figure 6.6: TRIPOLI-4® calculated group transfer cross sections (in units of cm^{-1}) for ZPPR-DCF homogeneous sub-assembly

$\Delta\Sigma_{s0}$(%)	1	2	3	4	5	6
1	-0.00	-	-	-	-	-
2	-0.79	0.06	-	-	-	-
3	0.84	-0.10	-0.04	-	-	-
4	0.06	0.21	-0.11	0.06	-	-
5	44.5	1.6	0.86	-0.11	-0.01	-
6	416	-1.8	9.0	1.5	0.39	0.21

Figure 6.7: Relative differences of group transfer cross sections of ZPPR-DCF homogeneous sub-assembly between ECCO and TRIPOLI-4® calculations

reactor sub-assembly. The chosen core simulation code is TRIPOLI-4® itself but under multi-group simulation mode. Figure 6.8 summarizes the validation procedure from the point of view of a core calculation code. Firstly, the point-wise TRIPOLI-4® simulation gives the conventional results which will be used as reference values (K_{eff}; flux spectrum; neutronic balance). Meanwhile, the multi-group constants can be produced if desired by users. Then, these multi-group constants are fed to a multi-group TRIPOLI-4® simulation performed in the same geometry as before. The second simulation will also give results such as K_{eff}, flux spectrum and neutronic balance. The final comparisons between these two simulation results will be made in order to validate the above generated multi-group cross sections since the multi-group TRIPOLI-4® solver is supposed to be accurate.

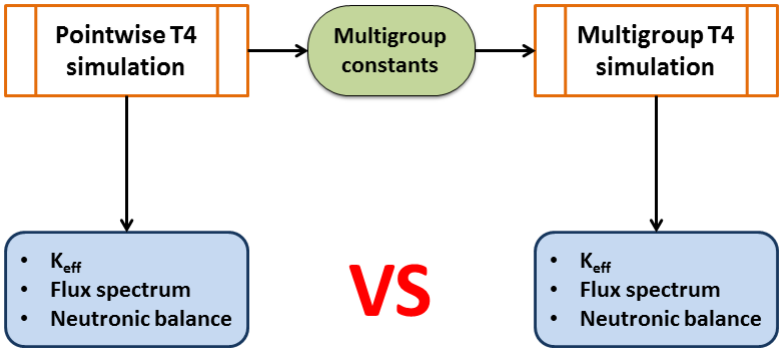

Figure 6.8: The TRIPOLI-4® produced multi-group constants validation scheme in core simulation code

The validation concept described is different from the one using multi-group constants in a deterministic core calculation code. We could definitely replace the multi-group TRIPOLI-4® simulation by another deterministic transport core simulation. As a reminder, it must be recalled that this chapter deals with the simplest case involving only energy condensation within TRIPOLI-4® and does not deal with the neutron leakage effect nor the anisotropy effect. In this situation, an exact conservation of the neutronic balance is expected from continuous-energy calculation to multi-group calculation. It could be considered more an academical study rather than an industrial application. Therefore, minimization of the approximations used in the transport core calculation code is the most desired criterion for the moment. This is the reason why a multi-group Monte-Carlo code is chosen here.

Moreover, the produced multi-group cross sections are not really used for a whole core calculation. In the present chapter, the geometry used in the multi-group TRIPOLI-4® simulation is the same as in the previous continuous-energy simulation step. The motivation of doing it this way is to check the preservation of neutronic balance as well as other characteristic parameters of each single sub-assembly from continuous-energy simulation to multi-group simulation. This validation step seems very important to the author even it is hardly found in other validation procedure of Monte-Carlo codes that produce the multi-group constants.

After having set the principal goal, the above-designed validation procedures will be executed in all the cases tested in the previous section. For the same reason, we always choose the SPX2 and ZPPR-DCF sub-assemblies to develop in detail here.

First of all, the calculated K_∞ values are respectively presented in Table 6.4 (SPX2 case) and Table 6.5 (ZPPR-DCF case). There are two kinds of evaluations used as input data for point-wise simulations: NJOY and NJOY + TABP. NJOY option leads TRIPOLI-4® to use NJOY code[37] processed cross sections. The resonances are reconstructed from the resonance parameters and models at 0 K. The cross sections are broadened at desired temperature. TABP option leads TRIPOLI-4® to use CALENDF code[91] produced probabilities tables in the unresolved resonance range. Both of them are collapsed into 6-group and 33-group cross sections. It results in a reactivity difference of around 300 pcm. The values in brackets beside the K_∞ values are their standard deviations in pcm. The last rows (ΔK_{eff}) in these two tables are the discrepancies between multi-group and point-wise K_∞ as well as the standard deviations which are all in pcm units. To remind again that the units "pcm" used in this work stands for $\times 10^{-5}$.

The comparisons in Table 6.4 and Table 6.5 show that a strict preservation of K_∞ values is confirmed with use of NJOY or CALENDF data under both 6-group and 33-group energy structures. A simple comparison of multiplication factors is not at all sufficient to validate the produced cross sections. Thus detailed analysis will be continued on three other important characteristics: flux spectrum; production rate and absorption rate. 33-group calculation results will be presented in the following sections with using both the NJOY and NJOY+TABP databases.

SPX2	6-GR NJOY	33-GR NJOY	6-GR TABP	33-GR TABP
K_∞ point-wise	1.34857(12)	1.34857(12)	1.35364(8)	1.35364(8)
K_∞ multi-group	1.34826(17)	1.34851(17)	1.35326(54)	1.35352(2)
ΔK_∞ (pcm)	-31(21)	-6(21)	-38(55)	-12 (8)

Table 6.4: Comparison of K_∞ values from point-wise and multi-group TRIPOLI-4® simulations for SPX2 sub-assembly

ZPPR-DCF	6-GR NJOY	33-GR NJOY	6-GR TABP	33-GR TABP
K_∞ point-wise	1.66284(9)	1.66281(9)	1.66832(9)	1.66832(9)
K_∞ multi-group	1.66295(23)	1.66287(22)	1.66817(23)	1.66818(3)
ΔK_∞	11(25)	6(24)	-15(25)	-14(9)

Table 6.5: Comparison of K_∞ values from point-wise and multi-group TRIPOLI-4® simulations for ZPPR-DCF sub-assembly

Flux spectrum comparison

First of all, attention is paid to the results using the NJOY evaluation. Figure 6.9 shows the continuous-energy TRIPOLI-4® calculated 33-group flux spectrum in red curve which will be used as reference. The dashed blue curve is the multi-group TRIPOLI-4® simulated flux spectrum using the self-produced 33-group cross sections. First of all, it could be said that the multi-group calculation can reproduce the energy distribution form of the neutron flux with respect to the reference one. The two curves clearly overlap and it is

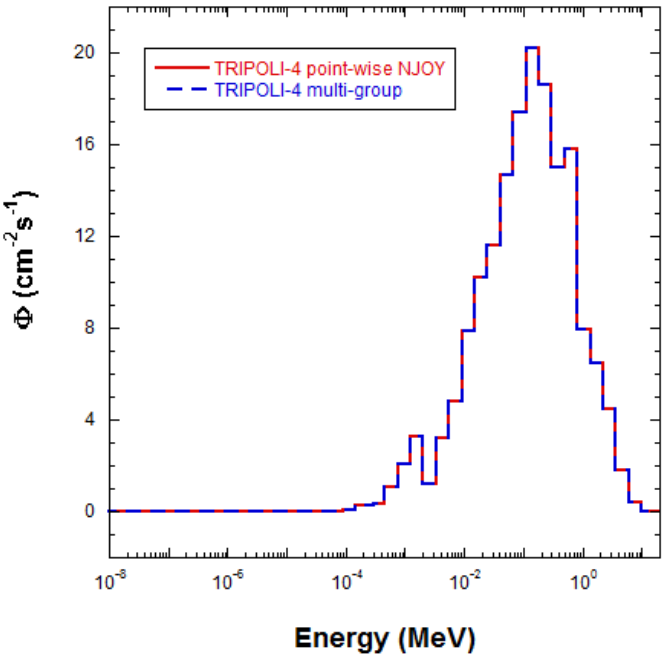

Figure 6.9: Flux spectra calculated by TRIPOLI-4® point-wise (NJOY) and multi-group simulations for homogeneous SPX2 sub-assembly

hard to distinguish the discrepancies.

The left part of Figure 6.10 presents the relative difference in percentage between the multi-group and point-wise spectra by the red curve. By the way, the standard deviations of this relative difference are plotted with green lines. Both TRIPOLI-4® continuous-energy and multi-group simulations can yield relative standard deviations for associated scores. They are respectively noted as $\frac{\delta\phi_{\text{pct}}}{\phi_{\text{pct}}}$ and $\frac{\delta\phi_{\text{hmg}}}{\phi_{\text{hmg}}}$. Then, a simple formula allows us to obtain the statistical error of the relative difference between the two TRIPOLI-4® simulations, cf Eq (6.22).

$$\delta(\frac{\phi_{\text{hmg}} - \phi_{\text{pct}}}{\phi_{\text{pct}}}) = \sqrt{(\frac{\delta\phi_{\text{pct}}}{\phi_{\text{pct}}})^2 + (\frac{\delta\phi_{\text{hmg}}}{\phi_{\text{hmg}}})^2} \times \frac{\phi_{\text{hmg}}}{\phi_{\text{pct}}} \tag{6.22}$$

The upper and lower green lines in Figure 6.10 correspond to $\pm 3 \times \delta(\frac{\phi_{\text{hmg}} - \phi_{\text{pct}}}{\phi_{\text{pct}}})$ which help to analyze the obtained relative difference $(\frac{\phi_{\text{hmg}} - \phi_{\text{pct}}}{\phi_{\text{pct}}})$. It must be clearly stated that both of them are in units of %. Above 100 eV, the relative differences are lower than the associated deviation. This indicates that the calculated multi-group cross sections can reproduce the consistent neutron flux spectrum in a transport core calculation. However, some great discrepancies are found in the lowest energy groups. Their absolute values even exceed 3 times of the standard deviations. The inconsistent phenomenon observed in the energy interval $[13.7; 148]\, eV$ is not that much of a problem because for a fast fuel sub-assembly, the importance weight of neutron in this energy interval is really

negligible. Neutrons can hardly be scattered into the low energy groups which results into high uncertainty. Moreover, the uncertainty induced by the energy transfer probability is not taken into consideration by the statistical errors in Figure 6.10. On the other hand, it is recommended that more attention be given to the gray zone where neutron plays a much more important role. Thus, a zoom of this energy domain is given on the right side of Figure 6.10.

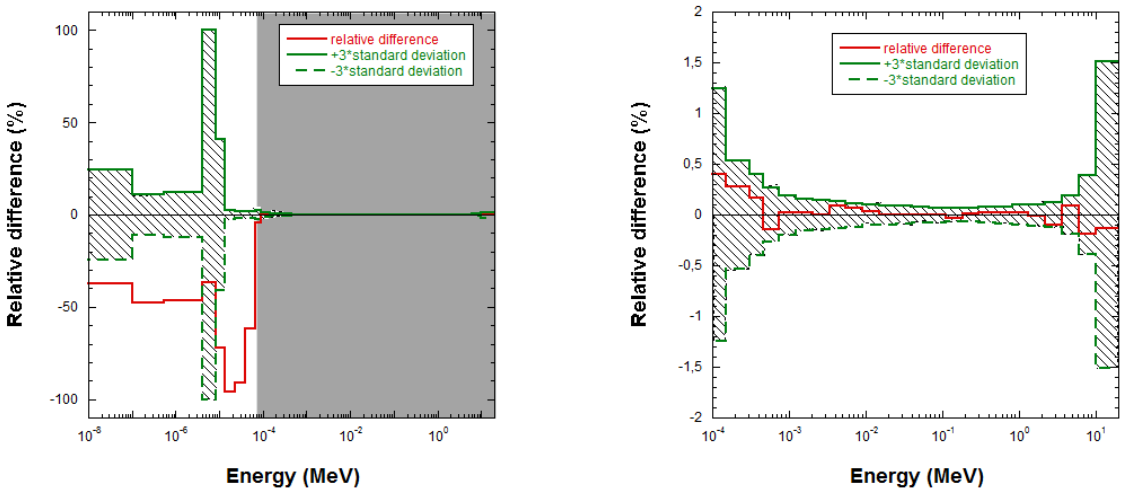

Figure 6.10: Comparison of flux spectra calculated by TRIPOLI-4® point-wise (NJOY) and multi-group simulations for homogeneous SPX2 sub-assembly

The right side of Figure 6.10 shows that the relative difference is limited to 0.5% and completely covered by the estimated error. The same consistency applies to the ZPPR-DCF sub-assembly case as well. Figure 6.11 represents the flux spectra calculated in ZPPR-DCF homogeneous geometry by continuous-energy and multi-group TRIPOLI-4® simulations. The two curves are very well overlapped. A closer analysis of their relative difference is shown in Figure 6.12. The left part gives a global image covering the whole energy domain; while the right one focuses only on the important energy range which represents 99.9% of production rate.

Other tested sub-assemblies will not be presented with their detailed spectra analysis here. All of them confirm that use of TRIPOLI-4® produced multi-group cross sections enables us to reproduce the neutron spectrum as simulated by the referential continuous-energy TRIPOLI-4® calculation. In the important energy range, the relative difference is limited to 0.5%. The greater discrepancies observed in the low energy groups are due to very few energy transfer events toward the low energy groups. Moreover, this important statistical errors related with transfer probability has not yet been considered in our simulated results. Fortunately, this has a very small impact on the whole neutronic balance. To verify this, the following analysis is to be carried out on the production rate and then on the absorption rate.

Production rate comparison

The production rate calculated as $P = \nu\Sigma_f\phi$ is an important characteristic parameter indicating the neutron regeneration density distribution probability in the whole energy

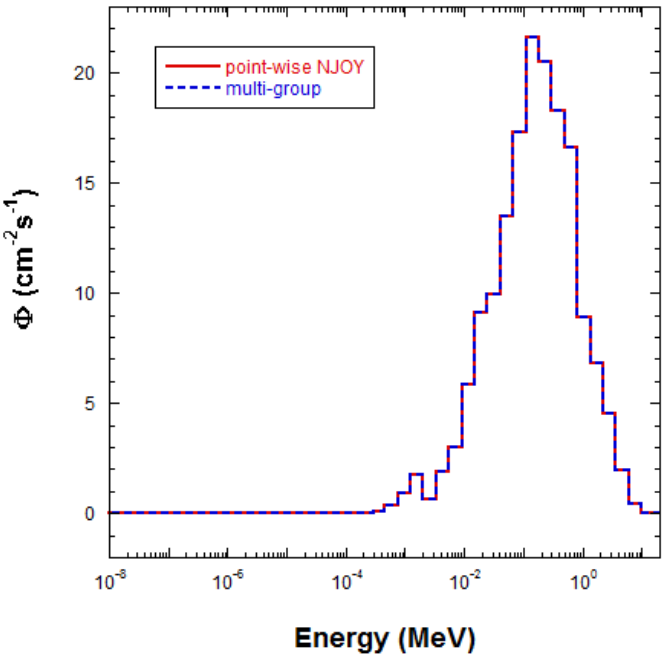

Figure 6.11: Flux spectra calculated by TRIPOLI-4® point-wise (NJOY) and multi-group simulations for homogeneous ZPPR-DCF sub-assembly

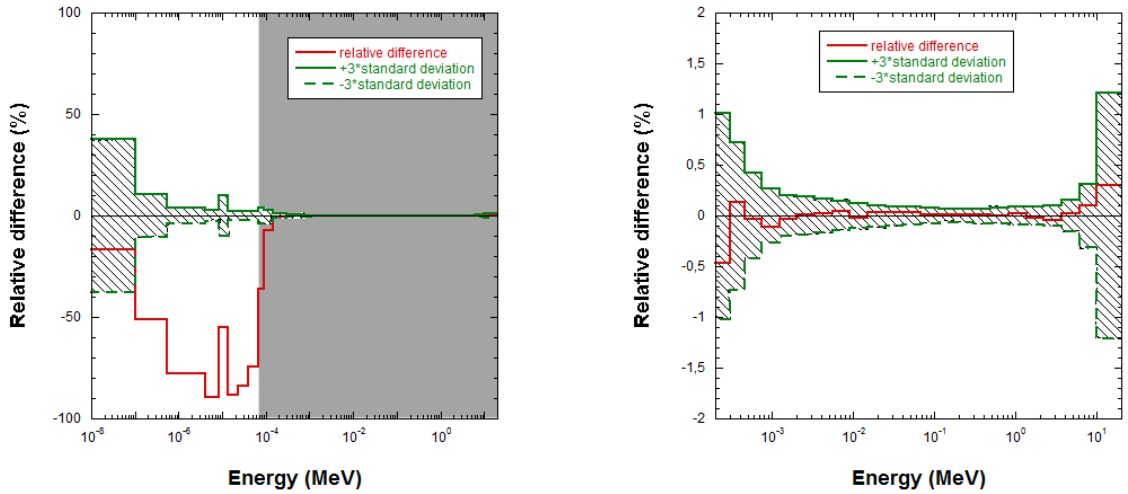

Figure 6.12: Comparison of flux spectra calculated by TRIPOLI-4® point-wise (NJOY) and multi-group simulations for homogeneous ZPPR-DCF sub-assembly

domain. In the TRIPOLI-4® simulation, whether under the continuous-energy or multi-group modes, the relationship below (Eq 6.23) is always valid. It is based on the fact that the neutron source is fixed to 1 in TRIPOLI-4® simulation. Apparently, different combination ways between $\nu\Sigma_{f,g}$ and ϕ_g could result in the right K (infinite or effective) value. Therefore, to validate the produced multi-group cross sections, besides having the appropriate estimation of K, a consistent production contribution from each group is also important. Sometimes, a compensation effect could achieve the right K value although it

could not really accomplish the requirements of an excellent homogenization and energy condensation work.

$$\int_{E\in\cup} \nu\Sigma_f(E)\phi(E)dE = \sum_g \nu\Sigma_{f,g}\phi_g = K \tag{6.23}$$

With this strict examining criterion, we shall present the production rates from both continuous-energy (NJOY) and multi-group TRIPOLI-4® simulations on SPX2 and ZPPR-DCF sub-assemblies. They are plotted in Figure 6.13 and Figure 6.14 respectively.

The left sides of the two figures represent the detailed production rates (in pcm units) distributed over the whole energy domain. The red curves are the point-wise results which are obtained directly from TRIPOLI-4® continuous-energy simulations. The blue dashed curves are the multi-group production rates which are the products between $\nu\Sigma_{f,g}$ from continuous-energy TRIPOLI-4® simulation and ϕ_g from multi-group TRIPOLI-4® simulation. So, it is more complicated to obtain their statistical errors which will be explained later. With the two left figures, it is clearly demonstrated that the multi-group production rates agree well with the point-wise rates.

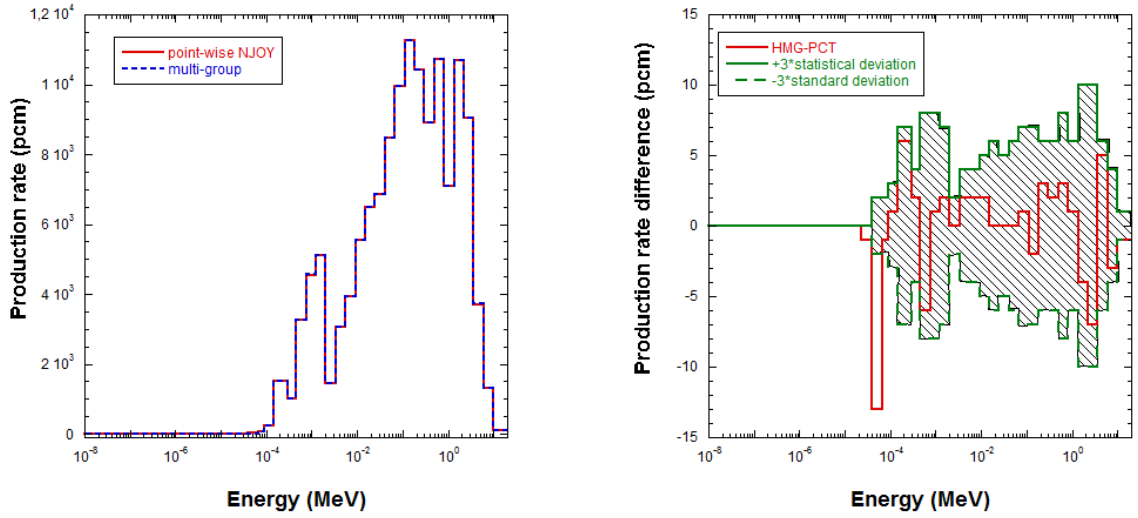

Figure 6.13: Production rate calculated by TRIPOLI-4® point-wise (NJOY) and multi-group simulations for homogeneous SPX2 sub-assembly and their comparison

In order to visualize the discrepancies between multi-group and point-wise production rates, their differences are plotted in red curves at the right side of Figure 6.13 and Figure 6.14. Moreover, three times the standard deviation (positive and negative) related to the difference are also given in the two figures on the right. The up and down curves define a closed confidential zone. The method used to calculate the standard deviation of the production rate difference is as follows: $\delta(P_{\text{hmg}} - P_{\text{pct}}) = \sqrt{(\delta P_{\text{hmg}})^2 + (\delta P_{\text{pct}})^2}$, where δP_{pct} is estimated from a point-wise simulation. As for δP_{hmg}, it is necessary to calculate at first its relative deviation $\dfrac{\delta P_{\text{hmg}}}{P_{\text{hmg}}}$ as in Eq (6.24). The absolute deviation δP_{hmg} can then be obtained easily by doing $\delta P_{\text{hmg}} = \dfrac{\delta P_{\text{hmg}}}{P_{\text{hmg}}} \times P_{\text{hmg}}$.

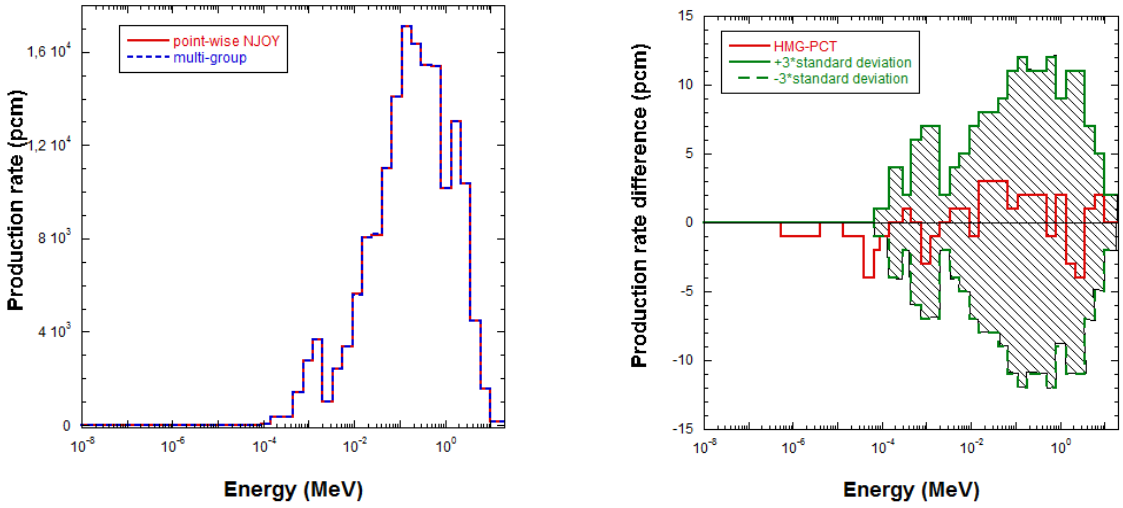

Figure 6.14: Production rate calculated by TRIPOLI-4® point-wise (NJOY) and multi-group simulations for homogeneous ZPPR-DCF sub-assembly and their comparison

$$\frac{\delta P_{\text{hmg}}}{P_{\text{hmg}}} = \sqrt{(\frac{\delta \nu \Sigma_{f,g}}{\nu \Sigma_{f,g}})^2 + (\frac{\delta \phi_g}{\phi_g})^2} \tag{6.24}$$

Several common points can be found from the right-sides of Figure 6.13 and Figure 6.14:

1- The production rate difference is less than 15 pcm for any energy group;

2- The production rate difference is completely covered by 3 times the standard deviation in the important energy domain. This proves that our produced multi-group cross sections are rather satisfactory;

3- For the low energy groups where there are barely neutrons, the production rate differences are sometimes higher than the 3 times of standard deviations. This is always due to a lack of statistics for energy transfer events in low energy domain. And this potential statistical error is not considered in our results. This is a common and inevitable problem for the Monte-Carlo codes. Anyway, the discrepancies found in these low-energy groups are negligible for the whole production rate analysis.

Absorption rate comparison

The absorption rate also contributes an important part to the neutronic balance. So, the ability to preserve the absorption rate from continuous-energy simulation to multi-group simulation is another indispensable challenge for produced multi-group cross sections. We continue to use the SPX2 and ZPPR-DCF homogeneous sub-assemblies as examples to analyze their results. Figure 6.15 and Figure 6.16 present respectively the absorption rates in SPX2 and ZPPR-DCF homogeneous geometry cases. The left parts of the figures contain the absolute absorption rates from point-wise simulation (the red line) and multi-group simulation (the blue dashed line). On the right-hand sides, the differences of absorption rates in units of pcm are plotted as well as three times the standard deviations.

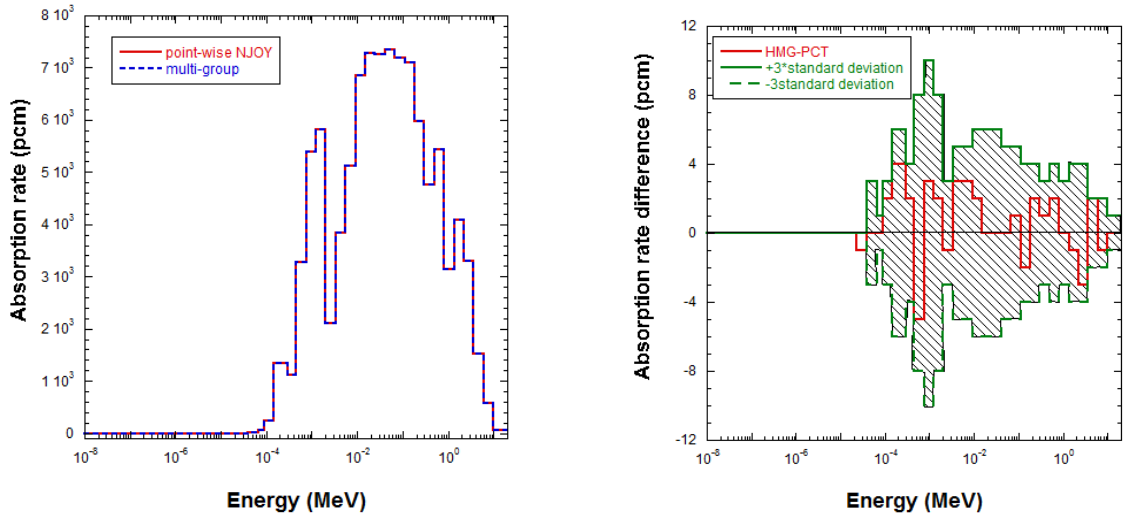

Figure 6.15: Absorption rate calculated by TRIPOLI-4® point-wise (NJOY) and multi-group simulations for homogeneous SPX2 sub-assembly and their comparison

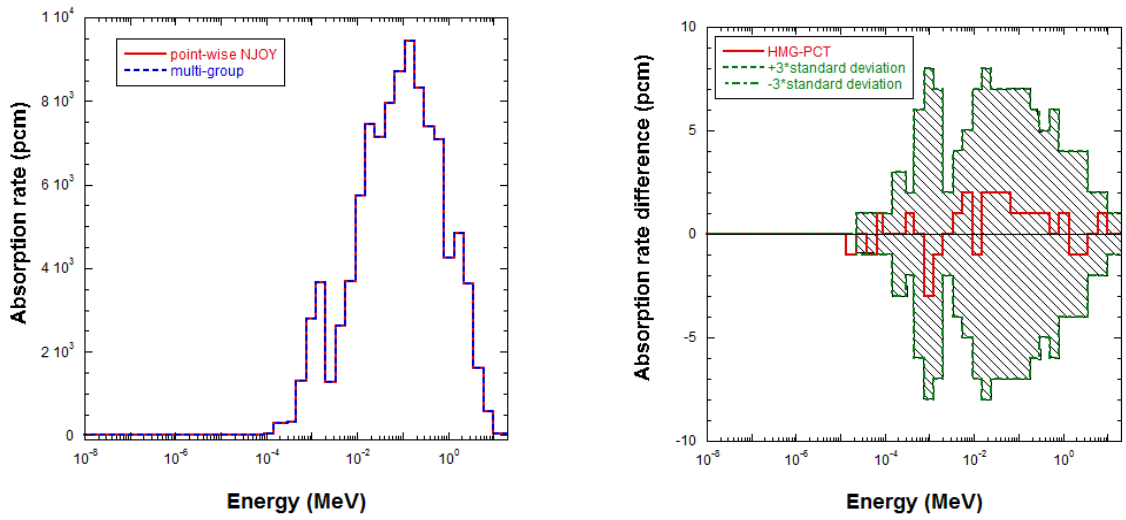

Figure 6.16: Absorption rate calculated by TRIPOLI-4® point-wise (NJOY) and multi-group simulations for homogeneous ZPPR-DCF sub-assembly and their comparison

Both figures confirm that the produced multi-group cross sections can be used in a multi-group transport calculation preserving the absorption rate compared to the point-wise reference values. A closer analysis is performed on the differences between the multi-group absorption rates and the point-wise rates. Their discrepancies (on an order of magnitude of a few pcm) have been found to be even smaller than those of the production rate. Additionally, they are well covered by the three times of standard deviations.

NJOY + TABP results

Until now, the neutronic balance and flux spectrum analysis have been accomplished using the NJOY library. We shall continue to present the results obtained with NJOY library and the probability tables. Unfortunately, the present release of TRIPOLI-4® code was not able to take consideration of probabilities tables in the homogenization and energy condensation routines. The first effort was to incorporate these unresolved resonant energy domain data into the multi-group constant production procedure. In addition, we have to make sure that the collision density and the macroscopic total cross section used to deduce our desired multi-group constants match well between themselves. Because in our first test, inconsistent total cross sections were respectively used in numerator and denominator parts of Eq (6.25) to calculate the weighting function, the scalar flux. Under the NJOY+TABP option, when collision occurs in the unresolved resonant region, the cross sections are sampled randomly from the possible sub-group values. However, the next step updating the multi-group constants does not use the same total cross section $\Sigma_t(\mathbf{r}, E)$ which is used to store the collision density $\omega(\mathbf{r}, E)$. In contrary, new sample work is carried out which could result in different point-wise total cross section $\Sigma'_t(\mathbf{r}, E)$. This bug impacted principally on heavy nuclei, such as ^{239}Pu and ^{235}U. Previous non-relevant results showed that this inadequate usage of probabilities tables data induced around 100 pcm of over-estimation for K_∞ values.

$$\Sigma_{t,g} = \frac{\int\limits_{E\in g} \omega(\mathbf{r}, E)dE}{\int\limits_{E\in g} \phi(\mathbf{r}, E)dE} = \frac{\int\limits_{E\in g} \omega(\mathbf{r}, E)dE}{\int\limits_{E\in g} \frac{\Sigma_t(\mathbf{r}, E)\phi(\mathbf{r}, E)}{\Sigma'_t(\mathbf{r}, E)}dE} \tag{6.25}$$

After having been assured that the NJOY+TABP option could work efficiently in homogenization and energy condensation routines, the same sub-assemblies are tested with the NJOY+TABP option. Figure 6.17 to Figure 6.20 illustrate the flux spectra as well as their relative differences with associated standard deviations. Figure 6.21 and Figure 6.22 represent the production rates as well as their comparisons for SPX2 and ZPPR-DCF sub-assemblies. At the end, absorption rate analysis are given in Figure 6.23 and Figure 6.24. In this part, no more detailed comments will be repeated for every single figure because they respect mostly the same tendency as the NJOY option calculation results.

It confirms that under the NJOY+TABP option, the homogenization and energy condensation routines in the corrected version of TRIPOLI-4® code are able to produce appropriate multi-group constants for infinite geometry case. Usage of the above produced multi-group constants in TRIPOLI-4® multi-group simulations guarantees consistent results compared with reference simulation results. Both flux spectrum and neutronic balance are well preserved in the important energy range which comprises more than 99.5% of production rate. Below this energy range, discrepancies come out between multi-group and point-wise TRIPOLI-4® simulations. It is owing to the fact that quite rare scattering events occur at such low energy domain. Therefore, it induces high uncertainty of low energy group transfer probabilities. Unfortunately, this is a bias inevitable in Monte-Carlo field. However, this bias is not very important for the final result because very low neutron production rate (less than 0.5%) belongs to this low energy domain.

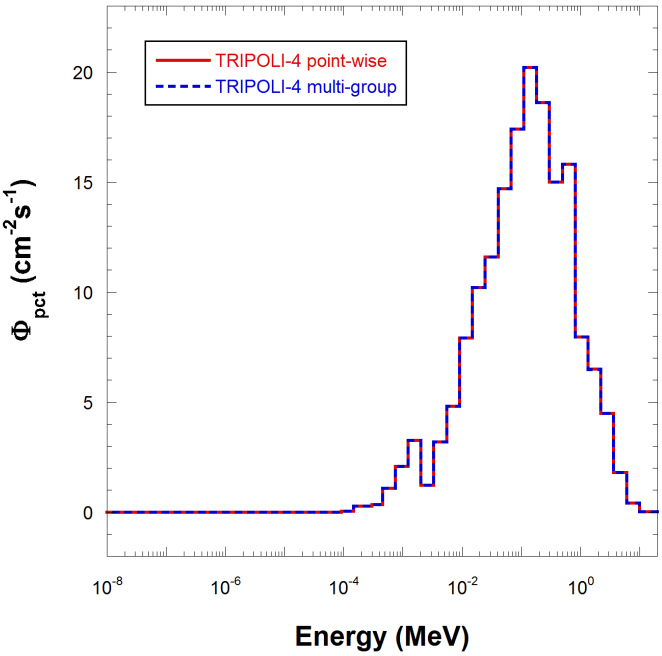

Figure 6.17: Flux spectra calculated by TRIPOLI-4® point-wise (TABP) and multi-group simulations for homogeneous SPX2 sub-assembly

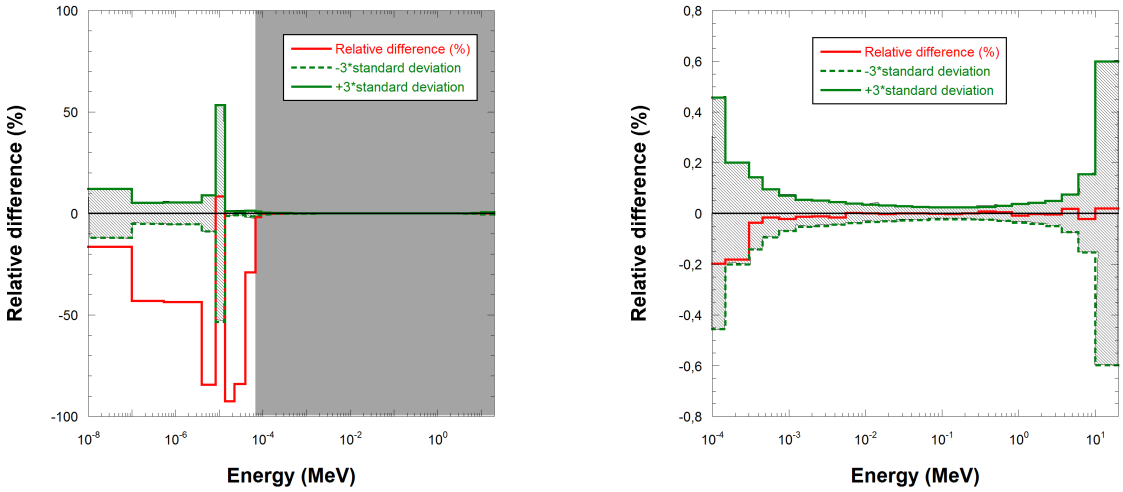

Figure 6.18: Comparison of flux spectra calculated by TRIPOLI-4® point-wise (TABP) and multi-group simulations for homogeneous SPX2 sub-assembly

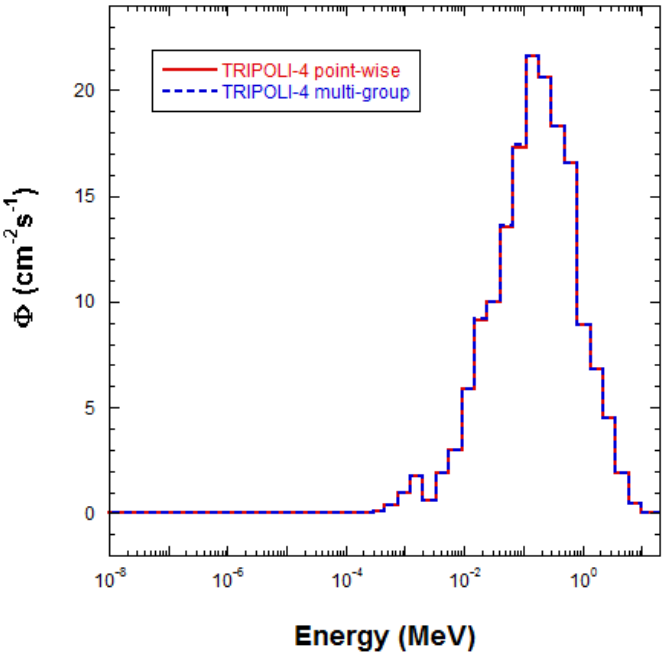

Figure 6.19: Flux spectra calculated by TRIPOLI-4® point-wise (TABP) and multi-group simulations for homogeneous ZPPR-DCF sub-assembly

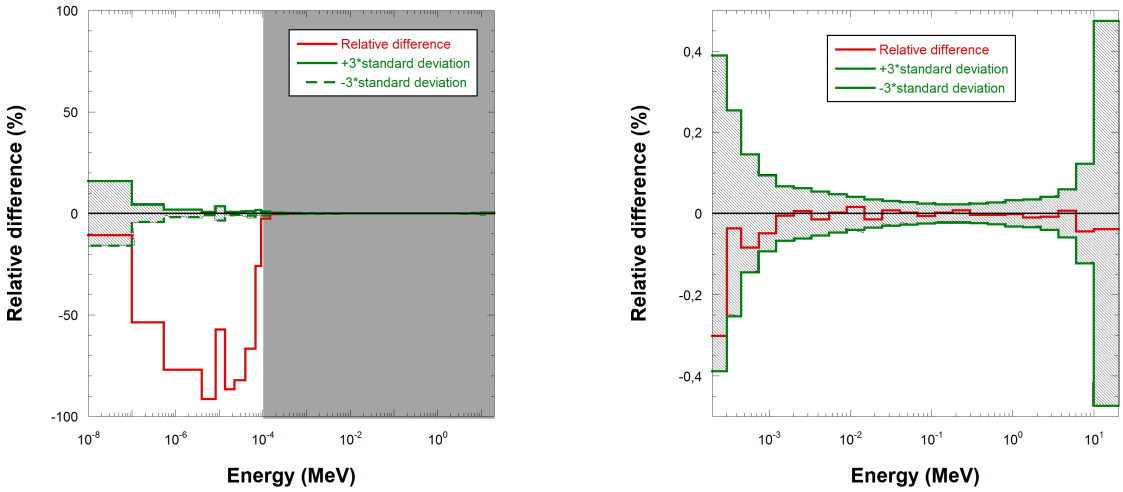

Figure 6.20: Comparison of flux spectra calculated by TRIPOLI-4® point-wise (TABP) and multi-group simulations for homogeneous ZPPR-DCF sub-assembly

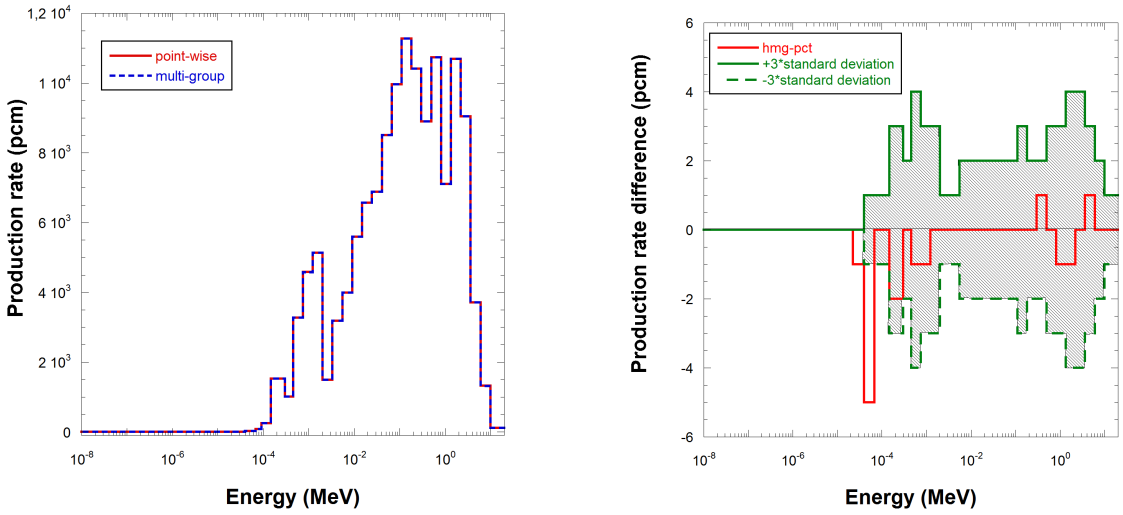

Figure 6.21: Production rate calculated by TRIPOLI-4® point-wise (TABP) and multi-group simulations for homogeneous SPX2 sub-assembly and their comparison

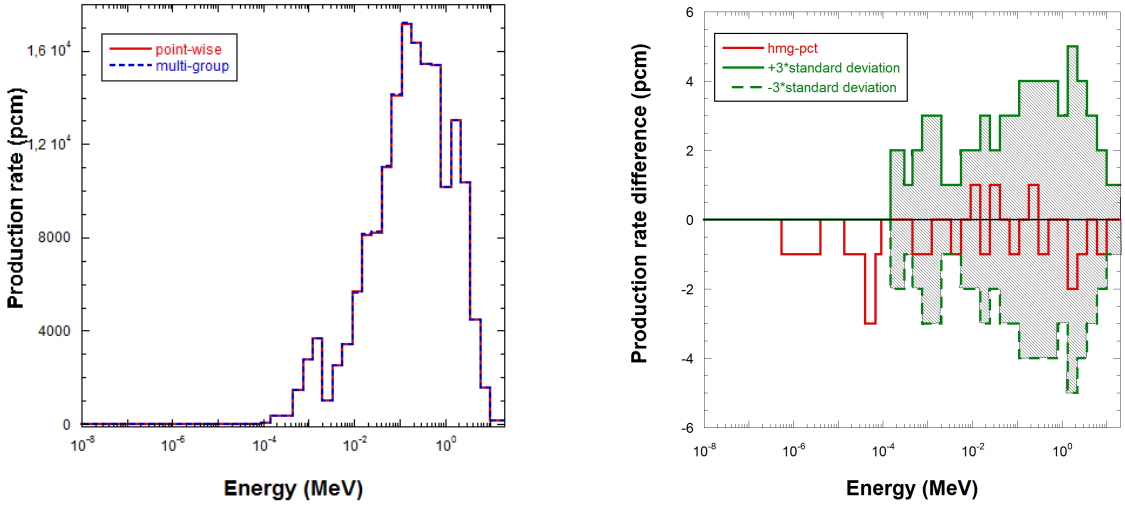

Figure 6.22: Production rate calculated by TRIPOLI-4® point-wise (TABP) and multi-group simulations for homogeneous ZPPR-DCF sub-assembly and their comparison

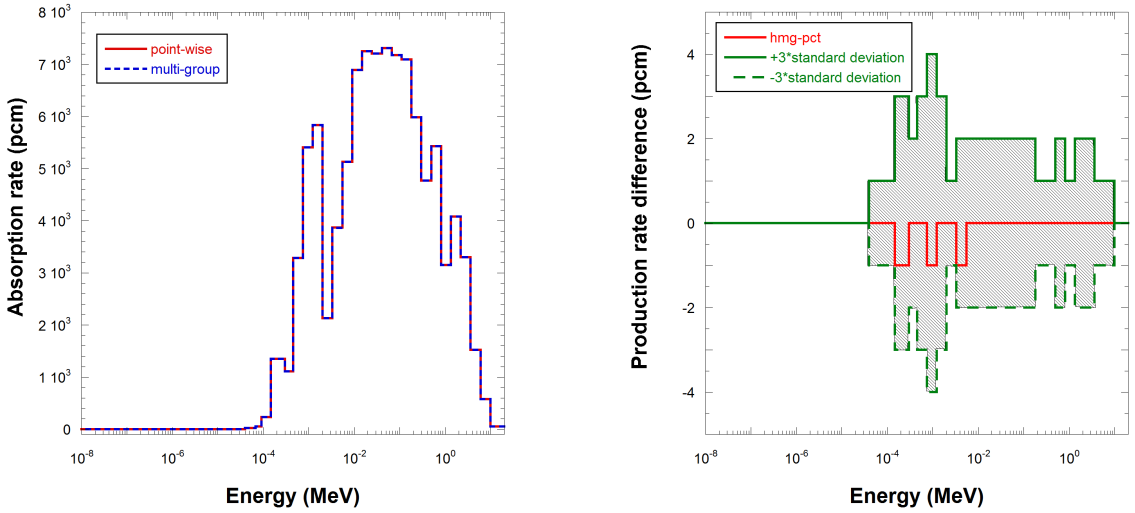

Figure 6.23: Absorption rate calculated by TRIPOLI-4® point-wise (TABP) and multi-group simulations for homogeneous SPX2 sub-assembly and their comparison

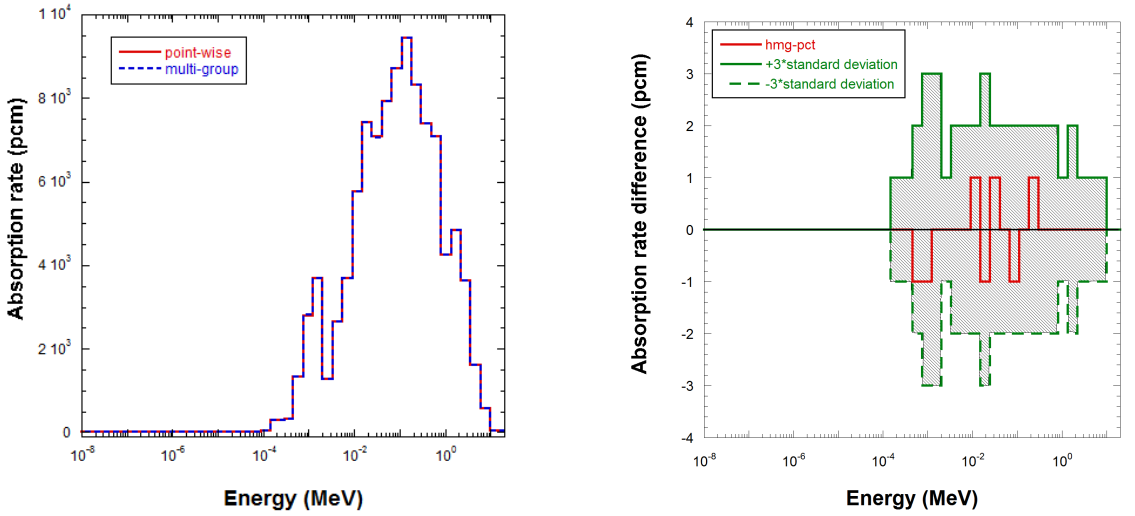

Figure 6.24: Absorption rate calculated by TRIPOLI-4® point-wise (TABP) and multi-group simulations for homogeneous ZPPR-DCF sub-assembly and their comparison

Conclusion

In this chapter, we focused on the validation work of energy condensation routines in TRIPOLI-4® in the simplest case which means no neutron-leakage effect is involved. Theoretical formula demonstrated that under this simplest case the flux spectra and neutronic balances should be preserved exactly between point-wise and multi-group simulations[49]. An initial examination work pointed out that several inconsistencies existed in the previous release of the code. To overcome these difficulties, three new Monte-Carlo estimators and some other computing techniques have been implemented. The new Monte-Carlo estimators handle three different multi-group parameters respectively: transfer probability, excess weight and fission spectrum.

Thanks to the use of the newly implemented estimators, the present version of TRIPOLI-4® code can produce appropriate multi-group cross sections comparable to those calculated by ECCO. These produced multi-group constants are used in Monte-Carlo transport multi-group simulations. Several important output characteristics are compared to the reference results from continuous-energy simulation. The comparisons show that our produced multi-group constants are able to preserve exactly the main features, such as K_∞, flux spectrum, production rate and absorption rate in case of using the NJOY or NJOY+TABP evaluation data. Generally, the condensation routines in the present version of the TRIPOLI-4® code are validated and proved to be capable of producing appropriate multi-group constants in a homogeneous non-leakage involved lattice calculation.

Chapter 7

Multi-group Anisotropy Treatment

Introduction

The previous chapter was limited to the treatment of infinite sub-assembly configurations where the anisotropy effect could be ignored. In this chapter, we continue to verify the multi-group constants production routines in TRIPOLI-4®, especially their capability to take into consideration of the scattering anisotropy effect induced by neutron leakage. To do this, the first step is to obtain a target geometry including neutron leakage phenomenon. The geometry construction work can be achieved by repeating the sub-assembly one by one until the multiplicative factor K_{eff} of the compound approaches 1. We may note that the boundary condition imposed on the geometry here is no more reflective nor periodic for all the surfaces. The advantage in creating a critical core-like lattice geometry lies in avoiding the approximations due to the leakage models incorporated in a sub-assembly calculation. At the same time, the heterogeneous effects are ignored as well.

It was found that even with use of the newly implemented estimators, we could not produce appropriate multi-group constants for a finite geometry to be used then in a transport core calculation code. Several examples are given in Table 7.1. They are all finite geometries constructed with the procedures described above. These geometries were at first simulated by TRIPOLI-4® with a continuous energy input data library NJOY option which gave reference K_{eff} values. The produced multi-group constants were then used in TRIPOLI-4® itself to run a multi-group transport Monte-Carlo simulation which gave another set of results. The difference of the multiplicative factors between the continuous energy simulation and the multi-group simulation noted as ΔK_{eff} were shown in Table 7.1 along with three times of their related standard deviation 3σ. The simulations were performed under 33-group and 6-group energy structures. All the results shown in Table 7.1 are in units of pcm.

We could tell from Table 7.1 that the discrepancies of the K_{eff} values largely exceed their statistical uncertainties. As we have already validated the infinite spectrum weighted multi-group cross sections in the previous chapter, the inconsistent results shown in Table 7.1 probably come from the multi-group anisotropy production method which is indeed related to the neutron leakage effect.

With this type of doubt, this chapter begins with a demonstrative analytical introduc-

Sub-assembly	ΔK_{eff}(33gr)	3σ (33gr)	ΔK_{eff}(6gr)	3σ (6gr)
MAS1B	158	48	179	45
ZONA2	400	39	614	39
SPX2	529	36	731	39
SPX1	203	39	354	39
ZPPR-DCF	676	39	1031	39
ZPPR-SCF	171	33	326	36

Table 7.1: Finite lattice calculations with improved Monte-Carlo estimators in TRIPOLI-4®

tion that points out the reason why we obtained inconsistent results. A theoretical deduction follows in order to find an appropriate method of handling the multi-group anisotropy representation. Its computational implementation is then carried out in TRIPOLI-4®. The method is finally validated through comparison with ECCO and continuous energy TRIPOLI-4® simulations in several cases.

7.1 Problematic introduction

In this section, we shall take the external fuel assembly of SuperPhénix (noted as SPX2) to construct an almost-critical lattice geometry to analyze the multi-group anisotropy calculation problem. Figure 7.1 shows the two principal steps for building up this almost-critical core-like lattice configuration. At first, the sub-assembly SPX2 is homogenized spatially. Then, the number of sub-assembly rings is increased one by one until the corresponding K_{eff} moves toward 1. The boundary condition used here is reflection for the axial direction and void for others.

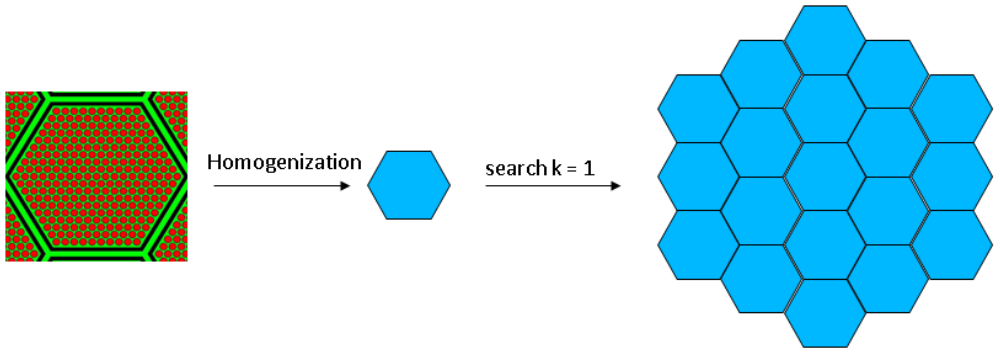

Figure 7.1: Illustration scheme for building up an almost-critical geometry

The obtained SPX2 based geometry is calculated by TRIPOLI-4® under both 33-group and 6-group energy structures which are from the validated reference code, ECCO. Both of them are specially used for fast reactor type lattice calculations. Inconsistent results from TRIPOLI-4® multi-group simulations reappear for both energy structures. Comparisons between the point-wise and multi-group TRIPOLI-4® results are shown in Table 7.2. The values in brackets are their standard deviations σ expressed in unit pcm (1 pcm = 10^{-5}).

Case	33-group	6-group
K_{eff} PCT	1.01570 (6)	1.01572 (9)
K_{eff} HMG	1.02099 (10)	1.02303 (9)
ΔK_{eff}(pcm)	529 (12)	731 (13)

Table 7.2: SPX2 calculation results from TRIPOLI-4® point-wise (PCT) with NJOY option & multi-group (HMG) simulations and their discrepancies

According to Table 7.2, the discrepancies of effective multiplicative factors ΔK_{eff} between TRIPOLI-4® multi-group and point-wise simulations are 529 ± 12 pcm under the 33-group energy structure and 731 ± 13 pcm under the 6-group energy structures. Obviously, the neutronic balance is not preserved in either of these two cases. In order to figure out where the problem revealed in TRIPOLI-4® comes from, the same geometry SPX2 is calculated by ECCO under the 6-group energy structure. Then, ECCO calculated multi-group cross sections are used by the deterministic core simulation code, BISTRO[43] which also belongs to the ERANOS code system. The K_{eff} results from BISTRO are compared with the TRIPOLI-4® point-wise simulation results which are used as reference. To note that in order to be comparable with ECCO simulation results, TRIPOLI-4® uses from now on the NJOY + TBAPS as input data option. This will result in a different K_{eff} value as reference but do not change our analysis work. Different types of comparisons are shown in Table 7.3. P1_TOTAL and P0_TOTAL correspond to two different energy condensation options in ECCO which will be detailed in the following text.

Case	K_{eff}	ΔK_{eff}(pcm)
TRIPOLI-4® PCT	1.01796 (9)	0
P1_TOTAL/ERANOS	1.01557	-239 (9)
P0_TOTAL/ERANOS	1.01550	-246 (9)
TRIPOLI-4® HMG(6GR)	1.02642(12)	+846(15)

Table 7.3: SPX2 geometry calculation results from TRIPOLI-4® (NJOY + TABP) and ECCO/ERANOS simulations.

To perform a lattice calculation with ECCO, it is necessary to understand that two different options exist for multi-group constant generation. They are named here option P0_TOTAL and option P1_TOTAL respectively. The differences between these two options originally come from the flux-current coupled P1 equations which are solved within ECCO. The system of equations is obtained by using the fundamental mode approximation which means that the angular flux is a combination between a periodic fundamental flux and a macroscopic flux shape e^{-ibx} as expressed in Eq (7.1). Then, the non spatial-dependent part of the flux is limited to a Polynomial development at first order, cf Eq (7.2). Both of Eq (7.1) and Eq (7.2) are specific for one-dimensional case. And x is the chosen direction; μ is the neutron direction projected on direction x; v is the neutron velocity.

$$\phi(x, v, \mu) = \phi(v, \mu) \times e^{-ibx} \tag{7.1}$$

$$\phi(v,\mu) = \frac{1}{2}\left[\phi_0(v) + 3\mu\phi_1(v)\right] \tag{7.2}$$

Substituting the decoupled form of flux as Eq (7.2) into a stationary one-dimensional Boltzmann equation, the flux-current coupled equations system could be derived. They are shown as follows:

$$\begin{cases} ib\phi_1(v) - \Sigma_t(v)\phi_0(v) + \dfrac{1}{2}\chi(v) + \int\limits_0^\infty dv'\Sigma_{s0}(v' \to v)\phi_0(v') = 0 \\ \\ ib\phi_0(v) - 3\Sigma_t(v)\phi_1(v) + 3\int\limits_0^\infty dv'\Sigma_{s1}(v' \to v)\phi_1(v') = 0 \end{cases} \tag{7.3}$$

The energy condensation work is then performed on the equation system (7.3) which results in another multi-group equation system (7.4):

$$\begin{cases} ib\phi_1^g - \Sigma_{t0}^g\phi_0^g + \dfrac{1}{2}\chi^g + \sum\limits_{g'} \Sigma_{s0}^{g'\to g}\phi_0^{g'} = 0 \\ \\ ib\phi_0^g - 3\Sigma_{t1}^g\phi_1^g + 3\sum\limits_{g'} \Sigma_{s1}^{g'\to g}\phi_1^{g'} = 0 \end{cases} \tag{7.4}$$

If we pay attention to the above equations, we see that the multi-group total cross sections Σ_t^g is defined in two different ways. One of them, Σ_{t0}^g, is weighted by the scalar flux $\phi_0(v)$. The other, Σ_{t1}^g, is weighted by the first moment of flux:$\phi_1(v)$. The latter is also known under the name of current. However, only one of them will be supplied to a core calculation. Therefore, to maintain a consistent form of Σ_t^g in the above equation system, two calculation modes are offered in ECCO. The first one, called P0_TOTAL option, means that the scalar flux weighted total cross section is chosen. Thus, the second equation in system (7.4) needs to be rewritten as follows:

$$ib\phi_0^g - 3\Sigma_{t0}^g\phi_1^g + 3\sum_{g'\neq g} \Sigma_{s1}^{g'\to g}\phi_1^{g'} + 3\widetilde{\Sigma_{s1}^{g\to g}}\phi_1^g = 0 \tag{7.5}$$

From the arranged Eq (7.5), it could be concluded that the in-group scattering cross section first order moment $\Sigma_{s1}^{g\to g}$ is corrected to preserve the neutron balance as shown in Eq (7.6).

$$\widetilde{\Sigma_{s1}^{g\to g}} = \Sigma_{t0}^g - \Sigma_{t1}^g + \Sigma_{s1}^{g\to g} \tag{7.6}$$

The same procedures could be applied to deduce the second option P1_TOTAL in ECCO. By using the current weighted total cross section Σ_{t1}^g in both equations from the system (7.4), the first one must be demanded to be reformed as in Eq (7.7). Thus, the in-group scattering cross section is modified similarly which is expressed in Eq (7.8).

$$ib\phi_1^g - \Sigma_{t1}^g\phi_0^g + \frac{1}{2}\chi^g + \sum_{g'\neq g} \Sigma_{s0}^{g'\to g}\phi_0^{g'} + \widetilde{\Sigma_{s0}^{g\to g}}\phi_0^g = 0 \tag{7.7}$$

$$\widetilde{\Sigma_{s0}^{g\to g}} = \Sigma_{t1}^g - \Sigma_{t0}^g + \Sigma_{s0}^{g\to g} \tag{7.8}$$

For both options of ECCO, the anisotropy (P0_TOTAL) or the within-group energy transfer law (P1_TOTAL) is changed before being used in a core calculation whatever through the form of $\widetilde{\Sigma_{s1}^{g\to g}}$ or $\widetilde{\Sigma_{s0}^{g\to g}}$. From Tab 7.3 we could find that these two options

remain in satisfactory agreement with respect to the TRIPOLI-4 ® reference value.

In order to make sure that the consistent results of ECCO/ERANOS simulations come from the fact that the anisotropy law in the ECCO simulation has been changed, a test was carried out with the P0_TOTAL option but without changing of $\Sigma_{s1}^{g\to g}$. This special test is marked as P0_TOTAL$^{\circledast}$ in Tab 7.4 and Tab 7.5. An over-estimated K_{eff} value which is similar to the one calculated in the TRIPOLI-4® multi-group simulation case is found by P0_TOTAL$^{\circledast}$/ERANOS simulation and shown in Tab 7.4. The same tendency between TRIPOLI-4® multi-group simulation and non-anisotropy-corrected ECCO simulation inspired us to review the multi-group anisotropy law in the TRIPOLI-4® code.

Case	K_{eff}	ΔK_{eff}
TRIPOLI-4® PCT	1.01796 (9)	0
P0_TOTAL/ERANOS	1.01550	-246 (9)
P0_TOTAL$^{\circledast}$ /ERANOS	1.02425	+629(9)
TRIPOLI-4® HMG(6GR)	1.02642(12)	+846(15)

Table 7.4: SPX2 geometry calculation results from TRIPOLI-4® (NJOY + TABP) and ECCO/ERANOS simulations. $\circledast$: without change of $\Sigma_{s1}^{g\to g}$

First of all, a comparison of produced multi-group cross sections is done between TRIPOLI-4® and ECCO. And a satisfactory agreement is shown between the two codes. Before comparing their produced multi-group anisotropy parameters, precisions deserve be given out on how these two codes calculate respectively the multi-group anisotropy parameters. In the deterministic ECCO case, $\overline{\mu}^{g\to h}$ is calculated according to Eq (7.9) where g could be the same as or different from h. In Monte-Carlo TRIPOLI-4® case, $\overline{\mu}^{g\to h}$ is calculated as the first order moment of the anisotropy parameter μ which respects its density distribution function $f(\mu|g\to h)$. The explicit formula will be given out in Section 7.3. It should be pointed out that in TRIPOLI-4® case, the multi-group anisotropy density distribution function $f(\mu)^{g\to h}$ is weighted by flux. This is different from ECCO case where $\overline{\mu}^{g\to h}$ is calculated via Eq (7.9) of which $\Sigma_{s1}^{g\to h}$ is weighted by current instead of flux.

$$\overline{\mu}^{g\to h} = \frac{\Sigma_{s1}^{g\to h}}{\Sigma_{s0}^{g\to h}} \tag{7.9}$$

After being aware of the methodology difference between these two codes in the aspect of calculating multi-group anisotropy parameters, we continue to compare their simulation results of SPX2 geometry under 6-groups energy structure. Important discrepancies are revealed for the in-group scattering anisotropy values from TRIPOLI-4® and ECCO(P0_TOTAL) simulation results which could be found in Tab 7.5. It is found that TRIPOLI-4® has globally under-estimated the $\overline{\mu}^{g\to g}$ compared with ECCO, especially for the low energy groups. That is the reason why TRIPOLI-4® multi-group simulation has over-estimated the K_{eff} value. Secondly, if we continue to compare TRIPOLI-4® results with non-anisotropy-corrected ECCO results, it is assured that they agree with each other even though they are based on completely different methods.

The above SPX2 geometry analysis pointed out that the present release of the TRIPOLI-4® code is not capable of handling the neutron leakage induced anisotropic lattice cal-

$\overline{\mu}^{g\to g}$	$1\to 1$	$2\to 2$	$3\to 3$	$4\to 4$	$5\to 5$	$6\to 6$
TRIPOLI-4®	0.432	0.261	0.087	0.034	0.019	0.014
ECCO(P0_TOTAL)	0.445	0.275	0.126	0.114	0.125	0.114
ECCO(P0_TOTAL)$^{\circledast}$	0.436	0.258	0.087	0.032	0.017	0.014

Table 7.5: $\overline{\mu}^{g\to g}$ values obtained for SPX2 geometry under TRIPOLI-4® (NJOY + TABP) & ECCO simulations with 6-group energy structure

culation while generating multi-group constants. The problem points especially to the multi-group anisotropy law production method in TRIPOLI-4®. Moreover, the fact that these two codes are based on completely different methods (one uses flux and the other uses current as weighting function) is not the key reason for the $\overline{\mu}^{g\to h}$ discrepancies. The detailed solution of this anisotropy issue will be developed in the following sections.

7.2 Multi-group Anisotropy Calculation Method

This section focuses on demonstrating the necessity of modifying the multi-group anisotropy distribution law as well as its exact mathematical formulation. The principle to be used here is inspired from the P1 consistent method[44]. The method, adopted in ECCO, is based on the fundamental mode approximation. This approximation is made for the purpose of facilitating deterministic calculation by separating spatial-dependence and energy-dependence out of flux term. However, in the Monte-Carlo simulation domain, this energy-space separating technique is not at all suitable. Therefore, exact formulation is indispensable in order to conduct the multi-group anisotropy law production work.

For a continuous-energy TRIPOLI-4® simulation, the neutron population obeys the steady-state Boltzmann transport equation which is recalled in Eq (7.10):

$$\widehat{\Omega}\cdot\vec{\nabla}\phi(\mathbf{r},E,\widehat{\Omega})+\Sigma_t(\mathbf{r},E)\phi(\mathbf{r},E,\widehat{\Omega})=\int_0^{\infty}\int_0^{4\pi}\Sigma_s(\mathbf{r},E'\to E,\widehat{\Omega}'\to\widehat{\Omega})\phi(\mathbf{r},E',\widehat{\Omega}')d^2\widehat{\Omega}'dE'+\frac{\chi(E)}{4\pi K_{\text{eff}}}Q_f(\mathbf{r}) \tag{7.10}$$

where $Q_f(\mathbf{r})$ stands for fission production term.

If we develop the angular flux and the double-differential scattering cross section with the spherical harmonics orthogonal system (cf Eq (7.11) and Eq (7.12)), the angular-dependent part could be omitted in the following homogenization and energy condensation procedures.

$$\phi(\mathbf{r},E,\widehat{\Omega})=\sum_{l=0}^{\infty}\frac{2l+1}{4\pi}\sum_{m=-l}^{l}\phi_l^m(\mathbf{r},E)R_l^m(\widehat{\Omega}) \tag{7.11}$$

$$\Sigma_s(\mathbf{r},E'\to E,\widehat{\Omega}'\to\widehat{\Omega})=\sum_{l=0}^{\infty}\frac{2l+1}{4\pi}\sum_{m=-l}^{l}\Sigma_{s,l}(\mathbf{r},E'\to E)R_l^m(\widehat{\Omega}')R_l^m(\widehat{\Omega}) \tag{7.12}$$

During a TRIPOLI-4® continuous-energy simulation, the input data library including the anisotropy information is assumed to be exact. This means that the development limit

L for angular flux $\phi(\mathbf{r}, E, \widehat{\Omega})$ and point-wise scattering cross section $\Sigma_s(\mathbf{r}, E' \to E, \widehat{\Omega}' \to \widehat{\Omega})$ is in fact $L = \infty$. Here, in order to give an analytical deduction, L is limited to 1. Thus, the angular flux and the scattering cross section are rewritten as in Eq (7.13) and Eq (7.14).

$$\phi(\mathbf{r}, E, \widehat{\Omega}) = \frac{1}{4\pi}\phi_0(\mathbf{r}, E) + \frac{3}{4\pi}\mathbf{J} \cdot \widehat{\Omega} \tag{7.13}$$

$$\Sigma_s(\mathbf{r}, E' \to E, \widehat{\Omega}' \to \widehat{\Omega}) = \frac{1}{4\pi}\Sigma_{s,0}(\mathbf{r}, E' \to E) + \frac{3}{4\pi}\Sigma_{s,1}(\mathbf{r}, E' \to E)\widehat{\Omega} \cdot \widehat{\Omega}' \tag{7.14}$$

After substituting the truncated angular flux and scattering cross section in the above Boltzmann equation (7.10), and with help of the vectorial analysis formula given in Eq (7.15), we obtain a 3D transport equation (7.16) projected on the spherical harmonics basis ($L = 1$) without any other physical approximation.

$$\vec{\nabla}(\vec{A} \cdot \vec{B}) = (\vec{A} \cdot \vec{\nabla})\vec{B} + (\vec{B} \cdot \vec{\nabla})\vec{A} + \vec{A} \times (\vec{\nabla} \times \vec{B}) + \vec{B} \times (\vec{\nabla} \times \vec{A}) \tag{7.15}$$

$$\begin{aligned} &\widehat{\Omega} \cdot \vec{\nabla}\phi_0(\mathbf{r}, E) + 3\widehat{\Omega}(\widehat{\Omega} \cdot \vec{\nabla})\mathbf{J}(\mathbf{r}, E) + \Sigma_t(\mathbf{r}, E)\phi_0(\mathbf{r}, E) + 3\Sigma_t(\mathbf{r}, E)\mathbf{J}(\mathbf{r}, E) \cdot \widehat{\Omega} = \\ &\int_0^\infty \Sigma_{s,0}(\mathbf{r}, E' \to E)\phi_0(\mathbf{r}, E')dE' + 3\int_0^\infty \Sigma_{s,1}(\mathbf{r}, E' \to E)\mathbf{J}(\mathbf{r}, E) \cdot \widehat{\Omega}dE' + \frac{\chi(E)}{K_{eff}}Q_f(\mathbf{r}) \end{aligned} \tag{7.16}$$

In order to eliminate angular impact on the above Boltzmann equation, the integral of Eq (7.16) and Eq (7.16)$\times\hat{\Omega}$ are done over the whole solid angle 4π. Therefore, we obtain an ECCO-like flux-current coupled equation system (7.17).

$$\begin{cases} \vec{\nabla} \cdot \mathbf{J}(\mathbf{r}, E) + \Sigma_t(\vec{r}, E)\phi_0(\mathbf{r}, E) = \int_0^\infty \Sigma_{s,0}(\mathbf{r}, E' \to E)\phi_0(\mathbf{r}, E')dE' + \dfrac{\chi(E)}{K_{eff}}Q_f(\mathbf{r}) \\ \vec{\nabla}\phi_0(\mathbf{r}, E) + 3\Sigma_t(\mathbf{r}, E)\mathbf{J}(\mathbf{r}, E) = 3\int_0^\infty \Sigma_{s,1}(\mathbf{r}, E' \to E)\mathbf{J}(\mathbf{r}, E')dE' \end{cases} \tag{7.17}$$

The energy condensation work is then performed on the above equation system. The main idea of energy condensation has already been presented previously in Chapter 3. Here, we directly give the multi-group flux-current coupled equation system (7.18).

$$\begin{cases} \vec{\nabla} \cdot \mathbf{J}_g(\mathbf{r}) + \Sigma_{t0,g}(\mathbf{r})\phi_{0,g}(\mathbf{r}) = \sum\limits_{g'} \Sigma_{s,0}^{g' \to g}(\mathbf{r})\phi_{0,g'}(\mathbf{r}) + \dfrac{\chi_g}{K_{eff}}Q_f(\mathbf{r}) \\ \vec{\nabla}\phi_{0,g}(\mathbf{r}) + 3\Sigma_{t1,g}(\mathbf{r})\mathbf{J}_g(\mathbf{r}) = 3\sum\limits_{g'} \Sigma_{s,1}^{g' \to g}(\mathbf{r})\mathbf{J}_{g'}(\mathbf{r}) \end{cases} \tag{7.18}$$

One declaration is necessary while passing the second flux-current coupled equation from continuous-energy form to multi-group form. There is an implicit rule to respect which is the following one:

$$\int_{E \in g} \Sigma_t(\mathbf{r}, E)\mathbf{J}(\mathbf{r}, E)dE = \Sigma_{t1,g}(\mathbf{r})\mathbf{J}_g(\mathbf{r}) \tag{7.19}$$

Mathematically, the above relationship is not always available. However, it is used in our work to give out a consistent multi-group form equation system.

It should be pointed out that the index 0 beside the cross sections means that it is weighted by the scalar flux ϕ_0. On the other hand, the index 1 stands for current weighted cross sections. So, there are two different definitions of total multi-group cross sections $\Sigma_{t0,g}(\mathbf{r})$ and $\Sigma_{t1,g}(\mathbf{r})$ which appear in the above equations system. This is similar to the ECCO case: one kind of total cross section is weighted by scalar flux; the other is weighted by current. Since there is not yet an accurate estimation of volumetric current in TRIPOLI-4®, we choose to continue the development with the scalar flux weighted total cross section. Imposing the use of $\Sigma_{t0,g}(\mathbf{r})$ in both equations in system (7.18), it is necessary to modify the second equation containing $\Sigma_{t1,g}(\mathbf{r})$. This could be replaced as follows:

$$\vec{\nabla}\phi_{0,g}(\mathbf{r}) + 3\Sigma_{t0,g}(\mathbf{r})\mathbf{J}_g(\mathbf{r}) = 3\sum_{g'\neq g}\Sigma_{s,1}^{g'\to g}(\mathbf{r})\mathbf{J}_{g'}(\mathbf{r}) + 3\widetilde{\Sigma_{s,1}^{g\to g}}(\mathbf{r})\mathbf{J}_g(\mathbf{r}) \tag{7.20}$$

From Eq (7.20) we find that the first order in-scattering multi-group cross section is modified in comparison to its conventional form. An new definition of $\widetilde{\Sigma_{s,1}^{g\to g}}(\mathbf{r})$ is given in Eq (7.21).

$$\widetilde{\Sigma_{s,1}^{g\to g}} = \Sigma_{s,1}^{g\to g} + \Sigma_{t0,g} - \Sigma_{t1,g} \tag{7.21}$$

where $\Sigma_{t1,g}$ is obtained from Eq (7.19). The fact, modifying the first order of moment in the in-group scattering cross sections is later referred to in the text as *P1 in-group anisotropy correction technique*. It proves that from the continuous-energy anisotropy law to multi-group domain, in order to preserve neutron balance adequately, delicate treatment is indispensable even for the Monte-Carlo simulation code. This makes the production of the high order scattering matrix different when compared to other conventional multi-group constants.

In this section, the analytical deduction is limited to $L = 1$. Thus, the multi-group anisotropy correction is also limited to the first order scattering cross section. However, the development of the angular flux and the scattering production term could be extended into a higher order. This implies that to have an exact neutron balance relationship between point-wise calculation and multi-group calculation, the non-zeroth order of in-group scattering cross sections all need to be corrected as:

$$\widetilde{\Sigma_{s,l}^{g\to g}} = \Sigma_{s,l}^{g\to g} + \Sigma_{t0,g} - \Sigma_{tl,g} \tag{7.22}$$

where $\Sigma_{s,l}^{g\to g}$ and $\Sigma_{tl,g}$ are both weighted by the l^{th} order moment of angular flux $\phi_l(\vec{r}, E)$; and l could be any integer. Obtaining these high order moments of flux is indeed a challenge for Monte-Carlo simulation. For this reason, my work is limited to the *P1 in-group anisotropy correction technique*. Furthermore, the computational implementation in TRIPOLI-4® has also been carried out on it.

7.3 Algorithm Treatment in TRIPOLI-4®

From the previous section, we have demonstrated that the energy collapsing effect on the in-group anisotropy distribution law is different compared to other conventional cross

sections. It is concluded from the above demonstration that in order to preserve the neutron balance relationship between an original point-wise calculation and a later multi-group calculation, *P1 in-group anisotropy correction technique* should be incorporated in TRIPOLI-4®. Detailed development and algorithm treatment will be presented in this section. They are classified in four principal steps.

1. First of all, it is necessary to remind readers of the multi-group anisotropy representation format produced by TRIPOLI-4®. In fact, the directly produced anisotropy parameters by TRIPOLI-4® are not the scattering cross section moments $\Sigma_{s,l}^{g\to h}$ expected by deterministic transport core calculation codes. TRIPOLI-4® generates an angular deviation probability distribution function for every multi-group energy transfer $g \to h$. We note this probability distribution function as $f(\mu|g \to h)$. The variable μ stands for the cosine of deviation angle which belongs to the interval $[-1; 1]$. Please note here that the constructed distribution function by the point-wise TRIPOLI-4® simulation is in fact a discrete function which is divided by 20 equal sub-intervals between $[-1; 1]$. With this probability distribution function, we may derive any order moment of angular deviation μ_l as follows:

$$\mu_l^{g\to h} = \int_{-1}^{1} \mu^l f(\mu|g \to h) d\mu \tag{7.23}$$

In a point-wise TRIPOLI-4® simulation, it could yield directly the nice first orders of moments which will be noted as $< \mu^l >^{g\to h}$, $l = 0, 1, 2, \cdots, 8$. Surely, when $l = 1$, it is the conventional average value and usually marked as $\overline{\mu}$.

2. The next step is to figure out how to relate the previously mentioned *P1 in-group anisotropy correction technique* to the probability distribution function $f(\mu|g \to h)$. As the anisotropy correction is involved only for the in-group scattering, this means that we need to reform the function $f(\mu|g \to h)$ only if $g = h$. For the sake of space, from now on, we use the simplified notation $f(\mu)$ to specify the in-group anisotropy distribution function.

Another definition of the average scattering angle $\overline{\mu}$ exists which is expressed in Eq (7.24).

$$\overline{\mu}^{g\to g} = \frac{\int_{-1}^{1} \mu \Sigma_s^{g\to g}(\mathbf{r}, \mu) d\mu}{\int_{-1}^{1} \Sigma_s^{g\to g}(\mathbf{r}, \mu) d\mu} = \frac{\Sigma_{s1}^{g\to g}(\mathbf{r})}{\Sigma_{s0}^{g\to g}(\mathbf{r})} \tag{7.24}$$

With the above formula, we can establish a similar relationship between the corrected first moment of scattering cross section $\widetilde{\Sigma_{s,1}^{g\to g}}$ and the corrected average scattering angle $\widetilde{\overline{\mu}^{g\to g}}$. It is noted as follows:

$$\widetilde{\overline{\mu}^{g\to g}} = \frac{\widetilde{\Sigma_{s,1}^{g\to g}}}{\Sigma_{s0}^{g\to g}} \tag{7.25}$$

If we substitute Eq (7.22) for Eq (7.25), we obtain:

$$\widetilde{\overline{\mu}^{g\to g}} = \overline{\mu}^{g\to g} + \frac{\Sigma_{t0,g} - \Sigma_{t1,g}}{\Sigma_{s0}^{g\to g}} \tag{7.26}$$

3. Until now, we have derived a correction term that can be used to modify the original TRIPOLI-4® simulated average scattering angle cosine $\overline{\mu}^{g\to g}$. Focusing on the correction term $\Delta\overline{\mu}^{g\to g} = \frac{\Sigma_{t0,g} - \Sigma_{t1,g}}{\Sigma_{s0}^{g\to g}}$, $\Sigma_{t0,g}$ and $\Sigma_{s0}^{g\to g}$ could be easily calculated by a continuous-energy TRIPOLI-4® simulation. However, the problem is how to calculate the current weighted total cross section with the TRIPOLI-4® simulation.

As it was mentioned previously, we encounter difficulties in estimating exact volumetric current due to the cancelation between positive and negative values during a TRIPOLI-4® simulation. An approximation from Todorova is at first used. It supposes that the spectrum of the flux gradient is proportional to the spectrum of flux: $\vec{\nabla}\phi(\mathbf{r}, E) \propto \phi(\mathbf{r}, E)$. The second approximation used to estimate current with TRIPOLI-4® simulation is the Fick's law. Precisely stated, we use the following relationship: $D(\mathbf{r}, E) = \frac{1}{3\Sigma_{tr}(\mathbf{r}, E)} = \frac{1}{3\left[\Sigma_t(\mathbf{r}, E) - \overline{\mu}(E)\Sigma_s(\mathbf{r}, E)\right]}$. The third approximation is inherent from Eq (7.19) with which we are able to replace the current vector by its normal value $||\mathbf{J}||$.

These three approximations allow us to estimate an approximate current weighted multi-group total cross section $\Sigma_{t1,g}$ according to Eq (7.27).

$$\Sigma_{t1,g}(\mathbf{r}) = \frac{\int\limits_{E\in g} \Sigma_t(\mathbf{r}, E)\frac{\phi(\mathbf{r}, E)}{\Sigma_t(\mathbf{r}, E) - \overline{\mu}\Sigma_s(\mathbf{r}, E)}dE}{\int\limits_{E\in g} \frac{\phi(\mathbf{r}, E)}{\Sigma_t(\mathbf{r}, E) - \overline{\mu}\Sigma_s(\mathbf{r}, E)}dE} \tag{7.27}$$

Please note that $\Sigma_t(\mathbf{r}, E)\phi(\mathbf{r}, E)$ represents the physical parameter "*collision density*" which can be estimated by the simulation weight of the concerned neutron $\omega(\mathbf{r}, E)$. The latter is exactly the same as that used for estimating conventional multi-group parameters in TRIPOLI-4®. As for $\Sigma_t(\mathbf{r}, E)$ and $\Sigma_s(\mathbf{r}, E)$, they are both calculated from the continuous-energy input library which is related to the incident neutron and its existing medium. By the way, the point-wise scattering cross section is obtained indirectly through the relationship: $\Sigma_s(\mathbf{r}, E) = \Sigma_t(\mathbf{r}, E) - \Sigma_a(\mathbf{r}, E)$.

More attention should be paid on calculating the average cosine of scattering angle in the laboratory reference. The continuous-energy dependent average values of scattering angles for each medium (which is defined to be homogenized) must be known in Eq (7.27). They are calculated at the beginning of each continuous-energy TRIPOLI-4® simulation as follows:

$$\overline{\mu}(E) = \frac{\sum\limits_i \sum\limits_j N_i\sigma_{i,j}^s(E)\overline{\mu}_{i,j}(E)}{\sum\limits_i N_i\sigma_i^s(E)} \tag{7.28}$$

with

- N_i: the atomic concentration of isotope i;

- $\sigma_{i,j}^s(E)$: the microscopic cross section of scattering type j with nuclide i at energy E;

- $\sigma_i^s(E)$: the microscopic scattering cross section of nuclide i at energy E;

- $\overline{\mu}_{i,j}(E)$: the average value of all the possible scattering angles for scattering reaction type j with isotope i at energy E. It is obtained as follows: $\overline{\mu}_{i,j}(E) = \int_{-1}^{1} \mu \times f_{i,j}(\mu) d\mu$ where $f_{i,j}(\mu)$ is the point-wise angular distribution law from the data library. For the moment, accounted reaction types include: the elastic scattering and the discrete inelastic scattering. For other scattering reactions, $\overline{\mu} = 0$.

With the elements described above, an estimator for $\Sigma_{t1,g}(\mathbf{r})$ could be deduced as:

$$\Sigma_{t1,g}(\mathbf{r}) = \frac{\sum_i \omega(\mathbf{r}_i, E_i) \times \frac{1}{\Sigma_t(\mathbf{r}_i, E_i) - \overline{\mu}\Sigma_s(\mathbf{r}, E)}}{\sum_i \omega(\mathbf{r}_i, E_i) \times \frac{1}{\Sigma_t(\mathbf{r}_i, E_i) \times [\Sigma_t(\mathbf{r}_i, E_i) - \overline{\mu}\Sigma_s(\mathbf{r}_i, E_i)]}} \tag{7.29}$$

where i indicates the collisions whose initial position and incident energy $(\mathbf{r}_i, E_i)$ belong to the macro region (V, g).

After having presented the method of calculating multi-group first order moment of total cross section, it is natural to extend the energy condensation work toward the spatial homogenization step. If several different macro regions must be homogenized, it is sufficient to distinguish each different medium while registering scores. Therefore, the homogenized multi-group first order moment of total cross section is weighted by the approximate scalar current spatially as well as energetically.

4. With knowledge of $\Sigma_{t1,g}$ at the end of the TRIPOLI-4® continuous-energy simulation, we finally obtain the expected new anisotropy parameter $\widetilde{\overline{\mu}^{g\to g}}$ or its correction term $\Delta\overline{\mu}^{g\to g}$. As shown in Eq (7.23), this first order moment of scattering angular cosine is in fact the expectation value of μ respecting its distribution law $f(\mu)$. Unfortunately, this value could not be used directly in a multi-group TRIPOLI-4® simulation nor a deterministic core simulation. Therefore, the final implementation step is to adapt the output file containing (homogenized) multi-group constants from the TRIPOLI-4® point-wise simulation for a transport core simulation code, whether dealing with a Monte-Carlo domain or a deterministic domain.

Different output formats of the in-group anisotropy law will be presented in the following according to the demands of the multi-group TRIPOLI-4® simulation or S_n solver platform PARIS. They correspond respectively to discrete in-group angular scattering distribution probability or the non-zeroth order in-group scattering cross section matrix.

7.3.1 Consistent discrete in-group angular scattering distribution probability

After having simulated all the batches desired by users, the conventional multi-group parameters, such as $\Sigma_{t,g}$ and $\Sigma_{s0}^{g\to g}$ can be correctly estimated. Otherwise, $\Sigma_{t1,g}$ could also be estimated by the approximate scalar current. With Eq (7.26), we could deduce a corrective term for the average scattering angle cosine $\Delta\overline{\mu}^{g\to g}$. The problem to be solved in this part consists in determining how to allocate this single correction value among the 20-equal intervals between $[-1; 1]$. Two different distribution methods have been implemented in TRIPOLI-4®. One is named linear correction; the other is named Dirac correction. The common goal of these two correction methods is to figure out a

corrected distribution function $\widetilde{f}(\mu) = f(\mu) + \Delta f(\mu)$ which could answer the requests:

$$\begin{cases} \int_{-1}^{1} \left[f(\mu) + \Delta f(\mu)\right] d\mu = 1 \\ \\ \int_{-1}^{1} \mu \left[f(\mu) + \Delta f(\mu)\right] d\mu = \overline{\mu}^{g\to g} + \Delta\overline{\mu}^{g\to g} \end{cases} \tag{7.30}$$

Linear correction

The linear correction is based on the hypothesis that the correction function $\Delta f(\mu)$ is a linear function of μ which could be expressed as Eq (7.31).

$$\Delta f(\mu) = \alpha\mu + \beta \tag{7.31}$$

After substituting $\Delta f(\mu)$ for Eq (7.31) into requested conditions Eq (7.30), α and β are solved which result in: $\Delta f(\mu) = \dfrac{3}{2}\Delta\overline{\mu}^{g\to g}\mu$. Thus, the new distribution probability in each sub-interval I_i with $i = 1; 2; 3; \cdots 20$ could be obtained as follows:

$$\widetilde{P}(\mu \in I_i) = \int_{\mu\in I_i} \widetilde{f}(\mu)d\mu = P(\mu \in I_i) + \frac{3}{4}\Delta\overline{\mu}^{g\to g} \times (\mu_{i+1}^2 - \mu_i^2) \tag{7.32}$$

We could find that with this linear correction method, the corrective term $\Delta\overline{\mu}^{g\to g}$ impacts on all the sub-intervals but with different weights $(\mu_{i+1}^2 - \mu_i^2)$. A hidden risk with this linear correction method is that the value of $(\mu_{i+1}^2 - \mu_i^2)$ is negative for the lower-half range $[-1; 0]$. If the correction term $\Delta\overline{\mu}^{g\to g}$ is important enough, it could result in a non-physical phenomenon: $\widetilde{P}(\mu \in I_i) < 0$. If this case happens, the negative probability will be imposed to be zero.

In terms of physics, the correction term biases the high-energy neutrons toward the forward escaping direction. It is thus reasonable and possible to reduce the over-estimated K_{eff} value as in Tab 7.2. However, the same effect could perform on low-energy neutrons which are also biased toward the forward escaping direction. The problem is that the forward biasing effect on low-energy neutrons does not represent the real case for a nuclear reactor. In order to overcome the negative probability shortcoming, another anisotropy correction method will be presented just below.

Dirac-like correction

The Dirac-like correction is inspired from the single peak form of Dirac function. Instead of imposing the positive correction effects on all the half of sub-intervals $[0; 1]$, the Dirac-like correction focuses only on the last bin $[0.9; 1]$ which represents the best chance to escape for neutrons. Based on this idea, the corrected anisotropy distribution function take the form as in Eq (7.33).

$$\widetilde{f}(\mu) = \alpha f(\mu) + \beta\delta_{\mu_0}(\mu) \tag{7.33}$$

where μ_0 indicates the peak position of the Dirac function and could be any value in the last interval $[0.9; 1]$. For the following deduction, we use $\mu_0 = 1$.

The above Dirac correction function must always satisfy the two conditions in Eq (7.30). This helps us to obtain: $\alpha = 1 - \beta = \dfrac{1 - \widetilde{\overline{\mu}^{g\to g}}}{1 - \overline{\mu}^{g\to g}}$. Thus, the corrected function is found to be:

$$\widetilde{f}(\mu) = \frac{1 - \widetilde{\overline{\mu}^{g\to g}}}{1 - \overline{\mu}^{g\to g}} f(\mu) + \frac{\Delta\overline{\mu}^{g\to g}}{1 - \overline{\mu}^{g\to g}} \delta_{\mu_0}(\mu) \tag{7.34}$$

The same procedure is then performed again as in the case of the linear correction case. We can calculate the new distribution probability for each sub-interval according to Eq (7.34):

$$\widetilde{P}(\mu \in I_i) = \int\limits_{\mu\in I_i} \widetilde{f}(\mu) d\mu = \begin{cases} \dfrac{1 - \widetilde{\overline{\mu}^{g\to g}}}{1 - \overline{\mu}^{g\to g}} P(\mu \in I_i); & \text{for i} = 1; 2; \cdots; 19 \\ \dfrac{1 - \widetilde{\overline{\mu}^{g\to g}}}{1 - \overline{\mu}^{g\to g}} P(\mu \in I_i) + \dfrac{\Delta\overline{\mu}^{g\to g}}{1 - \overline{\mu}^{g\to g}}; & \text{for i} = 20 \end{cases} \tag{7.35}$$

In a normal case, the corrected average cosine value of scattering angle is more important than the original $\widetilde{\overline{\mu}^{g\to g}} > \overline{\mu}^{g\to g}$. The latter relationship ensures that $\dfrac{1 - \widetilde{\overline{\mu}^{g\to g}}}{1 - \overline{\mu}^{g\to g}} < 1$. It could tell that the Dirac-like correction tries to overbalance a certain portion of probability from the first 19 sub-intervals $[-1; 0.9]$ into the last one $[0.9; 1]$. This processing technique shares the same objective as the previous linear correction method. Its advantage is that it reduces to a great extent the risk of getting a negative probability value for any sub-interval.

There is one possible situation where the negative probability problem persists. This happens when $\widetilde{\overline{\mu}^{g\to g}} > 1$. Even though it is non-sense to use an averaged cosine value higher to 1, this embarrassing case might be encountered, for example, when the current weighted multi-group total cross section is inferior to the flux weighted multi-group absorption cross section $\Sigma_{t1,g} < \Sigma_{a,g}$. There is no specific condensation rule declaring that the relationship $\Sigma_{t1,g} > \Sigma_{a,g}$ should be necessarily reached. That is why even for the validated lattice calculation code ECCO, it could happen to have the below relationship: $|\Sigma_{s1}^{g\to g}| > |\Sigma_{s0}^{g\to g}|$.

7.3.2 Consistent high-order in-group scattering cross section matrix

The original motivation of this work is to supply appropriate homogenized multi-group constants to deterministic calculation codes. In addition, we focus on feeding transport core calculation codes, such as PARIS. In order to be able to run a deterministic transport core simulation taking the anisotropy effect into consideration, we need the non-zeroth order group scattering cross sections. Generally, the higher-order scattering matrix elements could be obtained via the 0^{th} order ones as shown in Eq (7.36)

$$\Sigma_{sl}^{g\to h} = \Sigma_{s0}^{g\to h} \times \int\limits_{-1}^{1} P_l(\mu) \times f(\mu)^{g\to h} d\mu \tag{7.36}$$

where $P_l(\mu)$ is the l^{th} order moment of Legendre Polynomial and could be expressed as follows:

$$P_l(\mu) = \sum_{i=0}^{l} \alpha_i \mu^i \tag{7.37}$$

with α_i, each order associated normalization factor. The values used in this work are from Reuss's book[17].

Note that group h could be different or the same as group g in Eq (7.36). Actually, for in-group scattering $g = h$, the anisotropy distribution law is corrected according to Section 7.3.1. Therefore, we specify this in-group transfer case as follows:

$$\Sigma_{sl}^{g\to g} = \Sigma_{s0}^{g\to g} \times \int_{-1}^{1} P_l(\mu) \times \widetilde{f}(\mu)^{g\to g} d\mu \tag{7.38}$$

Substituting Eq (7.37) in Eq (7.38), and with knowledge of the nine first orders of moments of μ which are directly simulated by point-wise TRIPOLI-4®, we finally obtain:

$$\Sigma_{sl}^{g\to g} = \Sigma_{s0}^{g\to g} \times \sum_{i=0}^{l} \alpha_i \widetilde{<\mu>^i}^{g\to g} \tag{7.39}$$

with $\widetilde{<\mu>^i}^{g\to g}$: the corrected i^{th} order of moment for group g to itself.

Finally, a new multi-group anisotropy distribution law could be calculated by TRIPOLI-4® and its necessary routines are also implemented. Therefore, new calculations are performed on the previous almost-critical SPX2 geometry illustrated in Figure 7.1. Improvement (emphasized in red) could be observed on both K_{eff} value (Table 7.6) and multi-group anisotropy parameters (Table 7.7). The next step is to validate it with other geometries which forms the topic of the next section.

Case	K_{eff}	ΔK_{eff}
TRIPOLI-4® PCT	1.01796 (9)	0
P0_TOTAL/ERANOS	1.01550	-246 (9)
TRIPOLI-4® HMG(6GR)	1.02642(12)	+846(15)
TRIPOLI-4® corr HMG(6GR)	1.01771(12)	−25(15)

Table 7.6: SPX2 geometry calculation results from TRIPOLI-4® (before/after anisotropy correction) and ECCO/ERANOS simulations.

$\overline{\mu}^{g\to g}$	$1\to 1$	$2\to 2$	$3\to 3$	$4\to 4$	$5\to 5$	$6\to 6$
TRIPOLI-4®	0.432	0.261	0.087	0.034	0.019	0.014
ECCO(P0_TOTAL)$^{\circledast}$	0.436	0.258	0.087	0.032	0.017	0.014
TRIPOLI-4® corr	0.441	0.277	0.127	0.110	0.126	0.109
ECCO(P0_TOTAL)	0.445	0.275	0.126	0.114	0.125	0.114

Table 7.7: $\overline{\mu}^{g\to g}$ values obtained for SPX2 geometry under TRIPOLI-4® & ECCO simulations with 6-groups energy structure. $\circledast$: without change of $\Sigma_{s1}^{g\to g}$

7.4 Validation of In-Group Scattering Anisotropy Treatment

In this section, the In-group Scattering Anisotropy Treatment method is applied to various types of reactor cores or criticality experiments in order to validate its performance. The selected configurations are namely: three 1D homogeneous ISCBEP[2] benchmarks HMF-001, HMF-004, PMF-001; four 2D homogeneous configurations SNEAK7A-RZ, ZONA2A-RZ[38], ZONA2B-RZ[38], SuperPhénix-Pipaud-RZ; two 3D heterogeneous reactor cores MASURCA-1B[15] and SuperPhenix[39]. More descriptions are given in the following list:

- HMF-001: A highly uranium enriched bare sphere, also called GODIVA; criticality experiment
- HMF-004: A highly uranium enriched sphere reflected by H_2O
- PMF-001: A plutonium bare sphere, also named JEZEBEL
- SNEAK7A-RZ (IRPHE)[9]: A critical fast reactor type mock-up without sodium; composed of the MOX and graphite
- ZONA2A-RZ: A simplified RZ model with radial and axial blankets from CIRANO program in the mock-up of MASURCA
- ZONA2B-RZ: A simplified RZ model with steel-reflector and without blanket from the CIRANO program in the mock-up of MASURCA
- SuperPhénix-Pipaud-RZ: A simplified RZ model of sodium-cooled fast reactor SuperPhénix, with inserted control rods
- MASURCA-1B: A mock-up in the core of MASURCA with 30% of ^{235}U, FeO and graphite.
- SuperPhenix[39]: A 3D sodium-cooled fast reactor whose geometry description will be given out in Appendix C.

The validation procedure is the same as illustrated in Figure 6.8. For each configuration, a continuous-energy TRIPOLI-4® simulation is at first done to obtain In-Group Anisotropy Corrected homogenized multi-group constants as well as the reference results (K_{eff}, flux spectrum, neutronic balance). It should be noted here that the homogenization weighting function is naturally the same as the one used for energy condensation. This means that for the first moment of multi-group total cross section, the approximative current is used for both homogenization and energy condensation; while the flux is used for other multi-group constants. Then, the produced homogenized multi-group constants are used in the multi-group TRIPOLI-4® simulations. Comparisons between the two calculation steps above could help us to validate the In-Group Scattering corrected multi-group constants.

As for the number of regions to be homogenized, it varies according to each different case. For the three ISCBEP one-dimensional critical spheres and the four two-dimensional simplified RZ models, they are naturally homogeneous in each distinguished region, thus TRIPOLI-4® only needs to perform energy condensation work. For the two heterogeneous 3D cores, homogenization work is carried out at the same time as energy collapsing.

The same TRIPOLI-4® point-wise to multi-group calculation procedures are repeated but without use of the new anisotropy treatment method. Thus, a comparison between these two types of calculations will show the effects of the In-Group Scattering Correction method which will be noted as IGSC for the following text. Table 7.8 and Table 7.9 show respectively the K_{eff} results of all the tested cases under 6-group and 33-group. In each table, the column "K_{eff} PCT" contains the reference values with their own standard deviation in units of pcm. The column "K_{eff} HMG" stands for multi-group TRIPOLI-4® simulation without use of IGSC technique. On the other hand, "K_{eff} HMG IGSC" means multi-group simulation with the use of IGSC. The two last columns are respectively their discrepancies compared to the point-wise value.

case	K_{eff} PCT	K_{eff} HMG	K_{eff} HMG IGSC	ΔK_{eff}(pcm)	ΔK_{eff} IGSC(pcm)
HMF001	0.99678(0.4)	0.99974(6)	0.99689(6)	+296(6)	+11(6)
HMF004	0.99530(1.8)	0.99979(10)	0.99351(12)	+449(10)	-192(11)
PMF001	1.00020(0.4)	1.00189(2)	1.00010(2)	+169(2)	-10(2)
SNEAK7A	1.00665(4)	1.01312(9)	1.00617(9)	+647(10)	-49(10)
ZONA2A	1.00832(4)	1.01556(9)	1.00625(6)	+724(10)	-207(10)
ZONA2B	1.00941(5)	1.02824(9)	0.99049(9)	+1883(10)	-1892(10)
SPX Pipaud	1.05965(6)	1.06383(9)	1.05935(9)	+418(11)	-60(11)
MAS1B	1.00333(5)	1.03246(10)	1.00707(10)	+2913(11)	+374(11)
SPX	1.00424(5)	1.00798(8)	0.94989(8)	+374(9)	-5435(9)

Table 7.8: K_{eff} values from 6-group TRIPOLI-4® simulations with and without IGSC correction method compared to continuous energy TRIPOLI-4® simulation (NJOY option)

case	K_{eff} PCT	K_{eff} HMG	K_{eff} HMG IGSC	ΔK_{eff}(pcm)	ΔK_{eff} IGSC(pcm)
HMF001	0.99678(0.4)	0.99777(6)	0.99736(6)	+99(6)	+58(6)
HMF004	0.99530(1.8)	0.99338(11)	0.99127(9)	-192(11)	-403(9)
PMF001	1.00020(0.4)	1.00093(3)	1.00067(2)	+73(2)	+47(2)
SNEAK7A	1.00665(4)	1.01018(9)	1.00511(9)	+353(10)	-155(10)
ZONA2A	1.00832(4)	1.01331(9)	1.00577(9)	+499(10)	-255(10)
ZONA2B	1.00941(5)	1.02244(9)	0.99022(9)	+1303(10)	-1919(10)
SPX Pipaud	1.05965(6)	1.06279(9)	1.05939(9)	+314(11)	-26(11)
MAS1B	1.00333(5)	1.02864(10)	1.00784(10)	+2531(11)	+451(11)
SPX	1.00424(5)	1.00646(8)	0.95941(8)	+222(9)	-4483(9)

Table 7.9: K_{eff} values from 33-group TRIPOLI-4® simulations with and without IGSC correction method compared to continuous energy TRIPOLI-4® simulation (NJOY option)

At first, the results under 6-groups show that flux-weighted anisotropy law results into an over-estimation of K_{eff}. However, the IGSC method helps decrease efficiently the discrepancies of K_{eff} between multi-group and continuous-energy TRIPOLI-4® simulations in most cases. Two exceptions exist in the ZONA2B and SPX configurations which are marked in red. In ZONA2B core simulation, the IGSC method has under-estimated the multiplicative factor by about 2000 pcm instead of an over-estimation of 1883 pcm without use of the IGSC method. This means that the IGSC method is not at all suitable for the ZONA2B case. The problem is related to its steel-reflective boundary[77]. Because of its important heterogeneities located on the two sides of the steel boundary, more deli-

cate treatment is necessary for the sub-assembly homogenization around the fuel-reflector interface. It was investigated by Jacquet in his Ph.D. thesis [77]. Another exception is found in the SuperPhénix case. This important discrepancy (-5483 pcm) will be analyzed in the next chapter.

Our attention now moved now to the 33-groups results. It is confirmed that the flux-weighted energy condensation method has always over-estimated K_{eff} values except for one case of HMF-004. However, the quantities over-estimated under the 33-group are less important than under the 6-group. This was predicted by Rhanema[79] who pointed out that a more refined energy structure could yield a better core calculation result. An illusion is found while comparing the 6-groups and 33-groups multi-group simulation results using the IGSC method: the results from 6-groups are closer to reference values than the 33-groups results. This abnormal phenomenon will be explained by a further analysis on the neutronic balance. In the following paragraph, we shall take SNEAK7A-RZ as an example to carry out a detailed analysis on its flux spectrum and neutron balance.

7.4.1 Flux spectrum analysis

Figure 7.2 is a vertical cutting cross section of a simplified RZ model of the SNEAK7A reactor. It is divided into three homogeneous media: inner-core (yellow part); outer-core (purple part) and blanket (red part). Multi-group constants are generated for each medium. Thus, only energy condensation work is involved in this case.

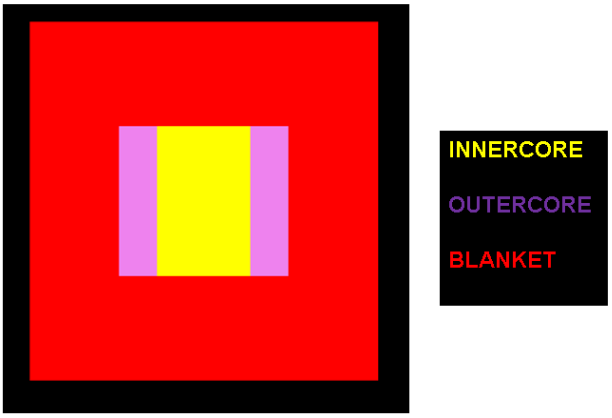

Figure 7.2: Illustration scheme for SNEAK7A-RZ core

As the core is composed of three parts, the flux spectrum analysis is naturally carried out within each medium. The results are given in Figure 7.3 to Figure 7.8. The first three figures correspond to 6-group calculation results while the others correspond to the 33-group flux analysis. For all of them, the left parts in the figures noted as a) are the reference flux spectra calculated by point-wise TRIPOLI-4® simulations with the NJOY data library. And the right parts noted as b) are the relative differences of flux expressed in percentages between multi-group and point-wise simulations.

It should be pointed out that there are two kinds of comparisons in our analysis. First of all, a discrepancy between a multi-group simulation calculated flux spectrum and a

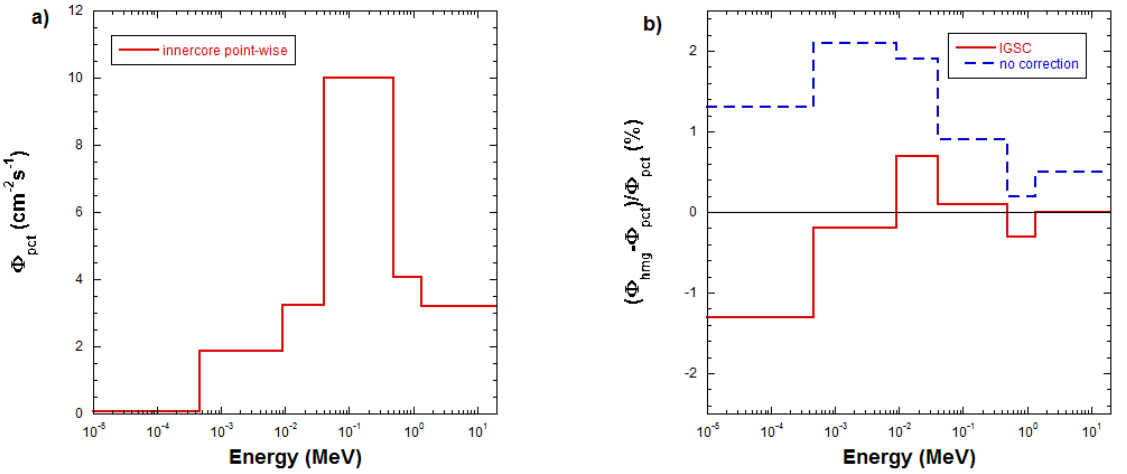

Figure 7.3: **a)**: 6-groups flux spectrum reference in innercore of SNEAK7A from continuous-energy TRIPOLI-4® simulation (NJOY) **b)**: Relative differences of flux spectra between multi-group TRIPOLI-4® simulation results (with use and without use of IGSC method) and the reference spectrum (left figure)

point-wise simulation calculated spectrum could indicate whether or not the produced multi-group constants are able to reproduce the consistent flux spectrum in a transport core simulation. The second comparison consists in analyzing the different discrepancies while using different multi-group constants calculated by different methods (IGSC or non-IGSC). The latter could help us to select the method which is more appropriate for producing multi-group constants from the point of view of a core simulation. By the way, the In-Group Scattering Correction method used in this chapter to produce corrected multi-group anisotropy parameters makes use of the linear correction technique presented in Section 7.3.1. In fact, for most of cases, there is no difference between the linear correction and Dirac correction techniques.

It must be mentioned here that, we do not give the standard deviations associated to flux spectra because the simulation results are well converged. For example, in the energy groups where there is an important neutron population, the relative standard deviation of neutron flux is less than 0.1%. Let us start with the 6-group flux analysis. Within all three media, the neutron energy distributions are similar owing to the fact that the majority of neutrons are found in the 3^{rd} group between [41; 498] keV. So, attention is moved to their relative differences plotted in Figure b). They show that the IGSC method brings the relative discrepancies closer to 0 compared to the situation where no correction is done for the multi-group anisotropy law. This is especially true in the energy domain where there is an important neutron population. Otherwise, in the 6^{th} energy group, the relative differences whether the IGSC method is used or not significantly greater compared to high energy groups. This phenomenon is normal because in the lowest energy group the statistical error is rather important.

As for the 33-group results, a more accurate flux spectrum is formed in each medium which could be found from Figure 7.6 to Figure 7.8. The three reference spectra look like a Maxwellian distribution function with the peak situated at around 0.2 MeV. In the inner-core and outer-core regions, we find a self-shielding phenomenon at 400 keV which

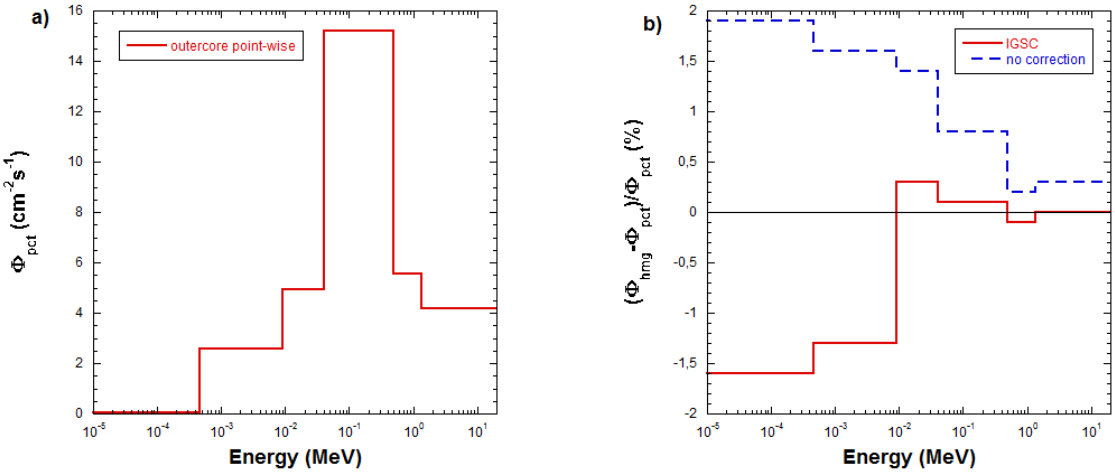

Figure 7.4: **a)**: 6-groups flux spectrum reference in outercore of SNEAK7A from continuous-energy TRIPOLI-4® simulation (NJOY) **b)**: Relative differences of flux spectra between multi-group TRIPOLI-4® simulation results (with use and without use of IGSC method) and the reference spectrum (left figure)

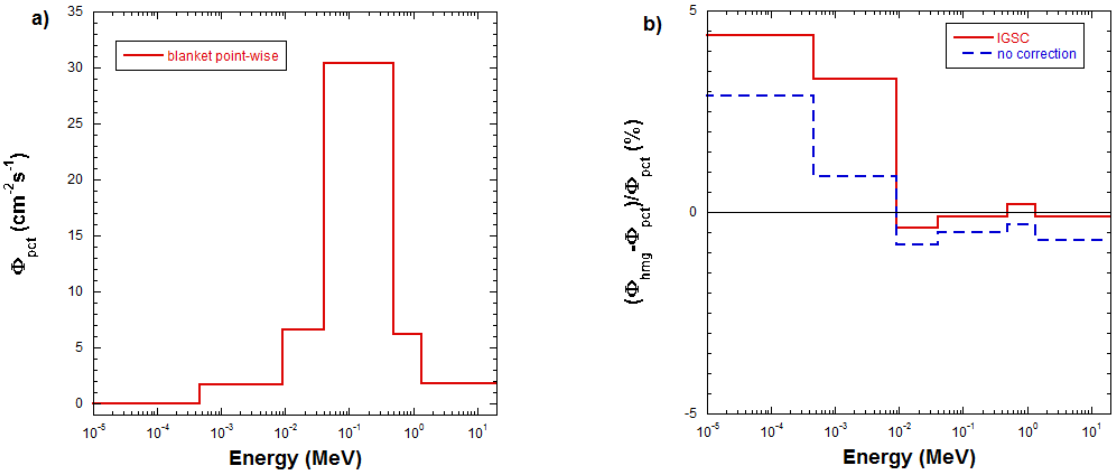

Figure 7.5: **a)**: 6-groups flux spectrum reference in blanket of SNEAK7A from continuous-energy TRIPOLI-4® simulation (NJOY) **b)**: Relative differences of flux spectra between multi-group TRIPOLI-4® simulation results (with use and without use of IGSC method) and the reference spectrum (left figure)

results from the resonance of oxygen. If we have a look at Figures b), compared to the 6-group cases, even more important discrepancies are found at the low energy domain. This could always be explained by the reason of lack of neutron statistics in low energy transfers. The more the energy structure is refined, the greater the statistical errors show up in the low energy groups.

Thus, more attention needs to be paid to the gray energy intervals as marked in figures a). 95% of neutron production occurs in this selected energy zone. The relative difference within this energy domain is zoomed specially in the comparison of Figures b). From the

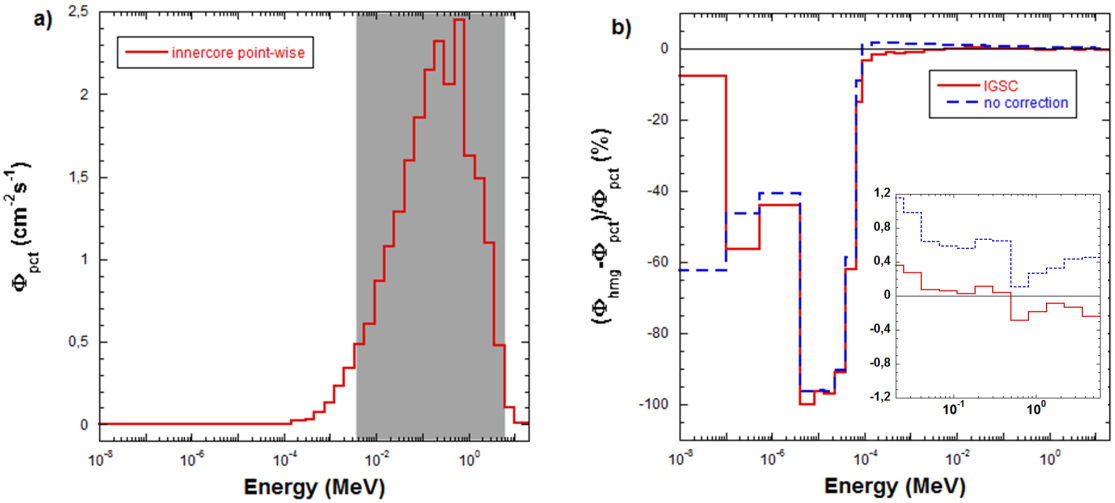

Figure 7.6: **a)**: 33-groups flux spectrum reference in innercore of SNEAK7A from continuous-energy TRIPOLI-4® simulation (NJOY) **b)**: Relative differences of flux spectra between multi-group TRIPOLI-4® simulation results (with use and without use of IGSC method) and the reference spectrum (left figure)

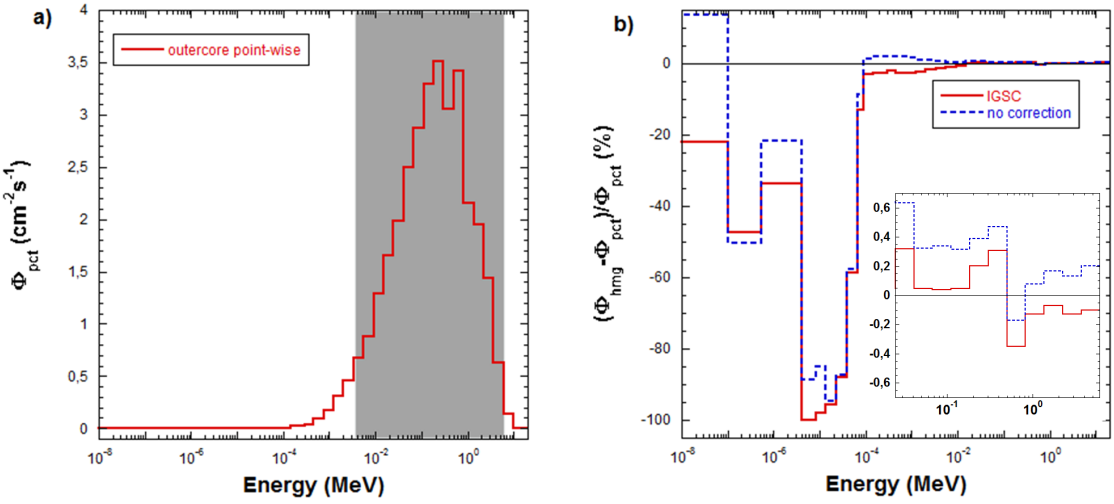

Figure 7.7: **a)**: 33-groups flux spectrum reference in outer-core of SNEAK7A from continuous-energy TRIPOLI-4® simulation (NJOY) **b)**: Relative differences of flux spectra between multi-group TRIPOLI-4® simulation results (with use and without use of IGSC method) and the reference spectrum (left figure)

zoom windows (covering the range of [2.49 keV; 6 MeV]), it is confirmed that the IGSC method efficiently reduces the discrepancies of flux spectra in a core calculation. However, an exception stands out in the 7^{th} group representing the energy interval of [500; 800] keV. For this energy group, the relative difference from the IGSC method has significantly exceeded the result without use of any correction. This occasional inconsistency comes probably from the approximative estimation of the current weighted total multi-group cross section described in Eq (7.29).

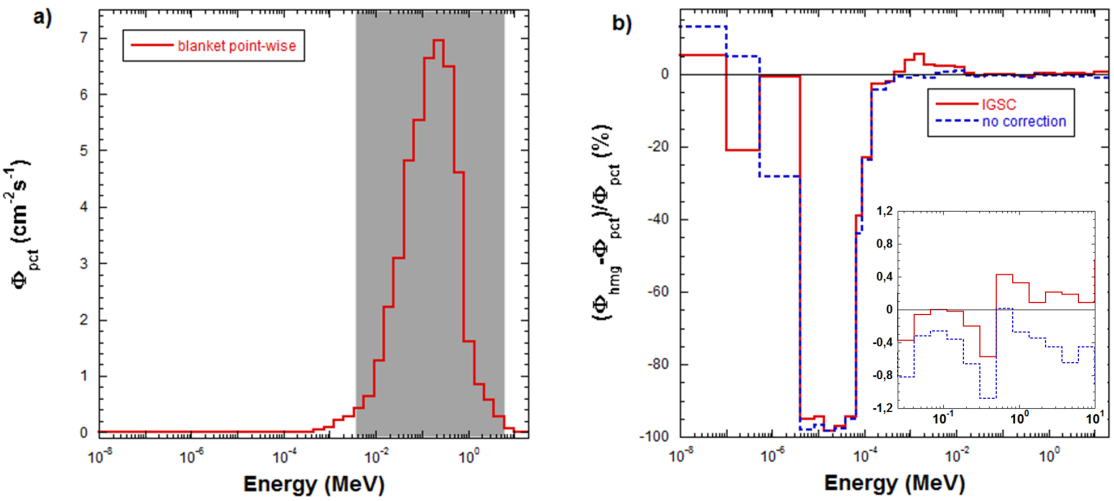

Figure 7.8: **a)**: 33-groups flux spectrum reference in blanket of SNEAK7A from continuous-energy TRIPOLI-4® simulation (NJOY) **b)**: Relative differences of flux spectra between multi-group TRIPOLI-4® simulation results (with use and without use of IGSC method) and the reference spectrum (left figure)

7.4.2 Neutronic balance analysis

In this section, neutronic balance is to be compared between the multi-group and point-wise TRIPOLI-4® simulations. Let us bear in mind that two kinds of multi-group calculations are performed in our tests. One makes use of the multi-group constants produced by the IGSC method which corrects the multi-group anisotropy law. The other one simply uses the non-corrected multi-group constants which are weighted by scalar flux.

Figure 7.9 shows the 33-group production rate discrepancies in two different situations. Part **a)** corresponds to use the IGSC method, while Part **b)** stands for non-use of any correction method. Both parts of Figure 7.9 contain the comparison associated with every medium as well as the whole core. If we at first pay attention to the inner-core (black line) and outer-core (blue dashed line) parts, it can be seen that the non-corrected multi-group constants have a tendency to over-estimate the production rate in a multi-group simulation. Moreover, the over-estimated production rates cover a rather large energy range from [750 eV; 3.68 MeV]. With the use of the IGSC method, the discrepancies in the two fissile media decrease, in particular in the inner-core part. In the outer-core region, the improvement of the production rate balance from the IGSC method seems less important compared to the inner-core region. However, the energy range of the residual discrepancies is limited to [454 eV; 9 keV]. As for the blanket fertile medium, using the non-corrected multi-group constants results in an under-estimation peak at around 2.5 MeV. This negative peak ($\sim$ 16 pcm) is lifted up by the IGSC method into a shaper and lower positive one. Finally, in the whole core, the over-estimation tendency of production rate difference with the use of the non-corrected multi-group constants has been more or less balanced with the help of the IGSC method. An over-corrected effect is found in the 7^{th} group. This negative difference $\sim$ 20 pcm results from the under-estimation of flux in

the same group. All in all, the IGSC method decreases the total discrepancy of production rate from +351 pcm to −157 pcm.

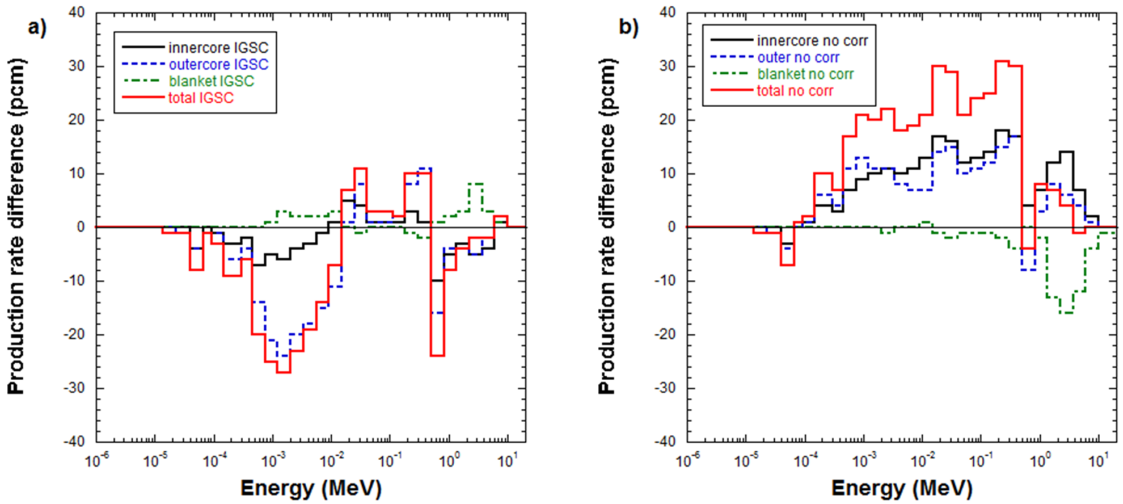

Figure 7.9: **a)**: Production rate comparisons between 33-groups (with use of IGSC method) and point-wise (NJOY) TRIPOLI-4® simulations in each medium of core SNEAK7A-RZ **b)**: Production rate comparisons between 33-groups (without use of IGSC method) and point-wise (NJOY) TRIPOLI-4® simulations in each medium of core SNEAK7A-RZ

We continue to analyze the absorption rate in the SNEAK7A simplified core. The differences between multi-group and point-wise simulations are plotted in Figure 7.10 in two different cases. Part **a)** represents the improved results with the aid of the IGSC method compared to Part **b)** using non-corrected anisotropy parameters in multi-group simulation. Efficient positive impact from the IGSC method is confirmed in the inner-core domain where we could tell that the absorption rate differences are very close to 0 with use of IGSC produced multi-group constants. A less efficient effect is revealed in the outer-core. Especially in low energy range [750 eV; 15 keV], the IGSC method seems to reverse the positive differences into negative ones. Globally, the discrepancies calculated with the IGSC method are much closer to zero line. This means that the IGSC method produced multi-group constants are better adapted in a multi-group simulation and preserve the absorption rate better compared to point-wise results.

In the SNEAK7A-RZ simplified core model, surely the neutron escapes from the most external boundary side. Thus the leakage rate will only be accounted for in the blanket. Figure 7.11 illustrates the leakage rate comparisons under conditions of use (green line) and non-use (yellow line) of the IGSC method. It could be clearly seen that the usage of IGSC method help to reduce the leakage discrepancies compared to non-use of the IGSC method. It is proved again that IGSC method could produce the anisotropy corrected multi-group constants which preserve the neutron balance better.

At the end of this section, we shall answer the question asked earlier: why do the 6-group calculated multiplicative factor results ($\Delta K_{\text{eff}} = -49 \pm 10$ pcm) seem better than the 33-group results ($\Delta K_{\text{eff}} = -155 \pm 10$ pcm)? The answer is indeed hidden in Figure 7.12. The red curve representing the 6-group leakage rate discrepancy shows an important compensation effect between the 4^{th} and 5^{th} energy groups. It is also with this

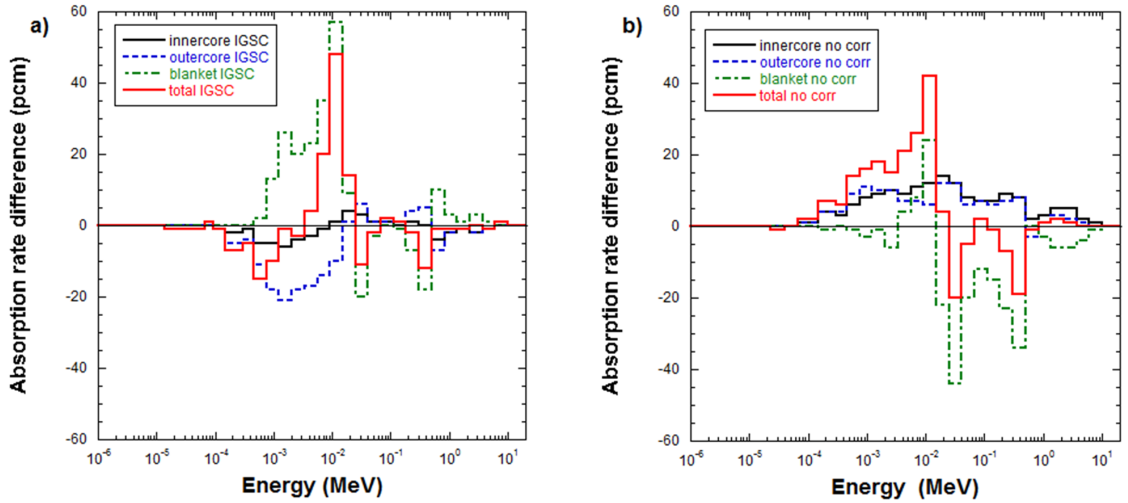

Figure 7.10: **a)**: Absorption rate comparisons between 33-group (with use of IGSC method) and point-wise (NJOY) TRIPOLI-4® simulations in each medium of core SNEAK7A-RZ **b)**: Absorption rate comparisons between 33-group (without use of IGSC method) and point-wise (NJOY) TRIPOLI-4® simulations in each medium of core SNEAK7A-RZ

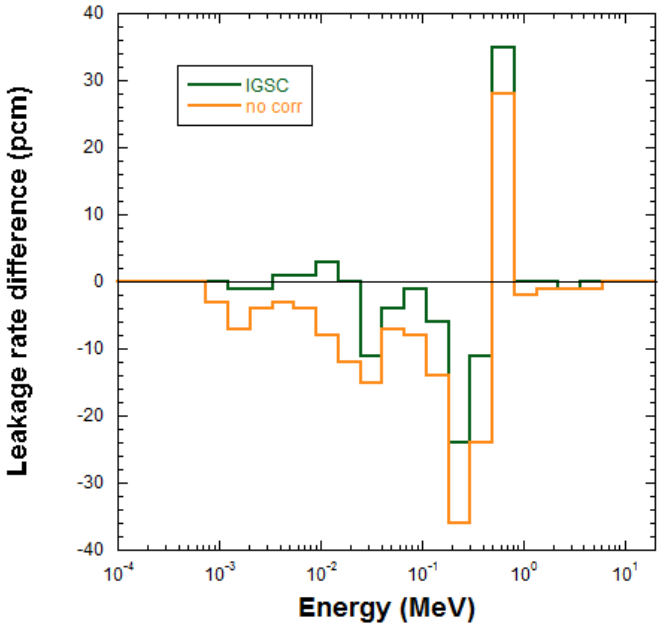

Figure 7.11: Leakage rate comparisons between 33-group (with/without use of IGSC method) and point-wise (NJOY) TRIPOLI-4® simulations in blanket medium

compensation effect that the 6-group calculation gives the illusion of estimating a better K_{eff} value.

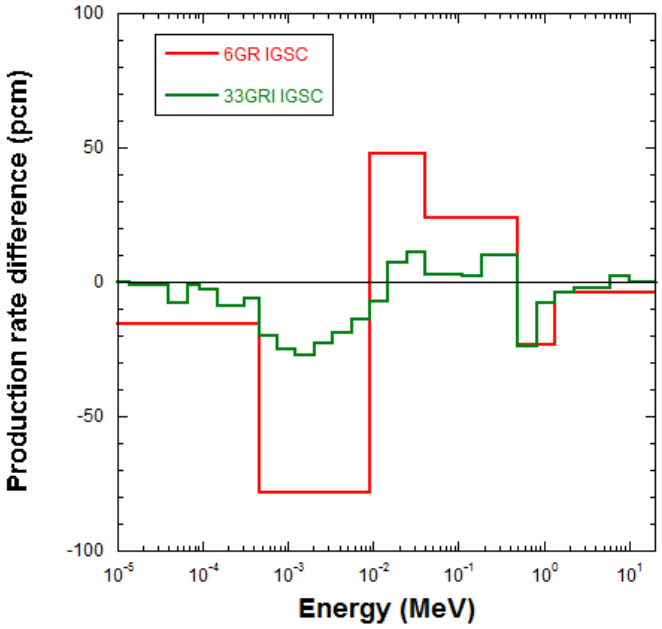

Figure 7.12: Total production rate differences between multi-group (with use of IGSC) and point-wise (NJOY) TRIPOLI-4® simulations

Conclusion

In this chapter, the lattice calculation ability is extended to account for the neutron leakage effect. This is a big step toward a more realistic representation of a reactor core compared to the lattice calculation used in Chapter 6. It should be noted that the concept of handling the leakage effect here is totally different from the conventional way, for example, using the B1 homogeneous leakage model. We tried to construct an almost-critical geometry to be tested by the TRIPOLI-4® code. This naturally critical lattice calculation could avoid the approximations used by a theoretical leakage model and takes advantage of the good precision of the Monte-Carlo simulation.

This work proves that in order to preserve exactly neutron balance from point-wise to multi-group calculations, an indispensable treatment (IGSC) should be performed to build up an appropriate multi-group anisotropy representation. Two different processing techniques are proposed by the author to adapt the IGSC method in the TRIPOLI-4® code.

The multi-group constants produced by the IGSC method are validated in two different ways. The first one is to compare them directly with the ECCO calculated multi-group constants. The second one is to use them in a multi-group transport simulation and then compare the key reactor features (K_{eff}; flux spectrum and neutronic balance) between the multi-group simulation and the reference results. Results of the comparison show that the IGSC method is generally able to produce appropriate multi-group constants for a core transport calculation. However, some exceptions happen when we treat a heterogeneous lattice which contains a diffusive nucleus, such as sodium in the SuperPhénix heterogeneous core. This highly diffusive problem will be diagnosed in the following chapter.

Chapter 8

Heterogeneous problem in lattice calculation

The previous chapter has shown that the scalar flux weighted multi-group constants could not guarantee the preservation of the effective multiplication factor from continuous-energy to multi-group Monte-Carlo calculations. Then, it has been demonstrated that this inconsistency originates from the neutron anisotropy phenomenon which is finally induced by the neutron leakage effect. A solution is proposed which aims to reconstruct the multi-group anisotropy distribution law. It is named by the author as the In-Group Scattering Correction (IGSC) method, and is tested by various configurations including one-dimensional, two-dimensional homogeneous geometries and three-dimensional heterogeneous geometries. Most of the tested cases prove that the IGSC method is able to produce appropriate multi-group constants which are then used in a transport core calculation code and give consistent results compared to the point-wise TRIPOLI-4® simulation results. However, two exceptions were encountered in the 2D ZONA2A-RZ reactor core model and the 3D realistic Superphénix core. The present chapter focuses on understanding and solving this problem.

8.1 Problem introduction

Table 8.1 helps us recall the difficulties we are confronted with in the two special cases using the IGSC method produced multi-group constants. The brackets in the below table contain the standard deviations in units of pcm. And ΔK_{eff} stands for the differences (in pcm) between multi-group TRIPOLI-4® simulations and their reference values.

case	K_{eff} reference NJOY		ΔK_{eff} IGSC(pcm)	ΔK_{eff} no corr (pcm)
SuperPhenix	6-GR	1.00748 (5)	-5483 (22)	+377 (13)
	33-GR	1.00739 (4)	-4459 (6)	+331 (6)
ZONA2B-RZ	6-GR	1.00941 (5)	-1892 (10)	+1883 (10)
	33-GR	1.00941 (5)	-1919 (10)	+1303 (10)

Table 8.1: K_{eff} comparisons between multi-group (with/without use of the IGSC method) and point-wise (NJOY) TRIPOLI-4® simulations of SuperPhénix and ZONA2B-RZ cores

The noticeable multiplicative factor discrepancies which are emphasized in red claim that the IGSC method is not at all adapted for the SuperPhénix reactor nor is it suitable

for ZONA2B-RZ model either. In order to explain why the IGSC method behaves differently in these two cases, several questions come to the mind: **1)** Are there some common points (geometry or isotope composition) between the SuperPhénix core and the ZONA2B simplified model? If so, could these common points induce the inconsistent results? **2)** What are the approximations used in the IGSC method which could potentially make mistakes for these two cases? **3)** How can these problems be identified?

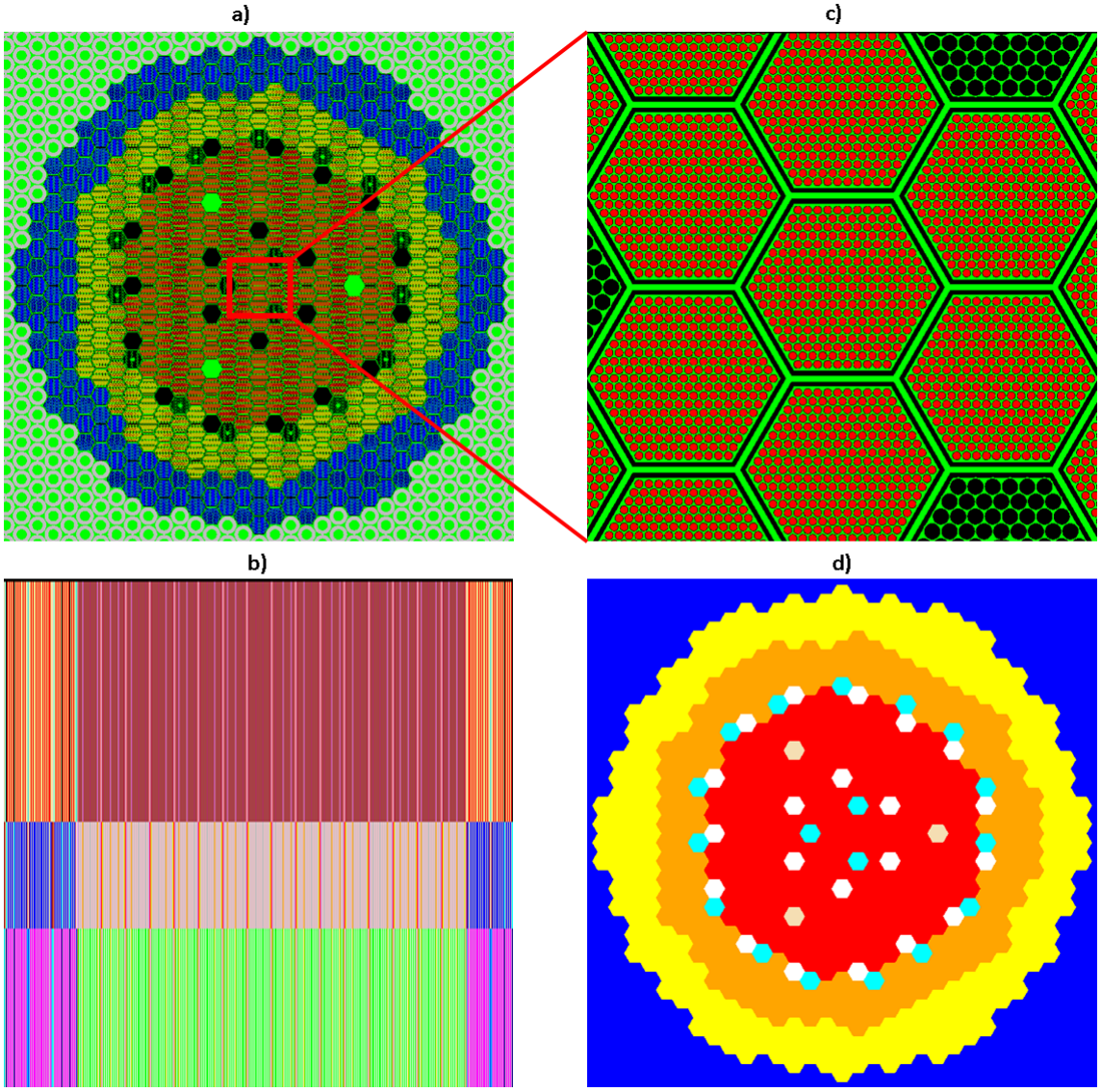

Figure 8.1: a): Radial cutting plan of the SuperPhénix core; b): Axial cutting plan of the SuperPhénix core; c): A zoom of the sub-assemblies of SuperPhénix; d): After homogenization illustration of the SuperPhénix core

The first question could be answered with Figure 8.1 and Figure 8.2 which are the geometrical descriptions of the SuperPhénix core and the ZONA2B-RZ simplification model. Apparently, the two configurations do not share the same geometrical construction concept since one is a hexagonal sub-assembly based on a heterogeneous core while the other is a cylindrical pre-homogenized RZ model. From the point of view of compositions, they

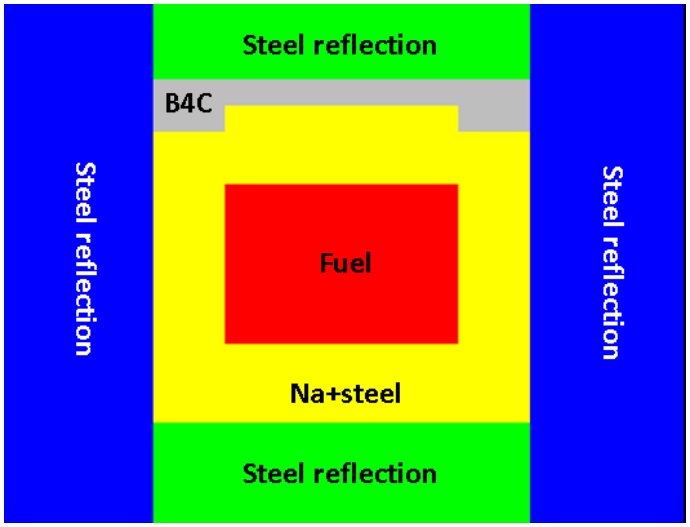

Figure 8.2: Vertical cutting view of the ZONA2B-RZ core model

both use oxide fuels mixed with plutonium which are surrounded by sodium. Up until now, it seemed that there was no visible common point between the two cores that could induce our inconsistency results.

As for the second question, there are indeed three approximations used in the IGSC method since TRIPOLI-4®, being a Monte-Carlo code, is limited to estimating a highly precise volumetric current. It is a common shortcoming of the Monte-Carlo family due to the cancelation between positive and negative values while performing a mathematical integration. Therefore, it probably induces high uncertainty associated to the estimated parameter. Here, the approximative current used in the IGSC method is recalled in Eq (8.1).

$$||\mathbf{J}|| \approx ||D\nabla\phi(\mathbf{r}, E, \hat{\Omega})|| \approx D\phi(\mathbf{r}, E, \hat{\Omega}) \approx \frac{\phi(\mathbf{r}, E, \hat{\Omega})}{3\left[\Sigma_t(\mathbf{r}, E) - \overline{\mu}\Sigma_s(\mathbf{r}, E)\right]} \tag{8.1}$$

The approximations involved are respectively:

1. Fick's diffusion theory to establish a relationship between current and the gradient of flux.

2. Transport corrected Boltzmann equation.

3. The spectrum of neutron flux is similar to the spectrum of the gradient of neutron flux.

Several remarks should be made. Firstly, Fick's law is founded to deal with a mono-energy problem and is supposed to be used in an isotropic medium. Then, when the mono-energy assumption is broken, an additional hypothesis is necessary to hold balance for the Boltzmann equation. That is to say the in-coming first order moment of the scattering rate equals the out-going quantity which is shown in Eq (8.2). This could help in obtaining the transport corrected Boltzmann equation. The third approximation is mostly available because the operator gradient will not impact on the dependence of

the energy variable especially in a homogeneous case. If the spatial heterogeneity becomes an outstanding feature, the flux spectrum could no longer represent the spectrum of its gradient within the whole heterogeneous domain, particularly near certain interfaces.

$$\int_0^\infty \Sigma_s(E' \to E)J(E')dE' = \Sigma_s(E)J(E) \tag{8.2}$$

All in all, the approximative current used in the IGSC method could be unsuitable to represent the accurate current in the two reactor cores. In the SuperPhénix core, the coolant sodium is a highly diffusive material compared to the heavy isotopes from the surrounding fuel. Thus, the favorite neutron propagation directions vary a lot according to their position. A similar situation is encountered again in the ZONA2B-RZ simplified core. As it is a pre-homogenized core model, there is no more heterogeneity in each macro region. However, the interface between these macro regions, such as the interface between the fuel and steel reflector, is always a big challenge for neutronic physicists. Some similar research was carried out by Jacquet with the deterministic code, ECCO during his Ph.D work [77].

The above clues seem to indicate that the current used in the IGSC method is not representative of the heterogeneous region where the material properties radically change. In order to verify this, a simple one-dimensional geometry which contains alternatively ^{239}Pu and ^{23}Na is designed and illustrated in Figure 8.3. The atomic concentrations for ^{239}Pu and ^{23}Na come from the realistic SuperPhénix outercore sub-assembly. And their volumetric proportion also respects the one used in the same sub-assembly. The boundary conditions imposed on this geometry are all reflections except for one side whose normal direction is just the direction of X. The thickness of this slab geometry is chosen in order to have it approach the criticality.

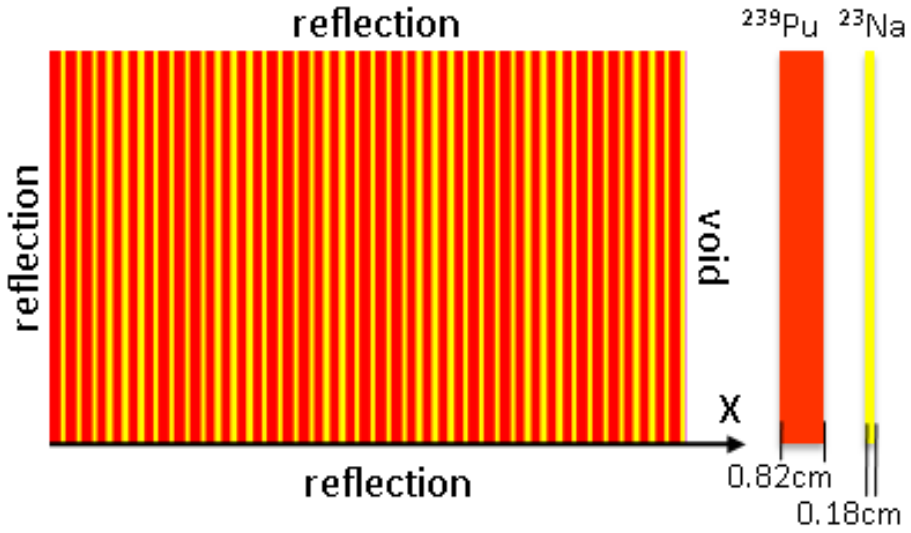

Figure 8.3: Pu-Na critical 1D geometry

Finally, the point-wise TRIPOLI-4® simulation with NJOY library gives the multiplicative factor for this designed configuration as follows: $K_{\text{eff}} = 1.00547 \pm 0.00011$. Meanwhile, 33-groups constants are produced with use of the IGSC method which exploits the approximate current as shown in Eq (8.1). Providing these multi-group constants into the multi-group TRIPOLI-4® simulation gives: $K_{\text{eff}} = 0.92770 \pm 0.00008$. An important discrepancy (-7777 ± 14 pcm) between multi-group and point-wise simulations is observed again with the above configuration. This great reproduced discrepancy helps confirm our previous guess: that the current used in the IGSC method is not representative of a heterogeneous case where the material properties change radically. This approximate current will be named the Todorova current in the following paragraph. Until now, the third question has been answered. The next step is to find a solution for this kind of problem.

8.2 Solution & Analysis

In the previous section, a 1D almost-critical geometry is designed in Figure 8.3. Its configuration property implies that the global current direction in this geometry follows the direction X. Therefore, its inspiration is to use an X-direction projected current instead of a Todorova current in the IGSC method. From the definition of current (cf Eq (8.3)), it is obvious to obtain its projection quantity on direction X which is written in Eq (8.4).

$$\mathbf{J}(\mathbf{r}, \hat{\Omega}, E) = \hat{\Omega}\phi(\mathbf{r}, \hat{\Omega}, E) \tag{8.3}$$

$$J_x(\mathbf{r}, \hat{\Omega}, E) = \Omega_x\phi(\mathbf{r}, \hat{\Omega}, E) \tag{8.4}$$

In a point-wise TRIPOLI-4® simulation, the information about neutron directions is always available at any moment during its trajectory history. And it is stored in a vectorial form noted as $(\Omega[0]; \Omega[1]; \Omega[2])$. The three components stand for the projection on direction X; Y and Z respectively. Therefore, an X-direction current weighted homogenized multi-group total cross sections could be expressed as follows:

$$\Sigma^V_{t1,g} = \frac{\int\limits_{\mathbf{r}\in V}\int\limits_{E\in g}\int\limits_{\hat{\Omega}} \Sigma_t(\mathbf{r}, E)\Omega_x\phi(\mathbf{r}, \hat{\Omega}, E)d^2\Omega dE d^3r}{\int\limits_{\mathbf{r}\in V}\int\limits_{E\in g}\int\limits_{\hat{\Omega}} \Omega_x\phi(\mathbf{r}, \hat{\Omega}, E)d^2\Omega dE d^3r} \tag{8.5}$$

where V indicates the macro-regions to be homogenized. Naturally, the new current weighted total cross sections could replace the previous ones weighted by a Todorova current in the IGSC method. For the sake of clarity, from now on we distinguish the new current as direction-X from the Todorova current.

Table 8.2 shows various K_{eff} values from point-wise and 6-group TRIPOLI-4® simulations on the previously described Pu-Na slab geometry. Three kinds of multi-group simulations are performed using different sets of constants produced respectively from the Todorova current and the direction-X current involving the IGSC method as well as the non anisotropy correction method. Their comparisons with respect to the reference point-wise value are also given in units of pcm with associated standard errors. It is observed from Table 8.2 that the direction-X current weighted multi-group constants improve the K_{eff} estimation importantly. The same improvement is also found with the use of no anisotropy corrected parameters. The later improvement of the K_{eff} value is pretty confusing because in Chapter 7 we have demonstrated that, for a leakage involved

geometry case, that multi-group anisotropy parameters need to be modified according to the IGSC method in order to preserve the neutron balance from point-wise simulation to multi-group simulation. However, this "good result" without anisotropy correction agrees well with what we found for the heterogeneous SuperPhénix core. The same result tendency confirms that the designed Pu-Na slab geometry can indeed represent the problem of SuperPhénix core. Thorough analysis is indispensable to understand why and how these three sets of multi-group constants behave differently in multi-group simulations. The analysis work is divided into three steps: multi-group constants comparison, current comparison and neutron balance comparison. They will be developed individually in the following parts.

K_{eff} PCT NJOY	1.00547(11)
K_{eff} HMG IGSC-Todorova	0.92770(8)
ΔK_{eff}	- 7777(14)
K_{eff} HMG IGSC-X	1.00072(10)
ΔK_{eff}	- 475(15)
K_{eff} HMG no-corr	1.00189(10)
ΔK_{eff}	- 358(15)

Table 8.2: K_{eff} comparisons between 6-groups (using the Todorova current & the direction-X current IGSC method as well as no correction) and point-wise (NJOY) TRIPOLI-4® simulations on critical Pu-Na slab geometry

8.2.1 Multi-group constant comparison

First of all, it should be stated that the three different methods in charge of multi-group constants production share exactly the same simulation algorithm to calculate the flux weighted multi-group parameters. So, there is no necessity to compare these multi-group constants which are namely total, absorption, fission cross sections as well as the group energy transfer probability matrix. The only difference exists in the production of the anisotropy distribution law. The non-correction method leaves the naturally produced anisotropy distribution probability in its original form, while the IGSC method re-calculates the anisotropy distribution probability according to Eq (7.32). The correction term $\Delta\overline{\mu}^{g\to g}$ involved in Eq (7.32) could be calculated via two different current weighted total cross sections. The first one which is used in chapter 7 is the Todorova current. The second is recently proposed in this chapter under the name of direction-X current.

The differently calculated $\overline{\mu}^{g\to g}$ which are homogenized over the whole region and collapsed into 6-groups are listed in Table 8.3. Meanwhile, the results are also plotted in Figure 8.4 to provide a clearer vision. From both Table 8.3 and Figure 8.4, it is obvious that important discrepancies exist between the Todorova results and the others. Moreover, the direction-X current estimated $\overline{\mu}^{g\to g}$ values are close to those without anisotropy correction in the first three groups.

The anisotropy correction effect revealed in Table 8.3 could potentially be impacted by both spatial homogenization and energy condensation. In order to distinguish the energy condensation effect on the anisotropy correction term, results of $\overline{\mu}^{g\to g}$ are also given out for only the plutonium medium (Table 8.4) and only the Na medium (Table 8.5).

$\overline{\mu}^{g\to g}$	$1\to 1$	$2\to 2$	$3\to 3$	$4\to 4$	$5\to 5$	$6\to 6$
IGSC-Todorova	0.8036	0.8210	0.4228	0.2384	0.5611	0.1783
IGSC-X	0.4477	0.2862	0.1304	0.0192	-0.4423	0.0741
no correction	0.4519	0.2741	0.1202	0.0348	0.0243	0.0383

Table 8.3: Averaged cosine values of in-group deviated angles calculated with different methods on the whole critical Pu-Na slab geometry

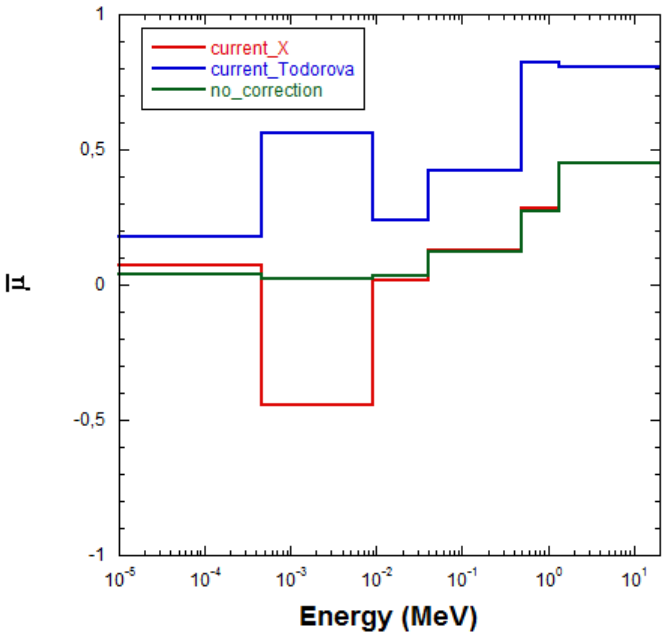

Figure 8.4: Illustration of averaged cosine values of in-group deviated angles calculated with different methods on the critical Pu-Na slab geometry

Several conclusions could be drawn out from the two above tables which are concerned mostly with energy condensation work. Firstly, in the Pu region, the corrected $\overline{\mu}^{g\to g}$ values are quite similar between the use of the Todorova current and direction-X current although, remarkable discrepancies are observed in the last two groups. This is due to poor statistics in the low energy groups. Secondly, if we compare the Todorova current results with no correction results from Table 8.3 with Table 8.5, we clearly see that the anisotropy correction effect is greater when treating heterogeneous medium in comparison to the homogeneous medium. Thirdly, if we compare the direction-X current results with those that use no correction in the three tables, it seems that the anisotropy correction from the Na region has a greater impact on the whole heterogeneous geometry than from the Pu region.

The above analyzed tendency can be demonstrated mathematically. Returning to the original anisotropy correction formula introduced by Eq (7.26), the specific form adapted to this Pu-Na slab geometry could be written as follows:

$$\widetilde{\overline{\mu}^{g\to g}_{a+b}} = \overline{\mu}^{g\to g}_{a+b} + \frac{\Sigma^{a+b}_{t0,g} - \Sigma^{a+b}_{t1,g}}{\Sigma^{a+b}_{s0,g\to g}} \tag{8.6}$$

$\overline{\mu}^{g\to g}$ Pu	$1\to1$	$2\to2$	$3\to3$	$4\to4$	$5\to5$	$6\to6$
IGSC-Todorova	0.6394	0.4264	0.2474	0.0347	0.0766	0.1988
IGSC-X	0.6379	0.4178	0.2259	0.0345	-0.067	1.0223
no correction	0.6393	0.2734	0.0971	0.0379	0.1321	0.0247

Table 8.4: Averaged cosine values of in-group deviated angles calculated with different methods on the region of Pu in the critical Pu-Na slab geometry

$\overline{\mu}^{g\to g}$ Na	$1\to1$	$2\to2$	$3\to3$	$4\to4$	$5\to5$	$6\to6$
IGSC-Todorova	0.4466	0.3441	0.1306	0.0413	0.3499	0.0255
IGSC-X	0.3925	0.2734	0.0971	0.0379	0.1321	0.0247
no correction	0.3788	0.2364	0.0723	0.0357	0.0286	0.0255

Table 8.5: Averaged cosine values of in-group deviated angles calculated with different methods on the region of Na in the critical Pu-Na slab geometry

where a and b stand for Pu region and Na region respectively. The homogenized multi-group total cross section $\Sigma^{a+b}_{t0,g}$ and its first moment $\Sigma^{a+b}_{t1,g}$ could indeed be decoupled into two parts. Each of them depends only on one single region property. They are shown in Eq (8.7) and Eq (8.8).

$$\begin{aligned}\Sigma^{a+b}_{t0,g} = &\frac{\int\limits_{\mathbf{r}\in a}\int\limits_{E\in g}\Sigma_t(\mathbf{r},E)\phi(\mathbf{r},\hat{\Omega},E)dEd^3r}{\int\limits_{\mathbf{r}\in a}\int\limits_{E\in g}\phi(\mathbf{r},\hat{\Omega},E)dEd^3r}\cdot\frac{\int\limits_{\mathbf{r}\in a}\int\limits_{E\in g}\phi(\mathbf{r},\hat{\Omega},E)dEd^3r}{\int\limits_{\mathbf{r}\in a+b}\int\limits_{E\in g}\phi(\mathbf{r},\hat{\Omega},E)dEd^3r}\\ &+\frac{\int\limits_{\mathbf{r}\in b}\int\limits_{E\in g}\Sigma_t(\mathbf{r},E)\phi(\mathbf{r},\hat{\Omega},E)dEd^3r}{\int\limits_{\mathbf{r}\in b}\int\limits_{E\in g}\phi(\mathbf{r},\hat{\Omega},E)dEd^3r}\cdot\frac{\int\limits_{\mathbf{r}\in b}\int\limits_{E\in g}\phi(\mathbf{r},\hat{\Omega},E)dEd^3r}{\int\limits_{\mathbf{r}\in a+b}\int\limits_{E\in g}\phi(\mathbf{r},\hat{\Omega},E)dEd^3r}\\ &=\Sigma^a_{t0,g}\cdot P^a_\phi+\Sigma^b_{t0,g}\cdot P^b_\phi \quad (8.7)\end{aligned}$$

$$\begin{aligned}\Sigma^{a+b}_{t1,g} = &\frac{\int\limits_{\mathbf{r}\in a}\int\limits_{E\in g}\Sigma_t(\mathbf{r},E)J(\mathbf{r},\hat{\Omega},E)dEd^3r}{\int\limits_{\mathbf{r}\in a}\int\limits_{E\in g}J(\mathbf{r},\hat{\Omega},E)dEd^3r}\cdot\frac{\int\limits_{\mathbf{r}\in a}\int\limits_{E\in g}J(\mathbf{r},\hat{\Omega},E)dEd^3r}{\int\limits_{\mathbf{r}\in a+b}\int\limits_{E\in g}J(\mathbf{r},\hat{\Omega},E)dEd^3r}\\ &+\frac{\int\limits_{\mathbf{r}\in b}\int\limits_{E\in g}\Sigma_t(\mathbf{r},E)J(\mathbf{r},\hat{\Omega},E)dEd^3r}{\int\limits_{\mathbf{r}\in b}\int\limits_{E\in g}J(\mathbf{r},\hat{\Omega},E)dEd^3r}\cdot\frac{\int\limits_{\mathbf{r}\in b}\int\limits_{E\in g}J(\mathbf{r},\hat{\Omega},E)dEd^3r}{\int\limits_{\mathbf{r}\in a+b}\int\limits_{E\in g}J(\mathbf{r},\hat{\Omega},E)dEd^3r}\\ &=\Sigma^a_{t1,g}\cdot P^a_J+\Sigma^b_{t1,g}\cdot P^b_J \quad (8.8)\end{aligned}$$

with definitions as follows:

- $\Sigma^a_{t0,g}$: flux weighted multi-group total cross section for region a (plutonium);

- $\Sigma^b_{t0,g}$: flux weighted multi-group total cross section for region b (sodium);

- $\Sigma^a_{t1,g}$: current weighted multi-group total cross section for region a (plutonium);

- $\Sigma^b_{t1,g}$: current weighted multi-group total cross section for region b (sodium);
- P^a_ϕ: proportion of integrated flux in region a (plutonium);
- P^b_ϕ: proportion of integrated flux in region b (sodium);
- P^a_J: proportion of integrated current in region a (plutonium);
- P^b_J: proportion of integrated current in region b (sodium).

To note that the current used in Eq (8.8) is a scalar quantity which could be the norm of the vectorial current or simply one part of the vectorial current, such as, J_x which is the projection on direction X.

Substituting Eq (8.7) and Eq (8.8) into Eq (8.6), a relationship could be established that links the whole geometry anisotropy correction quantity with each single medium anisotropy correction quantity, cf Eq (8.9).

$$\begin{aligned}
\Delta\overline{\mu}^{g\to g}_{a+b} = \widetilde{\overline{\mu}^{g\to g}_{a+b}} - \overline{\mu}^{g\to g}_{a+b} & \\
&= \frac{\Sigma^a_{t0,g} - \Sigma^a_{t1,g}}{\Sigma^a_{s0,g\to g}} \cdot \frac{\Sigma^a_{s0,g\to g}}{\Sigma^{a+b}_{s0,g\to g}} \cdot P^a_J - \frac{\Sigma^a_{t0,g}}{\Sigma^{a+b}_{s0,g\to g}} \cdot (P^a_J - P^a_\phi) \\
&+ \frac{\Sigma^b_{t0,g} - \Sigma^b_{t1,g}}{\Sigma^b_{s0,g\to g}} \cdot \frac{\Sigma^b_{s0,g\to g}}{\Sigma^{a+b}_{s0,g\to g}} \cdot P^b_J - \frac{\Sigma^b_{t0,g}}{\Sigma^{a+b}_{s0,g\to g}} \cdot (P^b_J - P^b_\phi) \\
&= \Delta\overline{\mu}^{g\to g}_a \cdot \frac{\Sigma^a_{s0,g\to g}}{\Sigma^{a+b}_{s0,g\to g}} \cdot P^a_J - \frac{\Sigma^a_{t0,g}}{\Sigma^{a+b}_{s0,g\to g}} \cdot (P^a_J - P^a_\phi) \\
&+ \Delta\overline{\mu}^{g\to g}_b \cdot \frac{\Sigma^b_{s0,g\to g}}{\Sigma^{a+b}_{s0,g\to g}} \cdot P^b_J - \frac{\Sigma^b_{t0,g}}{\Sigma^{a+b}_{s0,g\to g}} \cdot (P^b_J - P^b_\phi)
\end{aligned} \tag{8.9}$$

From the above equation, it is found that the anisotropy correction effect on a heterogeneous domain is not simply a linear combination of the anisotropy corrections from each homogeneous sub-domain. There are some other attached correction constants which are greatly influenced by the spatial distribution of current and flux. Therefore, the whole anisotropy correction comprises an energy condensation correction part $(\Delta\overline{\mu}^{g\to g}_a \cdot \frac{\Sigma^a_{s0,g\to g}}{\Sigma^{a+b}_{s0,g\to g}} \cdot P^a_J + \Delta\overline{\mu}^{g\to g}_b \cdot \frac{\Sigma^b_{s0,g\to g}}{\Sigma^{a+b}_{s0,g\to g}} \cdot P^b_J)$ and a spatial homogenization correction part $(-\frac{\Sigma^a_{t0,g}}{\Sigma^{a+b}_{s0,g\to g}} \cdot (P^a_J - P^a_\phi) - \frac{\Sigma^b_{t0,g}}{\Sigma^{a+b}_{s0,g\to g}} \cdot (P^b_J - P^b_\phi))$.

With the help of Eq (8.9), a numerical application is performed to this Pu-Na case. $\Delta\overline{\mu}^{g\to g}_a$ and $\Delta\overline{\mu}^{g\to g}_b$ are easily obtained from Table 8.4 and Table 8.5 through a subtraction operation. The multi-group cross sections (like $\Sigma^a_{t0,g}$; $\Sigma^{a+b}_{s0,g\to g}$ $\cdots$) are available in the cross section output file from TRIPOLI-4® point-wise simulation. Estimation of flux in the desired medium as well as within desired energy group is not difficult for the code. The only difficulty lies in how to calculate a volumetric current with TRIPOLI-4® since there is not yet an estimator enabling us to do this task. Details about how to estimate current quantity and the estimation results will be developed in next section. With knowledge of all the necessary elements, analytical calculation results are summarized in Table 8.6 (Todorova current case) and Table 8.7 (direction-X current case). The total analytical

correction values are decomposed into the energy condensation (E.C.) contribution term and the spatial homogenization (S.H.) contribution term which are both listed in the following tables.

Todorova	$\Delta\overline{\mu}$ E.C.	$\Delta\overline{\mu}$ S.H.	$\Delta\overline{\mu}_{a+b}$ analytical	$\Delta\overline{\mu}_{a+b}$ simulation	Re.diff %
$1 \to 1$	0.0210	0.3307	0.3516	0.3517	-0.02%
$2 \to 2$	0.0256	0.5212	0.5468	0.5469	-0.01%
$3 \to 3$	0.0292	0.2735	0.3027	0.3026	0.02%
$4 \to 4$	0.0024	0.2013	0.2038	0.2036	0.09%
$5 \to 5$	0.1098	0.4270	0.5369	0.5368	0.01%
$6 \to 6$	0.0930	-0.1153	-0.0233	0.1400	727.98%

Table 8.6: Anisotropy correction analysis with use of Todorova current

direction-X	$\Delta\overline{\mu}$ E.C.	$\Delta\overline{\mu}$ S.H.	$\Delta\overline{\mu}_{a+b}$ analytical	$\Delta\overline{\mu}_{a+b}$ simulation	Re.diff %
$1 \to 1$	0.0097	-0.0137	-0.0040	-0.0042	4.26%
$2 \to 2$	0.0299	-0.0169	0.0130	0.0121	6.71%
$3 \to 3$	0.0200	-0.0093	0.0107	0.0102	4.42%
$4 \to 4$	0.0019	-0.0083	-0.0064	-0.0156	142.45%
$5 \to 5$	0.0715	-0.0183	0.0532	-0.4666	976.79%
$6 \to 6$	0.5244	-0.0701	0.4543	0.0358	92.12%

Table 8.7: Anisotropy correction analysis with use of direction-X current

A good agreement between analytically calculated $\Delta\overline{\mu}_{a+b}$ values and TRIPOLI-4® estimated values is observed for the first 5 groups according to Table 8.6. Their relative differences are limited to 0.10%. As for the last group where the statistic is very poor, the relative difference is much more important. Globally, the decoupling between the energy condensation effect and the spatial homogenization effect on the anisotropy correction phenomenon is mathematically proved by the Todorova current used IGSC method. Moreover, it can be found that the homogenization effect is more important on the whole anisotropy correction term than energy condensation effect.

If attention is now directed to the direction-X current corrected anisotropy case, the agreement between analytically obtained anisotropy correction values and TRIPOLI-4® simulated values is confirmed again in the first three groups but with larger discrepancies. It is normal that the relative differences are greater when using the direction-X current because the projection of neutron direction on abscissa X could be positive and negative. Thus, this positive-negative cancelation phenomenon will amplify the standard deviation. As for the last three groups, their relative differences are much more important. However, it is not so serious either. An error propagation tested could eventually explain the discrepancy. For example, in the case of group transfer $4 \to 4$, if we want to obtain the same value as that from the TRIPOLI-4® simulation result: $\Delta\overline{\mu}_{a+b}^{4\to4} = -0.0156$, the deduced current proportion in Pu medium is $\widetilde{P_{J,4}^{a}} = 0.628$. Comparing this value to the originally estimated one by TRIPOLI-4® $P_{J,4}^{a} = 0.638$, their relative difference is 1.6% which is well covered by the standard deviation of this variable itself. Moreover, the direction-X current correction has no visible privilege between energy condensation and spatial ho-

mogenization. It is observed that the energy condensation work has a tendency to increase $\overline{\mu}^{g\to g}$ values while homogenization work tries to decrease the values. This compensation behavior seems more reasonable than in the Todorova current case where both the energy condensation and spatial homogenization help increase the anisotropy effect. The latter finally results in under-estimated K_{eff} values.

8.2.2 Current comparison

From the previous section, it seems that an appropriate estimation of current quantity in each region of the Pu-Na slab geometry is considerably important and influences the anisotropy correction level. Thus, this section focuses on comparing the different estimations of current by the TRIPOLI-4® simulations. Moreover, from Eq (8.9), we could tell that the difference between flux spectrum and current spectrum is also quite significant for the heterogeneous medium anisotropy correction term. Therefore, the flux distribution spectrum will also be presented.

Please note that the current discussed here is not in the conventional sense where it accounts for the number of neutrons passing through a certain surface in a given direction. Both the Todorova current and the direction-X current used in Chapter 7 and Chapter 8 are volumetric variables as flux quantity. Thus, the estimators for these two currents are inspired from the collision estimator for flux which are respectively shown as follows:

$$J_{\text{Todorova}} = \sum_i \frac{\omega(\mathbf{r}_i, E_i)}{\Sigma_t(\mathbf{r}_i, E_i)\left[\Sigma_t(\mathbf{r}_i, E_i) - \overline{\mu}(E_i)\Sigma_s(\mathbf{r}_i, E_i)\right]} \tag{8.10}$$

$$J_{\text{X}} = \sum_i \frac{\omega(\mathbf{r}_i, E_i)}{\Sigma_t(\mathbf{r}_i, E_i)}\Omega_x \tag{8.11}$$

where i is the index for the collisions whose incident energy E_i and position $\mathbf{r}_i$ belong to the desired energy group g and desired region(regions) V. 6-groups simulation results will be presented in the figures below for each of the regions. Figure 8.5 and Figure 8.6 correspond to the Todorova and the direction-X current spectra; while Figure 8.7 shows the flux spectrum.

At first, almost the same distribution form in the Pu region (red curve) and Na region (blue curve) could be observed from both the Todorova current (Figure 8.5) and the direction-X current (Figure 8.6) spectra as well as flux spectrum (Figure 8.7). Around 99% of the estimated scores are occupied by the first three groups from 20 MeV to 41 keV. Then, we find that the absolute amplitude of the Todorova current is several hundreds higher than from the direction-X current. Moreover, the whole estimated flux quantity is situated between the two current ones. This can be easily explained by comparing Eq (8.10) with Eq (8.11). The scores for the Todorova current are in fact amplified with respect to the flux scores; while the scores for the direction-X current are lower when compared to the flux scores.

Another important piece of information should be drawn from the three spectra figures: the spatial occupation ratio for flux or current between the Pu and Na regions. The ratio noted as ρ could be expressed by variables defined in Eq (8.12) and Eq (8.13) as follows:

$$\rho_J = \frac{P_J^a}{P_J^b} \tag{8.12}$$

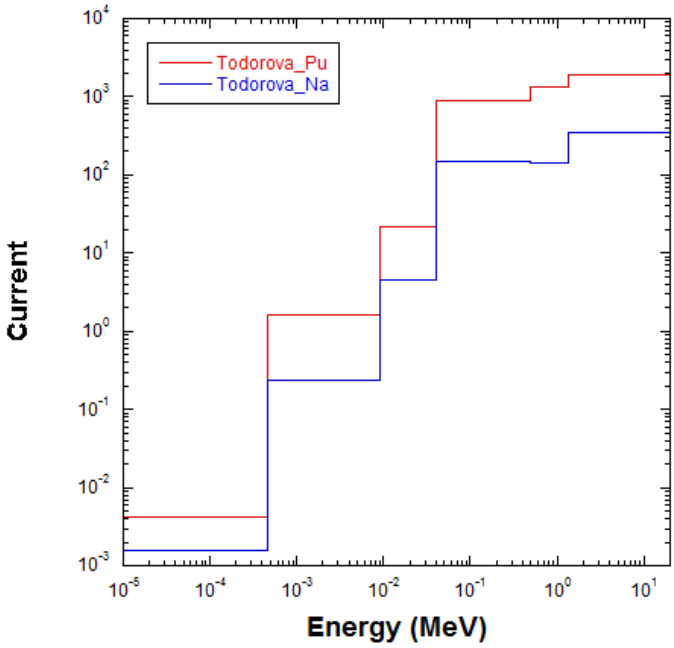

Figure 8.5: Todorova current spectrum in each single region of the almost-critical Pu-Na slab geometry

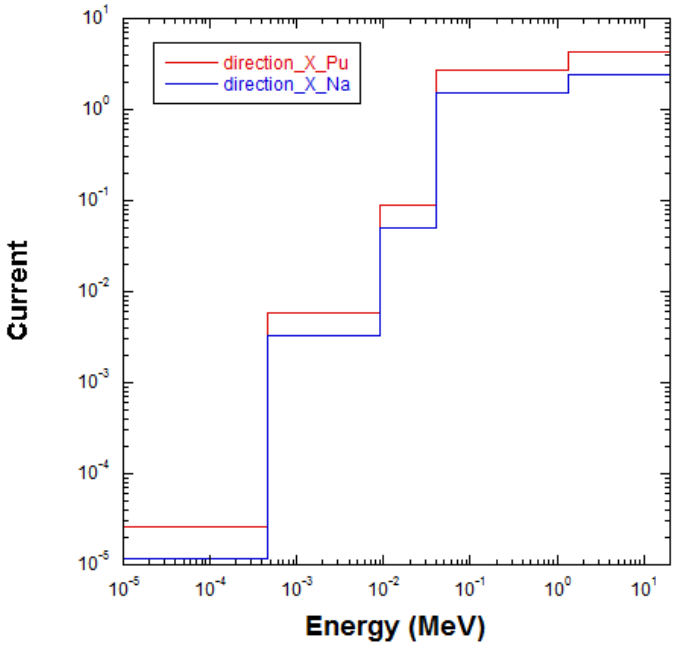

Figure 8.6: Direction-X current spectrum in each single region of the almost-critical Pu-Na slab geometry

$$\rho_\phi = \frac{P_\phi^a}{P_\phi^b} \tag{8.13}$$

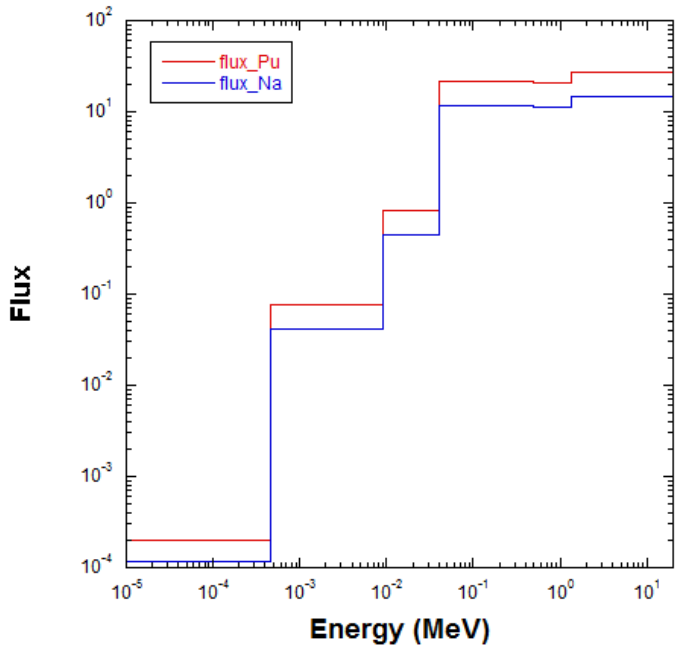

Figure 8.7: Flux spectrum in each single region of the almost-critical Pu-Na slab geometry

These ratio quantities are plotted in Figure 8.8. As we had previously pointed out that, since the important energy range runs from 20 MeV to 41 keV, attention should also be focused on these groups. According to Figure 8.8, the spatial ratio values are quite close between the direction-X current and the neutron flux spectra. This means that for J_X and ϕ, the quantity occupied in the Pu region is mostly twice that of the quantity occupied in the Na region. However, the ratio values are dramatically enhanced in the Todorova current case (blue curve). For the 1^{st} and 3^{rd} groups, the Pu region contains 5 times more of current quantity than the Na region. Furthermore, this ratio climbs up to 9.5 for the 2^{nd} group. This important difference between the Todorova current and the direction-X current is the origin that leads to different K_{eff} values. From another point of view, the similar spatial distribution proportion from the direction-X current and flux spectra make it easier to understand why the direction-X current corrected anisotropy parameters yield a similar K_{eff} result as from the no correction case.

Anyway, in the designed slab geometry case, the real current is indeed similar to the direction-X current. Therefore, we could use the latter to analyze the Todorova current. After making the comparison with Figure 8.8, it can be concluded that the approximations used to estimate the Todorova current are not at all adapted to this highly heterogeneous geometry case in which one region is very absorptive and the other is very diffusive. The consequence on the neutron balance will be analyzed in the next part.

8.2.3 Neutron balance comparison

In this part, we shall compare the reaction rates calculated with multi-group constants to those from the point-wise simulation. Three different sets of 6-group constants were used which came from the Todorova current involved IGSC method, the direction-X current involved IGSC method and the no correction method. Two reaction rates will be presented:

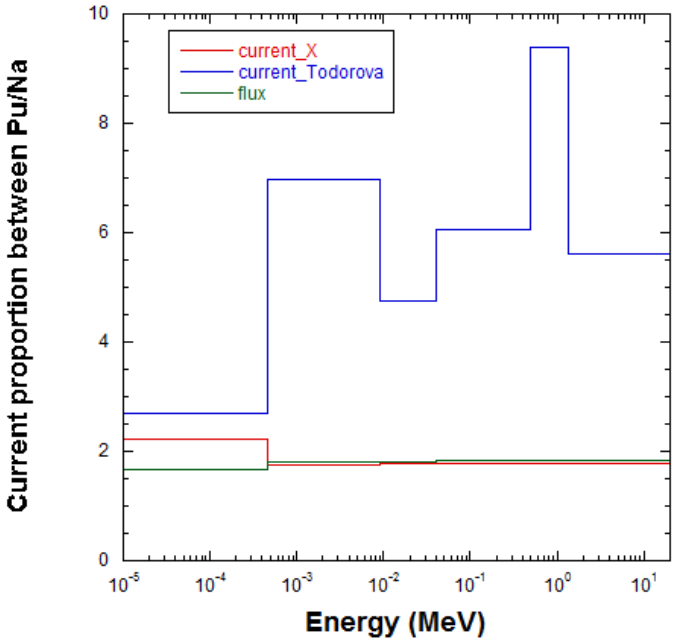

Figure 8.8: Spatial occupation ratio between the Pu and Na regions for current and flux spectra

the fission production and the neutron leakage. Their discrepancies expressed in units of pcm are respectively plotted in Figure 8.9 and Figure 8.10.

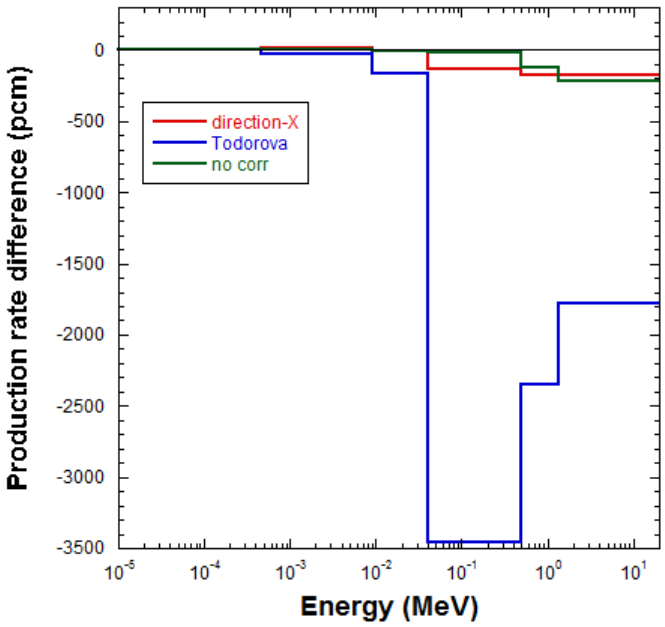

Figure 8.9: Production rate comparisons between multi-group (using the direction-X current, the Todorova current and the flux weighted 6-group constants) and point-wise TRIPOLI-4 simulations

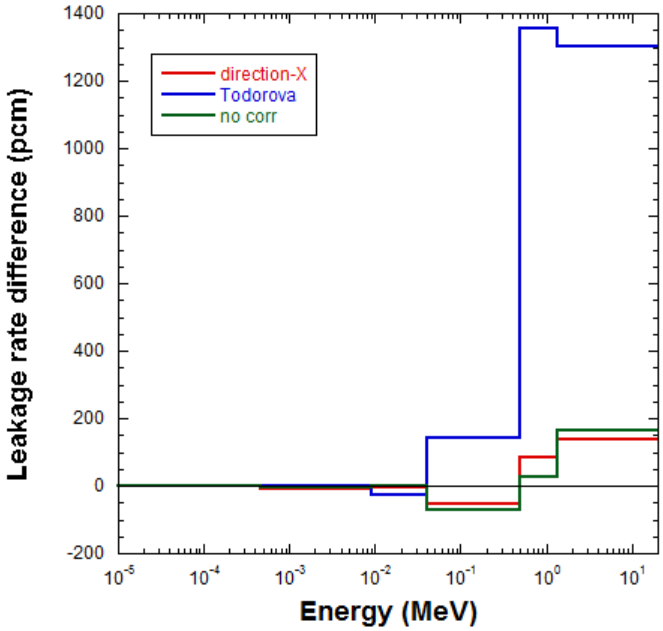

Figure 8.10: Leakage rate comparisons between multi-group (using the direction-X current, the Todorova current and the flux weighted 6-group constants) and point-wise TRIPOLI-4 simulations

Having a look at the blue curves which stand for the Todorova current correction case, the production differences in the three principal groups are greater than 1500 pcm. The sum of all the six groups results in the final under-estimation of the K_{eff} value by 7777 pcm. The same situation is found again for leakage rates. In the first two groups, the discrepancies of leakage rates are around 1300 pcm. These over-estimated leakage rates originate from the over-corrected $\widetilde{\overline{\mu}^{g\to g}}$ values for $g = 1; 2$. The Todorova current anisotropy correction effect too strongly enforces the high energy neutrons traveling forward until escaping from the geometry.

As for the direction-X current involved results (red curves), both production rate and leakage rate are greatly improved. The discrepancies of these two reaction types are limited to 200 pcm for each group. The improvement in the preservation of neutronic balance confirms that the direction-X current represents more correctly the real situation in the 1D slab configuration.

The unexpected point is that the non-corrected multi-group constants show mostly the same capacity as the direction-X current corrected multi-group constants in the multi-group TRIPOLI-4® simulation. The discrepancies of production rate or leakage rate are also less than 200 pcm for each group. The similar behavior to what we observed for the direction-X current estimated results is very confusing. One potential explanation is from the compensation effect between the energy condensation and the spatial homogenization. This means that the non-corrected multi-group constants over-estimate the fission production rate when only the energy condensation work is concerned. On the other hand, from spatial homogenization aspect, the non-correction anisotropy parameters will under-estimate the fission production rate. The two opposite effects make the final results seem better.

After having compared the multi-group constants ($\overline{\mu}^{g\to g}$), the estimated current/flux spectra and the neutronic balance, the problem associated with highly diffusive medium becomes comprehensible. The Todorova current is not adapted to the heterogeneous media where the material property varies a lot. The anisotropy correction imposed by the IGSC method could be distinguished by a homogenization aspect and energy condensation aspect. Using an inappropriate Todorova current extensively amplifies the correction effect from spatial homogenization aspect which finally results into an under-estimated K_{eff} value and fission production rates.

The proposed solution is to replace the Todorova current by a direction-X current in the IGSC method. The idea of using current projected on the X direction is feasible in slab geometry. The tested Pu-Na configuration showed that this direction-X current does indeed represent the good current existing in the geometry. Thus, it is able to correct the anisotropy parameters properly and yields better estimations for the K_{eff} value and reaction rates. This direction-X current will be applied to the fuel/reflector configuration which has been mentioned previously as a challenging topic for neutronic physicists.

8.3 Application to fuel-reflector calculation

Within the framework of the CIRANO program[38] which was carried out in the nuclear experimental facility, MASURCA, there was a core configuration named ZONA2B. This one is a typical fuel-reflector core example. Its fuel sub-assembly is composed of MOX and sodium rodlet, while its reflector sub-assembly consists of steel and sodium rodlet. Previous analysis on ZONA2B core revealed remarkable discrepancies between the deterministic calculation results and the Monte-Carlo reference results. In order to figure out this problem, a preliminary research was conducted during Jacquet's Ph.D. work[77]. A simplified core geometry, made up of a homogeneous fuel medium and a homogeneous reflector medium, was used by Jacquet. In this section,we shall apply the direction-X current involved IGSC method on the same geometry to verify the applicability of our method.

Figure 8.11 illustrates the fuel-reflector geometry, especially the spatial refinement required in deterministic calculations, in particular for ECCO code. The boundary conditions are reflective for the fuel side and void for the reflector side. And homogenized multi-group constants are produced for each distinguished medium as shown in Figure 8.11. It was pointed out in Jacquet's thesis that this explicit geometry modeling should be able to account for the fuel-reflector interface effect. However, unsatisfactory results persisted in the ECCO/BISTRO calculations which are quoted in Table 8.8. A brief resumé Jacquet's analysis procedure follows.

The reference K_{eff} value came from the TRIPOLI-4® point-wise simulation using the input library JEFF3.1 with probability tables. As for the ECCO calculation steps, a fine-group (1968 groups) calculation is at first performed with P1 approximation. Then, these 1968-groups cross sections were collapsed into 328-groups or 33-groups after a self-shielding treatment. It should be pointed out that the collapsed multi-group cross sections were produced for each individual mesh in Figure 8.11. Finally, these macroscopic multi-group cross sections were used in the core calculation code BISTRO.

Besides K_{eff} values, one-group flux and current were also compared. However, all the

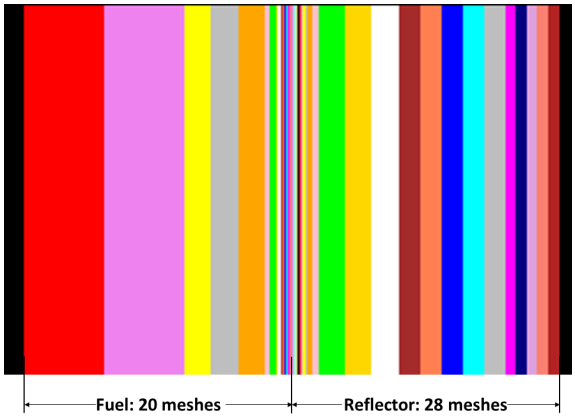

Figure 8.11: Illustration of a simplified core with steel reflector geometry

cases	K_{eff}	ΔK_{eff} pcm
TRIPOLI-4® reference	1.48707 ± 0.00023	—
ECCO/BISTRO 33GR	1.47055	-1652 ± 23
ECCO/BISTRO 328GR	1.48087	-620 ± 23

Table 8.8: K_{eff} comparisons between the ECCO-BISTRO calculations and TRIPOLI-4® reference simulation (all the values in this table are quoted from Jacquet's thesis)

comparisons concluded that the energy condensation functionalities used in ECCO could not treat the fuel-reflector case. It was proven that the current used in ECCO for energy collapsing deviated from the current calculated by the BISTRO code. According to the author's opinion, it seems reasonable to find this inconsistent current between the ECCO and BISTRO codes. The current calculated by ECCO is from the solution of B1 homogeneous fundamental equations; whereas the current solved by BISTRO is from a real leakage involved Boltzmann transport equation. It should be kept in mind that the fundamental mode approximation is mostly available for the central part of a reactor core where the neutron current can be regarded as the gradient of neutron flux. Apparently, if we always impose the same approximation for the fuel-reflector region where neutron anisotropy takes dominant place, there is no doubt that certain biases are introduced into calculation results.

Finally, new energy condensation methods were proposed by Jacquet which take consideration the neutron directional properties. Detailed information can be found in Section 3.5. However, the proposed methods are based on a deterministic solver. It is then quite easy to gain access to higher order moments ($l > 1$) of flux which is, in contrary, rather difficult for Monte-Carlo codes. That is why we did not adopt the conservative energy condensation method in this work.

After a short presentation on the history of the fuel-reflector problem, the recently introduced direction-X current seems a feasible solution suggested by the Monte-Carlo method since it is proven to be representative of the accurate volumetric current in a 1D geometry. Therefore, the same geometry in Figure 8.11 is calculated by the continuous-energy TRIPOLI-4® simulation. In the meantime, 33-group cross sections are produced

by the IGSC method using the direction-X current. In order to be assured that different types of behaviors will occur between the direction-X current and the Todorova current, another set of 33-group cross sections is generated by using the Todorova current. Both of them are then used in a multi-group TRIPOLI-4® simulation. Let us underline the fact that the produced multi-group cross sections are simply distinguished between the fuel part and reflector part. It is not divided into refined meshes as in Jacquet's case. Table 8.9 shows different K_{eff} values and their discrepancies ΔK_{eff} in pcm.

cases		$K_{\text{eff}} \pm \sigma$	$\Delta K_{\text{eff}} \pm \sigma$ (pcm)
TRIPOLI-4® point-wise		1.48576 ± 0.00014	—
TRIPOLI-4® multi-group	direction-X	1.48298 ± 0.00014	-278 ± 20
	Todorova current	1.47014 ± 0.00016	-1562 ± 21

Table 8.9: K_{eff} comparisons between multi-group and point-wise TRIPOLI-4® simulations on a simplified fuel-reflector geometry

Before comparing the results shown in Table 8.9 with those from Table 8.8, it should be pointed out the two TRIPOLI-4® reference calculations do not use the same input data. Jacquet used library JEFF3.1 with probability tables and here we use library JEFF3.1.1 without probability tables. That is the reason why the point-wise simulated K_{eff} values are not the same. However, we shall not compare the K_{eff} values directly but the discrepancies between the multi-group and its associated point-wise values. Thus, the different input libraries will not impact our conclusions.

At first, it is shown that the direction-X involved IGSC method is much more suitable for handling the fuel-reflector problem than the ECCO energy condensation method. With the same energy mesh and worse spatial refinement, the TRIPOLI-4® code with the direction-X current used IGSC method has successfully decreased the K_{eff} discrepancy by more than 1000 pcm. Moreover, even with better energy refinement (328 groups), the ECCO calculated multi-group cross sections are not as good as those from the TRIPOLI-4® simulation. The last comparison is done between the direction-X current and the Todorova current results. It confirms that the direction-X current could handle better the heterogeneous medium containing an interface surrounded by two completely different materials.

Apart from comparing multiplication factors between point-wise and multi-group simulations, another important indicator also attracts our attention and that is the current crossing the interface between the fuel and reflector regions. Two opposite directions are respectively plotted in part **a)** and **b)** of Figure 8.12 below. The red curves stand for reference current estimated from the point-wise TRIPOLI-4® simulation. The blue curves come from the multi-group TRIPOLI-4® simulation using the direction-X current produced 33-group constants while the green curves indicate the Todorova current produced 33-group constants. For both positive and negative directions, it can be demonstrated that, the multi-group surface current spectra calculated by using the direction-X current produced multi-group constants are much closer to the reference spectra.

Their relative differences between multi-group simulated current quantities and the reference currents are respectively plotted in Figure 8.13 **a)** (positive direction) and **b)**

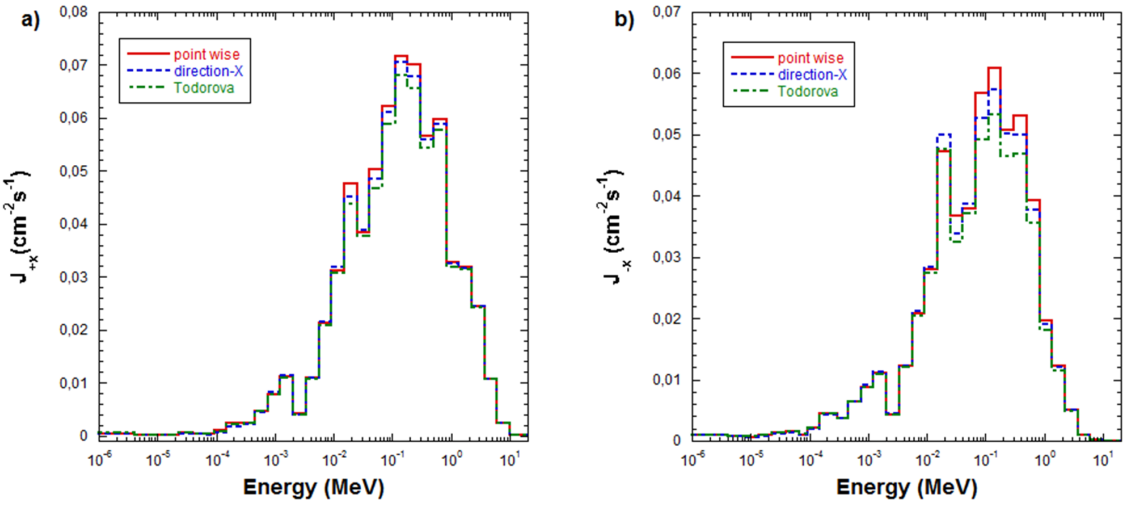

Figure 8.12: **a)**: Positive directional current across the interface between fuel and reflector; **b)**: Negative directional current across the interface between fuel and reflector

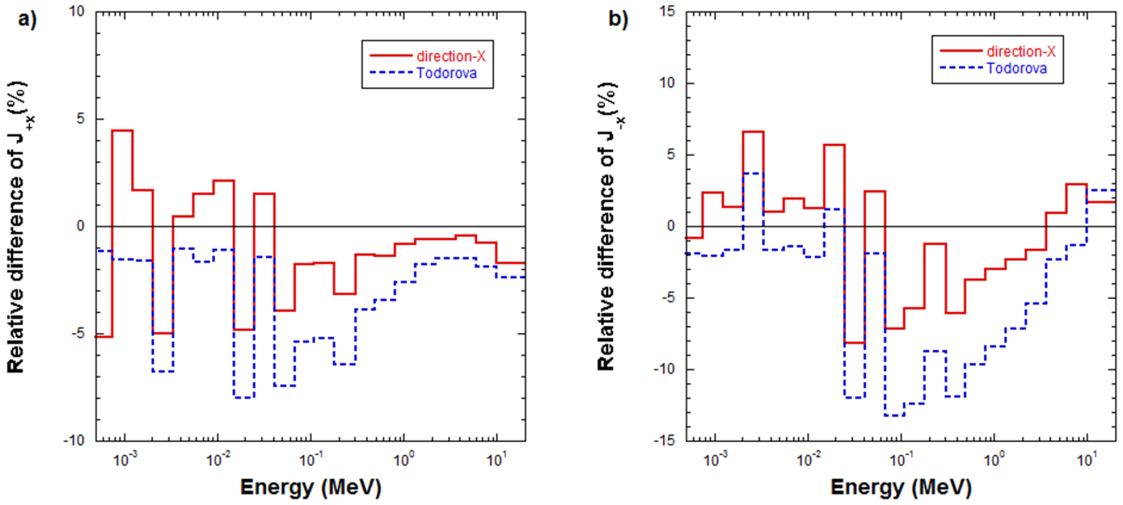

Figure 8.13: **a)**: Relative differences of positive directional current across the interface between fuel and reflector; **b)**: Relative differences of negative directional current across the interface between fuel and reflector

(negative direction). To note that the energy domain is limited between [500 eV; 20 MeV] in Figure 8.13 where there are more than 98% of total current quantity. It confirms that the relative discrepancies obtained with direction-X current are globally closer to zero line than those obtained with the Todorova current. This means that with the use of the direction-X involved IGSC method the produced multi-group constants almost enable us to preserve the current spectra information on the special surface which was a difficult problem for other cell calculation codes, such as ECCO.

Conclusion

The residual problem encountered in the SuperPhénix core and ZONA2B simplified model from Chapter 7 was thoroughly analyzed. The diagnosis results show that the Todorova current corrected anisotropy parameters are not suitable for heterogeneous geometries in which the partial material properties change dramatically. A new current under the name of the direction-X is proposed to improve this situation. Compared to the Todorova current, it avoids the diffusion theory based approximations and seems to be an appropriate representation of the realistic current, especially in a slab geometry.

An initial test using the direction-X current was performed on a Pu-Na slab geometry. Encouraging results (K_{eff}, current/flux spectra, neutronic balance) were obtained by using the direction-X current corrected multi-group constants. Therefore, its application was pursued to an historical problem for a deterministic cell calculation code: fuel-reflector interface problem. Improvements were again found with the multi-group constants generated by the direction-X current involved IGSC method in TRIPOLI-4®. The new method can reduce the reactivity bias by an order of magnitude of 1000 pcm compared with deterministic results.

Finally, the direction-X current involved IGSC method appropriately met the highly various heterogeneous media requirements but it is limited to a one-dimensional application for the moment. The constraint comes from a common shortcoming of the Monte-Carlo family as it was mentioned previously. Prospective studies about 2D current implementation work could be carried out in TRIPOLI-4®.

Part III

Leakage Model Development in TRIPOLI-4®

Chapter 9

History on neutron leakage model

Previous studies were focused to generate multi-group constants either with an infinite flux spectrum or with naturally almost-critical flux-current spectra. A sub-assembly calculation under a reflective or periodic boundary condition (cf. Chapter 6) is the primary and simplest step of multi-group constants production work. This imposed approximation on boundary conditions is more or less adequate for a thermal neutron reactor in which the sub-assembly geometry size is much larger than the neutron mean free path length, λ. Though, the same approximation is less available for fast neutron reactors which has a sub-assembly size comparable with respect to λ of neutrons. In this case, the adjacent sub-assemblies are more efficiently coupled among themselves. Thus, the neutron leakage effect should be considered especially when dealing with fast neutron type sub-assemblies.

Two different approaches are investigated in this work to account for the neutron leakage effect for each single assembly. The first one is a direct way which uses an almost-critical geometry to ensure the included sub-assemblies criticality property. So natural neutron leakage exists through the boundaries the neighbors of which are simply void. This doing way has been explicitly developed in Chapter 7 and Chapter 8. Its most remarkable advantage is the exploitation of intrinsic critical spectra without any approximation. On the other hand, the critical geometry construction for every special case is rather complicated and delicate. The second approach is to incorporate some leakage model within sub-assembly calculation under reflective or periodic boundary conditions. An artificial leakage rate is simulated mathematically to bring the sub-assembly from an infinite state towards a critical state. The advantage of the leakage model is that it is able to determine a critical state for the sub-assembly without knowledge of the exact operating conditions and materials surrounding it.

Three different leakage models have been developed in the Monte-Carlo environment thus far. The first one is based on the fundamental mode approximation which expresses the angular flux distributed in a whole core by a product of two terms. One is the fundamental flux which could be repeated in each single sub-assembly. The other is the macroscopic distribution form. This leakage model originates from deterministic lattice calculation codes. It was introduced into the Korean Monte-Carlo code McCard at KAERI. It was also used in the Finland Monte-Carlo code Serpent developed at VTT. An experimental multi-group Monte-Carlo algorithm implemented in module MC: of lattice code DRAGON5[71] has also exploited this fundamental mode approximation based leakage model.

The second leakage model is proposed by another Korean research team from KAIST[73]. The main idea of this method is to establish a critical spectrum via varying the reflection probability noted as *albedo* for neutrons which hit the boundary limits. The *albedo* value is solved as an eigenvalue problem by the MCNP5 simulation code. The critical flux eventually found in the related sub-assembly could be used to produce multi-group constants or in a Monte-Carlo depletion code, such as MONTEBURNS[78].

The third leakage model is proposed by Yamamoto from Kyoto University[93]. This method initially introduces complex-values as neutron simulation weights during continuous-energy Monte-Carlo procedure. The leakage correction term used by Yamamoto is the same as in the B_1 method but solved as an eigenvalue problem. Compared with the first two methods, the last idea of interpreting the neutron leakage rate is more appropriate because every neutron has its own leakage probability during its random walk. On the other hand, the two first leakage models assume that all the neutrons or the neutrons in each macro energy group share the same escaping probability. Even though the last leakage model has its own physical advantage, it is limited due to the application issue. For example, it demands a symmetrical geometry in order to cancel the imaginary part of the fission source.

A common point of the above Monte-Carlo codes that have certain leakage models is that they aim to produce few-group constants to be then used in a diffusion theory based core calculation code. So even if they succeed in obtaining a critical flux spectrum thanks to their own leakage model as a weighting function to generate isotropic multi-group cross sections, the challenging problem of appropriately producing multi-group diffusion coefficients remains. The author would like to point out once again that the motivation of this work is to produce multi-group constants for transport theory based core calculation codes. Leakage model development is also within this framework. Since incorporating a leakage model into TRIPOLI-4® is a totally unexplored field, the first methodology chosen to be implemented in the TRIPOLI-4® code is the basic B_1 leakage model. As this method is popularly used in several continuous-energy Monte-Carlo codes, it could be of help for the validation work. Even though the basic idea is the same as that used in other codes (Serpent or McCard), some innovative techniques are adapted in our code. In addition, an intensive validation work is proposed. Detailed development will follow in Chapter 10.

Chapter 10

The B_1 leakage model in TRIPOLI-4®

This chapter focuses on the leakage model implemented in the TRIPOLI-4® code which is based on B_1 fundamental equations. In formulating this first part, all the necessary information will be found in [6]. Thus, only a quick theory description will be provided. It is followed by the section which shows the implemented algorithm. The greatest effort is expended on the validation part.

10.1 Reviewing the B_1 homogeneous equations

The solution of the transport equation applied to a homogeneous infinite multiplicative geometry is defined as fundamental mode. The sub-assembly calculation is usually performed under reflective or periodic boundary conditions. As a result, a leakage model needs be introduced in the sub-assembly to enforce $K_{\text{eff}} = 1$. In this context, the fundamental mode approximation is showing up which aims to represent the angular flux by a combination of two terms. One is a fundamental flux $\varphi(\mathbf{r}, E, \hat{\Omega})$ which is available within every single assembly wherever its position. The other one noted as $f(\mathbf{r})$ is contributed to describe the spatial distribution in a whole core. Furthermore, $f(\mathbf{r})$ is assumed to be the solution of a Laplace equation which is characterized by the geometrical buckling value B^2:

$$\nabla^2 f(\mathbf{r}) + B^2 f(\mathbf{r}) = 0 \tag{10.1}$$

A generic solution of the above equation is: $f(\mathbf{r}) = \alpha e^{i\mathbf{B}\cdot\mathbf{r}}$. In addition, the spatial dependence in each sub-assembly is eliminated in the homogeneous situation. And finally, the angular flux is expressed as:

$$\phi(\mathbf{r}, E, \hat{\Omega}) = \varphi(E, \hat{\Omega}) e^{i\mathbf{B}\cdot\mathbf{r}} \tag{10.2}$$

where $\mathbf{B}$: the buckling vector which satisfies that $\mathbf{B} \cdot \mathbf{B} = B^2$.

After substituting this factorized flux into the continuous-energy Boltzmann equation and with use of a linearly anisotropic collision approximation, the homogeneous B_1 equation is obtained as seen below:

$$[i\hat{\Omega}\cdot\mathbf{B}+\Sigma_t(E)]\varphi(E,\hat{\Omega})=\int_0^\infty\frac{1}{4\pi}\{\Sigma_{s0}(E'\to E)\varphi(E')+3\Sigma_{s1}(E'\to E)\hat{\Omega}\cdot\mathbf{J}(E')\}dE' + \frac{1}{4\pi K_{\text{eff}}}\int_0^\infty\chi(E'\to E)\nu\Sigma_f(E')\varphi(E')dE' \quad (10.3)$$

where $\mathbf{J}(E)$: the fundamental current which is based on the fundamental angular flux as in Eq (10.4).

$$\mathbf{J}(E)=\int_{4\pi}\hat{\Omega}\varphi(E,\hat{\Omega})d^2\Omega \quad (10.4)$$

In order to remove the direction dependence of both $\mathbf{B}$ and $\mathbf{J}$, it is supposed to be true that the current vector has the same direction as the buckling vector: $BJ(E)=\mathbf{B}\cdot\mathbf{J}(E)$.

From the point of view of the sub-assembly code, it is better to have direct access to scalar flux for manipulation. Thus, two integration operations are proposed to Eq (10.3). The first one is a simple integration over the whole solid angle. The second is the same integration but after being weighted by a factor: $\frac{1}{i\hat{\Omega}\cdot\mathbf{B}+\Sigma_t(E)}$. Therefore, the two scalar quantities involved B_1 equations are listed as:

$$iBJ(E)+\Sigma_t(E)\varphi(E)=\int_0^\infty\Sigma_{s0}(E'\to E)\varphi(E')dE'+\frac{1}{K_{\text{eff}}}\int_0^\infty\chi(E'\to E)\nu\Sigma_f(E')\varphi(E')dE' \quad (10.5)$$

$$\frac{iJ(E)}{B}=\frac{1}{\gamma\left[B,\Sigma_t(E)\right]\Sigma_t(E)}\left\{\frac{1}{3}\varphi(E)+\int_0^\infty\Sigma_{s1}(E'\to E)\frac{iJ(E')}{B}dE'\right\} \quad (10.6)$$

where $\gamma\left[B,\Sigma_t(E)\right]$ is a newly introduced variable and defined as follows:

$$\gamma\left[B,\Sigma_t(E)\right]=\begin{cases}\dfrac{1}{3}\dfrac{\frac{B}{\Sigma_t(E)}\arctan\frac{B}{\Sigma_t(E)}}{1-\frac{\Sigma_t(E)}{B}\arctan\frac{B}{\Sigma_t(E)}} & \text{if}\quad B^2>0\\ \dfrac{B^2}{3\Sigma_t(E)}\dfrac{\ln\frac{\Sigma_t(E)+Im(B)}{\Sigma_t(E)-Im(B)}}{2Im(B)-\Sigma_t(E)\ln\frac{\Sigma_t(E)+Im(B)}{\Sigma_t(E)-Im(B)}} & \text{if}\quad B^2<0\\ 1+\dfrac{4}{15}\left(\dfrac{B}{\Sigma_t(E)}\right)^2-\dfrac{12}{175}\left(\dfrac{B}{\Sigma_t(E)}\right)^4+\cdots & \text{if}\quad B^2\approx 0\end{cases} \quad (10.7)$$

One remark should be made in order to ensure that $iJ(E)/B$ always remains real and finite when the buckling value approaches zero. In fact, $J(E)$ could be a real or imaginary number which depends on the homogeneous medium. If it is in super-critical state, $J(E)$ is imaginary and B is a positive number. If the medium is in sub-critical state, $J(E)$ is real and B is an imaginary number.

Then, the diffusion coefficient according to Fick's law is introduced as in Eq (10.8).

$$d(B,E) = \frac{1}{B}\frac{iJ(E)}{\varphi(E)} \tag{10.8}$$

Replacing the above diffusion coefficient in Eq (10.5) and Eq (10.6), another set of B_1 equations could be rewritten as Eq (10.9) and Eq (10.10).

$$\left[\Sigma_t(E) + d(B,E)B^2\right]\varphi(E) = \int_0^\infty \Sigma_{s0}(E' \to E)\varphi(E')dE' + \frac{1}{K_{\text{eff}}}\int_0^\infty \chi(E' \to E)\nu\Sigma_f(E')\varphi(E')dE' \tag{10.9}$$

$$d(B,E) = \frac{1}{\gamma\left[B, \Sigma_t(E)\right]\Sigma_t(E)}\left\{\frac{1}{3} + \int_0^\infty \Sigma_{s1}(E' \to E)d(B,E')\frac{\varphi(E')}{\varphi(E)}dE'\right\} \tag{10.10}$$

With knowledge of the continuous-energy B_1 homogeneous equations, their multi-group forms could be easily obtained via energy collapsing. They are given in Eq (10.11) and Eq (10.12) respectively.

$$\Sigma_{t,g}\varphi_g + d_g B^2\varphi_g = \sum_{g'=1}^{G}\Sigma_{s0}^{g' \to g}\phi_{g'} + \frac{1}{K_{\text{eff}}}\sum_{g'=1}^{G}\chi(g' \to g)\nu\Sigma_{f,g'}\varphi_{g'} \tag{10.11}$$

$$d_g = \frac{1}{\Sigma_{t,g}\gamma_g}\left\{\frac{1}{3} + \sum_{g'=1}^{G}\Sigma_{s1}^{g' \to g}\frac{\varphi_{g'}}{\varphi_g}d_{g'}\right\} \tag{10.12}$$

The definitions of multi-group constants are listed as below:

- φ_g: multi-group flux in group g

$$\varphi_g = \int_{E \in g}\varphi(E)dE \tag{10.13}$$

- d_g: multi-group diffusion coefficients in group g:

$$d_g = \frac{1}{\varphi_g}\int_{E \in g} d(B,E)\varphi(E)dE \tag{10.14}$$

- γ_g: one approximation is used here to simplify the energy collapsing on γ which supposes that:

$$\gamma_g \approx \gamma(B, \Sigma_{t,g}) \tag{10.15}$$

- $\Sigma_{i,g}$: one-dimensional multi-group cross section, for example: total collision, absorption, fission production.

$$\Sigma_{i,g} = \frac{\int_{E \in g}\Sigma_i(E)\varphi(E)}{\int_{E \in g}\varphi(E)dE} \tag{10.16}$$

- $\Sigma_{s0}^{g'\to g}$: the 0^{th} order moment of the multi-group scattering cross section

$$\Sigma_{s0}^{g'\to g} = (\Sigma_{t,g'} - \Sigma_{a,g'}) \times P(g' \to g) \tag{10.17}$$

where $P(g' \to g)$ is multi-group energy transfer probability.

- $\Sigma_{s1}^{g'\to g}$: the 1^{st} order moment of multi-group scattering cross section

$$\Sigma_{s1}^{g'\to g} = \Sigma_{s0}^{g'\to g} \times \overline{\mu}^{g'\to g} \tag{10.18}$$

where $\overline{\mu}^{g'\to g}$ stands for the averaged scattering angle cosine value from group g' to g.

Please note that φ_g, d_g, γ_g are the unknowns while other multi-group cross sections are known which could be obtained from the TRIPOLI-4® point-wise simulation. The detailed B_1 equations resolving methodology will follow in the next section.

10.2 Algorithm implemented in TRIPOLI-4®

This section is specified to introduce the algorithm implemented in TRIPOLI-4® for solving the coupled B_1 homogeneous equations (10.11) and (10.12). The fission power iteration procedure is necessary to obtain the multi-group solutions. The iteration loops are separated into two levels: the inner loop which is executed with a fixed B^2 value in order to get the converged multi-group flux φ_g and K_{eff}; the outer loop which is designed to vary the buckling value B^2 according to the rule expressed in Eq (10.19) until $K_{\text{eff}} = 1$.

$$B^2_{(n+1)} = B^2_{(n)} + \left(\frac{1}{K_{\text{eff}}^{exp}} - \frac{1}{K_{\text{eff}}^{(n)}}\right) \frac{\overline{\nu\Sigma_f}^{(n)}}{\overline{d}^{(n)}} \tag{10.19}$$

- (n): the index for the outer iteration loop;

- K_{eff}^{exp}: the expected multiplicative factor given by users;

- $\overline{\nu\Sigma_f}^{(n)}$: the n^{th} loop converged flux weighted average production cross section, calculated as in Eq (10.20).

$$\overline{\nu\Sigma_f}^{(n)} = \frac{\sum_{g=1}^{G} \nu\Sigma_{f,g}\varphi_g^{(n)}}{\sum_{g=1}^{G} \varphi_g^{(n)}} \tag{10.20}$$

- $\overline{d}^{(n)}$: the n^{th} loop converged flux weighted average diffusion coefficient, calculated as in Eq (10.21).

$$\overline{d}^{(n)} = \frac{\sum_{g=1}^{G} d_g^{(n)}\varphi_g^{(n)}}{\sum_{g=1}^{G} \varphi_g^{(n)}} \tag{10.21}$$

In fact, Eq (10.19) is deduced from the one-group multiplicative factors relationship:

$$K_{\text{eff}} = \frac{K_\infty}{1 + M^2B^2} \tag{10.22}$$

where

- K_∞: the infinite multiplicative factor which can be obtained via mono-energy macroscopic cross sections:

$$K_\infty = \frac{\nu\Sigma_f}{\Sigma_a} \tag{10.23}$$

- M^2: the migration area which is expressed as follows in one-group diffusion theory:

$$M^2 = \frac{D}{\Sigma_a} \tag{10.24}$$

After having inverted Eq (10.22), a linear relationship is obtained as in Eq (10.25). Thanks to the latter, the rule according to which B^2 is varied until the critical state is reached.

$$\delta B^2 = \frac{\nu\Sigma_f}{D}\delta(\frac{1}{K_{\text{eff}}}) \tag{10.25}$$

A detailed calculation scheme is plotted in Figure 10.1. The left part represents the point-wise TRIPOLI-4® simulation; while the right part stands for the routine in charge of solving B_1 homogeneous equations. Two bridges connect the left and right parts in the algorithm scheme. The first one is the converged multi-group cross sections produced by the point-wise TRIPOLI-4® simulation and will be used as known variables for solving B_1 equations. The other is the solved leakage coefficients $d_g B^2$ from B_1 equations and will be used in the point-wise TRIPOLI-4® simulation as a fictive cross section.

Some specific details need to be provided for the three criteria involved in the above algorithm scheme. The first criterion is used to judge if the multi-group cross sections calculated by the point-wise TRIPOLI-4® simulation are well converged. In order to avoid the convergence problem for certain groups, defined batch numbers can be imposed by users. For example, the cycle length used to obtain the results in section 10.3 are 4000 batches (10000 particles per batch) which explains the statistical deviations of the multi-group total cross sections at the order of magnitude of $10^{-3}\%$ for the important energy groups.

The second criterion is selected for the solution of B_1 homogeneous equations. Since the right half routine in Figure 10.1 is based on a deterministic method, the chosen convergence criterion of the K_{eff} value is rather strict. This means that $|K_{\text{eff}} - 1| < 0.00001$.

The third criterion involves determining when the whole simulation procedure will be ended. It depends on the point-wise TRIPOLI-4® simulated K_{eff} value. The latter should satisfy the condition as follows:

$$\left|K_{\text{eff}} - K_{\text{eff}}^{\text{exp}}\right| < 0.001 + 3\sigma \tag{10.26}$$

where σ is related to the TRIPOLI-4® estimated K_{eff} value and should be lower than 20 pcm. And 0.001 (100 pcm) stands for our convergence tolerance. This is a compromise between simulation time and the precision of the calculated B^2 value, because the routine in charge of solving B_1 equations has not yet been parallelized.

As presented in the previous section, buckling value B^2 could be positive (super-critical medium) or negative (sub-critical medium). Thus, different treatments should be provided for each case.

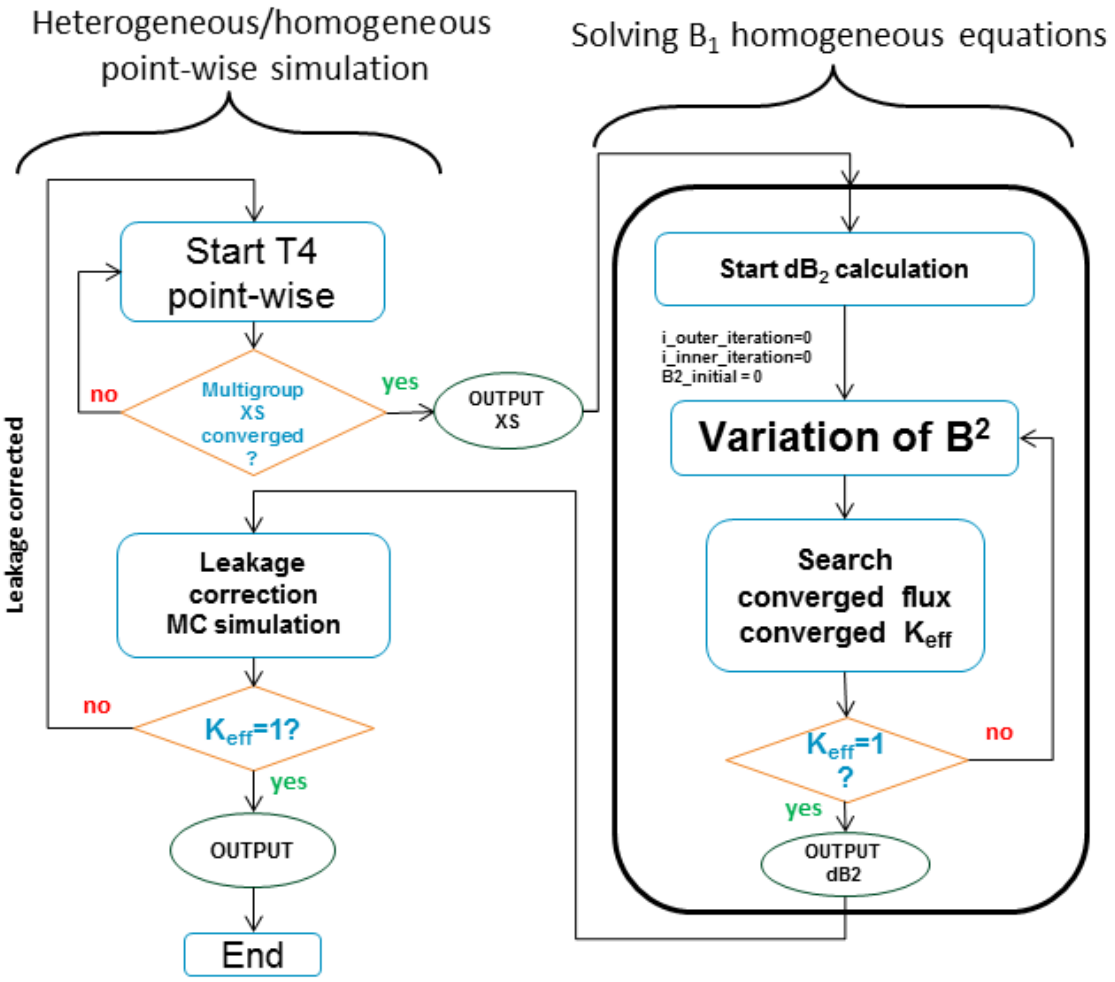

Figure 10.1: Leakage model algorithm in the TRIPOLI-4® code

1- if $B^2 > 0$, the leakage coefficients $d_g B^2$ are considered as multi-group fictive absorption cross sections. It could be treated by changing the neutron simulation weight as in Eq (10.27). In this work, the correction factor is applied to each neutron simulation weight before doing the collision in the transport procedure. So for the first cycle calculation where the leakage coefficients $d_g B^2 = 0$, the corrective factor is equal to 1.

$$\omega' = \omega \times \frac{\Sigma_t(\mathbf{r}, E)}{\Sigma_t(\mathbf{r}, E) + d_g B^2} \tag{10.27}$$

Doing things this-way is equivalent to the one proposed by Martin in his thesis work[71]. Within the framework of the multi-group Monte-Carlo code DRAGON[42], there is also a B_1 leakage model which uses the calculated leakage coefficients $d_g B^2$ to estimate a leakage probability P_{leak} expressed in Eq (10.28). This leakage probability will be used to determine whether the neutron will escape or stay in the geometry.

$$P_{\text{leak}} = \frac{d_g B^2}{d_g B^2 + \Sigma_{t,g}} \tag{10.28}$$

Another point should be underlined is that as DRAGON is a multi-group Monte-Carlo code, it is natural to match every group leakage coefficient $d_g B^2$ with the corresponding group total cross section $\Sigma_{t,g}$. However, it is different in the TRIPOLI-4® case because the latter is a continuous-energy Monte-Carlo code. Therefore the same multi-group leakage coefficient $d_g B^2$ is used for all the neutrons whose incident energy belongs to group g.

2- if $B^2 < 0$, the leakage coefficient $d_g B^2$ could be moved from the left disappearance side to the right production side of the Boltzmann equation. Thus, it will be considered as a multi-group fictive production cross section. For the moment, this sub-critical case is not yet considered in the TRIPOLI-4® code because according to the author's opinion this negative situation is not really physically justified.

There is one deficiency associated with this algorithm which is not able to estimate the statistical error for the critical buckling value B^2. For each single simulation, only one value of B^2 is obtained. A prospective exists in parallelizing the routine of solving B_1 equations.

10.3 Validation of the B_1 leakage model

This section is devoted to validating the implemented leakage model in the TRIPOLI-4® code. The validation for a Monte-Carlo concerned method is always difficult because the method itself is usually assumed to be the reference compared to other deterministic codes. There has not been a clear validation procedure so far. Here, we propose an analytical case which will be ultimately termed as "numerical experiment" and is calculated with a continuous-energy TRIPOLI-4® simulation. The latter consists of a one-dimensional homogeneous critical geometry. Thanks to its natural criticality, its flux spectrum, reaction rates and produced multi-group cross sections will be used as references for those artificial leakage models implemented in different codes namely, TRIPOLI-4®; Serpent and ECCO.

The validation work will be performed by using a homogeneous assembly from the Zero Power Plutonium Reactor Double Column Fuel (ZPPRDCF)[87, 86, 52]. This configuration represents an important leakage probability (42%) with its infinite multiplicative factor $K_{\text{eff}} = 1.67$. This feature makes the leakage treatment work more complicated. Several parameters (B^2, D_g, ϕ_g) calculated with the four methods mentioned above will be compared respectively. To make sure the results are comparable with each other, the same JEFF3.1.1 library with probability tables is used in different codes. At the end, the multi-group cross sections produced by the leakage model in TRIPOLI-4® will be used in core calculation codes: the TRIPOLI-4® multi-group simulation and PARIS/SNATCH code system[33]. Their simulation results (K_{eff}, neutronic balance) will also be compared to the reference values from the numerical experiment.

10.3.1 Critical buckling value comparison

Calculating a critical buckling value is not difficult for the sub-assembly codes including leakage models. However, the real challenge is to find out the reference value from a critical experiment. This question turns to figuring out the macroscopic distribution function $f(\mathbf{r})$ in Eq (10.1).

Figure 10.2 illustrates the geometry of the above described critical experiment which is numerically simulated. It is indeed an 1D homogeneous slab with a critical height H_c^*. With this 1D configuration, the macroscopic distribution function is simplified to $f(z)$ depending only on the direction of its height. Moreover, besides these two extremities, there are two identical extrapolation distances d. Normally, the sum of these three parts $H_c = H_c^* + 2d$ could help to deduce the critical buckling value according to Eq (10.29). As a matter of fact, we have no information about calculating this extrapolation distance exactly. However, it is certain that the macroscopic distribution form (the red curve in Figure 10.2) respects a cosine function $\alpha\cos(B_c z)$. This offers a possibility to obtain the critical buckling B_c via doing a fit for the distribution function. Consequently, the last point to verify is which physical variable is well presented by the macroscopic distribution function $f(z)$.

$$B_c = \frac{\pi}{H_c} \tag{10.29}$$

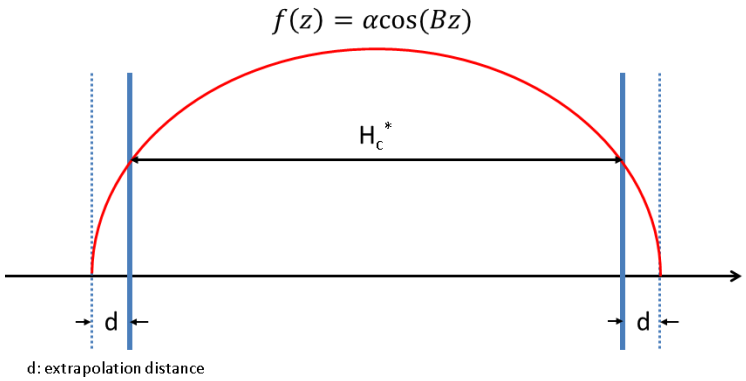

Figure 10.2: Illustration of the geometry of the analytical case

Mostly, $f(z)$ is considered as the scalar flux $\phi(z)$ integrated over the whole energy domain. This is perfectly valid only in the context of the fundamental mode approximation applied over a global reactor featuring a periodic lattice of unit cell or sub-assemblies. As for the nuclear reactor experimenters, they always use the macroscopic reaction rate (for example: fission rate of ^{239}Pu) to deduce the buckling value. The method is equal to using the global energy scalar flux $\phi(z)$ as $f(z)$.

Here, we seek a more precise expression of the distribution function in a real critical homogeneous configuration as shown in Figure 10.2. The detailed formulation is given in Appendix D. The deduction result shows that $f(z)$ is in fact an inner product of two fluxes described in Eq (10.30).

$$f(z) = \int_0^\infty \varphi^+(E)\phi(z,E)dE \tag{10.30}$$

The definitions of these two fluxes are respectively:

- $\varphi^+(E)$: the adjoint fundamental flux in a critical homogeneous sub-assembly which is independent of space.

- $\phi(z, E)$: the direct flux in a critical core which is dependent on space and energy.

In our test, $\varphi^+(E)$ is calculated under 1968-groups by two different methods. One is the newly developed functionality in the TRIPOLI-4® code which enables users to calculate continuous energy adjoint flux with the Monte-Carlo method and then collapses them into multi-group flux[26]. This could be considered as a reference method to calculate adjoint flux although this new functionality cannot be used under the leakage model calculation mode. So the only approximation used here is that we neglect the difference between an infinite adjoint flux spectrum and a critical one. The other method of obtaining the 1968-groups adjoint flux is performed in two steps within the ERANOS code system. The ECCO code is at first used to generate 1968-groups leakage-corrected cross sections as well as the critical buckling value. A reflective homogeneous core is then calculated taking into consideration the above critical buckling by BISTRO[43]. The latter is able to provide the 1968-groups adjoint flux. As for the direct flux $\phi(z, E)$, it is easy to get it via the continuous-energy TRIPOLI-4® simulation.

The two sets of adjoint fluxes are then used as microscopic cross sections in a continuous energy TRIPOLI-4® simulation. The fictitious reaction rates representing $f(z)$ are scored in different position along the direction z. Finally, with knowledge of the distribution curve, we can deduce the corresponding buckling value with the help of a cosine fit.

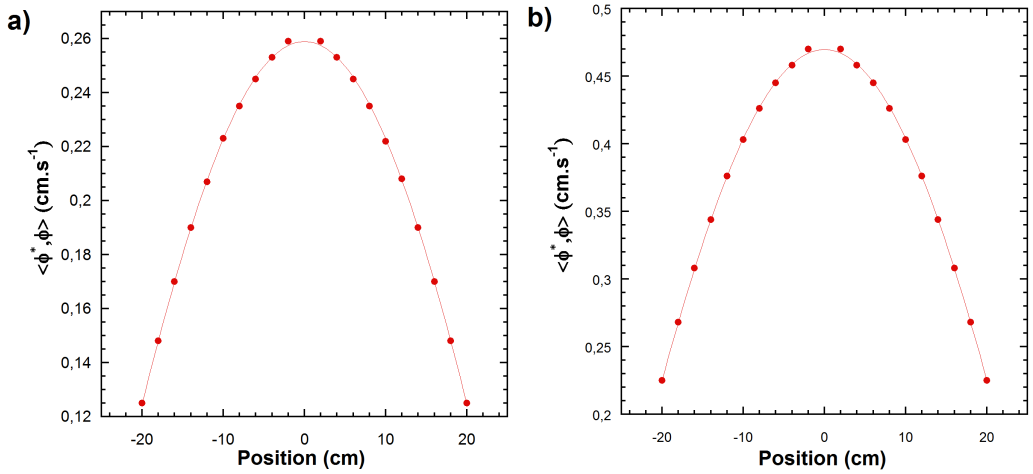

Figure 10.3: **a)** Axial distribution of the TRIPOLI-4® calculated adjoint flux weighted reaction rates **b)** Axial distribution of the ERANOS calculated adjoint flux weighted reaction rates

The two curves obtained with the TRIPOLI-4® (left) and ERANOS (right) adjoint flux are shown in Figure 10.3. The dots are the measured scores and the lines correspond to their fitting curves. In the above figures, the statistical deviations are not plotted because the obtained results are quite well converged. Their relative deviations are limited in the order of magnitude of 10^{-1}%. The critical height of the homogeneous sub-assembly ZPPR-DCF is at 51.4 cm. In order to ignore the edge impact, the cosine fit is done within the region $[-20;\ 20]\,cm$. The results are presented in Table 10.1 which also contains the critical buckling values calculated with the artificial leakage models in TRIPOLI-4®, Serpent2.1.16 and the ECCO codes under 33-group energy structure.

	Numerical Experiment		TRIPOLI-4®	Serpent	ECCO
	curve a)	curve b) **ref**			
B^2 $(10^{-3} \cdot cm^{-2})$	2.854	2.869	2.812	2.807	2.747
Rel. diff (%)	-0.52	—	-2.0	-2.2	-4.3

Table 10.1: Critical buckling comparisons among different leakage model codes and numerical experiments.

In Table 10.1, the value extracted from curve **b)** is used as the reference one because the 1968-group adjoint flux calculated by TRIPOLI-4® is performed under infinite spectrum conditions. A tiny difference of 0.52% is observed between the results of the two curves. As for the results from the three leakage model codes, TRIPOLI-4® gave the closest value with respect to the reference one. This is thanks to our iteration algorithm between the point-wise Monte-Carlo simulation and the routine for solving the B_1 homogeneous equations. This procedure ensures a final critical state from the point of view of the point-wise TRIPOLI-4® simulation. This means that in the TRIPOLI-4® leakage model, critical flux weighted multi-group constants are used to solve the B_1 equations; whereas in Serpent, the multi-group constants are weighted by infinite flux spectrum. Another reason explaining the difference between TRIPOLI-4® and Serpent results is their standard deviations associated with the produced multi-group cross sections. In this fast spectrum sub-assembly case, important uncertainties show up in the thermal groups which produce some unreliable cross sections. Therefore, the discrepancies between low energy group cross sections impact the deterministic solution of B_1 equations. However in any case, these two Monte-Carlo codes including the leakage models agree quite well for the calculated buckling values. Otherwise, greater discrepancy (4.3%) is found between the ECCO calculation and the reference value.

10.3.2 Comparisons of critical flux spectrum, D_g and leakage rate

Critical flux spectrum comparison

In Figure 10.4 ,we compare the critical flux spectra calculated with different leakage model codes as well as the one extracted from the numerical experiment. No error bars are given for the numerical experiment result because it is well converged and the standard deviations are around 0.01%. These flux spectra are all normalized to achieve the condition: $\sum_{g=1}^{G} \phi_g = 1$ where $G = 33$.

According to Figure 10.4 **a)**, all the four curves overall have the same tendency which proves that the leakage models in TRIPOLI-4®, Serpent and ECCO are able to reproduce the form of a realistic critical flux spectrum. The gray zone plotted in Figure 10.4 **b)** indicates the energy domain of interest, containing more than 95% of neutron production.

The relative differences between each leakage model result and the reference one within the interesting energy domain are plotted in Figure 10.5. It can be seen that on the high energy half part, the three leakage models have under-estimated the flux. And on the left half part, the leakage models have on the contrary over-estimated the critical flux compared with the numerical experiment result.

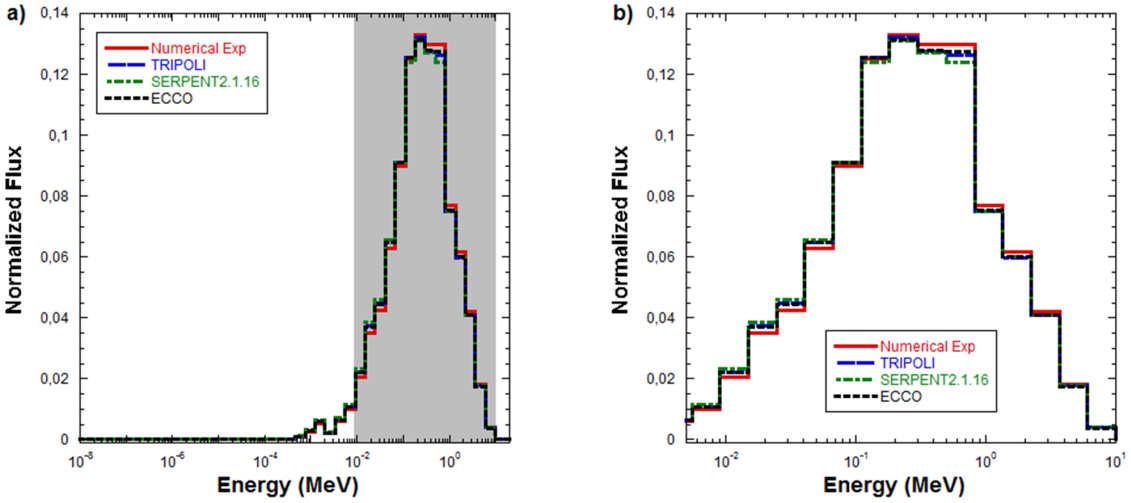

Figure 10.4: Normalized critical flux spectra comparison

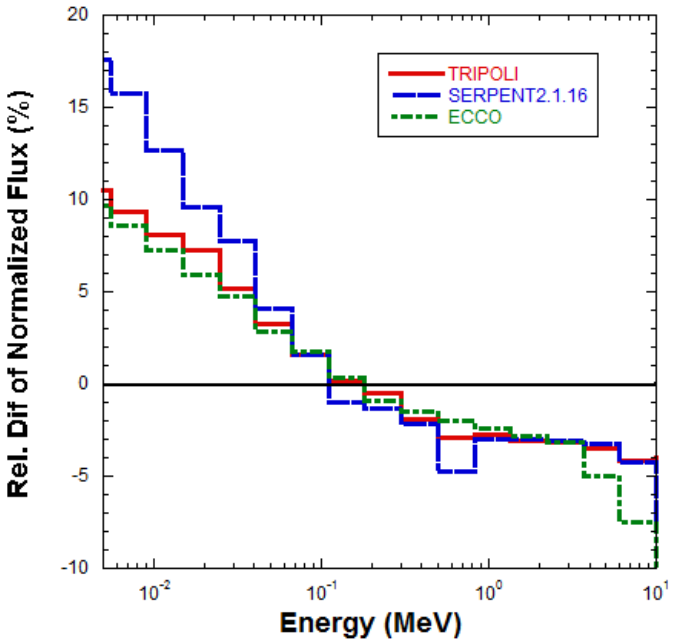

Figure 10.5: Relative difference between leakage model simulated critical flux spectra with the reference one from numerical experiment

Diffusion coefficient comparison

Obtaining the diffusion coefficient is not our original goal because transport core calculations will be fed with our produced multi-group cross sections, rather than a diffusion core calculation. However, we could always compare the obtained diffusion coefficients from different codes in order to evaluate the artificial leakage rates with respect to the real leakage terms from the numerical experiment.

Figure 10.6 **a)** shows the 33-group diffusion coefficients obtained respectively with

the TRIPOLI-4® continuous-energy calculation (TRIPOLI_PCT_trans), the TRIPOLI-4® leakage model (TRIPOLI_MF), the Serpent and ECCO calculations. Please note that the TRIPOLI_PCT_trans result is obtained by using the P_1 approximation formula:

$$D_g = \frac{1}{3\Sigma_{tr,g}} = \frac{1}{3\left(\Sigma_{t,g} - \overline{\mu}_g \Sigma_{s,g}\right)} \tag{10.31}$$

with $\Sigma_{t,g}$, $\Sigma_{s,g}$, and $\overline{\mu}_g$ obtained with the Monte-Carlo simulation. The three leakage models make use of the B_1 approximation. Therefore, it is normal that the red curve differ a bit from the others.

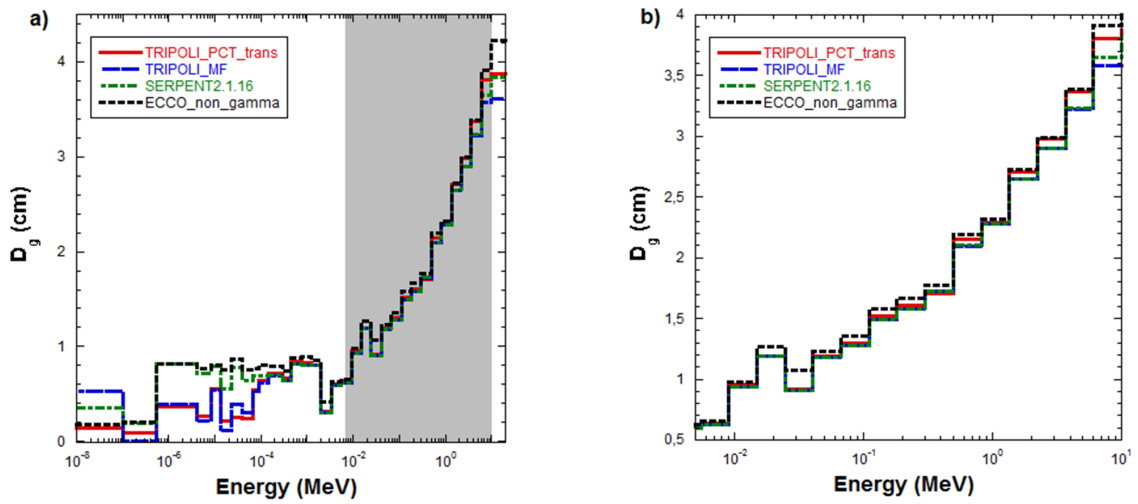

Figure 10.6: Diffusion coefficient comparison

From Figure 10.6 **a)**, a similar tendency is shown by the three leakage model curves. However, there are some important discrepancies in the epithermal energy domain (1eV $\sim$ 100 eV) which come from poor statistical scores and do not retain our interest.

The gray zone attracts more attention for the same reason as for the above critical flux spectrum and so it is specially plotted in Figure 10.6 **b)**. We can see that the leakage model curves agree rather well among themselves even with the P_1 transport approximation calculation. The relative difference between the Serpent/ECCO and TRIPOLI-4® calculated diffusion coefficients are shown in Figure 10.7. It proves that a very satisfactory agreement is found between the Serpent and TRIPOLI-4® leakage models. Larger discrepancies are revealed between ECCO and TRIPOLI-4® results.

Leakage rate comparison

Previously, we focused on comparing every single parameter calculated from leakage models. However, the physical motivation of leakage models consist in trying to simulate artificially the approximated leakage rates ($d_g B^2 \phi_g$) in an appropriate manner. In order to verify the reliability of our implemented leakage model, we shall compare the simulated leakage rates to the real one which is the score of neutrons traveling through the boundary

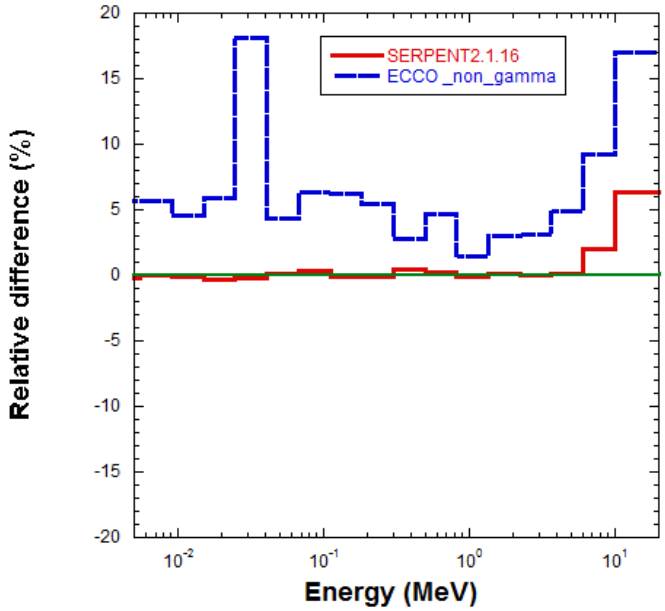

Figure 10.7: Relative difference of diffusion coefficients between Serpent/ECCO and the TRIPOLI-4 leakage model calculations

surface in the numerical experiment.

In Figure 10.8, the discrepancies of leakage rates between the three leakage models and the numerical experiment are plotted versus energy groups. It could be observed that for all 3 leakage model codes, there is a compensation effect between the higher energy part (over-estimated leakage) and the lower energy part (under-estimated leakage). The absolute discrepancies in each group are less than 0.005. This effect comes from the intrinsic approximation of the B_1 fundamental mode which assumes that the neutron spectrum is not dependent on spatial position within the sub-assembly. This is not the case in a real sub-assembly where the neutron spectrum is harder on the edge than in the center where the fundamental mode approximation is more suitable. Thus, there are less fast neutrons escaping on the edge of a real geometry. This explanation matches well with the over-estimation peak around 2 MeV.

10.3.3 Application of leakage-corrected cross sections in core calculation

In this section, we return back to the original motivation of this work: performing core calculations with the leakage-corrected multi-group cross sections. These constants can be used directly in a Monte-Carlo based TRIPOLI-4® multi-group calculation or converted to a compatible format and then used in an S_n method based PARIS[33] calculation. The obtained multiplicative factors and their discrepancies compared with the numerical experimental reference value are shown in Table 10.2. Through ΔK_{eff} values and their corresponding standard deviations, consistent results are found between the two transport core calculation codes by using the same TRIPOLI-4® leakage model produced multi-group constants. Compared to the reference K_{eff}, they both under-estimated about 300 pcm using these multi-group constants produced from the TRIPOLI-4® leakage model.

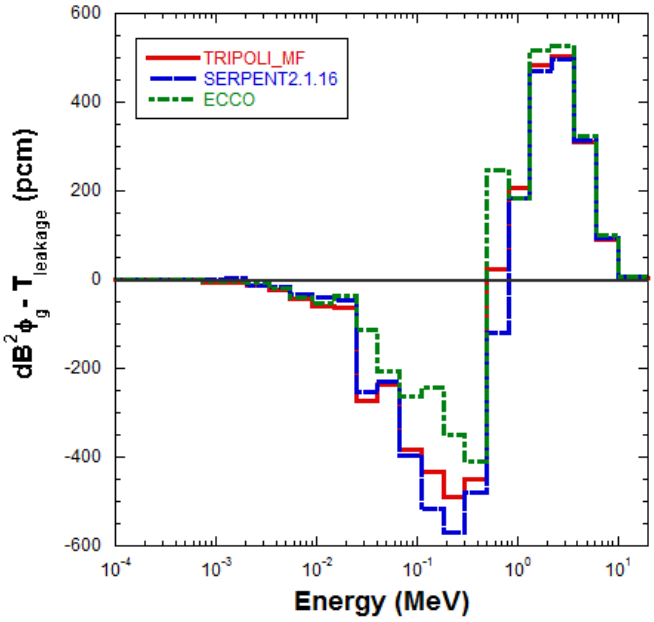

Figure 10.8: Leakage rates comparison

Meanwhile, another set of multi-group cross sections are directly produced with the critical experiment geometry and they are considered as reference multi-group constants and used in the same core codes. Their K_{eff} results are shown in Table 10.3. So if we compare the K_{eff} values in Table 10.2 and Table 10.3 vertically, a good agreement is deduced between our leakage model produced multi-group constants and those directly generated from critical geometry. It can be observed that both sets of multi-group constants show the same order of magnitude of discrepancies compared to the reference K_{eff} value. This assures us that the newly implemented leakage model in TRIPOLI-4® is pertinent. It must be emphasized that all the multi-group constants used in core calculations are always treated with the IGSC method (using the Todorova current) to guarantee their adequate performance in core calculations. Moreover, the multi-group scattering matrix used in PARIS calculations (both Table 10.2 and Table 10.3) are limited to the fifth order (P_5[1])

	Numerical Experiment	TRIPOLI-4® MG	PARIS (P_5)
K_{eff}	0.99923 ± 0.00005	0.99657 ± 0.00012	0.99574
ΔK_{eff}	—	-0.00266 ± 0.00013	-0.00349 ± 0.00005

Table 10.2: Comparison of K_{eff} values in multi-group TRIPOLI-4® and PARIS calculations with use of 33-group cross sections produced by the TRIPOLI4® leakage model

Furthermore, detailed analysis is done for the flux spectrum and neutronic balance. Figure 10.9 **a)** shows the normalized flux spectra from the multi-group TRIPOLI-4® (T4_LM_HMG) and PARIS (T4_LM_PARIS) simulations. Both of them use the multi-

[1]In TRIPOLI-4® calculation of anisotropy moments which will be used to construct the scattering cross sections for PARIS simulation, the IGSC method is only applied to first order moment.

	Numerical Experiment	TRIPOLI-4® MG	PARIS (P_5)
K_{eff}	0.99923 ± 0.00005	0.99685 ± 0.00012	0.99581
ΔK_{eff}	—	-0.00238 ± 0.00013	-0.00342 ± 0.00005

Table 10.3: Comparison of K_{eff} values in multi-group TRIPOLI-4® and PARIS calculations with use of 33-group cross sections produced with critical experiment geometry

group constants produced by the leakage model in TRIPOLI-4®. The reference numerical experiment flux spectrum (point-wise reference) is shown as well. Overall, these three spectra are well superimposed.

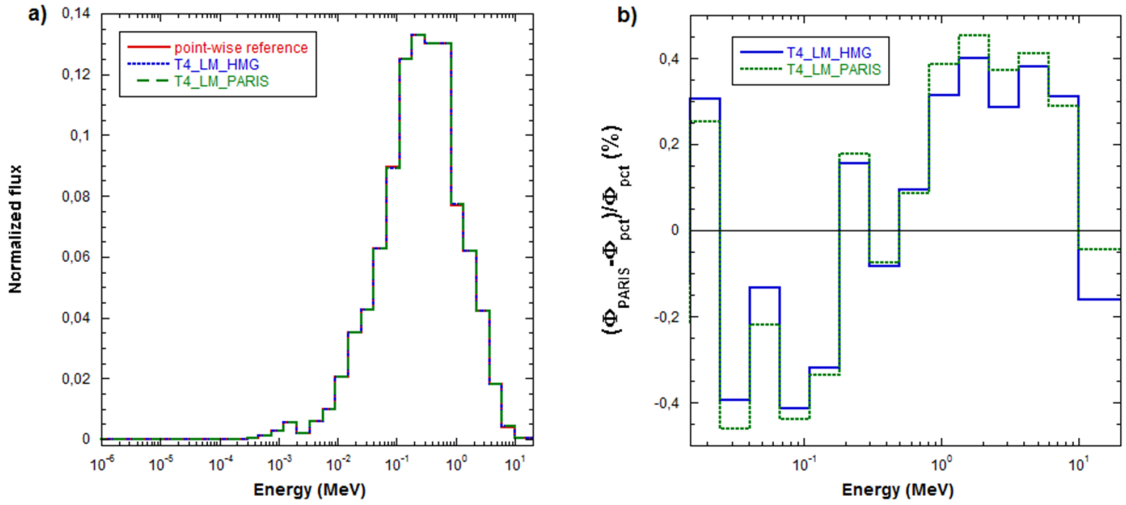

Figure 10.9: Critical flux spectra comparisons

In addition to this, the relative differences between multi-group TRIPOLI-4® or PARIS calculated flux spectra and the reference spectrum are plotted in Figure 10.9 **b)**. It must be pointed out that Figure 10.9 **b)** covers partially the energy domain which contains 98% of the fission production rate. It has been seen that their relative differences are quite tiny which are less than 0.5%. This satisfying result confirms that the multi-group constants produced by the TRIPOLI-4® leakage model are suitable to be used in core simulation codes to reproduce consistent flux spectra.

Figure 10.10 shows the reaction rate discrepancies. Part **a)** illustrates the differences of production rates, absorption rates and leakage rates between multi-group and point-wise TRIPOLI-4® simulations. Part **b)** presents the differences of production rates and absorption rates between PARIS (using TRIPOLI-4® leakage model produced 33-group constants) and point-wise TRIPOLI-4® simulations. Both of them show that the 33-group constants produced by the TRIPOLI-4® leakage model have mostly under-estimated the production rate as well as the absorption rate. The oxygen resonance peak located at 400 keV induced about -50 pcm of production. Another resonance peak situated around 130 keV is probably from the structure isotope (^{56}Fe; ^{52}Cr). There is a deficiency in the PARIS calculation that does not offer us the possibility of obtaining exact neutron leakage rate. Therefore, the leakage rate comparison is only available in Figure 10.10 **a)**. It is

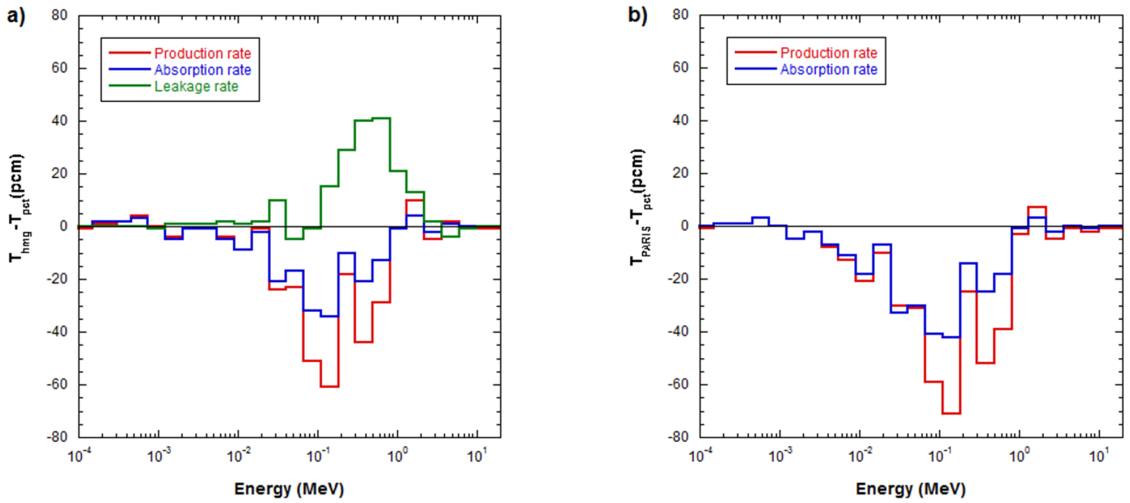

Figure 10.10: **a)**: Reaction rates comparisons between multi-group and point-wise TRIPOLI-4® simulations; **b)**: Reaction rates comparisons between the PARIS and point-wise TRIPOLI-4® simulations

normal to find a under-estimation tendency for production rate since the leakage rate is on the contrary over-estimated. However, the discrepancies compared to reference reaction rates are less than 60 pcm in any group.

In addition to this, we would like to compare our produced leakage-corrected multi-group constants with those from the ECCO code. The basic idea is using them in the PARIS calculation. In Table 10.4, results from the ECCO-PARIS and TRIPOLI-4®-PARIS calculations are respectively compared with the reference one. Here, the scattering matrix produced by both TRIPOLI-4® and ECCO are limited to $l = 1$. It could be concluded from Table 10.4 that similar estimations of K_{eff} are obtained between using the TRIPOLI-4® and ECCO leakage models produced multi-group constants.

	Numerical Experiment	TRIPOLI-4®-PARIS (P_1)	ECCO-PARIS (P_1)
K_{eff}	0.99923 ± 0.00005	0.99440	0.99447
ΔK_{eff}	——	-0.00483 ± 0.00005	-0.00476 ± 0.00005

Table 10.4: Comparison of K_{eff} values with use of the ECCO and TRIPOLI-4® leakage model produced 33-group cross sections in PARIS calculations

In order to better understand where the difference of K_{eff} comes from, we compare respectively the production rates from TRIPOLI-4®-PARIS and ECCO-PARIS simulations to the reference one from the numerical experiment in Figure 10.11. Generally, the two simulations have both under-estimated the production rate which is consistent with the multi-group TRIPOLI-4® simulation. However, the ECCO-PARIS calculation showed more discrepancies than the TRIPOLI-4®-PARIS simulation in the high energy domain and behaved similarly in lower energy domain.

At the end of this subsection, analysis work is carried out on the fission rate distribution

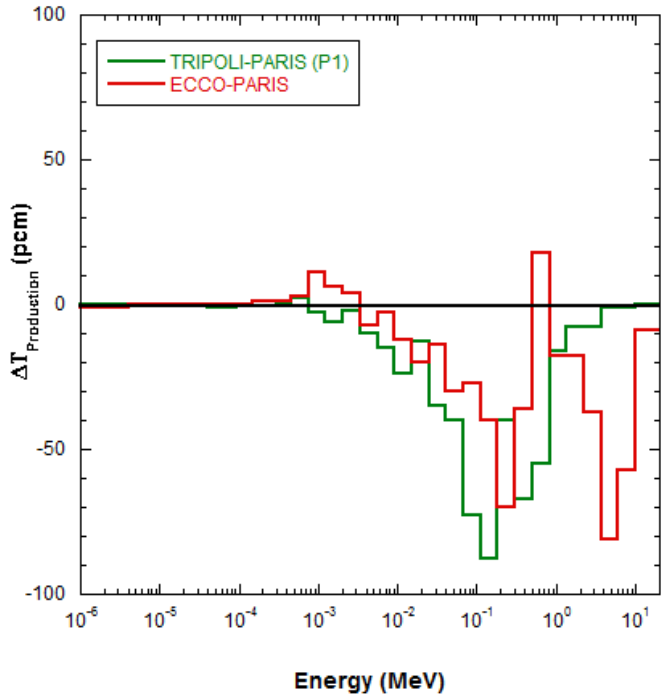

Figure 10.11: Production rate comparison between PARIS (using respectively TRIPOLI-4® leakage model and ECCO produced 33-groups constants) and referential point-wise TRIPOLI-4® simulations

in the 1D critical geometry. The point-wise TRIPOLI-4® simulation provides the reference values which are plotted in Figure 10.12**a)**. It shows clearly that the central part of the core contributes the most important fission reactions. Comparisons are then made between the PARIS simulations results and the previous reference result. It should be noted that three different sets of multi-group constants are used which are namely: the 33-group constants produced by TRIPOLI-4® for the critical geometry (Figure 10.12**b)**); the 33-group constants produced by the TRIPOLI-4® leakage model (Figure 10.12**c)**); the 33-group constants produced by ECCO (Figure 10.12**d)**). All the discrepancy values are expressed in units of pcm. If we take a vertical look at these three figures, it can be seen that their discrepancies are gradually enforced from the natural leakage case to the TRIPOLI-4® leakage model and then to the ECCO leakage model. However, the discrepancies using these three sets of multi-group constants in the PARIS calculation compared to the reference case are quite small and no more than 10 pcm per *cm* in the whole region.

10.3.4 Impact of leakage model

Before ending the leakage model validation work, it is of interest to show its impact on a core calculation, especially when considering the calculations using infinite flux spectrum weighted multi-group constants. This subsection focuses on comparing three important physical parameters: flux spectrum, effective multiplicative factor and fission production rate.

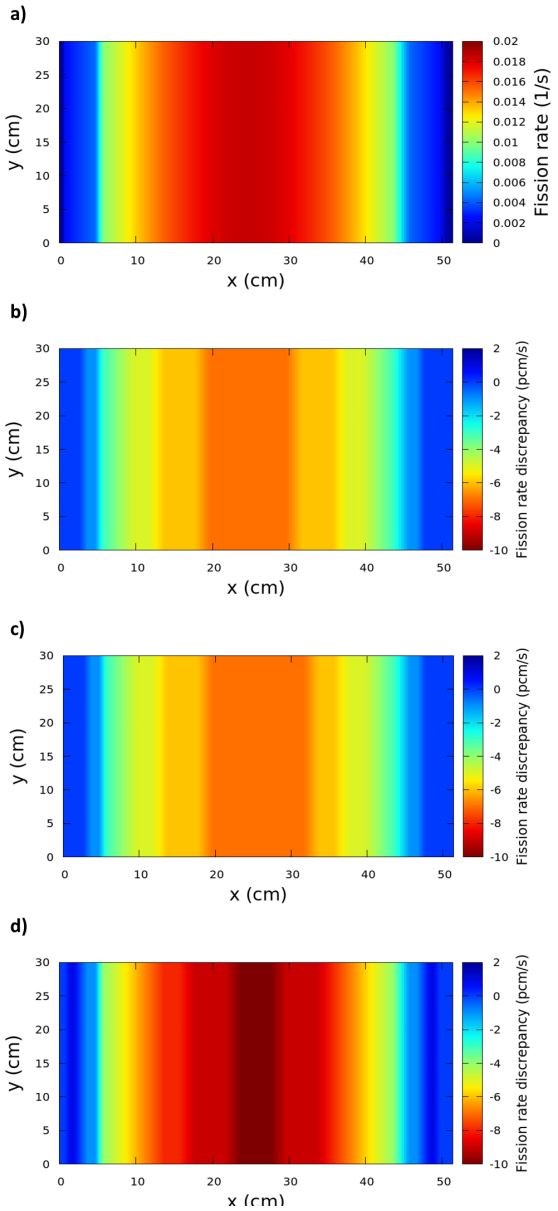

Figure 10.12: **a)**: Reference fission rate spatial distribution; **b)**: Discrepancy of fission rate spatial distribution between PARIS (using 33-group constants produced by TRIPOLI-4® for the critical geometry) and reference calculations; **c)**: Discrepancy of fission rate spatial distribution between PARIS(P_5) (using 33-group constants produced by TRIPOLI-4® leakage model) and reference calculations; **d)**: Discrepancy of fission rate spatial distribution between PARIS(P_1) (using 33-groups constants produced by ECCO) and reference calculations

Flux spectrum comparison

First, we shall compare the difference between the infinite flux spectrum and critical one. They are plotted in Figure 10.13**a)** with red and blue curves respectively. We must specify that both of them come from point-wise TRIPOLI-4® simulations. The infinite spectrum is obtained under reflective boundary conditions while the critical spectrum is obtained

via the leakage model in the TRIPOLI-4® code. No statistical errors are shown in figures because they are well converged. In the important energy groups, the relative deviations are in the order of magnitude of 10^{-2}%. It can be observed that the critical flux spectrum is harder than the infinite one. This is totally reasonable because, in infinite geometry, neutrons could be more easily slowed-down rather than directly escape from the geometry as in the critical case. Their relative difference is plotted in Figure 10.13**b)**. It again shows the visible discrepancies between infinite and critical flux spectra.

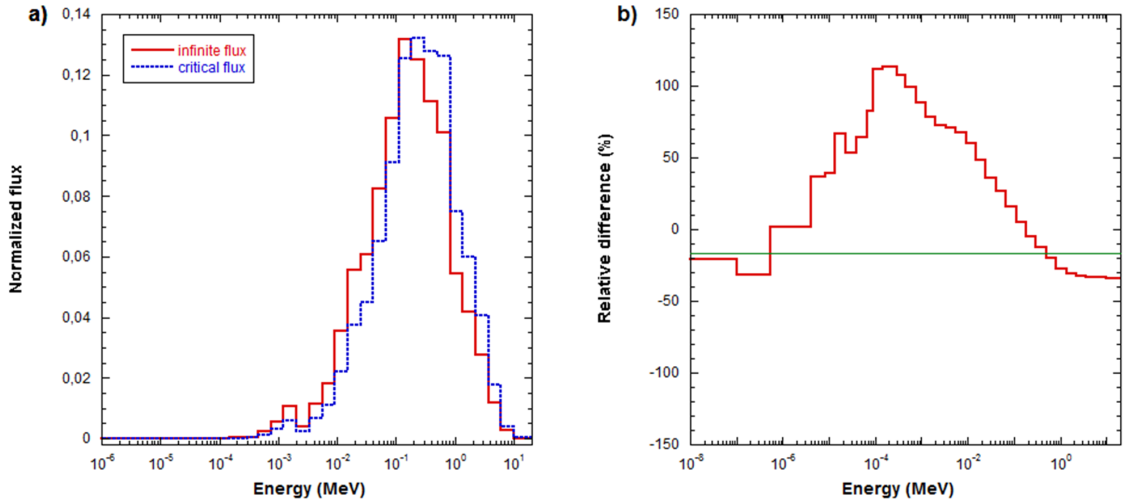

Figure 10.13: **a)**: Comparison between infinite flux spectrum and critical flux spectrum of ZPPR-DCF homogeneous sub-assembly from the TRIPOLI-4® simulations; **b)**: Relative difference between infinite and critical flux spectra

K_{eff} & Production rate comparisons

Previously, it was shown that the leakage model produced multi-group constants are able to preserve the K_{eff} value quite well and also the neutronic balance. Here, we shall use the multi-group constants produced without using any leakage model and verify their behavior in core simulation code. With this aim, multi-group constants are generated by TRIPOLI-4® (no leakage model option) with and without use of the IGSC method. The two sets of cross sections are then used in multi-group TRIPOLI-4® simulations. The K_{eff} values are given in Table 10.5.

		Reference	multi-group TRIPOLI-4®	ΔK_{eff} (pcm)
infinite spectrum	IGSC	0.99921 ± 0.00005	0.99092 ± 0.00013	-831 ± 13
	no-IGSC		1.00197 ± 0.00012	276 ± 13
critical spectrum	IGSC		0.99687 ± 0.00012	-266 ± 13

Table 10.5: Comparison of K_{eff} values between with and without use of TRIPOLI-4® leakage model produced 33-group cross sections in multi-group TRIPOLI-4® calculations

According to Table 10.5, we can tell that the multi-group constants produced by TRIPOLI-4® with infinite spectrum but always with IGSC method results in an under-

estimated K_{eff}. Its discrepancy compared to the reference value has been degraded. Otherwise, if neither the leakage model nor the IGSC technique are exploited for multi-group constant production work, the multi-group TRIPOLI-4® calculated K_{eff} value is quite satisfactory. This "good" result is unexpected and surprising. In order to make sure that there is no hidden effect, we continue to analyze the neutronic balance. Figure 10.14 shows the production rate discrepancies between multi-group and point-wise TRIPOLI-4® simulations respectively under 33-group and 6-group energy structures.

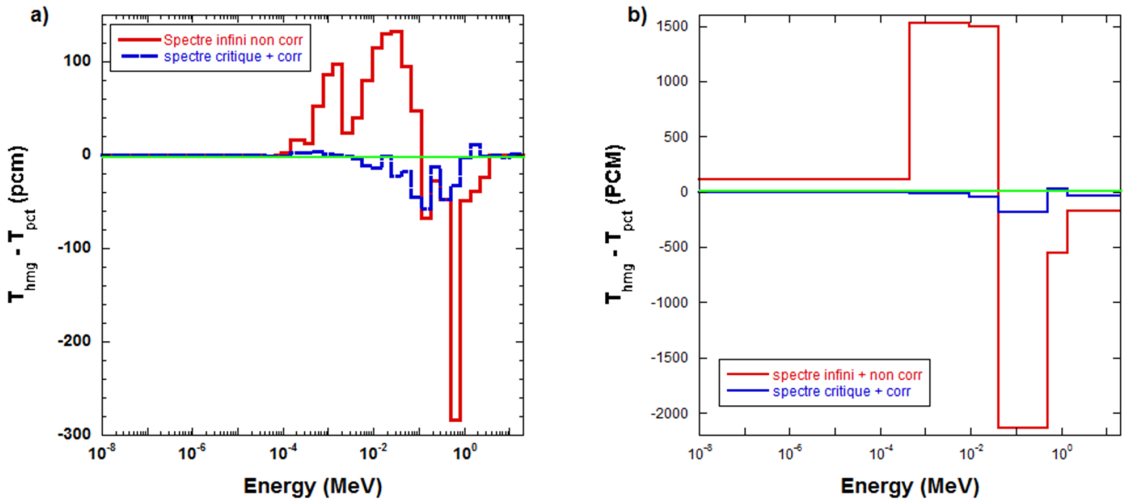

Figure 10.14: **a)**: Production rate discrepancies between 33-groups and point-wise TRIPOLI-4® simulations; **b)**: Production rate discrepancies between 6-groups and point-wise TRIPOLI-4® simulations

From both 33-group and 6-group case, it can be seen with infinite spectrum weighted multi-group constants, that an important compensation effect between higher energy and lower energy groups (red curves) exists. This means that even the rather "good" multiplicative factor is obtained with core simulation but we could not really trust these multi-group constants. On the contrary, the production rate discrepancies calculated with critical spectrum (with the IGSC method) are much more reasonable and there is no visible compensation effect between energy groups. Finally, it proves that critical spectrum is necessary for multi-group constants production work, especially for fast neutron reactor type sub-assembly calculations. Incidentally, the IGSC method is indispensable in order to take the anisotropy effect into account.

Conclusion

A B_1 homogeneous equation based leakage model has been implemented in the continuous-energy Monte-Carlo code TRIPOLI-4®. This leakage model makes use of the Monte-Carlo method generated multi-group cross sections to solve B_1 equations in order to get few-group leakage coefficients. The innovative point of our method is that these few-group leakage coefficients are re-used in a continuous-energy Monte-Carlo simulation iteratively with coupling of the solving of B_1 equations until reaching a critical state according to the Monte-Carlo point-wise simulation. Meanwhile, the multi-group constants produced can be used in the transport theory based core calculation code PARIS.

An intensive validation work is performed using a critical geometry based numerical experiment as a reference case. In particular, a high leakage probability ($\sim$ 42%) sub-assembly geometry is tested. Various leakage characteristic parameters are compared between our leakage model calculations and those from Serpent2.1.16 and ECCO. Overall, there is a good agreement among the three leakage model codes as well as the numerical experiment case. However, a methodology flaw is revealed while comparing the leakage model simulated multi-group leakage rates with the realistic referential ones. This non-completely consistent phenomenon is related to the intrinsic approximation from the fundamental mode. In order to be able to answer this question, a more physically representative leakage model needs be investigated and this will be introduced in the perspective chapter.

General Conclusion

The objective of this work was to produce multi-group cross sections with the Monte-Carlo code TRIPOLI-4® and use these generated multi-group constants in transport theory based deterministic core simulation codes. This document summarizes the work which has been performed to develop and validate the associated functionalities in the TRIPOLI-4® code.

At the beginning of this document, existing work is presented recalling the energy condensation and spatial homogenization methods used in different deterministic codes. In addition, a summary is given on the existing Monte-Carlo codes having the capacity to produce homogenized multi-group cross sections. The intrinsic differences between deterministic and Monte-Carlo approaches (e.g. easy access to the moments of flux or cross sections in deterministic method but hardly available in Monte-Carlo method) determine that we cannot easily adopt the deterministic way in TRIPOLI-4® code. As for other Monte-Carlo codes which can generate homogenized multi-group cross sections, they are mostly focused on supplying their produced multi-group constants to some diffusion theory based deterministic codes. However, we aim to use here these produced multi-group constants in **transport theory** based calculation codes. The fact that we have different objective leaves us in a situation where some new and undiscovered difficulties would come up. Thereby, it should be reminded that the goal is not to directly copy these deterministic or Monte-Carlo methods in our development work but rather use them in comparison of results and validation work.

As pointed out by Hébert in his Ph.D. work[49], the neutronic balance should be exactly preserved in a homogeneous infinite lattice calculation, especially during the passage from fine-group to few-group energy collapsing. The latter inspires us to verify whether the existing homogenization and condensation routines in TRIPOLI-4® code are capable to answer this criterion. It was found irrelevant to preserve the neutronic balance while performing a homogeneous infinite lattice calculation. The latter required a thorough and rigorous verification of the whole algorithm concerning the homogenization and condensation functionalities. Graceful to this work, it was proved that the problems lay in the estimations of the following multi-group parameters: the energy transfer probability matrix, the excess weight and the fission spectrum. Therefore, new Monte-Carlo estimators of the above variables were developed and implemented in TRIPOLI-4® code. Their validation work was at first done by comparing the produced multi-group constants respectively from ECCO and the updated TRIPOLI-4® code. Secondly, the TRIPOLI-4® produced multi-group constants were used in Monte-Carlo multi-group simulations which give several important outputs: the flux spectrum, the K_∞ values and the reaction rates. These multi-group calculation results were then compared with those from continuous-energy simulations and confirmed the conservation theory mentioned previously.

After having been assured of the good performance of the TRIPOLI-4® code in homogeneous infinite lattice calculation, the research work was continued towards some finite lattice geometries. For the latter case, special attention should be paid on the anisotropy effect which is induced by the leakage of neutrons. This multi-group anisotropy representation is always a challenging issue for neutronic physicists. In this work, a new technique, in-group scattering correction (IGSC), was developed to modify the naturally TRIPOLI-4® produced in-group scattering anisotropy matrix in order to better preserve the neutronic balance. For doing this, a volumetric current quantity is required as a weighting function which makes the remarkable difference compared to the conventional scalar flux. Being a Monte-Carlo code, TRIPOLI-4® is limited to calculate an exact volumetric current owing to the cancelation of negative and positive quantities. The first current developed in Chapter 7 is termed "Todorova's current" which is strongly based on the approximation: the flux gradient spectrum is proportional to the flux spectrum. With use of Todorova's current corrected in-group scattering anisotropy matrix, consistent results (flux spectra, neutronic balance, K_{eff}) were obtained between multi-group and point-wise TRIPOLI-4® simulations for homogeneous finite and even for several heterogeneous finite geometries. However, great discrepancies showed up while handling highly heterogeneous geometry case. This made us to look deeply inside the heterogeneity problem and finally figured out a solution which proposes a new calculation method of the volumetric current for one-dimensional geometries. The second current developed in Chapter 8 is termed "direction-X current" which represents an accurate one-dimensional current adapted to our hand-made 1D highly heterogeneous geometry. The results calculated by using direction-X current showed important improvement compared to the previous Todorova's current calculation results. And it proves that the IGSC technique, in addition with an exact current estimation, plays a key factor in the energy condensation and spatial homogenization work, especially for a highly heterogeneous geometry. This methodology is finally applied to a fuel-reflector case and it confirms again that it can improve greatly the estimation of the K_{eff} value as well as the associated current and flux quantities.

The direction-X current seems very powerful and reliable to treat highly heterogeneous geometries, and is even capable of handling the fuel-reflector issue. However, this current is limited to a one-dimensional geometry. In future work, it could be extended to two-dimensions. To achieve this, at first, a favorite escaping direction should be decided for each neutron at any position. This direction could be chosen by linking the central point of the geometry and the actual position of the neutron. This way of doing things helps to find the most probable direction for neutrons to escape from the system. Then, the current quantity associated to this neutron could be projected on this direction in order to obtain the desired 2D current quantity.

Another approach to account the neutron leakage effect is through an artificial leakage model. The latter constitutes the last part of this document. After comparing the leakage models existing in various Monte-Carlo codes, it was the one based on the B_1 homogeneous equations which was chosen to be implemented in TRIPOLI-4® code. The innovative points revealed from our leakage model are that: **1)**, it takes use of critical spectrum weighted cross sections to solve the B_1 homogeneous equations; **2)**, the solved multi-group leakage coefficients are then taken account in the continuous-energy Monte-Carlo simulation which helps to establish a critical state from the Monte-Carlo point of view; **3)**, the continuous-energy TRIPOLI-4® simulation is coupled with the routine in

charge of solving the B_1 homogeneous equations until reaching the expected criticality. To be mentioned that, the leakage model produced multi-group constants are always treated with the IGSC techniques developed previously. A rigorous validation work of this leakage model is performed with use of a critical geometry based numerical experiment as reference case. A particularly high leakage probability ($\sim 42\%$) sub-assembly geometry, ZPPR-DCF, is used. First of all, various characteristic leakage parameters (D_g, B^2, leakage rate) were compared between our leakage model to those from Serpent2.1.16 and ECCO codes. Globally, there is a very good agreement among these three leakage model codes as well as with the numerical experiment case. Moreover, the TRIPOLI-4® leakage model produced multi-group constants were used in multi-group TRIPOLI-4® and PARIS[33] calculations which corresponded to the initial motivation of this work. Both Monte-Carlo and deterministic transport core calculations produced consistent results compared to those of the numerical experiment simulated under continuous-energy TRIPOLI-4® condition. It was shown that using TRIPOLI-4® leakage model produced multi-group constants in PARIS simulation could have better estimations of K_{eff} and neutronic balance than using ECCO produced multi-group constants. Finally, the impact of a leakage model in a fast reactor type sub-assembly calculation was revealed originally by this work. With help of the same geometry as previously used, we prove that critical spectra weighted multi-group constants are indispensable to preserve exactly the neutronic balance. Without use of leakage model nor the IGSC technique produced multi-group constants could also estimate a "satisfactory but trapping" K_{eff} value since the neutronic balance was not at all preserved with this latter way of doing things.

Even though our implemented B_1 homogeneous equation based leakage model is efficient to produce appropriate multi-group constants for transport core simulation codes, there exist still some limitations related to the fundamental mode approximation. As shown in Figure 10.8, the leakage rates estimated by the B_1 leakage model are only preserved in the total quantity but not in every energy group quantity. This is because that the fundamental mode approximation is suitable especially in an homogeneous and infinite geometry. But in a realistic finite core geometry, the spectrum of flux is harder at the edge than in the center. Thus, more fast neutrons escape from the geometry than lower energy neutrons. This is why we observed a compensation effect between high energy groups and lower ones (Figure 10.8). To improve this fundamental mode approximation, some other leakage models could be continued to be investigated in the future. A possible way is to combine the fundamental mode approximation leakage model with the albedo leakage model. That is to say, the group-wise leakage quantity per volume $d_g B^2 \phi_g$ could be converted to the neutron quantity per surface hitting on the boundary of the geometry $(1 - \alpha_g)J^+$. The relationship could help to determine the group-wise albedo leakage parameter which respects the physical aspect better.

This document comes to an end with some general comments. First of all, the Monte-Carlo methodology shows clearly the advantages in the sub-assembly calculation step compared to the conventional deterministic way, principally for the problems of self-shielding, anisotropy data and complex geometry. This makes the Monte-Carlo method produced multi-group cross sections to be used as a robust tool contributing to validate and analyze the deterministic sub-assembly calculation codes. The calculation routines developed during this thesis could serve in the French fast reactor prototype ASTRID analysis. However, the Monte-Carlo method is a computing-intensive technique which is not really compatible with the industrial calculation criteria. Therefore, future development concerning the

parallelization remains an interesting mission for Monte-Carlo method based multi-group cross section production work.

Appendix A

Atomic Concentration of Tested Homogeneous Sub-assemblies

ZPPRDCF

nuclide	$\times 10^{-24}.\mathrm{cm}^{-3}$
C12	1.065E-03
SI28	1.651E-04
SI29	8.380E-06
SI30	5.530E-06
CR50	1.361E-04
CR52	2.625E-03
CR53	2.977E-04
CR54	7.409E-05
MN55	2.658E-04
FE54	8.490E-04
FE56	1.333E-02
FE57	3.078E-04
FE58	4.096E-05
NI58	9.527E-04
NI60	3.670E-04
NI61	1.595E-05
NI62	5.086E-05
NI64	1.295E-05
MO92	6.917E-05
MO94	4.312E-05
MO95	7.421E-05
MO96	7.775E-05
MO97	4.451E-05
MO98	1.125E-04
MO100	4.489E-05
CU63	3.072E-05
CU65	1.369E-05
N14	1.700E-06
O16	7.568E-03
U235	1.482E-05
U238	6.669E-03
PU239	1.772E-03
PU240	2.347E-04
PU241	2.074E-05
PU242	4.580E-06
AM241	1.434E-05
NA23	8.805E-03
H1	9.540E-06
AL27	5.820E-06

ZPPRSCF

nuclide	$\times 10^{-24}.\mathrm{cm}^{-3}$
C12	1.048E-03
SI28	1.526E-04
SI29	7.750E-06
SI30	5.110E-06
CR50	1.240E-04
CR52	2.391E-03
CR53	2.711E-04
CR54	6.749E-05
MN55	2.417E-04
FE54	6.971E-04
FE56	1.094E-02
FE57	2.527E-04
FE58	3.363E-05
NI58	8.570E-04
NI60	3.301E-04
NI61	1.435E-05
NI62	4.575E-05
NI64	1.165E-05
MO92	3.566E-05
MO94	2.223E-05
MO95	3.825E-05
MO96	4.008E-05
MO97	2.295E-05
MO98	5.798E-05
MO100	2.314E-05
CU63	2.957E-05
CU65	1.318E-05
N14	1.700E-06
O16	1.446E-02
U235	1.819E-05
U238	8.252E-03
H1	9.310E-06
NA23	8.715E-03
PU239	8.880E-04
PU240	1.176E-04
PU241	1.090E-05
PU242	2.480E-06
AM241	7.210E-06
AL27	4.600E-06

SPX2

nuclide	$\times 10^{-24}.\mathrm{cm}^{-3}$
U234	6.860E-08
O16	1.656E-02
U235	3.552E-05
U236	6.802E-08
U238	6.709E-03
NP237	3.229E-08
PU238	7.346E-06
PU239	1.127E-03
PU240	3.600E-04
PU241	7.445E-05
PU242	2.837E-05
AM241	1.782E-05
SI28	2.122E-04
SI29	1.077E-05
SI30	7.102E-06
TI46	8.099E-06
TI47	7.304E-06
TI48	7.237E-05
TI49	5.311E-06
TI50	5.085E-06
CR50	1.669E-04
CR52	3.218E-03
CR53	3.649E-04
CR54	9.084E-05
MN55	3.208E-04
FE54	7.802E-04
FE56	1.225E-02
FE57	2.828E-04
FE58	3.764E-05
NI58	1.908E-03
NI60	7.348E-04
NI61	3.194E-05
NI62	1.018E-04
NI64	2.594E-05
MO92	4.998E-05
MO94	3.115E-05
MO95	5.361E-05
MO96	5.617E-05
MO97	3.216E-05
MO98	8.126E-05
MO100	3.243E-05
CU63	4.476E-05
CU65	1.995E-05
NA23	8.409E-03

SPX1

nuclide	$\times 10^{-24}.\mathrm{cm}^{-3}$
O16	1.683E-02
U235	3.767E-05
U238	7.115E-03
NP237	2.665E-08
PU238	5.210E-06
PU239	9.184E-04
PU240	3.069E-04
PU241	5.837E-05
PU242	2.262E-05
AM241	2.088E-05
NA23	8.732E-03
SI28	2.122E-04
SI29	1.077E-05
SI30	7.101E-06
TI46	8.098E-06
TI47	7.303E-06
TI48	7.236E-05
TI49	5.310E-06
TI50	5.085E-06
CR50	1.669E-04
CR52	3.218E-03
CR53	3.649E-04
CR54	9.083E-05
MN55	3.207E-04
FE54	7.801E-04
FE56	1.225E-02
FE57	2.828E-04
FE58	3.764E-05
NI58	1.907E-03
NI60	7.347E-04
NI61	3.194E-05
NI62	1.018E-04
NI64	2.593E-05
MO92	4.997E-05
MO94	3.115E-05
MO95	5.361E-05
MO96	5.617E-05
MO97	3.216E-05
MO98	8.125E-05
MO100	3.243E-05
CU63	4.475E-05
CU65	1.995E-05

MAS1B

nuclide	$\times 10^{-24}.cm^{-3}$
C12	5.646E-02
FE54	2.248E-04
FE58	1.085E-05
CR53	1.029E-04
NI60	2.179E-04
NI64	7.707E-06
CU63	4.150E-07
SI29	1.786E-06
CO59	5.427E-06
FE56	3.529E-03
CR50	4.704E-05
CR54	2.560E-05
NI61	9.470E-06
CU65	1.850E-07
SI30	1.177E-06
FE57	8.224E-05
CR52	9.070E-04
NI58	5.656E-04
NI62	3.020E-05
SI28	3.537E-05
MN55	4.748E-05
B11	1.010E-07
H1	6.335E-06
MO100	1.495E-06
MO92	2.304E-06
MO94	1.436E-06
MO95	2.472E-06
MO96	2.590E-06
MO97	1.483E-06
MO98	3.746E-06
NB93	8.440E-07
TI46	1.494E-06
W182	3.770E-07
W183	2.040E-07
W184	4.360E-07
W186	4.050E-07
U235	2.514E-03
U238	5.792E-03

ZONA2

nuclide	$\times 10^{-24}.cm^{-3}$	nuclide	$\times 10^{-24}.cm^{-3}$
O16	1.432E-02	MO95	2.560E-06
U235	1.745E-05	MO96	2.680E-06
U236	6.300E-07	MO97	1.540E-06
U238	5.237E-03	MO98	3.880E-06
PU238	3.440E-06	MO100	1.550E-06
PU239	1.522E-03	NA23	9.326E-03
PU240	3.689E-04	CO59	8.080E-06
PU241	2.581E-05	W182	3.700E-07
PU242	1.329E-05	W183	2.000E-07
AM241	5.175E-05	W184	4.400E-07
K39	4.800E-07	W186	4.100E-07
FE54	4.198E-04	NB93	8.400E-07
FE56	4.634E-03	TI46	5.500E-07
FE57	1.494E-04	H1	1.240E-06
FE58	1.992E-05		
CR50	8.476E-05		
CR52	1.635E-03		
CR53	1.853E-04		
CR54	4.614E-05		
NI58	6.565E-04		
NI60	2.529E-04		
NI61	1.099E-05		
NI62	3.504E-05		
NI64	8.930E-06		
AL27	4.300E-07		
C12	2.755E-05		
N14	3.130E-06		
CU63	2.140E-06		
CU65	9.500E-07		
SI28	9.379E-05		
SI29	4.760E-06		
SI30	3.120E-06		
CA40	2.730E-06		
MN55	1.252E-04		
P31	1.140E-06		
S32	1.820E-06		
MO92	2.390E-06		
MO94	1.490E-06		

Appendix B

Energy Structures Used in TRIPOLI-4®

33-group energy structure limits

1.96E+01	1.00E+01	6.07E+00	3.68E+00	2.23E+00	1.35E+00	8.21E-01
4.98E-01	3.02E-01	1.83E-01	1.11E-01	6.74E-02	4.09E-02	2.48E-02
1.50E-02	9.12E-03	5.53E-03	3.35E-03	2.03E-03	1.23E-03	7.49E-04
4.54E-04	3.04E-04	1.49E-04	9.17E-05	6.79E-05	4.02E-05	2.26E-05
1.37E-05	8.32E-06	4.00E-06	5.40E-07	1.00E-07	1.00E-11	

6-group energy structure limits

1.96E+01	2.23E+00	4.98E-01	4.09E-02	9.12E-03	4.54E-04	1.00E-11

Appendix C

Spatial homogenization illustration of SuperPhénix core

Radial cutting illustration of homogenized SuperPhénix core

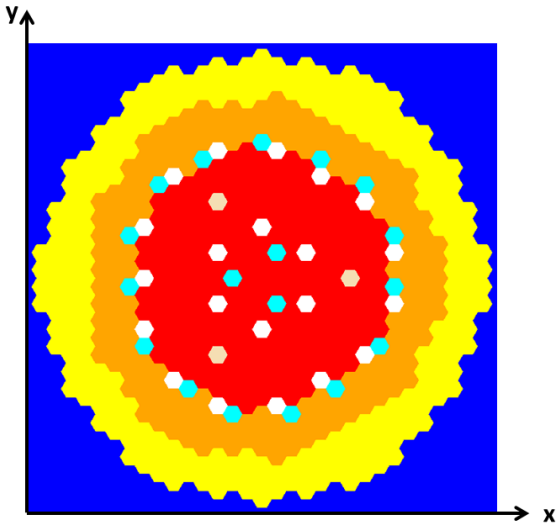

Axial cutting illustration of homogenized SuperPhénix core

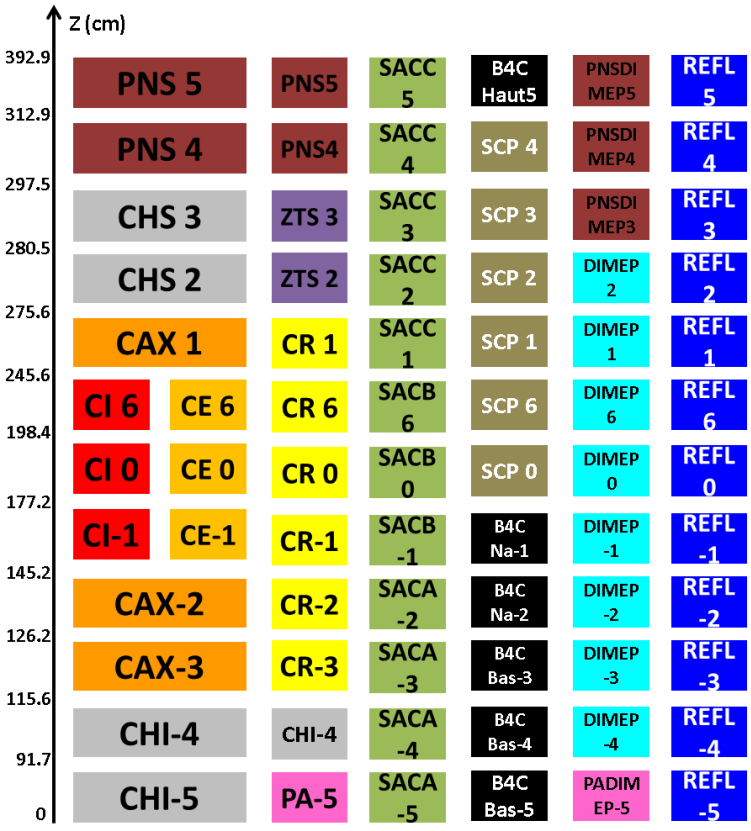

CI: inner-core sub-assembly
CE: external-core sub-assembly

CAX: axial blanket
CR: radial blanket

CHS: upper extension chamber
CHI: lower extension chamber

PNS: upper neutronic protection
PA: sub-assembly base
ZTS: upper transition zone
SAC*: complementary stop system
B4C*/SCP: control rod
*DIMEP: measurement device
REFL: steel reflector

The whole SuperPhénix core is divided into 75 regions.

Appendix D

Fundamental Mode in the Center of a Homogeneous Core

In the central part of a homogeneous assembly geometry, the diffusion equation are written in both direct and adjoint forms:

$$D(E)\nabla^2\Phi(\mathbf{r},E)-\Sigma_t(E)\Phi(\mathbf{r},E)+\int_0^\infty dE'\Sigma_s(E'\to E)\Phi(\mathbf{r},E')+\chi(E)\int_0^\infty dE'\nu\Sigma_f(E')\Phi(\mathbf{r},E')=0 \tag{D.1}$$

$$D(E)\nabla^2\Phi^+(\mathbf{r},E)-\Sigma_t(E)\Phi^+(\mathbf{r},E)+\int_0^\infty dE'\Sigma_s(E\to E')\Phi^+(\mathbf{r},E')+\nu\Sigma_f(E)\int_0^\infty dE'\chi(E')\Phi^+(\mathbf{r},E')=0 \tag{D.2}$$

The two above equations can be simplified with the diffusion operator M and its adjoint operator M^+ as following:

$$\nabla^2\Phi(\mathbf{r},E)+M\Phi(\mathbf{r},E)=0 \tag{D.3}$$

$$\nabla^2\Phi^+(\mathbf{r},E)+M^+\Phi^+(\mathbf{r},E)=0 \tag{D.4}$$

The eigenvalues and the corresponding vectors of M and M^+ are:

$$M\varphi_i(E)=\lambda_i\varphi_i(E) \tag{D.5}$$

$$M^+\varphi_i^+(E)=\lambda_i\varphi_i^+(E) \tag{D.6}$$

with $i=0,1,2\cdots$; $\int_0^\infty dE\varphi_i^+(E)\varphi_j(E)=<\varphi_i^+,\varphi_j>=\alpha_i\delta_{ij}$.

If we develop $\Phi(\mathbf{r},E)$ and $\Phi^+(\mathbf{r},E)$ respectively with their eigenvectors:

$$\Phi(\mathbf{r},E)=\sum_i f_i(\mathbf{r})\varphi_i(E) \tag{D.7}$$

$$\Phi^+(\mathbf{r},E)=\sum_i f_i^+(\mathbf{r})\varphi_i^+(E) \tag{D.8}$$

with $f_i(\mathbf{r})=\frac{<\varphi_i^+,\Phi>}{\varphi_i^+,\varphi_i}$; $f_i^+(\mathbf{r})=\frac{\Phi^+,\varphi_i}{\varphi_i^+,\varphi_i}$.

After substituting Eq(19) and Eq(20) into the first two diffusion equations, we obtain:

$$\sum_i[\nabla^2 f_i(\mathbf{r})+\lambda_i f_i(\mathbf{r})]\varphi_i(E)=0 \tag{D.9}$$

$$\sum_i[\nabla^2 f_i^+(\mathbf{r})+\lambda_i f_i^+(\mathbf{r})]\varphi_i^+(E)=0 \tag{D.10}$$

It means that: $f_i(\mathbf{r}) \propto f_i^+(\mathbf{r})$, and $\nabla^2 f_i(\mathbf{r}) + \lambda_i f_i(\mathbf{r}) = 0$ where $\lambda_0 = B^2$.

So for $i = 0$, we get:

$$\nabla^2 f_0(\mathbf{r}) + B^2 f_0(\mathbf{r}) = 0 \tag{D.11}$$

with $f_0 = \int_0^\infty dE\varphi^+(E)\Phi(\mathbf{r}, E) = \int_0^\infty dE\varphi(E)\Phi^+(\mathbf{r}, E)$. The detailed definitions of the different flux are given below:

- $\varphi^+(E)$: the adjoint flux in a critical homogeneous assembly;
- $\varphi(E)$: the direct flux in a critical homogeneous assembly;
- $\Phi(\mathbf{r}, E)$: the direct flux in a critical core;
- $\Phi^+(\mathbf{r}, E)$: the adjoint flux in a critical core.

Bibliography

[1] Report on nuclear design methods. Technical report, Japan Nuclear Cycle Development Institute, May 2000. (in Japanese).

[2] ICSBEP : International Criticality and Safety Benchmark Evaluation Project. Technical Report NEA/NSC/DOC(95)03, NEA, 2005.

[3] Application for the change of a nuclear reactor facility - JAEA Fast Reactor Development Center - About the nuclear design. Technical Report 111A-2-1, Nuclear and Industrial Safety Agency, September 2007. (in Japanese).

[4] Application for the change of a nuclear reactor facility - JAEA Fast Reactor Development Center - Mechanical design of the fuel. Technical Report 111A-1-5, Nuclear and Industrial Safety Agency, September 2007. (in Japanese).

[5] NEA-1716 TRIPOLI-4 VERS. 8.1., 2013.

[6] A. Hébert. *Applied Reactor Physics.* Presses internationales Polytechnique, 2009.

[7] A. Kavenoky. The SPH Homogenization Method. In *Proc. Specialists Mtg. Homogenization Methods in Reactor Physics*, 1978. Lugano, Switzeland, Nov 13-15.

[8] International Atomic Energy Agency. Uranium: Resources, Production and Demand (The Red Book), 2011. http://www.iaea.org/OurWork/ST/NE/NEFW/Technical-Areas/NFC/uranium-production-cycle-redbook.html.

[9] OCDE Nuclear Energy Agency. IRPhEP: International Reactor Physics benchmark Experiments (IRPhE) Project, 2013. www.oecd-nea.org/science/wprs/irphe/.

[10] World Nuclear Association. World Energy Needs and Nuclear Power, August 2014. http://www.world-nuclear.org/info/Current-and-Future-Generation/World-Energy-Needs-and-Nuclear-Power/.

[11] N. Authier. *Mise au point d'un estimateur ponctuel du flux et des taux de réactions dans les calculs de transport de particules neutres par la méthode de Monte Carlo.* PhD thesis, Thèse de l'Université de Paris XI Orsay, 1998.

[12] R. Barjon. *Physique des Réacteurs Nucléaires.* Presses Universitaires de Grenoble, 1993.

[13] L. Boltzmann. *Weitere Studien über das Wärmegleichgewicht unter Gasmoilekülen.* Wiener Berichte, 1872.

[14] L. Boltzmann. *Théorie cinétique des gaz, Trad. francaise.* Éditions Jacques Gabay, 1987.

[15] Y. H. Bouget et al. Physics Performances of a Heterogeneous Fast Reactor Core Concept Studied in MASURCA. *Nuclear Technology*, 44:61–75, 1979.

[16] Brookhaven National Laboratory. *ENDF-6 Formats Manual – Data Formats and Procedures for the Evaluated Nuclear Data File ENDF/B-VI and ENDF/B-VII*, m. herman and a. trkov edition, June 2009.

[17] J. Bussac and P. Reuss. *Traité de neutronique*. Paris: Hermann, DL, 1978.

[18] S. Callens. *Les Maîtres de l'erreur - Mesure et probabilité au XIX siècle*. Presses Universitaires de France, 1997.

[19] L. Le Cam. The central limit theorem around 1935. *Statistical Science*, 1:78– 91, 1986.

[20] CEA. *La neutronique*. Le Moniteur, 2013.

[21] G. Chiba and K. Numata. Development of the fast reactor group constant set JFS-3-J3.2R based on the JFS-3-J2. Technical Report TN9400 2001-124, JNC, 2002. (in Japanese).

[22] A. Santamarina et al. The JEFF-3.1.1 nuclear data library. Technical Report NEA No 6807, OCDE, NEA, 2009.

[23] E. Brun et al. *Overview of TRIPOLI4 version 7 Continuous-energy Monte Carlo Transport Code*. 2011.

[24] G. Rimpault et al. The ERANOS code and data system for fast reactor neutronic analyses. In *PHYSOR 2002, Oct 7-10, 2002, Séoul, Corée du Sud*, 2002.

[25] G. Rimpault et al. The ERANOS code and Data System for Fast Reactor Neutronic Analyses. In *Physor The Role of Reactor Physics toward a Sustainable Future*, 2002. Seoul, Korea, OCTOBER 7 - 10.

[26] G. Truchet et al. Continuous-Energy Adjoint Flux and Perturbation Calculation using the Iterated Fission Probability Method in Monte Carlo code TRIPOLI-4 and Underlying Applications. In *Joint International Conference on Supercomputing in Nuclear Application and Monte Carlo*, 2013. Paris, France, October 27 - 31.

[27] H. J. Park et al. Generation of Few Group Diffusion Theory Constants by Monte Carlo code McCARD. *Nuclear Science and Engineering*, 172(1):66 – 77, 2012.

[28] H. J. Shim et al. McCARD: Monte Carlo Code for Advanced Reactor Design and Analysis. *Nuclear Engineering and Technology*, 44:161– 176, 2012.

[29] J. F. Vidal et al. An improved energy-collapsing method for core-reflector modelization in sfr core calculations using the paris platform. In *Physor The Role of Reactor Physics toward a Sustainable Future*, 2012. Knoxville, USA, Apr 15 - 20.

[30] J. M. Ruggieri et al. ERANOS-2.1: The International Code System for GEN-IV Fast Reactor Analysis. In *ICAPP'06, June 4-8, 2006, Reno, Nevada*, 2006.

[31] J. P. Both et al. A survey of TRIPOLI4. In *Int. Conf. on Radiation Shielding*, 1994. Arlington, USA.

[32] K. Sasaki et al. Analysis of Reactivity Characteristics of the MONJU Initial Core Using JENDL-3.2. Technical Report JAERI-CONF-98-003, Japan Atomic Energy Research Institute (JAERI), 1998.

[33] L. Gastaldo et al. High-order discrete ordinate transport in non-confirming 2d cartesian meshes. In *Int. Conf. on Mathematics and Computational Methods Applied to Nuclear Science and Engineering*, 2009. New York, USA, May 3-7.

[34] N. Metropolis et al. Monte Carlo Calculations on Intranuclear Cascades. *Physical Review*, 110:185– 203, 1958.

[35] Z. Y. Liu et al. A new three-dimensional method of characteristics for the neutron transport calculation. *Annals of Nuclear Energy*, 38:447–454, 2011.

[36] F. Jeanpierre and M. Livolant. Report CEA. Rapport technique. Technical Report CEA-R-4533, CEA.

[37] R. E. Mac Farlane and D. M. Muir. NJOY-99.0 : Code System for Producing Pointwise and Multigroup Neutron and Photon Cross Section from ENDF/B Data. Technical Report PSR-480, Los Alamos National Laboratory Report, 2000.

[38] P. J. Finck et al. The CIRANO Experimental Program in Support of Advanced Fast Reactor Physics. In *Proceedings of International Conference on the Physics of Reactors, PHYSOR'96*, Mito, Japan, September, 16-20 1996.

[39] G. Flamenbaum and T. Newton. Superphenix Core-Loading Strategy Using the Checkerboard Pattern. *Nuclear Science and Engineering*, 106:11–17, 1990.

[40] T. B. Fowler, D. R.Vondy, and G. W.Cunningham. Nuclear Reactor Analysis Code: CITATION. Technical Report ORNL-TM-2496, Oak Ridge National Laboratory, 1971.

[41] E. Fridman and J. Leppänen. On the use of Monte Carlo code for few-group cross section generation. *Ann. Nucl. Energy*, 38:1399–1405, 2011.

[42] G. Marleau, A. Hébert, and R. Roy. New Computational Methods used in the Lattice Code Dragon. In *Proc. Int. Topl. Mtg. on Advances in Reactor Physics*, Charleston, USA, 1992.

[43] G. Palmiotti. Optimized two-dimensional Sn transport(BISTRO). *Nuclear Science and Engineering*, 104:26 – 33, 1990.

[44] G. Rimpault. Algorithmic features of the ECCO cell code for treating heterogeneous fast reactor assemblies. In *Int. Conf. on Mathematics and Computations, Reactor Physics, and Environmental Analyses*, 1995. Portland, USA, May 1-5.

[45] R. C. Gast. A Procedure for Obtaining Neutron-Diffusion Coefficients from Neutron-Transport Monte Carlo Calculations. Technical Report WAPD-TM-1446, Bettis Atomic Power Laboratory, 1981.

[46] Generation-IV International Forum. A technology roadmap for Generation-IV nuclear energy systems. In *Gen-IV International Forum/US DoE*, Washington DC, 2002.

[47] J. Gourdon and B. Mesnage. An Overview of Superphenix Commissioning Tests. *Nuclear Science and Engineering*, 106:1–10, 1990.

[48] J. Guidez. *Le Retour d'Expérience*. CEA, 2012.

[49] A. Hébert. *Developpement de la method SPH: Homogeneisation de cellules dans un reseau non uniforme et calcul des parametres de reflecteur*. PhD thesis, CEA, 1980.

[50] E. L. Redmond II. *Multigroup cross section generation via Monte Carlo methods*. PhD thesis, Massachusetts Institue of Technology, 1997.

[51] H. Ikeda and T. Takeda. A new nodal Sn transport method for three-dimensional hexagonal geometry. *Journal of Nuclear Science and Technology*, 31, 1994.

[52] T. Ikegami. ZPPR-9 Experiment: A 650 MWe-Class Sodium-Cooled MOX-Fueled FBR Core Mock-Up Critical Experiment with Clean Core of Two Homogeneous Zones. Technical Report ZPPR-LMFR-EXP-002, IRPhEP Benchmark, 2006.

[53] G. Ilas and F. Rahnema. A Monte Carlo based nodal diffusion model for criticality analysis of spent fuel storage lattices. *Ann. Nucl. Energy*, 30:1089–1108, 2003.

[54] J. E. Hoogenboom, V. A. Khotylev, and J. M. Tholammakkil. Generation of Multi-Group Cross Sections and Scattering Matrices with the Monte Carlo code MCNP5. In *Joint International Topical Meeting on Mathematics & Computations and Supercomputing in Nuclear Applications*, 2007. Monetery, USA, APRIL 15 - 19.

[55] J. Leppänen. *Development of a New Monte Carlo Reactor Physics Code*. PhD thesis, 2007.

[56] J. P. Both, Y. K.Lee, and P. J. Finck. Computations of Homogenised Multi-group Cross Sections with the Monte Carlo code TRIPOLI4. In *Proc. SARATOGA JIC MM SNA*, Saratoga Springs New York, 1997.

[57] Ph. Johnson. *A History of Set Theory*. Prindle, Weber & Schmidt, 1972.

[58] K. S. Smith. *Spatial Homogenization Methods for Light Water Reactor Analysis*. PhD thesis, Massachusetts Institue of Technology, 1980.

[59] K. Sasaki, T. Suzuku, and Y. Itagaki. Operational results of the prototype FBR Monju - Analysis of measured reactivity characteristics using JENDL-3.2. In *Trans. ENC'98*, 1998. Nice, France, Oct 25-28.

[60] K. Koebke. A New Approach to Homogenization and Group Condensation. Technical Report IAEA-TECDOC-231, International Atomic Energy Agency, 1978.

[61] P. S. Laplace. Mémoire sur les approximations des formules qui sont fonctions de très-grands nombre. *Mémoires de la Classe des sciences mathématiques et physiques de l'institut de France*, pages 353 – 415, 1809.

[62] P. S. Laplace. Supplement au mémoire sur les approximations des formules qui sont fonctions de très-grands nombre. *Mémoires de la Classe des sciences mathématiques et physiques de l'institut de France*, pages 559 – 565, 1809.

[63] J. Leppänen. Serpent - a Continuous-energy Monte Carlo Reactor Physics Burnup Calculation Code User's Manual. Technical report, VTT Technical Research Centre of Finland, 2013.

[64] J. Leppänen. Methodology for spatial homogenization in Serpent 2. Technical Report Memo 140526, VTT Technical Research Centre of Finland, 2014.

[65] Los Alamos National Laboratory. *MCNP - A General Monte Carlo N-Particle Transport Code*, j.f. briesmeister edition, 2000.

[66] I. Lux and L. Koblinger. *Monte Carlo Particle Transport Methods: Neutron and Photon Calculations*. CRC Press, 1991.

[67] M. Coste and S. Mengelle. Implementation of a sub-group method for self-shielding calculations in APOLLO2 code. In *Physor The Role of Reactor Physics toward a Sustainable Future*, 1996. Mito, Japan, SEPTEMBER 16 - 20.

[68] M. Edenius and B. H. Forssen. CASMO-3 A Fuel Assembly Burnup Program User's Manual. Technical Report Studsvik/NFA-89-3, Rev.2, Studsvik AB, 1992.

[69] M. J. Grimstone, J. D. Tullett, and G. Rimpault. Accurate Treatments of Fast Reactor Fuel Assembly Heterogeneity with the ECCO Cell Code. In *Int. Conf. on the Physics of Reactors: Operation, Desing and Computation-PHYSOR 90*, 1990. Marseille, FRANCE, April 23-27.

[70] B. Morillon. *Méthode de Monte Carlo non analogue, application à la simulation des neutrons*. PhD thesis, thesis report, Note CEA-N-2805, 1996.

[71] N. Martin. *Application de la méthode des sous-groupes au calcul Monte-Carlo multigroup*. PhD thesis, Université de Montréal, 2011.

[72] N. Metropolis and S. Ulam. The Monte Carlo Method. *Journal of the American Statistical Association*, 44:335– 341, 1949.

[73] N. Z. Cho, S. Yun, and J. Lee. Generation of Homogenized Nodal Parameters by Monte Carlo method with Non-Zero Leakage Spectra in Global-Local Iteration Framework. *Transactions of the American Nuclear Society*, 101:707 – 710, 2009.

[74] M. Nakagawa, J. Abe, and W. Sato. Code System for Fast Reactor Neutronics Analysis. Technical Report JAERI-M 83-066, JAERI, 1982.

[75] M. Nakagawa and K. Tsuchihashi. SLAROM: A code for Cell Homogenization Calculation of Fast Reactor. Technical Report JAERI 1294, JAERI, 1984.

[76] Nam Zin Cho, Sunghwan Yun, and Jaejun Lee. Generation of Homogenized Nodal Parameters by Monte Carlo method with Non-Zero Leakage Spectra in Global-Local Iteration Framework. *Transactions of the American Nuclear Society*, 101:707 – 710, 2009.

[77] P. Jacquet. *Nouvelles méthodes de modélisation neutronique des réacteurs rapides de quatrième Génération*. PhD thesis, Université de Grenoble, 2011.

[78] D. L. Poston and H. R. Trellue. User's Manual, Version 2.0 for MONTEBURNS Version 1.0, LA-UR-99-4999. Technical report, 1999.

[79] F. Rahnema, S. Douglass, and B. Forget. Generalized Energy Condensation Theory. *Nuclear Science and Engineering*, 160:41–58, 2008.

[80] P. Reuss. *Précis de neutronique*. EDP Sciences, 2003.

[81] R. Y. Rubinstein. *Simulation and the Monte Carlo method*. John Wiley & Sons, 1981.

[82] S. C. van der Marck, J. C. Kuijper, and J. Oppe. Homogenized Group Cross Sections by Monte Carlo. In *Physor The Role of Reactor Physics toward a Sustainable Future*, 2006. Vancouver, Canada, SEPTEMBER 10 - 16.

[83] S. Douglass and F. Rahnema. Consistent Generalized Energy Condensation Theory. *Annals of Nuclear Energy*, 40(1):200–214, February 2012.

[84] R. Sanchez. Assembly homogenization techniques for core calculations. *Progress in Nuclear Energy*, 51:14–31, 2009.

[85] R. Sanchez et al. APOLLO II: a user-oriented, portable, modular code for multigroup transport assembly calculations. *Nuclear Science and Engineering*, 100:352–362, 1988.

[86] T. Sanda. ZPPR-18A EXPERIMENT: A 1,000 MWe-class sodium-cooled MOX-fueled FBR core Mock-Up critical experiment with two-homogeneous zones and control-rod withdraw, where enriched uranium is used with the shape of a sector in the outer core. Technical Report ZPPR-LMFR-EXP-003, NESI, Inc., IRPhEP Benchmark, 2006.

[87] T. Sanda. ZPPR-18C EXPERIMENT: A 1,000 MWe-class sodium-cooled MOX-fueled FBR homogeneous core Mock-Up critical experiment in the state of removal of one of eighteen half-inserted control rods, where enriched uranium is used with the shape of a sector in the outer core. Technical Report ZPPR-LMFR-EXP-008, NESI, Inc., IRPhEP Benchmark, 2006.

[88] J. F. Sauvage. *Phénix, 30 years of history: the heart of a reactor*. CEA, 2004.

[89] I. M. Sobol. *A Primer for the Monte Carlo Method*. Library of congress cataloging-in-Publication Data, 1994.

[90] J. Spanier and E. M. Gelbard. *Monte Carlo Principles and Neutron Transport Problems*. Addison-Wesley, 1969.

[91] J. C. Sublet, P. Ribon, and M. Coste-Delclaux. CALENDF-2010: User Manual. Technical Report 6277, CEA Report, 2011.

[92] T. Ohsawa T. Nakagawa, T. Kawano. Japanese evaluated nuclear data library Version 3 Revision-2: JENDL3.2. *Journal of Nuclear Science and Technology*, 32:1259–1271, 1995.

[93] T. Yamamoto. Monte Carlo method with complex weights for neutron leakage-corrected calculations and anisotropic diffusion coefficient generations. *Annals of Nuclear Energy*, 50:141–149, December 2012.

[94] G. TODOROVA, H. NISHI, and J. ISHIBASHI. Transport Criticality Analysis of FBR MONJU Initial Critical Core in Whole Core Simulation by NSHEX and GMVP. *Journal of Nuclear Science and Technology*, 41:493–501, April 2004.

[95] M. Tohjoh, M. Watanabe, and A. Yamamoto. Application of continuous-energy Monte Carlo code as a cross-section generator of BWR core calculations. *Ann. Nucl. Energy*, 32:857–875, 2005.

[96] J. Tommasi. Private communication. 2005.

[97] B. A. Worley and A. F. Henry. Spatial Homogenization of Diffusion Theory Parameters. Technical Report MITNE-210, Department of Nuclear Engineering, M.I.T., 1977.